ВІСНИК
КИЇВСЬКОГО НАЦІОНАЛЬНОГО УНІВЕРСИТЕТУ ІМЕНІ ТАРАСА ШЕВЧЕНКА

ISSN 1728-2306

РАДІОФІЗИКА ТА ЕЛЕКТРОНІКА (1)19/2013

Засновано 1999 року

УДК 517

Публікуються результати експериментальних та теоретичних досліджень у галузях фізичної електроніки, фізики плазми, фізики поверхні твердого тіла, емісійної електроніки, кріогенної та мікроелектроніки, нанофізики та наноелектроніки, високотемпературної надпровідності, квантової радіофізики, функціональної електроніки, твердотільної електроніки, мобільного зв'язку, медичної радіофізики, методів отримання діагностичної інформації та її комп'ютерної обробки.

Для науковців, викладачів вищої школи, студентів.

Experimental and theoretical contributions are published in the following fields: physical electronics, plasma physics, solid-state surface physics, emission electronics, cryogenic electronics, microelectronics, nanophysics and nanoelectronics, high-temperature supercondactive electronics, solid-state electronics, functional electronics, microwave electronics, quantum electronics, mobile communication, medical radiophysics, methods of receipt and computer processing of diagnosis information

Designed for researches, university teachers, students.

Адреса редколегії	**03127, м. Київ-127, проспект акад. Глушкова, 4 Г радіофізичний факультет ☎ (38044) 526 05 60**
Затверджено	**Вченою радою радіофізичного факультету 15.10.12 (протокол № 2)**
Атестовано	**Вищою атестаційною комісією України. Постанова Президії ВАК України № 1-05/1 від 10.02.10**
Зареєстровано	**Зареєстровано Міністерством юстиції України. Свідоцтво про державну реєстрацію КВ № 15797-4269Р від 02.10.09**
Засновник та видавець	**Київський національний університет імені Тараса Шевченка, Видавничо-поліграфічний центр "Київський університет". Свідоцтво внесено до Державного реєстру ДК № 1103 від 31.10.02**
Адреса видавця	**01601, Київ-601, б-р Т.Шевченка, 14, кімн. 43 ☎ (38044) 239 31 72, 239 32 22; факс 239 31 28**

ЗМІСТ

СОДЕРЖАНИЕ

CONTENTS

UDC: 538.911, 621.317

Yu. Boyko, Assoc. Prof., Department of Computer Engineering,
Faculty of Radiophysics, Taras Shevchenko National University of Kyiv;
D. Gryaznov, assist., V. Zinchuk, engineer, Information and Computer Centre,
Taras Shevchenko National University of Kyiv; S. Korin, post grad. stud.,
Department of Mathematics, Theoretical Physics and Computer Science,
Institute of High Technologies, Taras Shevchenko National University of Kyiv

DLTS SPECTROMETER MODIFICATION TO RETRIEVE TIME DEPENDENCIES OF CAPACITY RELAXATION

A principal hardware changes to existing automated relaxation spectrometers of deep levels in semiconductors for complete relaxation curves measurements are offered. The results are demonstrated the diode series D231A.

Keywords: DLTS, spectrometer, capacity relaxation, deep levels.

Introduction. The DLTS method [5], which is proposed in 1974 by Lang, allows observing the processes of emission of carriers from the deep energy levels during the thermal scan and gets the key parameters of deep centers such as the thermal capture cross section, activation energy and concentration of defects.

Due to the method's simplicity and high measurement speed and accuracy, the method has gained great popularity, which led to the development of automated systems for the of semiconductor materials studying. One such system was established in the 90s at the Kiev National University named after Taras Shevchenko at the Radiophysics Faculty. In contrast to the classical method, in which capacity difference in two time points are measured, that system used the correlation function, which measures the difference between averaged values of capacity during two time intervals [1]. As a result, it allowed improving the signal-to-noise ratio in the spectrum and increasing sensitivity to low concentrations of deep levels.

In the above approaches, only two points or two parts of the relaxation curve are processed, but in other parts there is also information that can be used to study the parameters of semiconductor materials. Also technical limitations of method do not allow using emission windows larger than 50ms.

Considering the modern technology requirements to more complete and accurate information that could not be obtained by previous methods of spectroscopy and existing of modern mathematical methods for results processing based on Laplace transformation (Laplace-DLTS) [3]) and artificial neural networks [2,4], the transition to complete relaxation curve measuring approach was made. It also provided an opportunity to use the emission windows rate more than 50 ms.

As a result, the question regarding possibility of modifying existing DLTS system to directly obtain the capacity relaxation curves was raised.

Analysis and researches. Information processing block of typical systems for the spectrum retrieving has the form shown in fig.1 and consists of a high-frequency amplifier, which reinforces signal from semiconductor sample in wide frequency range, and an analog multiplier to select capacity component from signal.

A signal at the entrance of the two-channel boxcar is proportional to the sum of the barrier and relaxation capacities. It has been proposed to measure the described signal by an ADC.

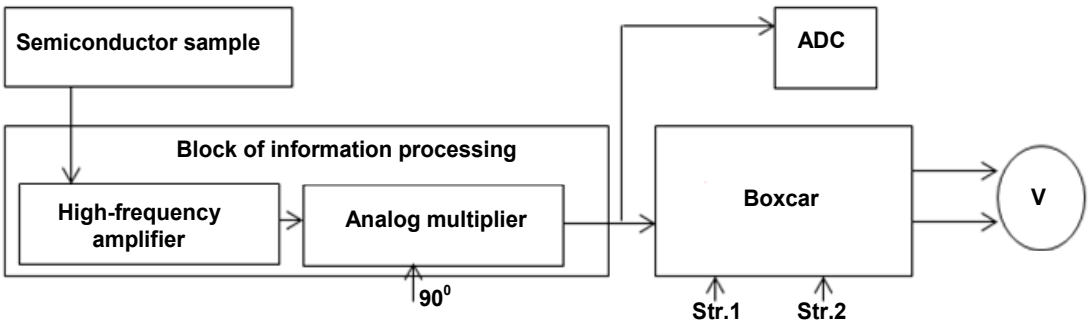

Fig. 1. The partial block diagram of system

Implemented changes allow making temperature scanning of D231A diode. So a family of relaxation curves at different temperatures was retrieved (fig.2).

To check the reliability of the measurements results, the spectrometer's correlation function was programmatically applied to the received data for the spectrum construction (fig.3), and the classical DLTS spectrum for the same diode was measured (fig.4). As you could notice there is the peaks congruence on temperature.

The obtained relaxation curves (fig. 2) represent the sum of a barrier capacity and relaxation capacity caused by the direct emission of carriers from deep centers. So finally we have a signal Cc (T) + Cr (t,T). However, to measure the concentration of deep levels, the measurement of constant capacity component should be performed to retrieve ratio ΔC (T) / Cc (T).

The spectrometer allows using the windows of emission up to 50 ms, that due to the correlation function leads to the maximum bias pulse duration up to 170 ms. It is not enough to finish relaxation from deep levels at certain temperatures, as one can see from presented family of curves (fig.2).

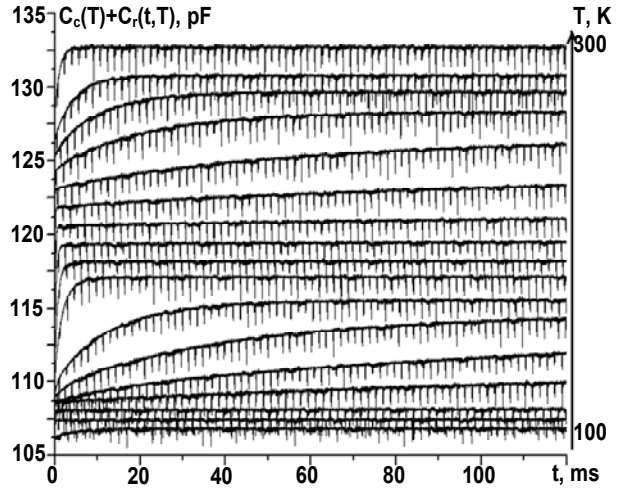

Fig. 2. The family of relaxation curves

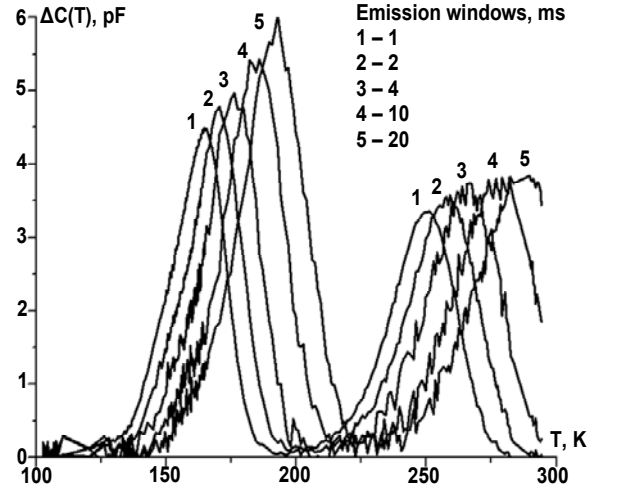

Fig. 3. DLTS diode spectrum based on the programmatically processing of the family of relaxation curves

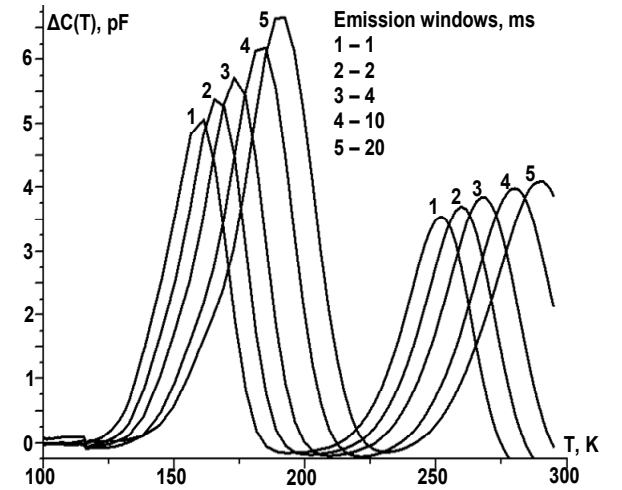

Fig. 4. DLTS diode spectrum

Therefore, modification (dash-dotted line in fig. 5) to the filling and reverse bias (FB) pulse shaper block was proposed. It was decided to remove connections to FB from the low-frequency generator (AG), which is used to control the power supply and the generation of filling and reverse bias pulses. Instead, a permanent voltage impulse was supplied to key 1 to keep it in open state in order to supply a semiconductor with constant reverse bias.

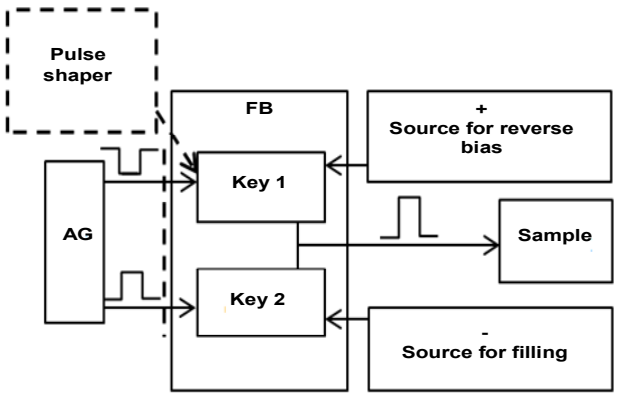

Fig. 5. The block diagram of the filling and reverse bias pulse shaper (FB)

As a result, measurements of the signal constant component and its dependencies on temperature were held (fig.6). The output allowed obtaining ΔC (T) / C_c (T) data required for processing by modern mathematical methods.

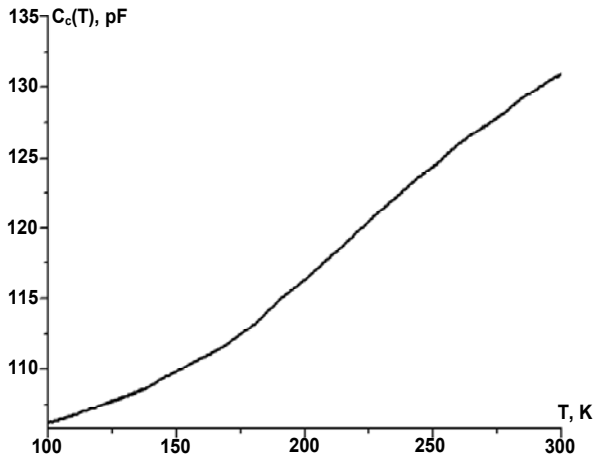

Fig. 6. Dependence of constant capacitance on temperature

Conclusions. Thus, the proposed modifications allow making quick and easy changes into existing automated relaxation spectrometers to meet the modern technological requirements and obtain data required for processing by advanced mathematical methods.

Reference

1. Boiko Y.V., Tretyak, O.V., Shmatov A.A. Generator of low-frequency pulses for a deep-level transient spectrometer // Instruments and Experimental Techniques. – 1994. – Vol. 36, №3, P. 317–320. 2. Gryaznov D.B., Korin S.A, Opylat V.J., Tretyak O.V, Artificial neural networks method fitting for deep-level transient spectroscopy signals analysis // Sensor Electronics and Microsystem Technologies. – 2012. — Vol. 3 (9), № 4. P. 81–89. 3. Dobaczewski L., Peaker A.R., Nielsen K.B., Laplace-transform deep-level spectroscopy: The technique and its applications to the study of point defects in semiconductors // Journal of Applied Physics. – 2004. – Vol. 96. – №9. P. 4689–4728. 4. Korin S.A, Gryaznov D.B., Boyko Yu.V. Examination of processes and methods of training neuronet for processing DLTS signals//Bulletin of the Taras Shevchenko National University of Kyiv. Series: Radiophysics & Electronics. – 2009. – 12. P. 23–27. 5. Lang D.V. Deep-level transient spectroscopy: A new method to characterize traps in semiconductors. // Journal of Applied Physics. – 1974. – Vol. 45, №7. P. 3023–3032.

Submitted on 30.04.13

Ю. Бойко, канд. фіз.-мат. наук,
каф. комп'ютерної інженерії, радіофізичний факультет,
Д. Грязнов, асист., В.Зінчук, інж.,
інформаційно-обчислювальний центр,
С. Корінь, асп., каф. математики, теоретичної фізики та комп'ютерних технологій,
інститут високих технологій, КНУ ім. Тараса Шевченка, Київ

МОДИФІКАЦІЯ РСГР СПЕКТРОМЕТРА ДЛЯ ОТРИМАННЯ ЧАСОВИХ ЗАЛЕЖНОСТЕЙ РЕЛАКСАЦІЇ

Запропоновано принципові апаратні зміни до існуючих автоматизованих релаксаційних спектрометрів глибоких рівнів у напівпровідниках для отримання повних релаксаційних кривих. Отримані результати продемонстровано на діоді серії Д231А.

Ключові слова: РСГР, спектрометр, релаксація ємності, глибокі рівні.

Ю. Бойко, канд. физ.-мат. наук,
каф. компьютерной инженерии, радиофизический факультет,
Д. Грязнов, ассист., В. Зинчук, инж.,
информационно-вычислительный центр,
С. Коринь, асп., каф. математики, теоретической физики и компьютерных технологий,
институт высоких технологий, КНУ им. Тараса Шевченка, Киев

МОДИФИКАЦИЯ РСГУ СПЕКТРОМЕТРА ДЛЯ ПОЛУЧЕНИЯ ВРЕМЕННЫХ ЗАВИСИМОСТЕЙ РЕЛАКСАЦИИ

Предложены принципиальные аппаратные изменения к существующим автоматизированным релаксационным спектрометрам глубоких уровней в полупроводниках для получения полных релаксационных кривых. Полученные результаты продемонстрированно на диоде серии Д231А.

Ключевые слова: РСГУ, спектрометр, релаксация емкости, глубокие уровни.

UDC 533.9.08

A. Veklich, Ph.D.,
A. Ivanisik, Ph.D.,
A. Lebid, post grad. stud.
Taras Shevchenko National University of Kyiv, Faculty of RadioPhysics

LASER ABSORPTION SPECTROSCOPY OF ELECTRIC ARC DISCHARGE PLASMA WITH COPPER IMPURITIES

Technique of laser absorption spectroscopy was applied for diagnostics of electric arc plasma between composite Cu-Mo electrodes. Spatial brightness distributions of laser emission were registered by CCD-matrix in realized experimental scheme. The graphical user interface for experimental data treatment was developed. Expected experimental errors are estimated. Obtained spatial distributions of copper atomic energy level $^5D_{5/2}$ population were used for calculation of plasma composition in assumption of local thermodynamic equilibrium.

Keywords: optical emission spectroscopy, plasma of electric arc discharge.

Introduction. Diagnostic of plasma is important part of numerous scientific investigations and industrial applications. The optical emission spectroscopy is the most widely used method for arc plasma diagnostic [7]. It is well known, that laser based techniques can significantly expand capabilities of plasma diagnostics.

Different approaches of laser based techniques were applied for arc plasma diagnostics. In work [6] distribution of tungsten impurities in atmospheric arc was obtained by techniques of laser-induced fluorescence. Thomson scattering of laser emission were used in work [8] for obtaining of electron density, gaseous and electron temperature distributions. Two dimensional distribution of electron density was obtained by Shack-Hartman method in work [5]. This method provides determination of refractive indexes, which depends on electron density in plasma.

Methods based on absorption of laser emission by plasma components also can be applied for arc plasma diagnostics. Particularly, method of linear laser absorption spectroscopy (LAS) provides simultaneous registration of plasma properties in different spatial points [1, 9].

Applications of copper based composite materials in the electrical engineering industry stimulate the interest in studying of the arc discharge plasma between such electrodes. It is reasonable to investigate such plasma by LAS with using of copper vapor laser.

The main aim of this work is determination of spatial distribution of copper atoms in the plasma of electric arc discharge between Cu-Mo electrodes by LAS. Analysis of obtained results is carried by specially developed graphical user interface. Obtained results are discussed as well as occurred errors.

Experimental setup. The arc was ignited between non-cooled electrodes in argon flow 6.4 slpm. The discharge gap was 8 mm and arc current was 3.5 A. Cu-Mo composite electrodes fabricated by electron beam evaporation and following condensation in vacuum were used. These electrodes have layered structure, content of molybdenum changes from layer to layer in range 1%–20%; average content of molybdenum was 12%.

Copper vapor laser "Kriostat 1" was used as source of probing emission on wavelength 510.5 nm, which is absorbed by copper atoms in arc plasma volume. Grade of laser emission absorption depends on population of copper atomic energy level $^2D_{5/2}$. As diameter of laser beam exceeds dimensions of arc plasma, so absorption distribution for different spatial points can be simultaneously registered by CCD-matrix (Fig.1).

Registered brightness distributions of reference laser beam and absorbed emission were used for determination of plasma properties. Reference image of spatial distribution of brightness in laser beam without arc is shown in Fig.2, *a*. The image obtained in presence of the arc is shown in Fig.2, *b*. These images were registered at the same operation conditions. CCD-matrix dynamic range selection was realized by changing of exposure time.

Graphical user interface for treatment of brightness spatial distribution (images) was specially developed. It allows:

- visualization of obtained brightness distributions;
- interactive selection of studied cross-section;
- determination of absorption characteristics for selected cross-section;
- determination of local values of absorption coefficient by Abel transformation.

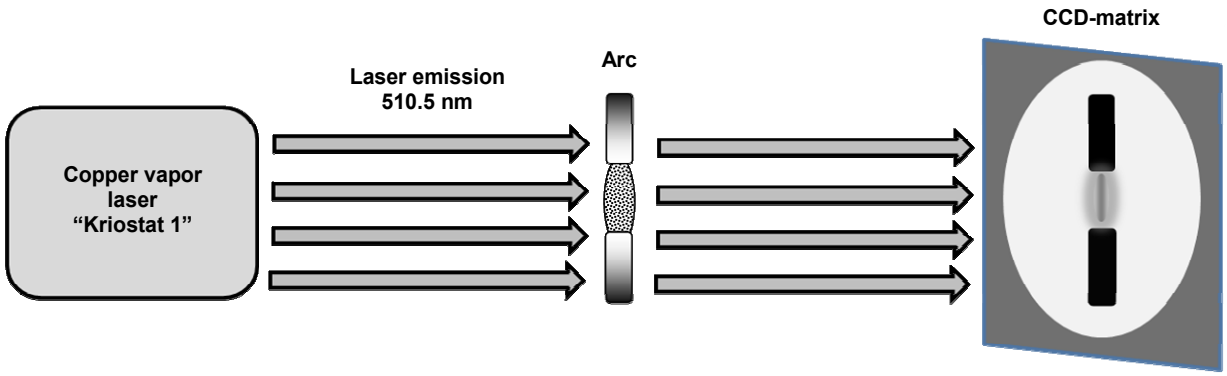

Fig. 1. Optical scheme of linear laser absorption spectroscopy

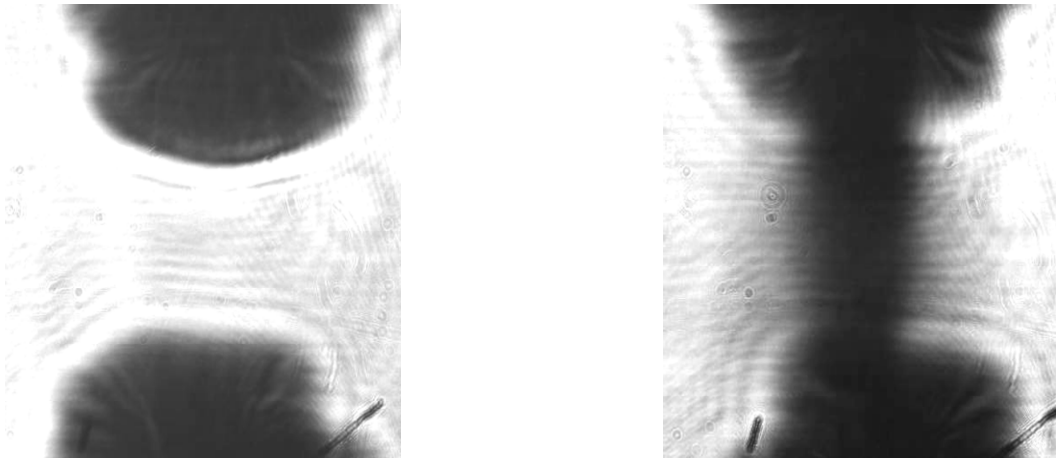

a) **b)**

Fig. 2. Spatial distributions of brightness in reference laser beam (a) and in presence of the arc (b)

Optical thickness τ at fixed wavelength and at every spatial point can be given as:

$$\tau = \ln \frac{b_{ref}}{b_{absorbed} - b_{arc}} \rightarrow \tau = \ln \frac{b_{ref}}{b_{absorbed}}, \; if \; b_{arc} = 0,$$

where b_{ref} and $b_{absorbed}$ are brightness of reference and absorbed by plasma laser emission; b_{arc} is brightness of own arc emission. It has been experimentally found that influence of own arc emission is negligible in studied experimental conditions. Absorption characteristics were calculated for middle cross-section of the arc column; radial profile of optical thickness τ is shown in Fig.3, *a*.

As soon as side-on (lateral) registration of intensity distribution has place in proposed experimental setup, therefore local values of absorption coefficient κ can be obtained from τ by solving of Abel equation:

$$\kappa = -\frac{1}{\pi} \int_{r}^{r_0} \frac{\tau'}{\left(x^2 - r^2\right)^{\frac{1}{2}}} dx,$$

where r_0 is radius of visible arc region, τ' is spatial derivative of optical thickness.

Generally it is complicated problem, which can be significantly simplified in case of axisymmetric arc configuration. The method [4] of Abel transformation was applied:

$$\kappa_j = \frac{1}{r_0} \sum\nolimits_k a_{jk} \cdot \tau_k,$$

where j and k are indexes of local and observed characteristics, a_{jk} are appropriate transformation coefficients. Obtained in this way local values of absorption coefficient κ are shown in Fig.3, *b*.

As far as half width of laser spectral line is narrower than absorption line of plasma, so κ can be assumed as absorption in the center of spectral line. Population of absorbing atomic level $^2D_{5/2}$ was calculated with regard to spectral line contour. Since, Doppler broadening dominates for this line at 3.5 A current, so its profile can be described by Gaussian function with half width $\Delta\lambda_D$.

$$\Delta\lambda_D = 7.16 \cdot 10^{-7} \cdot \lambda \cdot \sqrt{\frac{T}{M}},$$

where M is atomic weight, T is previously measured plasma temperature [3].

So, population N_k (Fig.4) of lower energy level can be given as:

$$N_k = \frac{\kappa \cdot \Delta\lambda_D}{8.19 \cdot 10^{-20} \cdot f_{ki} \cdot \lambda^2},$$

where f_{ki} and λ are oscillator strength and wavelength of the absorbing spectral transition.

It must be noted, that these population values are independent on local thermodynamic equilibrium assumption.

Calculation of plasma composition. Distribution of copper atom concentration N_{Cu} (Fig.5) can be calculated according to Boltzmann law with using of previously obtained temperature profile:

$$N_{Cu} = \frac{N_k \cdot \Sigma_{Cu}}{g_i \cdot \exp\left(-\frac{E_i}{kT}\right)},$$

where Σ_{Cu} is partition function of copper atom, g_i and E_i statistical weight and energy of absorbing level.

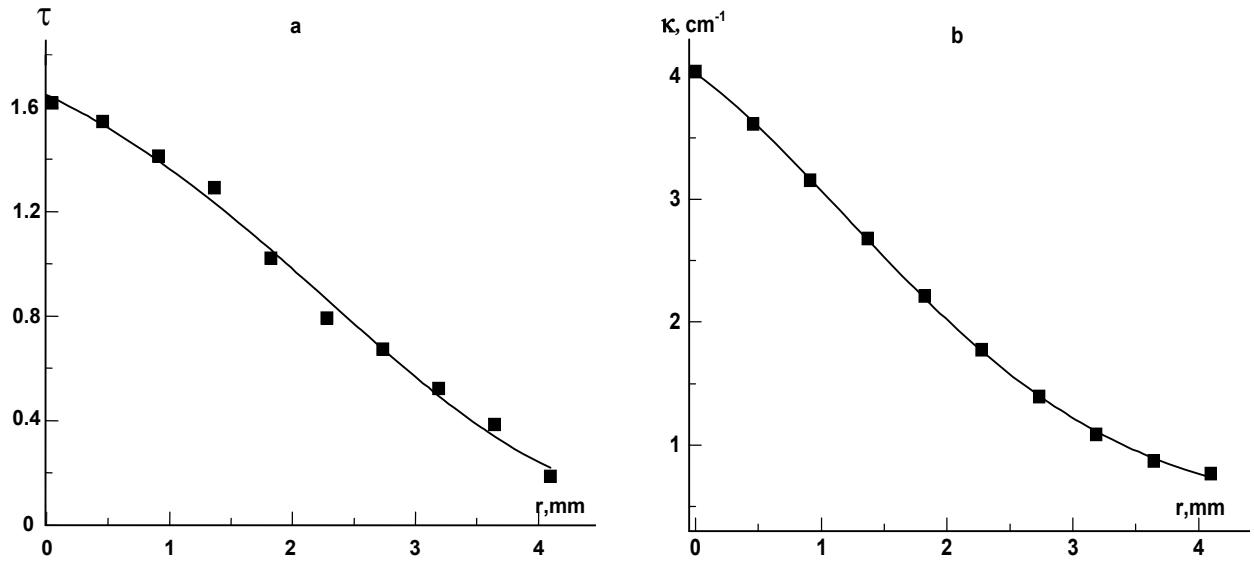

Fig. 3. Radial profiles of optical thickness τ (a) and local values of absorption coefficient κ (b)

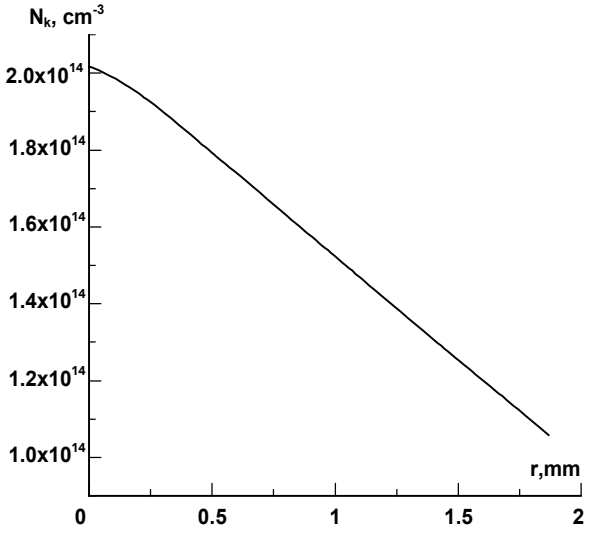

Fig. 4. Radial profiles of population of lower energy level N_k

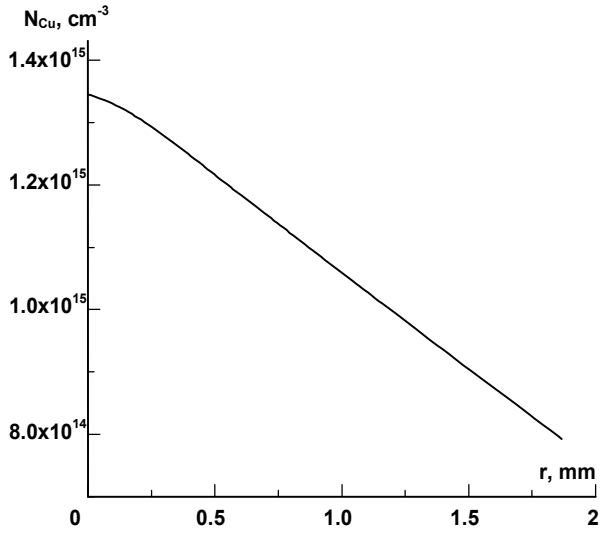

Fig. 5 Radial profiles of concentration of copper atoms

Plasma of electric arc discharge between Cu-Mo in argon flow generally contains atoms and ions of copper, molybdenum and argon. Plasma in state of local thermodynamic equilibrium can be described by equations set [2], which consist of Saha equations for each plasma component, equation of charge neutrality, perfect gas law. Additionally, expression for ratio of Cu and Mo atoms' concentration in plasma volume were included into equations set. This expression can be obtained from ratio of CuI 510.5 and MoI 550.6 nm spectral lines intensities:

$$\frac{N_{Cu}}{N_{Mo}} = \frac{I_{Cu} \cdot \Sigma_{Cu} \cdot \lambda_{Cu}^2 \cdot (gf)_{Mo} \cdot e^{\frac{E_{Cu}}{kT}}}{I_{Mo} \cdot \Sigma_{Mo} \cdot \lambda_{Mo}^2 \cdot (gf)_{Cu} \cdot e^{\frac{E_{Mo}}{kT}}}$$

where Σ_{Cu} are Σ_{Mo} are partition functions of copper and molybdenum atoms, $(gf)_{Cu}$, $(gf)_{Mo}$ and E_{Cu}, E_{Mo} are oscillator strengths and energies of appropriate spectral lines. I_{Cu} and I_{Mo}, λ_{Cu} and λ_{Mo} are intensities and wavelengths.

Calculated in this way plasma composition is shown in Fig. 6. One can see that atomic argon is dominant plasma component.

Electric conductivity of plasma channel mainly supports by ionization of copper. Contribution of molybdenum ions in plasma conductivity is relatively low, because amount of molybdenum vapors is lower than copper one. However, ionization degree of molybdenum is high, the main reason of that is low ionization potential of molybdenum in comparison with copper and argon.

It would be interesting to follow influence of initial electrodes' composition and structure on plasma properties.

In work [2] were performed investigations of Cu-Mo composite electrodes composed of 50 % copper and 50 % molybdenum (by mass), which was fabricated by methods of powder metallurgy. Contents of metallic vapor for powder metallurgy technology (curve 1) and for electron beam evaporation and following condensation in vacuum (curve 2) are shown in Fig. 7. One can see that in case of the last technology the content of metallic vapor is lower. So, erosion properties of these electrodes are better at conditions of experiment.

Content of metallic vapor were calculated as:

$$X_{Me} = \frac{N_{Cu} + N_{Cu+} + N_{Mo} + N_{Mo+}}{N_{Cu} + N_{Cu+} + N_{Mo} + N_{Mo+} + N_{Ar} + N_{Ar+}} \cdot 100\%,$$

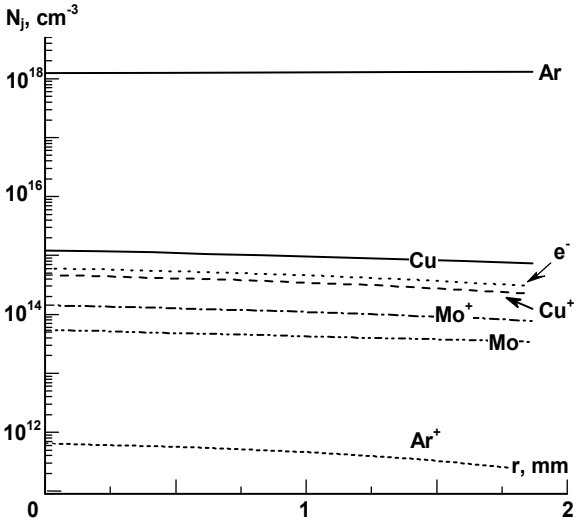

Fig. 6. Calculated plasma composition

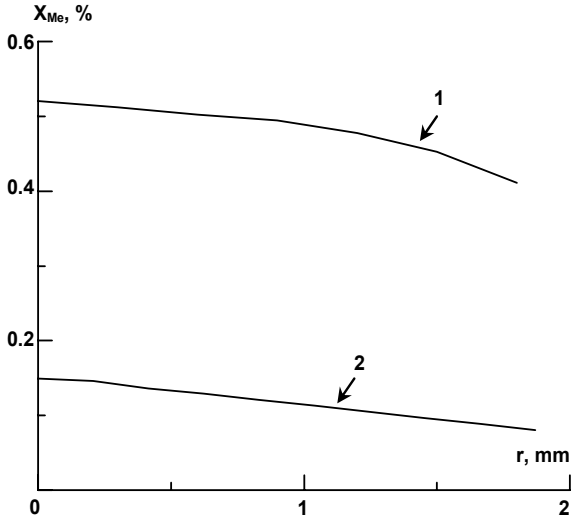

Fig. 7. Content of metallic vapor in plasma of electric arc discharge between Cu-Mo electrodes fabricated by different technology

Estimation of errors. As far as technique of linear laser absorption spectroscopy based on measurement of brightness b_{ref} and $b_{absorbed}$, so standard deviation of optical thickness $\Delta\tau$ can be estimated as:

$$\Delta\tau = \left(\left(\frac{\partial\tau}{\partial b_{ref}} \cdot \Delta b_{ref} \right)^2 + \left(\frac{\partial\tau}{\partial b_{absorbed}} \cdot \Delta b_{absorbed} \right)^2 \right)^{1/2},$$

or in explicit form:

$$\Delta\tau = \left(\left(\frac{\Delta b_{ref}}{b_{ref}} \right)^2 + \left(\frac{\Delta b_{absorbed}}{b_{absorbed}} \right)^2 \right)^{1/2}.$$

Error in determination of local values of absorption coefficient κ caused by Abel transformation, according to method [4], it can be estimated as

$$\Delta\kappa = \Delta\tau \sqrt{\sum_k a_{jk}^2},$$

where a_{jk} is appropriate Bockasten's coefficients.

Population of absorption level N_k linearly depends on κ, therefore:

$$\Delta N_k = N_k \cdot \frac{\Delta\kappa}{\kappa}.$$

As N_{Cu} depends on population of absorbing level N_k and plasma temperature T, so standard deviation can be estimated as:

$$\Delta N_{Cu} = \left(\left(\frac{\partial N_{Cu}}{\partial N_k} \cdot \Delta N_k \right)^2 + \left(\frac{\partial N_{Cu}}{\partial T} \cdot \Delta T \right)^2 \right)^{1/2}.$$

After substitution and simplifying it can be given as:

$$\frac{\Delta N_{Cu}}{N_{Cu}} = \left(\left(\frac{\Delta\kappa}{\kappa} \right)^2 + \left(\frac{E_i}{kT} \right)^2 \cdot \left(\frac{\Delta T}{T} \right)^2 \right)^{1/2}.$$

In assumption of typical inaccuracy of brightness measurements $\Delta I / I = 0.1$ or 10% and acceptable inaccuracy of plasma temperature determination no more than 10%, relative error of copper concentration N_{Cu} does not exceed 27%.

Conclusions. Technique of laser absorption spectroscopy was applied for diagnostics of electric arc discharge between Cu-Mo composite electrodes. Experimental setup and graphical user interface for data acquisition and treatment are developed.

Proposed technique allows determination of copper atoms concentration profiles, which were used in calculation of plasma composition in assumption of local thermodynamic equilibrium.

Obtained results indicate, that atomic argon is dominant plasma component, while electric conductivity of plasma channel mainly supports by ionization of copper and in smaller degree by molybdenum ionization.

Content of metallic vapors in plasma of electric arc discharge between composite electrodes fabricated by electron beam evaporation and following condensation in vacuum are significantly lower than for electrodes fabricated by powder metallurgy.

Occurred errors are estimated with regards to uncertainty of registration and treatment. Relative error of copper concentration N_{Cu} does not exceed 27% in the worst case.

Reference

1. Babich I.L., Boretskij V.F., Veklich A.N. Ivanisik A.I. Spectroscopy of electric arc discharge plasma with copper impurities // Electrical contacts and electrodes. Frantsevich Institute for Problems of Materials Science. – 2008. – P. 4–13. 2. Investigations of electric arc discharge plasma between composite electrodes on copper base / Babich I.L., Boretskij V.F., Veklich A.N. et al. // Electrical contacts and electrodes. Frantsevich Institute for Problems of Materials Science. – 2012. – P. 91–100. 3 Investigations of thermal plasma with metal impurities. Part II: Peculiarities of spectroscopy by WI, MoI and CuI spectral lines properties / Veklich A.N, Lebid A.V., Soroka P.V et al. // International Conference-School on Plasma Physics and Controlled Fusion: Book of abstracts, Alushta, Ukraine, September 17–22, 2012. 4. Bockasten K. Transformation of observed radiances into radial distribution of the emission of a plasma // Journ. of Opt. Soc. of Am. – 1961. – Vol. 51, № 9 – P. 943–947. 5. Shack–Hartmann type laser wavefront sensor for measuring two-dimensional electron density distribution over extinguishing arc discharge / Inada Y., Matsuoka S, Kumada A. et al. // J. Phys. D: Appl. Phys. – 2012. – 45, № 43. 6. Kühn G., Könemann F., Kock M. 2D display of tungsten impurity in a free-burning arc using laser-induced fluorescence // J. Phys. D: Appl. Phys. – 2002. – 35, № 17, – P. 2096–2104. 7. Murphy A. The effects of metal vapour in arc welding // J. Phys. D: Appl. Phys. – 2010. – 43, № 43. 8. Snyder S.C., Lassahn G.D., Reynolds L.D. Direct evidence of departure from local thermodynamic equilibrium in free-burning arc-discharge plasma // Phys. Rev. E – 1993. – Vol. 48. № 5. – P 4124–4127. 9 Zaydel A. N., Ostrovskaya G. V. Laser methods for plasma diagnostics – Leningrad, 1977.

Submitted on 20.11.12

**Веклич А., канд. фіз.-мат. наук, доц. каф. фізичної електроніки,
Іванісік А., канд. фіз.-мат. наук, доц. каф. медичної радіофізики,
Лебідь А., асп. каф. фізичної електроніки,
радіофізичний факультет, КНУ імені Тараса Шевченка, Київ**

ЛАЗЕРНА АБСОРБЦІЙНА СПЕКТРОСКОПІЯ ПЛАЗМИ ЕЛЕКТРОДУГОВОГО РОЗРЯДУ З ДОМІШКАМИ МІДІ

Для діагностики плазми електродугового розряду між композитними Cu-Mo електродами застосовано методику лінійної лазерної абсорбційної спектроскопії. Реалізовано експериментальну схему реєстрації просторових розподілів інтенсивності лазерного випромінювання за допомогою ПЗЗ-матриці. Розроблено програмний інтерфейс користувача для обробки експериментальних даних, визначено ймовірну експериментальну похибку. Отримані просторові розподіли заселеності $^5D_{5/2}$ рівня атомів міді використано для розрахунку складу плазми у припущенні локальної термодинамічної рівноваги.

Ключові слова: лазерна абсорбційна спектроскопія, плазма електродугового розряду.

**Веклич А., канд. физ.-мат. наук, доц. каф. физической электроники,
Иванисик А., канд. физ.-мат. наук, доц. каф. медицинской радиофизики,
Лебедь А., асп. каф. физической электроники,
радиофизический факультет, КНУ имени Тараса Шевченко, Киев**

ЛАЗЕРНАЯ АБСОРБЦИОННАЯ СПЕКТРОСКОПИЯ ПЛАЗМЫ ЭЛЕКТРОДУГОВОГО РАЗРЯДА С ПРИМЕСЬЮ МЕДИ

Для диагностики плазмы электродугового разряда между композитными Cu-Mo электродами применена методика лазерной абсорбционной спектроскопии. Реализована экспериментальная схема регистрации пространственных распределений интенсивности лазерного излучения с помощью ПЗС-матрицы. Разработан программный интерфейс пользователя для обработки экспериментальных данных и определена ожидаемая ошибка эксперимента. Полученные пространственные распределения заселенности энергетического уровня $^5D_{5/2}$ атомов меди использованы для расчета компонентного состава плазмы в предположении локального термодинамического равновесия.

Ключевые слова: лазерная абсорбционная спектроскопия, плазма электродугового разряда.

UDC 536.2

**V. Vysotskii, D.Sci., Department Mathematics and Theoretical radiophysics,
Faculty of Radiophysics, Taras Shevchenko National University of Kyiv,
V. Vassilenko, PhD, Centre of Physics and Technological Research (CeFITec),
Faculty of Sciences and Technology, NOVA University of Lisbon,
Campus FCT UNL, 2829–516 Caparica, Portugal,
A. Vasylenko, post grad. stud., Department Mathematics and Theoretical radiophysics,
Faculty of Radiophysics, Taras Shevchenko National University of Kyiv**

PROPAGATION OF TEMPERATURE WAVES IN MEDIUM WITH INTERNAL THERMAL RELAXATION

In this article the wave solutions of heat transfer equations, for classical model and for two alternative non-stationary models (hyperbolic and model with a time delay) have been studied. Modeling of temperature impulse propagation was performed according to dispersion relations obtained from heat transfer equations. It was shown that propagation of temperature impulse in non-stationary models could significantly differ from temperature diffusion in classical model. This can be used for signal transmission and that temperature waves could be used for delay line construction.

Keywords: wave heat transfer, non-stationer models of heat transfer, temperature impulse propagation, undumped temperature waves, dispersion of temperature waves.

Introduction. For the long time the heat transfer problems were regarded using only a classical Fourier's hypothesis that heat flux is proportional to a module of temperature gradient and have opposite direction. In the 50th of the last century first attempt to regard non-stationary heat transfer processes were made by Cattaneo and Vernotte, what leads to a hyperbolic equation for temperature field [2, 12]. Since then the hyperbolic and non-linear parabolic heat transfer models were intensively studied and a big amount of new heat transfer regimes were established, such as traveling waves, blow-up regimes and some others [7–11]. Hypothesis of finite velocity of thermal signal propagation became especially popular in last two decades. Also the non-stationary solutions, such as the temperature waves, started to attract attention of researchers, especially for application in the scanning thermo wave microscopy (STWM), which is one of the method to investigate the under layers of surface for the purpose to determine heat conductivity [1, 5, 6]. In present work we regard thermal wave solutions not only for a classical heat transfer model but also for non-stationary models: hyperbolic and with time delay. Obtained relations of dispersion were used for modeling of temperature impulse propagation, regarding the possibility to use temperature field for signals transmission.

Wave solutions of heat transfer equations. General form of classical heat transfer equation is

$$\rho c \frac{\partial T(x,t)}{\partial t} = \lambda \Delta T(x,t) \tag{1}$$

where ρ is density, c is heat capacity and λ is heat conductivity. Suppose that:

$$T = T_0 e^{i(\omega t - kx)} \tag{2}$$

From (1) and (2) and regarding that k is a complex value $k = k_1 + ik_2$ dispersion relation could be obtained:

$$i\rho c\omega = -\lambda\left(k_1^2 - k_2^2\right) - i2\lambda k_1 k_2 \tag{3}$$

It gives the system of equations:

$$\begin{cases} \lambda\left(k_1^2 - k_2^2\right) = 0 \\ \rho c\omega + 2\lambda k_1 k_2 = 0 \end{cases} \tag{4}$$

In a second half of twenty century the hyperbolic heat transfer equation became more common, especially in the problems of laser impulse interaction with matter. Since the duration of laser impulses could be very short, it yields to non-stationary problems of heat transfer [6]. Hyperbolic heat transfer equation is as follows:

$$\rho c \frac{\partial T(x,t)}{\partial t} + \tau \rho c \frac{\partial^2 T(x,t)}{\partial t^2} = \lambda \Delta T(x,t) \tag{8}$$

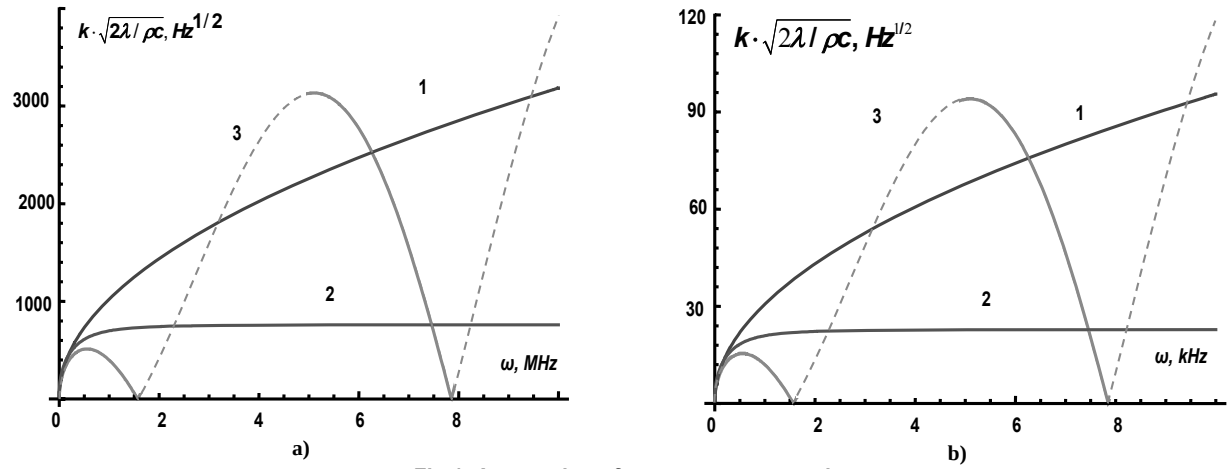

Fig.1. Attenuation of temperature waves in
1 – classical model, 2 – hyperbolic model, 3 – model with delay.
The dashed line corresponds to areas of frequencies in which $\cos\omega\tau < 0$ and thermal waves are not generated

Here τ is a relaxation time, parameter that describes the relaxation of local macroscopic subsystems to equilibrium thermal distribution. By the same way as it was done for the classical model, the dispersion relations for the hyperbolic model could be found as follows:

$$\begin{cases} \rho c\omega + 2k_1k_2\lambda = 0 \\ \lambda\left(k_1^2 - k_2^2\right) - \tau\rho c\omega^2 = 0 \end{cases} \quad (9)$$

For such model the temperature waves becomes as:

$$\begin{cases} T = T_0 e^{\pm(k/\beta_+)x} e^{i(\omega t \pm k\beta_+ x)} \\ T = T_0 e^{\pm k\beta_- x} e^{i(\omega t \pm (k/\beta_-)x)} \end{cases} \quad (10)$$

Where

$$\beta_\pm = \sqrt{\sqrt{\omega^2\tau^2 + 1} \pm \omega\tau} \quad (11)$$

From (10) it can be seen that for the hyperbolic model were obtained two different possible situations for the same conditions. It has also be notices that in both cases attenuation do not increase to infinity with frequency.

In last two decades gained popularity single- and dual-phase-lag heat conduction models [3,4]. Here we consider only single-phase-lag equation, also called as equation with time delay. It has the next from:

$$\rho c \frac{\partial T(x, t+\tau)}{\partial t} = \lambda \Delta T(x,t) \quad (12)$$

Analysis of dispersion relations for this model:

$$\begin{cases} \rho c\omega\cos\omega\tau + 2k_1k_2\lambda = 0 \\ \lambda\left(k_1^2 - k_2^2\right) - \tau\rho c\omega\sin\omega\tau = 0 \end{cases} \quad (13)$$

lead to the next temperature waves:

$$T = T_0 e^{\pm k\frac{\cos\omega\tau}{\sqrt{1+\sin\omega\tau}}x} e^{i\left(\omega t \pm k\sqrt{1+\sin\omega\tau}x\right)} = T_0 e^{\pm k\sqrt{1-\sin\omega\tau}x} e^{i\left(\omega t \pm k\frac{\cos\omega\tau}{\sqrt{1-\sin\omega\tau}}x\right)} \quad (14)$$

This model with delay predicts not only the possibility of attenuation decreasing with frequency at $\cos\omega\tau > 0$, but also predicts the existence of undamped thermal waves at $\omega\tau = 2n\pi + \pi/2,\ n = 0,1,2...$. The excitation of thermal waves is impossible at $\cos\omega\tau < 0$, because of unlimited increasing amplitude of such waves when $x \to \infty$. The frequency dependence of attenuation absolute value is shown on fig. 1 a) and b) for relaxation time equal to microseconds and milliseconds respectively.

Modeling of temperature impulse evolution. The modeling of single temperature impulse evolution was performed for normalized temperature. The initial impulse is given with a formula:

$$T_0(x=0,t) = \frac{T(x=0,t) - T_{\min}}{T_{\max} - T_{\min}} = h\left(t + \frac{P}{2}\right) - h\left(t - \frac{P}{2}\right) \quad (15)$$

Where P – duration of impulse, $h(t)$ - Heaviside function.

In what follows F[.] means Fourier transform operator. Fourier transform of initial impulse is:

$$T_0(\omega) = F[T_0(x=0,t)] = \frac{P}{\sqrt{2\pi}} Sinc\left(\frac{\omega P}{2}\right) \quad (16)$$

Evolution of thermal impulse will be given with:

$$T_0(x,t) = F^{-1}[T_0(\omega)\cdot e^{i(\omega t - k(\omega)x)}] \quad (17)$$

On fig. 2 results of modeling are shown. For the calculations the next parameters were used: $G = \lambda / c\rho = 3.10^{-3}\, cm^2/s$, $\tau = 10\, s$. On fig. 2 a),b) is shown evolution of temperature impulse according to a classical equation, it is obviously that according to this model propagation of thermal impulse is impossible because of dispersion initial impulse loose it's form, and in a distant spot it is impossible to detect beginning and end of thermal impulse. Opposite situations take a place in Fig. 2 c), d). In hyperbolic heat transfer model traveling impulse solution is possible, but also deformation of impulse form takes a place due to the dispersion. Nevertheless, it is possible to detect beginning and end of impulse. It makes possible to use temperature field to transfer information, but it should be mentioned that propagation of information in thermal field is very slow comparing to electromagnetic field and acoustics waves. It means that temperature field could be used for information transfer only when there is a need to create delay between two signals. But still as it is shown on fig. 2 c), d) amplitude of temperature impulse decrease very fast with distance from initial source. Situation on fig. 2 e), f) differ a lot from previous. Also traveling wave solution take a place but contour of wave differs from the one of initial impulse. On Fig. 3 the thermal waves appears as a response of medium on single impulse heating. All those results could be important in problems of microchips cooling, because many modern microchips works at frequencies comparable with $\frac{1}{\tau}$.

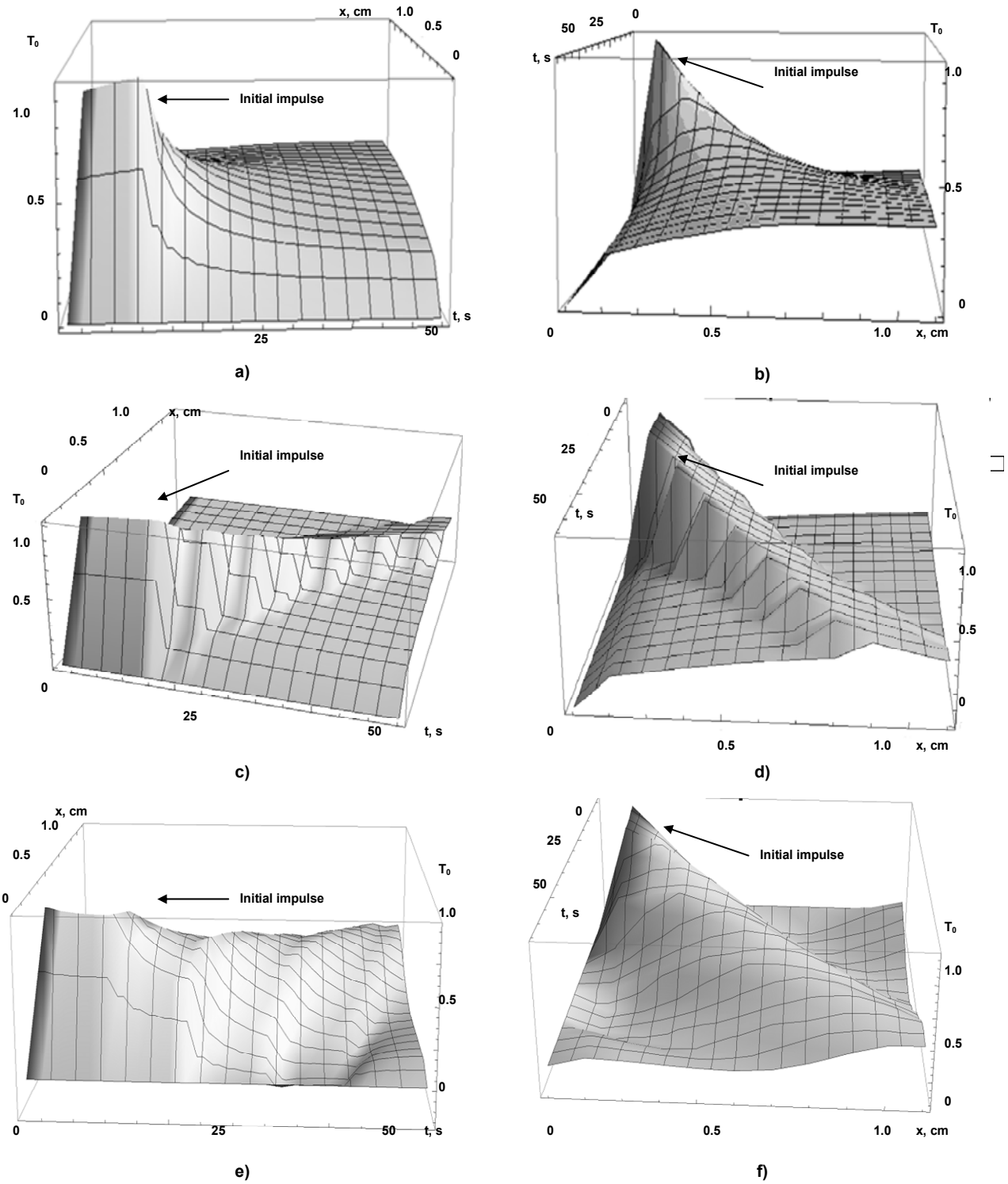

Fig. 2. Numerical evaluation of thermal impulse propagation
a),b) – classic model; c),d) – hyperbolic model; e),f) – delay model with denied zones in specter

Conclusions. It was shown that for the non-stationary models of heat transfer with hypothesis of the relaxation time propagation of traveling temperature the impulse is possible. What theoretically creates the possibility to use temperature field for the purpose of slow signal transfer and constructing of the delay lines.

Performed modeling reveals a possibility to use the temperature field as a filter, what follows from modeling shown on figure 3. It should be mentioned that the model with time delay also is a filter, because there are zones in the specter where amplitude of waves should increase. Even the fact that temperature waves can't transfer energy can't explain the possibility for existing of such kind of waves. This kind of system will be not stable and any small fluctuation will lead to a macroscopic periodic processes. However, it is more natural to regard it as a limitation of model with delay. Thus in modeling amplitudes of waves in denied zones were forcefully made to be zero. In the Fig. 3 was shown a transformation of initial thermal impulse into temperature waves due to the different value of attenuation coefficient at different frequencies.

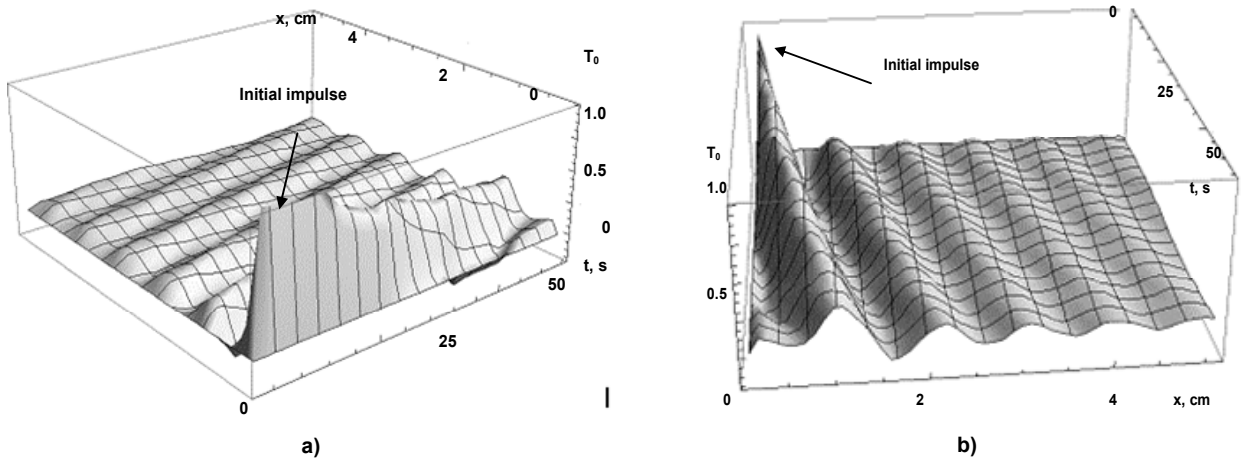

Fig.3. Numerical evaluation of thermal impulse propagation
a), b) delay model with denied zones in specter transformation of thermal impulse into thermal waves

Also should be taken into consideration the fact that both, hyperbolic heat transfer equation and equation with time delay, are not precisely from kinetic equation, since in both cases some simplifications were made. However these models are more accurate for non-stationary problems than for classical equation. In order to obtain the last one a time derivative of distribution function is suppose to be equal to 0, while non-stationary models are obtained in assumption that time derivative is not zero but a small value and, approximately, could be regarded as a difference. Of course for the models when high harmonics have significant amplitudes the assumptions on what the non-stationary models with relaxation time hypothesis are based becomes not appropriate.

Undamped slow thermal waves with velocity

$$v_n = \sqrt{2G\omega_n},\ \omega_n = (2n\pi + \pi/2)/\tau,\ n = 0,1,2... \qquad (18)$$

can be used for signal transmission and at delay line construction. Such slow waves also can be used in thermo-optic deflectors (analog of acoustic-optic deflectors) for angular control and modulation of weak laser radiation.

Reference

1. Araki N., Yang J., Tang D. and Makino A. Measurement of the Thermal Conductivity of Layered Film by Periodic Heating // High Temp.-High Press. – 1998. – Vol. 30. – pp. 321–326. 2. Cattaneo C. R. Sur une forme de l'équation de la chaleur éliminant le paradoxe d'une propagation instantanée // Comptes Rendus. – 1958. – Vol. 247. – pp. 431–433. 3. Lin Cheng, Mingtian Xu, Liqiu Wang From Boltzmann transport equation to single-phase-lagging heat conduction // Int. J. Heat Mass Trans. – 2008. – Vol. 51. – pp. 6018–6023. 4. Mingtian Xu, Liqiu Wang Dual-phase-lagging heat conduction based on Boltzman transport equation // Int. J. Heat Mass Trans. – 2005. – Vol. 48. – pp. 5616–5624. 5. Ohmyoung Kwon, Li Shi, Arun Majumdar Scanning Thermal Wave Microscopy (STWM) // Transactions of the ASME. – 2003. – Vol. 125. – pp. 156–163. 6. Salazar A., Mendioroz A. Propagation of thermal waves across a wedge // Jour. of Appl. Phys. – 2012. – V.112. – pp. 063511 – 063511 7. Samarskii A.A., Galaktonov V.A., Kurdyumov S.P., Mihailov A.P. Blow-up regimes – M: SCIENCE, 1987. – 481p. 8. Shashkov A.G., Bubnov V.A., Yanovskii S.Yu. Wave heat transfer – M.:Editorial URSS, 2004. – 296p 9. S.L. Sobolev Local non-equilibrium models of transfer processes // UFN. – october 1997. – Vol. 167. – P. 1095–1106. 10. Telegin A.S., Shvydkiy V.S., Yaroshenko Yu.G. Heat and mass transfer – M:Akademkniga, 2002. – 455p. 11. Tzou D. Y. Shock wave formation around a moving heat source in a solid with finite speed of heat propagation // Int. J. Heat Mass Trans. – 1979. – Vol. 32(10). – pp. 1979–1987. 12. Vernotte P. Les paradoxes de la theorie continue de l'équation de la chaleur // Comptes Rendus. – 1958. – Vol. 246. – pp 3154–3155.

Submitted on 17.01.13

В. Висоцький, д-р фіз.-мат. наук, каф. математики та теоретичної радіофізики,
радіофізичного факультету, КНУ ім. Тараса Шевченка, Київ
В. Василенко, канд. фіз.-мат. наук, центр фізичних та технологічних досліджень (CeFITec),
факультет науки та технологій, Ліссабонский університет НОВА,
Кампус ФНТ УНЛ, 2829-516 Капаріка, Португалія
А. Василенко, асп. каф. математики та теоретичної радіофізики
радіофізичного факультету, КНУ ім. Тараса Шевченка, Київ

РОЗПОВСЮДЖЕННЯ ТЕМПЕРАТУРНИХ ХВИЛЬ В СЕРЕДОВИЩАХ З ТЕПЛОВОЮ РЕЛАКСАЦІЄЮ

У роботі розглянуто хвилеві розв'язки рівнянь теплопровідності для класичної моделі, а також для двох альтернативних нестаціонарних моделей. Представленні результати моделювання поширення температурних імпульсів з урахуванням дисперсійних співвідношень отриманих на основі класичної моделі теплопровідності, гіперболічної моделі теплопровідності та моделі з часом затримки. Показано, що при умові співрозмірності тривалості температурних імпульсів із часом релаксації середовища в нестаціонарних моделях має місце поширення температурних фронтів, що за своїм характером суттєво відрізняється від дифузії тепла в класичній моделі і може бути використано при передачі інформації, зокрема в лініях затримки.

Ключові слова: хвилева теплопровідність, нестаціонарні моделі теплопровідності, розповсюдження температурного імпульсу, незатухаючі температурні хвилі, дисперсія температурних хвиль.

В. Высоцкий, д-р физ.-мат. наук, каф. математики и теоретической радиофизики
радиофизического факультета, КНУ им. Тараса Шевченка, Киев
В. Василенко, канд. физ.-мат. наук, центр физических и технологических исследований (CeFITec),
факультет науки и технологий, Лиссабонский университет НОВА,
Кампус ФНТ УНЛ, 2829-516 Капарика, Португалия
А. Василенко, асп. кафедра математики и теоретической радиофизики
радиофизического факультета, КНУ им. Тараса Шевченка, Киев

РАСПРОСТРАНЕНИЕ ТЕМПЕРАТУРНЫХ ВОЛН В СРЕДАХ С ТЕПЛОВОЙ РЕЛАКСАЦИЕЙ

В статье рассмотрены волновые решения уравнений теплопроводности для классической модели, а также для двух альтернативных нестационарных моделей. Представлены результаты моделирования распространения температурных импульсов, с учетом дисперсионных соотношений полученных основываясь на классической модели теплопроводности, гиперболической модели теплопроводности и модели со временем задержки. Показано, что при условии соизмеримости длительности температурных импульсов со временем релаксации среды в нестационарных моделях возможно распространение температурных фронтов, что по своему характеру существенно отличается от диффузии тепла в классической модели и может быть использовано для передачи информации, в частности в линиях задержки.

Ключевые слова: волновая теплопроводность, нестационарные модели теплопроводности, распространение температурного импульса, незатухающие температурные волны, дисперсия температурных волн.

UDC 537.86

Yu. Hayday Ph.D, V. Sidorenko Ph.D,
O. Sinkevych eng., I. Serdega eng.
Department Quantum Radiophysics, Faculty of Radiophysics,
Taras Shevchenko National University of Kyiv

FORCED FREQUENCY SYNCHRONIZATION EFFECT IN THE MICROWAVE MICROSCOPE WITH THE ACTIVE PROBE

Forced frequency synchronization of the active probe of the microwave microscope is considered. A method of probe's sensitivity increasing based on the quasiperiodic regime with high curvature of the frequency characteristic was proposed.
Keywords: near-field microwave microscope, forced frequency synchronization

Scanning near-field microwave microscopy (SNMM) [1] is a modern method of dielectrics and semiconductors properties examination. It provides local measurements with high sensitivity to dielectric permittivity and losses and can be combined with other types of scanning probe microscopy.

Microwave microscopy is based on measuring of the resonant frequency and quality factor of the microwave probe while scanning the sample under study. One of the most widespread types of resonator is λ/4 coaxial resonator with the needle on the central line. To measure f_{res} and Q with the maximal accuracy different modulation and compensation schemes are applied. We proposed a microwave probe scheme of active type [5], which is simpler and provides sensitivity $\Delta\varepsilon/\varepsilon \sim 10^{-3}$ with spatial resolution $\Delta x \sim 10$ mkm. In a proposed scheme a resonator is a frequency driving element of a microwave generator. Thus the output signal frequency is measured directly by the counter with high accuracy.

Microwave microscopy is widely used for low-contrast and subsurface inhomogeneities visualization. Fig.1 shows a result of scanning of a TM5 microscheme fragment. One can see a hidden layer on the SNMM image.

Optical image

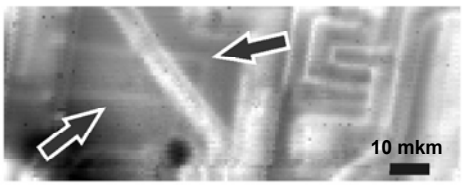

SNMM image

Fig. 1. Obtained image of the TM 5 microscheme with a hidden layer

Except inhomogeneities visualization and dielectric properties measurement SNMM can be used for local field imaging [3]. In a standard microscope scheme a detector is connected to the resonator and its output is proportional to external field amplitude. Such system is sensitive to vertical component of electric field of resonant (or close enough) frequency.

In [2] an electric-field probe design was proposed, sensitive to both normal and tangential spatial-field components.

The purpose of this work is to study the particular qualities of filed visualization using microwave microscope with an active probe.

In contrast to described devices, which are simply passive resonant receivers with subsequent signal amplification, our microscope is actually a generator. Thus, we observed forced frequency synchronization effect, when external field is applied to the resonator. Fig.2 shows the dependence of the measured signal frequency (from the probe's output) from the external field frequency. This dependence is often plotted as a dependence of beat frequency from the mistuning. Area 1 is a quasiperiodic regime. Generation frequency is not changed here, but the "effective" of "observed" frequency, which is measured by the frequency counter, is changed. Segment 2 is a bifurcation area. Frequency cannot be measured here; its width is defined by the noise level of external source and resonant frequency stability. Finally, area 3 is forced synchronization regime.

The output signal of active probe was observed also on C4-27 spectrum analyzer. Two distinct spectrum components were observed in area 1, which merged in one in area 2 and only one frequency signal was observed in synchronization area 3. These results correlate with the classic theory of forced frequency synchronization [4].

According to geometry of microwave resonator (inset in Fig.3) such probe is sensitive to vertical component of electrical field only. Nevertheless by modifying probes' tip geometry we can achieve sensitivity to required component of electric or magnetic field.

We measured the dependence of the width of the forced frequency synchronization area from the power of external source. This series of measurements allowed us to plot a so called Arnold tongue – parametric plot of synchronization area.

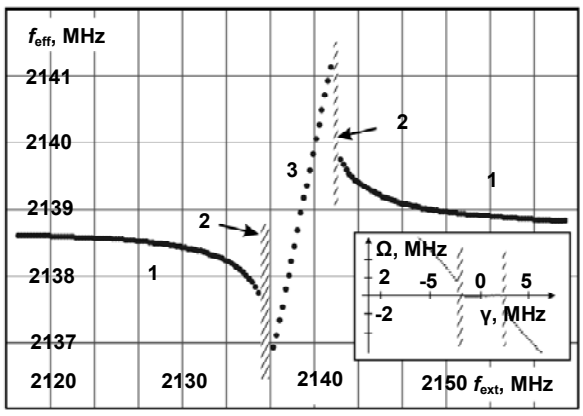

Fig. 2. Dependence of the measured frequency of the active probe signal from the external source frequency

It is known, that for the frequencies close to resonance, even an external signal with small amplitude can cause forced frequency synchronization effect. Thus, the described method can be used for detecting electromagnetic fields with low intensity.

Unfortunately, for the power level less than 1 mW, we could not measure synchronization area width because of

external source's low stability and low accuracy of frequency setup. Generator Г4-122 did not provide sufficient values of the parameters stated above.

We also should note that the dependence in Fig.3 has unusual form because we plotted the dependence from the power of the external signal, not from its amplitude.

As we stated above, one of the widespread SNMM application is hidden inhomogeneities visualization. This however requires high sensitivity and corresponding signal-to-noise ratio.

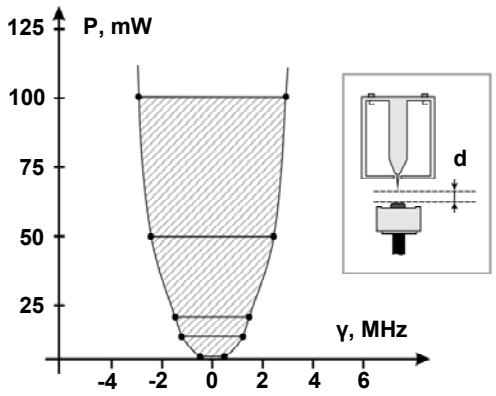

Fig. 3. Parametric plot of forced frequency synchronization area

We proposed to use a quasiperiodic regime with high curvature to increase sensitivity of our scheme. As it shown in Fig.4 when close to the bifurcation point, the effective frequency shift Δf_{eff} can significantly exceed resonant frequency shift Δf_r .

When close to bifurcation point, beat frequency dependence from mistuning can be approximated as $\Omega \sim \sqrt{\gamma - \gamma_{max}}$.

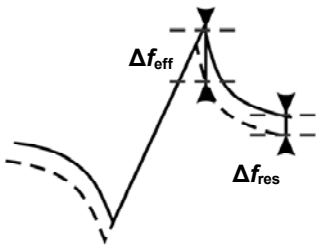

Fig. 4. Shift of resonant Δf_r and effective Δf_{eff} frequency of the loaded probe with external field "highlight"

According to this, signal amplification coefficient will be nonlinear. But as we consider this method only for small signals linear approximation can be used. In linear approximation effective frequency shift is determined by Δf_r and external generator stability Δf_s

$$\Delta f_{eff} \approx \beta \, (\Delta f_s + \Delta f_r \,),$$

where β is frequency characteristic curvature.

This effect was demonstrated by scanning defects in ceramic sample with/without external "highlight" (Fig.5). External signal was filed to the probe's tip by means of microstrip line. Informal signal increment in this experiment was only ~1.5 times because of low stability and frequency setup accuracy of the Г4-122 generator that was used in this experiment as external signal source. At the same time by interpolating curve in area 2 (Fig.2) we can calculate amplification coefficient β~6 for Δf_r < 200 kHz.

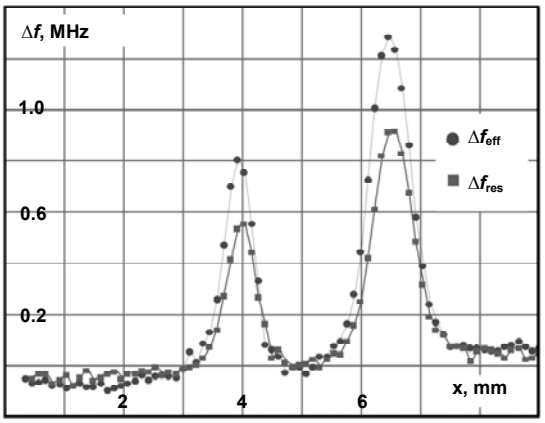

Fig. 5. Shift of resonant Δf_r and effective Δf_{eff} frequency when scanning test sample

We also found that amplification can be considered linear for such small frequency shifts. By using low-noise frequency synthesizer signal amplification β~10 and more can be achieved. Furthermore, this element can be built in the active probe scheme directly and described regime can be used optionally for studding samples with low dielectric contrast.

Conclusion. Particular qualities of field visualization regime using microwave microscope with active probe were described. Synchronization area for different power value of external field was measured. We also proposed a method of active probe sensitivity increasing, which is based on frequency shift signal measuring while using external field source to put the generator (active probe) in quasiperiodic regime. This method is suitable for resonant meters of generator type.

Reference

1. B.T. Rosner, D.W. Van Der Weide // Review of scientific instruments. – 2002. – Vol. 73, № 7. – P. 2505–2522. 2. R. Kantor, I.V. Shvets // IEEE Transactions on Microwave Theory and Techniques. – 2003. – Vol. 51, № 11. – P. 2228–2234. 3. S.K. Dutta, C.P. Vlahacos, D.E. Steinhauer, A.S. Thanawalla, B.J. Feenstra, F.C. Wellstood, S.M. Anlage, H.S. Newman // Applied physics letters. – 1999. – Vol. 74, № 1. – P. 156–158. 4. А. Пиковский, М. Розенблюм, Ю. Куртс // Синхронизация. Фундаментальное нелинейное явление. – М.: Техносфера, 2003. – 496 с. 5. В.С. Сидоренко, Ю.О. Гайдай, О.В. Сінькевич, С.В. Жила. // Пат. № 60519 Україна, МПК7 G 01 B 7/34. – № 2002119038; заявл. 13.11.2002; опубл. 15.10.2003, Бюл. № 10.

Submitted on 9.04.13

Ю. Гайдай, канд. фіз.-мат. наук, В. Сидоренко, канд. фіз.-мат. наук, О. Сінькевич, інж., І. Сердега, інж., каф. квантової радіофізики, радіофізичний факультет, КНУ імені Тараса Шевченка, Київ

ЕФЕКТ ВИМУШЕНОЇ СИНХРОНІЗАЦІЇ ЧАСТОТИ У МІКРОХВИЛЬОВОМУ МІКРОСКОПІ З АКТИВНИМ ЗОНДОМ

Розглянуто ефект вимушеної синхронізації частоти активного зонда мікрохвильового мікроскопа при дії зовнішнього поля з частотою близькою до резонансної. Запропоновано використати квазіперіодичний режим для підвищення чутливості зонда до малих змін діелектричної проникності.

Ключові слова: ближньопольовий мікрохвильовий мікроскоп, вимушена синхронізація частоти.

**Ю. Гайдай, канд. физ.-мат. наук, В. Сидоренко, канд. физ.-мат. наук,
О. Синькевич, инж., И. Сердега, инж.
каф. квантовой радиофизики, радиофизический факультет,
КНУ имени Тараса Шевченко, Киев**

ЭФФЕКТ ВЫНУЖДЕННОЙ СИНХРОНИЗАЦИИ ЧАСТОТЫ В МИКРОВОЛНОВОМ МИКРОСКОПЕ С АКТИВНЫМ ЗОНДОМ

Рассмотрен эффект вынужденной синхронизации частоты активного зонда микроволнового микроскопа под действием внешнего поля с частотой близкой к резонансной. Предложено использовать квазипериодический режим для повышения чувствительности зонда к малым изменениям диэлектрической проницаемости.

Ключевые слова: ближнеполевой микроволновый микроскоп, вынужденная синхронизация частоты

UDC 535.51, 535.36

**A. Goloborodko, Ph. D., Department Nanophysics and nanoelectronics,
Faculty of Radiophysics, Taras Shevchenko National University of Kyiv**

COHERENT LIGHT PROPAGATION IN OPTICALLY INHOMOGENEOUS MEDIA

Phenomenon of a depolarization for an optical signals which were propagated in media with the statistically distributed parameters has been investigated theoretically. Polarization characteristics were calculated by using a coherent matrix method. The dependence of polarization degree of wave on parameters of scattering medium has been calculated for the Fraunhofer diffraction zone.

Key words: degree of polarization, statistically inhomogeneuos medium.

Introduction. The coherent light propagation through optically inhomogeneous medium is one of the most important problem of the statistical optics [2]. Description of such propagation we could consider using of Maxwell formalism as a detailed analyze of an electromagnetic waves scattering under every fluctuation [7]. This problem takes on special significance for multiple scattering because of corresponding coefficients of stochastic equations are random field [5, 6]. Usually, such equations have not analytical solutions and are difficult for numerical analyze. Therefore, it is interesting to construct more simple models for description of the propagation process of waves through inhomogeneous medium with multiple scattering.

The model of phase screen could be considered as possible approximation for this case. Method of phase screen is familiar for scalar approximation of a diffraction problems, including, for example, wave propagation through turbulent atmosphere [4]. It can be proper for multiple scattering at some restriction. Then the propagation process of waves is considered as propagation through set of the phase screen with corresponding statistical properties.

In this work the theoretical method of the description of coherent light propagation through statistically inhomogeneous anisotropic medium by the phase screen method was proposed. Also we considered systems with multiple scattering using offered method.

Correlation matrix transformation. Correlation matrix method is the most convenient for investigation of polarization properties of the scattered light. In this case light propagation by the statistically stratified medium could be obtained as linear integral transform. The parameters of kernel of this transform are determined by the statistics of the medium. The advantage of this method consist in indifference between the statistically stratified mediums, where inhomogeneous could be produced by the inhomogeneous of relief fluctuation or refraction index fluctuations.

Let us consider general principles that were underlay our scattering model. The scattering geometry is depicted on the Fig. 1. Gaussian beam of wavelength λ normally irradiates the statistically stratified medium, which could be represented as phase screen with local inhomogeneties of refraction index (n_x=n_x(ρ), n_y=n_y(ρ), where ρ={ξ, η} is the coordinate in the plane of phase screen) and set of local heights h=h(ρ).

Complex amplitude of the electromagnetic wave in the registering plane arbitrary point r={x, y} could be given by Jones vector [3]:

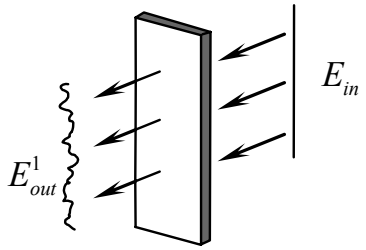

Fig. 1. Geometry of light scattering by phase screen

$$E(\mathbf{r}) = \begin{pmatrix} E_x(\mathbf{r}) \\ E_y(\mathbf{r}) \end{pmatrix}. \qquad (1)$$

The relation between the vectors of scattered wave $E(\mathbf{r})$ in arbitrary point $\mathbf{r}$ with the vector $E_0(\rho)$ in general case can be expressed by the linear integral [1]:

$$E(\mathbf{r}) = \int_{-\infty}^{\infty}\int_{-\infty}^{\infty} H(\mathbf{r},\rho)E_0(\rho)d^2\rho\,, \qquad (2)$$

where $H(\mathbf{r},\rho)$ is random coherent point spread function (PSF) of linear optical channel. This PSF could be expressed by the Green function, which in approaching of the anisotropic phase screen could be given as:

$$H(\mathbf{r},\rho) = \frac{1}{i\lambda z}\exp\left(i\left(\tfrac{2\pi}{\lambda}|\mathbf{r}-\rho| + \phi_j(\rho)\right)\right)\cos(\mathbf{n},\mathbf{r}-\rho)\,. \qquad (3)$$

here φ_x and φ_y is the random phases, which formed by the casual relief or refraction index fluctuation, and could be expressed as:

$$\phi_j(\rho) = \frac{2\pi}{\lambda}n_j(\rho)h(\rho);\ j = x, y\,, \qquad (4)$$

where $n_x(\rho)$ and $n_y(\rho)$ is the fluctuations of anisotropic index of refraction, $h(\rho)$ is the random distribution of relief inhomogeneous. So the formula (2) for the Fraunhofer diffraction zone is transforming in:

$$E^1_{out}(\mathbf{r}) = \frac{\exp\left(i\frac{\pi}{z\lambda}\left(x^2+y^2\right)\right)}{i\lambda z}\int_{-\infty}^{\infty}\int_{-\infty}^{\infty}\exp\left(i\frac{2\pi}{z\lambda}\left(x\xi+\eta y\right)\right)\times$$

$$\times E_0\exp\left(i\frac{\pi}{z\lambda}\left(\xi^2+\eta^2+zn(\rho)h(\rho)\right)\right)d\xi d\eta\,, \qquad (5)$$

where x, y are coordinates in registering plane; ξ, η are coordinates in the scattering plane; z is the distance between the scattering and registering planes. Let us make denotation:

$$\Phi(\mathbf{r}) = \exp\left(i \frac{\pi}{z\lambda} \left(x^2 + y^2 \right) \right)$$
$$E_0(\rho) = \frac{1}{i\lambda z} E_0 \exp\left(i \frac{\pi}{z\lambda} \left(\xi^2 + \eta^2 + zn(\rho)h(\rho) \right) \right), \quad (6)$$

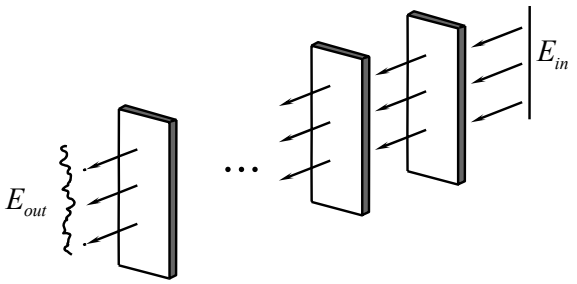

Fig. 2. Geometry of light scattering by the set of phase screens

where $\Phi(\mathbf{r})$ is the phase of the scattered wave and $E_0(\rho)$ is the gain-phase distribution of the wave in the scattering plane. In this case (5) could be expressed as:

$$E(r) = \Phi(r)\hat{F}_2 E_0(\rho). \quad (7)$$

here $\hat{F}_2$ is the linear integral 2D Fourier transform. In the case of the set phase screens (Fig. 2) total amplitude of the wave scattered by the set of phase screens are giving in the next form:

$$E^n(r) = \hat{F}_2^{n-1}\left(\Phi(r)\left(\hat{F}_2 E_0(\rho) \right) \right). \quad (8)$$

where n is the order of scattering. Expressions (8) let us the possibility to find the components of electrical field vector for scattered wave. So it becomes clear that it some aperture averaging of the random field and if it so that it reduce to defocusing scattered image.

The results of the theoretical calculations of components of electrical field are shown on fig.3.

Fig. 3 shows Capricorn constellation, which distorted by atmospheric turbulence. The parameters of turbulence are: correlation length r_k=50λ, inhomogeneous dispersions are (b) – σ=0.001n, (c) – σ=0.005n, (d) – σ=0.01n, (c) – σ=0.015n, where n is the mean refraction index. For reference fig. 3.a. is depicted original non distorted image. As can be seen from these graphs the increasing of inhomogeneous dispersion lead to image quality loss and some noise occurrence. This noise and defocusing are stir to spot of stars. In addition, the images of some stars simply meet and it is impossible to see one star of on a background of other.

For the polarization properties analyzing the elements of the coherent matrix could be giving as:

$$G_{jk}^n(\mathbf{r}) = E_j^n(\mathbf{r})\left(E_k^n(\mathbf{r}) \right)^*; j,k = x,y. \quad (9)$$

In general case it had to make the averaging of the components of coherent matrix under the aperture of a beam:

$$\left\langle G_{jk}^n \right\rangle = \int_{-a}^{a} G_{jk}^n(\mathbf{r}) d^2\mathbf{r}, \quad (10)$$

where a is the averaging aperture. Thus, it is possible to define the degree of polarization of the scattered waves using expressions for the elements of the coherent matrix (10):

$$P = \sqrt{1 - \frac{4\left(\left\langle G_{xx}^n \right\rangle \left\langle G_{yy}^n \right\rangle - \left\langle G_{xy}^n \right\rangle \left\langle G_{yx}^n \right\rangle \right)}{\left(\left\langle G_{xx}^n \right\rangle + \left\langle G_{yy}^n \right\rangle \right)^2}}, \quad (11)$$

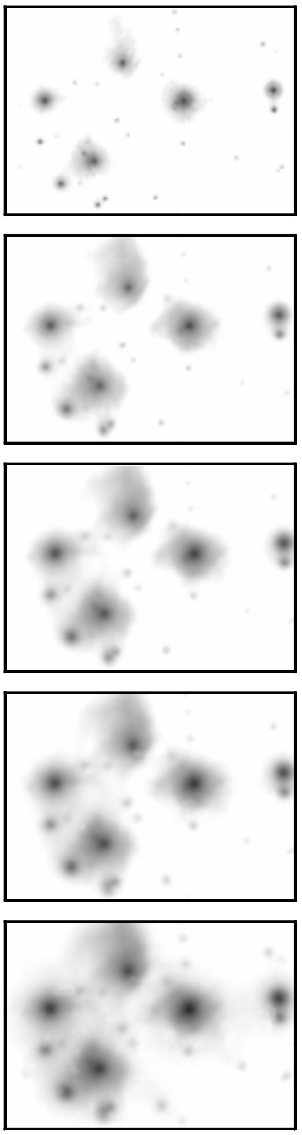

a) original image

b) σ=0.001*n*

c) σ=0.005*n*

d) σ=0.01*n*

e) σ=0.015*n*

Fig. 3. Image distortion by atmospheric turbulence

If the incident wave is completely polarized, the wave scattered by diffuse surface will change the degree of polarization, because the factorization of the correlation matrix is impossible [1]. It is understandable, that any fluctuations of propagation media have to influence on light polarization.

The main results of the polarization experimental measurements [5] and theoretical calculations (11) are shown on fig.4.

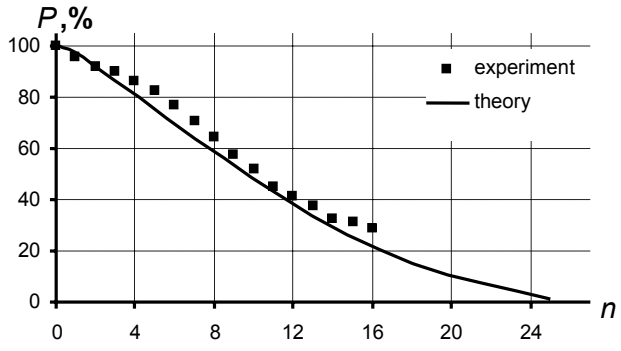

Fig.4. Dependencies of polarization degree on the order of scattering

As can be seen from these graphs the degree of polarization of the scattered wave depends on the order of scattering. Thus, every wave becomes partially depolarized on each phase screen at each scattering act. So if the number of screens is increasing ($n \to \infty$) that the depolarization to tend to a limit which of equal to 100%.

Conclusions. The mathematical model of light propagation through media with multiple scattering which was based on the approximation by sequence of the anisotropic phase screens. It has been considered case of the stratified medium, in which anisotropy is sequent of statistical inhomogeneous of the layers interfaces. The essential depolarization effect at the light propagation has been confirmed experimentally. This fact was submitted to theoretical results which obtained from proposed model.

Reference

1. Goodman G.W. Statistical optics /G.W.Goodman. John Wiley and Sons: New York-Chichester-Brisbane-Toronto-Singapore, 1985. – 487p. 2. Alloin D. M. Adaptive Optics for Astronomy / D. M. Alloin, J.-M. Mariotti. NATO ASI Series: Kluwer Academic Publ., 1994. – .423 p. 3. Azzam R.M.A. Ellipsometry and polarized light. 5th ed./ R.M.A.Azzam, N.M.Bashara. Elsevier: North Holland. 2003. – 387p. 4. Andrews L.S. Propagation of a Gaussian-beam wave through a random phase screen/ L.S.Andrews, R.L.Phillips, A.R.Weeks// J. Waves Random Media. – 1997. – Vol. 7. – P.229–244. 5. Barchuk O.I. Experimental investigations of light depolarization under multiple scattering / O.I.Barchuk, A.A.Goloborodko, V.N.Kurashov, Y.A. Oberemok, S.N. Savenkov // Proceedings of SPIE. – 2006. – Vol.6254 – 62540W. 6. Дерюгина А.И. Поляризационная структура дифрагованого излучения, распространяющегося в турбулентной атмосфере / А.И. Дерюгина, В.Н. Курашов, А.И. Мащенко // Радиотехника и электроника. – 1988. – Том 23, №11 – С. 2399–2408. 7. Kurashov V.N. Polarization changes in coherent electromagnetic radiation scattering by the rough surface/ V.N. Kurashov, V.V. Marienko, T.V. Molebna, A.G.Chumakov // Proceedings of SPIE. – 1995. – Vol. 2647. – P. 48–56.

Submitted on 19.10.12

А. Голобородько, канд. фіз.-мат. наук, каф. нанофізики та наноелектроніки, радіофізичний факультет, КНУ імені Тараса Шевченка, Київ

РОЗПОВСЮДЖЕННЯ КОГЕРЕНТНОГО ВИПРОМІНЮВАННЯ В ОПТИЧНО НЕОДНОРІДНОМУ СЕРЕДОВИЩІ

Проведено теоретичний аналіз явища деполяризації оптичних сигналів, що розповсюджуються оптичним середовищем зі статистично розподіленими параметрами. Дослідження поляризаційних характеристик випромінювання виконано з використанням методу кореляційної матриці. Розглянуті поляризаційні властивості оптичних полів, що сформовані в зоні дифракції Фраунгофера.

Ключові слова: ступінь поляризації, статистично неоднорідне середовище.

А. Голобородько , канд. физ.-мат. наук, каф. нанофизики и наноэлектроники радиофизический факультет, КНУ имени Тараса Шевченко, Киев

РАСПРОСТРАНЕНИЕ КОГЕРЕНТНОГО ИЗЛУЧЕНИЯ В ОПТИЧЕСКИ НЕОДНОРОДНОЙ СРЕДЕ

Проведен теоретический анализ явления деполяризации оптических сигналов, распространяющихся в оптической среде со статистически распределенными параметрами. Исследование поляризационных характеристик излучения выполнены с использованием метода корреляционной матрицы. Рассмотрены поляризационные свойства оптических полей, сформированных в зоне дифракции Фраунгофера.

Ключевые слова : степень поляризации, статистически неоднородная среда.

UDC 576.535; 577.151.45; 577.037; 577.325.5

O. Ivanyuta, Ph.D.
Department Electrophysics, Faculty of Radiophysics,
Taras Shevchenko National University of Kyiv

ELECTROPHYSICS PROPERTIES THE DNA AND DNA:AU MOLECULAR CLUSTERS ON SAPPHIRE

The films DNA, DNA: Au, clusters from gel solution, which can be magnetic and electrical active in biosensor systems and to detect their functional properties by microwave techniques. Research has been focused on the application of I - V characteristics and spectra methods to recognise and predict these molecular interactions based on primary structure and associated physic-chemical properties. In results have actually shown that these molecular cluster layers on Al_2O_3 substrates can to conduct electric current and respond on power of microwave.

Keywords: DNA, UV-VIS-NIR spectra, low-energy electron point source, current-voltage characteristics.

Introduction. Deoxyribonucleic acid (*DNA*) encodes the architecture and function of living cells. DNA is made of a sequence of four bases: adenine (*A*), guanine (*G*), thymine (*T*) and cytosine (*C*) (Fig. 1), attached to a phosphate-sugar backbone and is about 0,34 nm long. Any particular sequence forms a single strand of *DNA*. Two strands may come together through hydrogen bonding of the bases *A* with *T* (*A T*) and *G* with *C* (*GC*) [1–4].

DNA's electronic and self-assembly properties bear enormous importance in nanoscience. The electrophysics properties *DNA* are interest in several disciplines in nanoscience because of their relevance to damage and mutation in molecules. The charge transport for electrophysics properties of *DNA* is central to such developments. For instance, electrophysics detection of structural changes, due to protein binding or base mismatches examined. New read-out schemes on *DNA* chips can detect for the presence of different *DNA* sequences, might exploit her a electronic properties. The phosphate ion carries a negative charge in the *DNA* molecule, which results in electrostatic repulsion of the two strands. In order to keep the two strands together, positive ions must be present in the solution to keep the negative charges neutralized. Charge transport in *DNA* can shed new light on the transport properties of other systems with supramolecules (Fig. 2). *DNA* could be a *Au* conductor because of the formation of a molecules band across the different bases. The stacking molecule is important in the conducting properties of several other organic molecules, that DNA might conduct started to be pursued with more vigor. The electron transfer through *DNA* was responsible for fluorescence quenching of an excited molecule [2–5, 9, 10].

DNA behaves as a conductor, semiconductor, or insulator, in what seems to be contradictory conclusions. The apparent contradictions have been attributed to the large phase space in which *DNA* can be prepared and probed. Many experimental conditions and attributes of the specific *DNA* used, including base sequence, length, orientation, countering, temperature, electrode contact, adsorption surface, fluctuations, and so on, could affect its conducting properties. As a consequence, although much

progress has been made, *DNA*'s transport properties are still in question. The electrophysics properties free metal (*Au*) clusters sensitively depend on the exact number atoms *N* in island films to study the influence of a supporting or embedding medium on the electronic level structure. The island film for conserving the distinct energy spacing's of a deposited cluster, it would be possible to generate a clusters with adjustable electronic and optical properties. The size cluster determines surface reactivity film. As illustrated in Fig. 3, this method involved attaching noncomplementary *DNA* oligonucleotides to the surfaces of two batches of *Au* particles capped with thiol groups, which bind to gold (see Fig. 2). The presence a surface will significantly influence the electronic level structure in the cluster at a large distance the only common energy is the vacuum energy, E_{vac}. As the temperature is reduced, the two strands will eventually come together by diffusion and rehybridize to form the double stranded structure. These properties of the *DNA* can be utilized in the ordering and assembly of artificial structures if these structures can be attached to *DNA* [4–6, 9, 10].

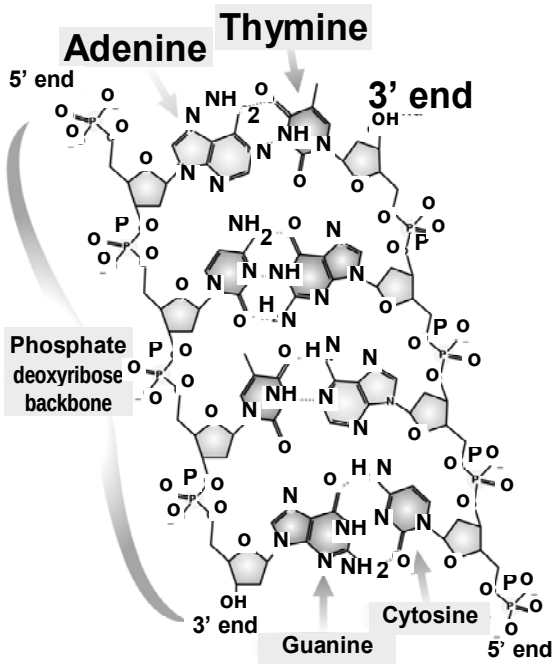

Fig. 1. Chemical structure of DNA (from Wikipedia)

Results and discussion. Direct measurements *DNA* in vacuum are showed good conduct properties. It was found that *DNA* is a conductor, with a resistance comparable to that of conducting polymers. So far, the most widely used attachment scheme utilizes the covalent bond between *DNA* and *Au*. The experiment was done in gel, where a drop of solution containing *DNA – Au* was placed onto sapphire with a foil gold-covered with $3\ \mu m$.

The DNA ropes were then broken by using a tungsten tip. The tip was also used to apply a bias across the DNA. A $600\ nm$ portion of a *DNA* rope produced a resistance of the electrodes in series with a resistor $R = 100\ k\Omega$ or $1\ M\Omega$. At low bias voltages, no current is measured, $2{,}5\ M\Omega$ [4, 10]. The experiments were done using a *DNA* oligomer 250 base pairs $56{,}2\ nm$ long. An electrostatically trapping technique was used to position single *DNA* molecules between two electrodes $10\ nm$ apart (see Fig. 3). Electrical contacts between *DNA* molecules and Au electrodes were made by using the electrostatic trapping method [4, 12]. *DNA* was researched with a low-energy electron point source (LEEPS) microscope with not radioactively damage *DNA*. [4–5].

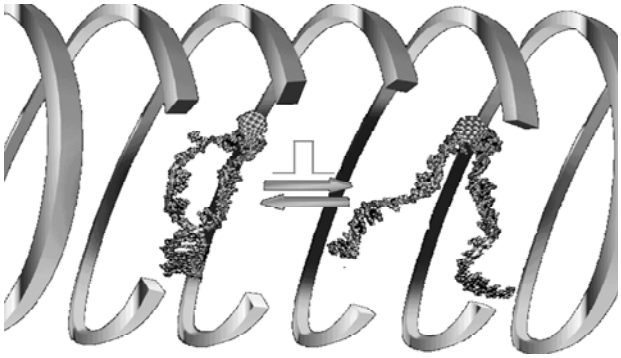

Fig. 2. DNA/*Au* nanoparticles as building blocks formation

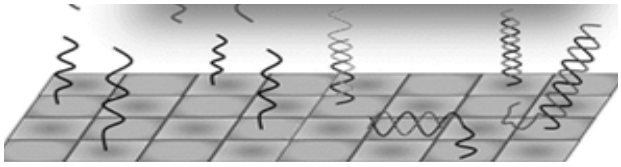

Fig. 3. Size cluster was 3 μm and determines surface reactivity film

When two oligonucleotides which are complementary to the two grafted sequences are introduced, the nanoparticles self-assemble into aggregates. This process could also be reversed when the temperature was increased due to the melting of the *DNA* oligonucleotides. Because of the molecular recognition properties associated with the *DNA* interconnects, this strategy allows one to control interparticle distance, strength of the particle interconnects, and size and chemical identity of the particles in the targeted macroscopic structure. The sample was then dried with a flow of nitrogen. The current (I) – voltage (U) characteristics are measured using the equipment, which is the same to the *LEEPS*. Sensitivity the measurement of current is $10\ pA$. The time was to writing of the characteristic under the change of the voltage from $-10\ V$ to $+10\ V$ with step $10\ mV$ for 100 seconds. The measurement was made in air at $T = 300\ K$. This provides an upper value for the resistance of DNA, since some finite contact resistance is expected to contribute. Since the experiment was done in vacuum, ionic conduction could not account for the transfer mechanism. However, this experiment does not rule out that ions trapped by the *DNA* might have changed its electronic structure, allowing for higher conductivity. There has also been some evidence that *LEEPS* imaging contaminates the *DNA* and can account for the conducting behavior observed in this experiment. The visible absorption spectra of these gels in quartz cuvetes were recorded on *UV – VIS* spectrophotometer with double-beam mode through CDD (cooled double detection) Specord 200, Analytik Jena AG. The transmission spectra Au / *DNA* nanosystems was in 2D - plates and *DNA* molecule in adsorbed layers from gels on dielectric substrate. *IR* spectra of the adsorbed layers from these gels on dielectric substrate KRS - 5 were recorded using a Bruker IFS 66v spectrometer in the range of $800 \div 1500\ cm^{-1}$ at $T = 300\ K$ [2–4, 9–13].

In other direct measurements have found that DNA acts as a large bandgap semiconductor. With decreasing separation the energy barrier between cluster and sonde will also decrease. The cluster level structure might change when compared to the corresponding free system. As is

clear from Figure 4 and Figure 5, the *DNA* oligomers does not conduct charge for voltage below about 2 V at room temperature, which shows that the human chromosome Ch 22 behaves like a semiconductor with a large bandgap. This characteristic have following features: a non-linearity and unsymmetrical behavior. The tip is held at 2 V A Coulomb blockade like staircase is observed whose origin is still unclear. Then, a voltage of up to 5 V was applied to while the current rises rapidly above a certain threshold voltage. In addition, a large hysteresis is seen by comparing the upward and the downward sweeps. After trapping *DNA* molecules between electrodes, the sample was dried with a nitrogen gas and characterized using precision microwave parameter analyzers (P1 – 59, P1 – 61, P1 – 67). At a higher bias, the *DNA* becomes conductive. Surprisingly, the $I - V$ characteristics were dependent on the direction of the scan rate, yielding different I - V curves. By depositing more silver and thereby growing a thicker *Au* – *DNA*, the noncurrent region was reduced from 5 V to 0,5 V , demonstrating crude control over the electrical properties of these systems. In addition, control experiments where one of the components (*DNA* or *Au*) was removed from the assembly produced no current, establishing that all of the components are necessary to form the conducting *Au* films [3–6, 10–14].

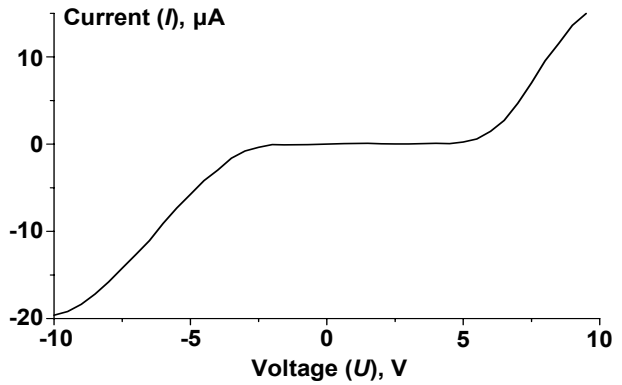

Fig. 4. Current – voltage characteristics of double-strand *DNA* sequence for oligomer 250 base pairs the human chromosome Ch22 [4, 9]

The details of the binding determine whether the highest occupied level in the cluster adjusts to the substrate Fermi energy E_f (Fig. 6). In this case the contact potential would induce a local charge accumulation. Also, the core levels might shift. On a *Au* surface the cluster forms a metallic bond and often likes to wet the substrate sapphire. If the cluster is of the same material as the surface it will form an epitaxial layer. On a non-metallic and weakly interacting surface clusters might keep their identity and have structures close to those of the free clusters in vacuum. The homogeneous sequence is ideal for overlap of π - orbital's in adjacent base pairs. The next part of these features can be conditioned to the electronic structure of these layers and a interface in heterostructures conductance, $(dI/dV)/(V)$ (see Fig. 6), that represents the shape of density of states of *t*. These results do not rule out the possibility that ions could be attached to the DNA, thus modifying its electronic structure. The voltage dependence of the differential conductance as well as normalized conductance exhibits a clear peak structure, which represent a local level of energy that is typical in the polymers *Au* nanoparticles, which have nonmetallic properties. In order to study the electronic structure I investigated the shape of the normalized differential the layer. The different curves show repeated measurements. The telemetric *DNA* sequence, when treated as a quantum wire in the fully coherent low and room temperature regime, works as an excellent semiconductor. Although the origins of voltage gap and hysteresis are not clear, I speculate that the voltage gap and/or the hysteresis are at least partly related to the contacts between electrodes and DNA molecules. In order to study the innocence caused by the contacts, the four probe measurements need to be performed. *G* have peculiar sequence of *H* - bond donor or acceptor groups, and because it has the lowest oxidation potential among the *DNA* bases, which favors self-assembly and carrier transport. Such a *G* in supramolecular assembly has the form of long ribbons, with a strong intrinsic dipole moment along the ribbon axis that causes current rectification in transport experiments. The devices exhibit a maximum voltage gain of 0,79 eV. This approach has potential to express control the size and the packing density of the *Au* nanocrystals by simply adjusting external experimental conditions such as *pH*, temperature, and ion concentration [4, 12–15].

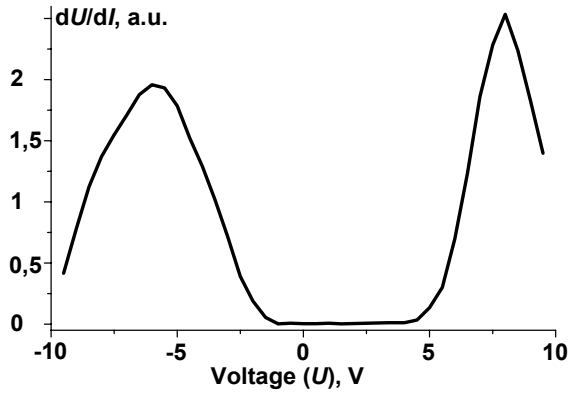

Fig. 5. The differential resistance – voltage characteristics of double-strand *DNA* sequence for oligomer 250 base pairs the human chromosome Ch22

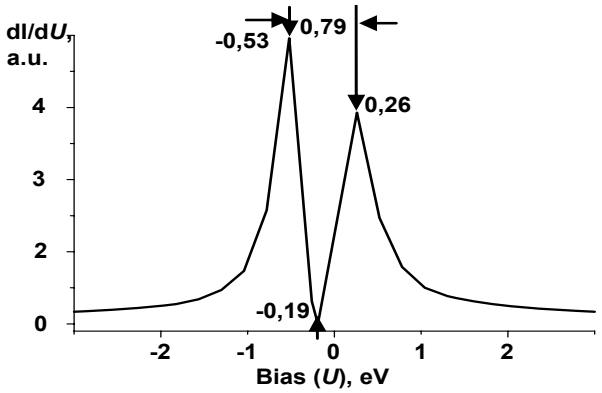

Fig. 6. The differential conductivity – voltage characteristics of double-strand *DNA* sequence for oligomer 250 base pairs the human chromosome *Ch* 22

It can be seen from normalized differential conductance – voltage curves that there is a voltage gap at low applied bias. The value of energy gap for the *Au* clusters was estimated from the range with minimum of DOS near the Fermi level (in Fig. 6. near the point $U = 0$ V). It is turned out that $E_g = 0{,}79$ eV . Using the data of the band gap of *Au* clusters was estimate the cluster diameter: $E_g = 0{,}79$ eV are two dimensional (2*D*) clusters (cluster diameter is approximately 2,4 nm).The change in conductivity due to

the different compressions can be explained as follows: If the charge transport relies on a very organized *DNA* chain, then compression will disrupt the channel conductivity greatly. The compression could be o f such a magnitude that the single strands in the *DNA* duplex are essentially independent. Islands with two layers of gold and a band gap of $0,3 \cdot eV$ are found to be most effective for catalyzing reaction. These results suggest that supported clusters may have unusual catalytic properties as one dimension of the clusters becomes smaller than three atomic spacing's. Its conclude that the observed tailoring of the properties of small *Au* clusters by altering the cluster size and its support could prove to be universal for a variety of metals and will likely be quite useful in the design of nanostructured materials for catalytic applications [6, 13–16].

Ionization potential has electric field difference between two isolated bases ($U_{max} = 0,6$ eV between *G* and *T*). A high *DNA* surface density on the *Au* nanoparticle is expected to provide advantage in particle stabilization the hybridization efficiency. The *dc* impedance spectrum of this gap electrode gives rise to a conductive non large hysteresis with a charge transfer resistance of about $1\ M\Omega$, as shown in the inset of Fig. 7. This resistance (*R*) the layer from *DNA* polymerized molecules versus temperature (*T*) change has exponential decrease at the temperature increase. If it is assumed that there are no other single *DNA* molecules stretched over the gap and this bundle of *DNA* molecules contributes all of the electrical conduction, the resistance of this bundle will be about 10^{-7} cm^{-2}. The rectified type of *I* - *V* characteristic for the structure metal (*Au* or *Ag*) – the layer from *DNA* polymerized molecules networks on sapphire has been confirmed. The spectrum still shows a conductive non large hysteresis with a charge-transfer resistance of $20\ M\Omega$, about 20 seconds times larger than the one measured before the enzyme application.

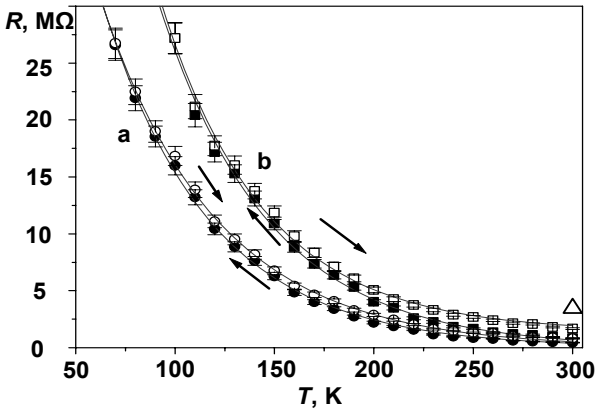

Fig. 7. The resistance (*R*) versus temperature (*T*) curves of the layer from *DNA* polymerized molecules networks on Al_2O_3 (■ and □- points) and on Al_2O_3 after several temperature cycling (×and ◊ points) surfaces (*a* and *b*, respectively). These curves correspond to measurements at one temperature cycling (temperature decreases from 300 K to 70 K and increases from 70 K to 300 K). The value of the resistance of this layer on Al_2O_3 (Δ– point) after temperature cycling is indicated

I cannot degrade all characteristics of double-strand *DNA* sequence for oligomer *A*, *C*, *G*, *T*. After repeated temperature cycling is indicated DNA molecules inside for bundle oligomers 250 base pairs under the applied experimental condition. They fail to respond to changes in the external environment (Δ - point in Fig. 7.) Such behavior of the resistance of the layer from DNA polymerized molecules networks on sapphire under the temperature increase is typical for a semiconductor. Similar results for the layer from *DNA* - linked *Au* nanoparticles in networks have been obtained. But both the resistance of this layer of and its change were less.

However, it should remove all other damaged (stretched) single *DNA* or small bundles of DNA molecules As a result it can be reasonably assumed that this bundle of no degraded *DNA* molecules contributes all of the electrical conduction measured with the *ac* impedance spectroscopy. The resistance is about 10^{-6} cm^{-2} for this *DNA* bundle that may contain about 250 molecules since the diameter for a single *DNA* is about 2,4 nm that implies a monolayer of *DNA* molecules. As *Au* nanoparticles are linked together via *DNA* hybridization, electromagnetic coupling between the nanoparticles result in significant damping of their surface Plasmon resonances. The amount of extinction due to scattering is also influenced by the interparticle spacing. Interparticle distance also influences van der Waals and electrostatic forces between the particles, weakly affecting duplex *DNA* stability and hybridization / dehybridization properties.

Can microwaves disrupt the covalent bonds of DNA? The fundamentals of thermodynamics and physics indicate

this is impossible. The majority of these factors have electromagnetic nature. For the spectrum range, where $h\nu << kT$, all the kinds of the biological activity to a certain degree have been already found. The case is somewhat different with the rest of wide range of electromagnetic spectrum, where $h\nu << kT$. This range includes diapasons from the microwaves to infra low frequency. For a long time to infra low frequency range is considered not to influence on alive organisms. The simple physical considerations led for such conclusions: as energy quantum in the spectrum range considerably less, from than the average kinetic energy of molecules ($h\nu << kT$), then infra low frequency absorption in alive tissue may be associated only with the amplification of a molecule rotation, i.e. with the transformation of electromagnetic energy into thermal one [4, 16]. Its studies have demonstrated that microwaves are capable of breaking the covalent bonds of DNA (Fig. 8.).

The exact nature of this phenomenon is not well understood, and no theory currently exists to explain it [4, 17, 19]. Nevertheless, polar molecules are those which possess an uneven charge distribution and respond to an electromagnetic field by rotating. The angular momentum developed by these molecules results in friction with neighboring molecules and converts thereby to linear momentum, the definition of heat in liquids and gases. Because the molecules are forced to rotate first, there is a slight delay between the absorption of microwave energy and the development of linear momentum, or heat. There are some minor secondary effects of microwaves, including ionic conduction, which are negligible in external heating. Microwave heating is, therefore, not identical to external heating, at least at the molecular level, and the existence of a microwave effect is not precluded simply because the macroscopic heating effects of microwaves are indistinguishable from those of external heating.

The change of the resistance (Δ*R*) of the layers from *DNA* polymerized molecules networks (see Fig. 8.) and from *DNA* – linked *Au* nanoparticles in networks [4, 17, 18] on sapphire under rise of the microwave power (*P*) was increased. Resistance of the layer of *DNA* polymerized molecules networks on sapphire increases on $R = 80 \cdot \Omega$ in the range from 0 to $9 \cdot mW$. These changes decrease for this layer after ageing under *UV – VIS* illumination (Fig. 9.). Resistance of the layer from DNA – linked *Au* nanoparticles

in networks on sapphire in the same range increases on $\Delta R = 96 \cdot \Omega$ [4, 17].

The energy level of a microwave photon is only, whereas the energy required to break a covalent bond is $10 \cdot eV$, or a million times greater. Such a behavior the resistance of these layers could be defined by partially breaking part district or changing of the bonds in *DNA* polymerized molecules. There is plenty of evidence to indicate that there are alternate mechanisms for causing *DNA* covalent bond breakage without invoking the energy levels of ionizing radiation. The electrical conductivity of *DNA* was affected with humidity regardless of single or double stranded *DNA* since those measured signals might reflect only the ionic transport. Still, no theory currently exists to explain the phenomenon of *DNA* fragmentation by microwaves although research is ongoing which may elucidate the mechanism. The experiments shows a common pattern – for the first few minutes of irradiation there is no pronounced effect, and then a cascade of microbial destruction occurs. The data pattern greatly resembles the dynamics of a capacitor; first there is an accumulation of energy, and then a catastrophic release. It may simply indicate a threshold temperature has been reached, or it may indicate a two-stage process is at this work.

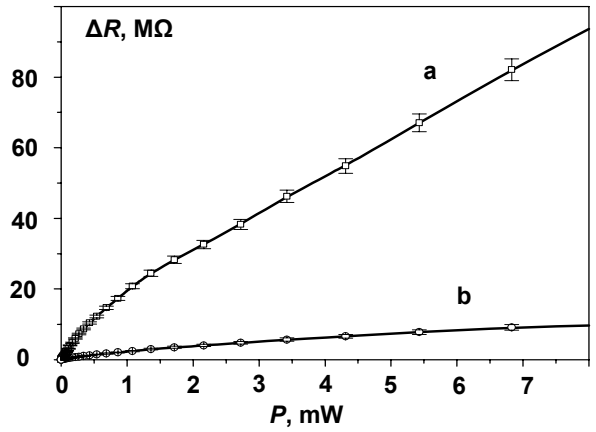

Fig. 8. The change of the resistance (Δ*R*) of the layer from *DNA* polymerised molecules networks on Al_2O_3 (□– points) under microwave power (*P*) and *T* = 300 K [10, 11]. The measurements after temperature cycling (the Δ*R* versus *P*, curve *a*) and after *UV – VIS* spectroscopy (the Δ*R* versus *P*, curve *b*) have been carried out

The second stage of this process may very well be the accumulation of oxygen radicals, which would certainly seem to be primary suspects as they have a considerable propensity for dissociating the covalent bonds of *A*, *C*, *G*, *T* and oxygen radicals can be generated by the disruption of a hydrogen bond on a supermolecule. These molecules exist alongside single *DNA* molecules as "bound" system, two or three layers thick [9]. These molecules share a hydrogen bond with component atoms of the *DNA* backbone, including carbon, nitrogen and other oxygen atoms. At any given point in time one of the hydrogen atoms may be primarily bonded to either an oxygen atom on the supermolecule, or to an oxygen (or other) atom on the *DNA* backbone. The fluctuating character of these shared and exchanged bonds is enhanced by temperature and by the dynamics induced by microwaves. Although the amount of oxygen radicals which may be produced by this process cannot presently be determined, the production of some number of oxygen radicals is inevitable in these circumstances. It must be noted here though, that most of the oxygen radicals produced in this manner would exist only briefly, as they would almost immediately bond to the nearest available site. If this site is an oxygen atom on the *DNA* backbone, I get a covalent bond break, albeit probably only a brief one. The *ac* conductivity measurements of single and double stranded *DNA*s using precision microwave parameter analyzers in the centimeter and millimeter spectral range under different humidity. On the basis of the present results and discussion, the electron transport through a double stranded *DNA* should follow a one-dimensional pathway. However, the double stranded *DNA* molecules in their films were naturally coiled and randomly distributed. They could not be expected to give rise to any electrically conductive signals under this circumstance. Due to extremely high frequencies, the ionic conduction is also negligible. Therefore, these measurements may only reveal the dipole relaxation behavior of solution trapped inside the films in the microwave spectral range. According to the diagram adsorption of solution per nucleotide as a function of humidity in this literature [4, 6, 20], the double and single - stranded *DNA* molecules were identical. This can explain why their *ac* conductivity is identical under that measurement condition. The data about the ac conductivity of the double stranded *DNA* molecules under 0 % and 90 % of relative humidity upon various frequencies suggested that at a high humidity, the ac conductivity of the *DNA* molecules was close to that of water, which is an electrical insulator under a normal condition [1, 18].

The absorbance of *DNA* is the reason radiation can be used the absorbed energy destroys (cause mutations) and kills the organism. When a *DNA* helix is denatured to become single strands, e.g. by heating, the absorbance is increased about 30 percent (see Fig. 9.).

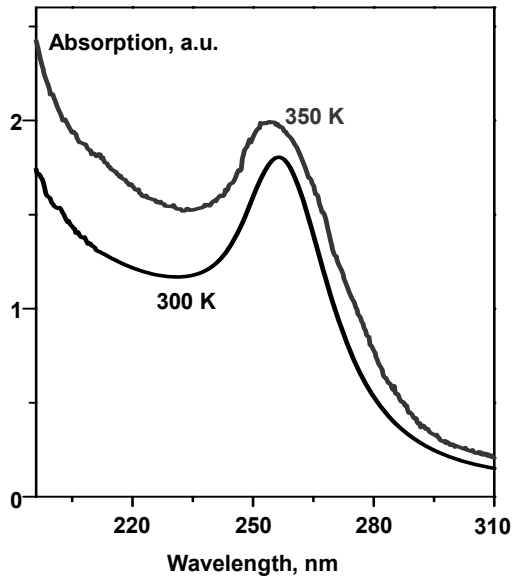

Fig. 9. Absorption in the *UV* spectra of Au / *DNA* nanosystems at two temperatures

Each of the four nucleotide bases has a slightly different absorption spectrum, and the spectrum of *DNA* is the average of them. A pure *DNA* solution appears transparent to the eye, and absorption doesn't become measurable until 320 nm. Moving further into the *UV* region, there is a peak at about 260 nm , followed by a dip between 220 and 230, and then the solution becomes essentially opaque in the far *UV* region. A solution of double stranded, native *DNA*, with a concentration of 0,04 mg/mL has an absorbance of about 1,0 At at the 260 nm peak [6, 19]. This increase, called the

hyperchromic effect, reveals the interaction between the electronic dipoles in the stacked bases of the native helix. Under a high relative humidity, both number and freedom of the water molecules trapped inside the *DNA* films were increased so that the ac conductivity of *DNA* was close to that of water. Although *DNA* tends to repair itself naturally, the simultaneous breakage of a sufficient number of covalent bonds would lead to a catastrophic failure of the entire *DNA* molecule. Due to the exceedingly large number of bonds involved, the matter boils down to a reproducible function of pure probabilities.

The optical properties *Au* nanoparticles are conferred by the interaction of light with electrons on the surface *Au* / *DNA* nanosystems. As an example, the emission spectra for *Au* nanoparticles (Figure 10) are shown. At a specific wavelength (frequency) of light, collective oscillation of electrons on the *Au* nanoparticle surface cause a phenomenon called surface Plasmon resonance resulting in strong extinction of light. The particular wavelength, or frequency, of light where this occurs is strongly dependant on the *Au* nanoparticle size, shape, and surface, and agglomeration state as described. The intensive absorption by all of the nucleotides in the *UV* range is almost entirely determined by purine and pyridine bases. The interaction of the four nucleotide bases causes electronic perturbations in the complexes. When incorporated into *DNA* duplexes, *G* and *C* are able to be oxidized by excited-state 2-aminopurine (*Ap*). Since the reaction of the excited state of *Ap* with the base analog in sine (*I*) is not thermodynamically favorable, charge transfer between *G* or *C* and photo excited *Ap* can be evaluated using inside containing duplexes as references [1, 4, 14].

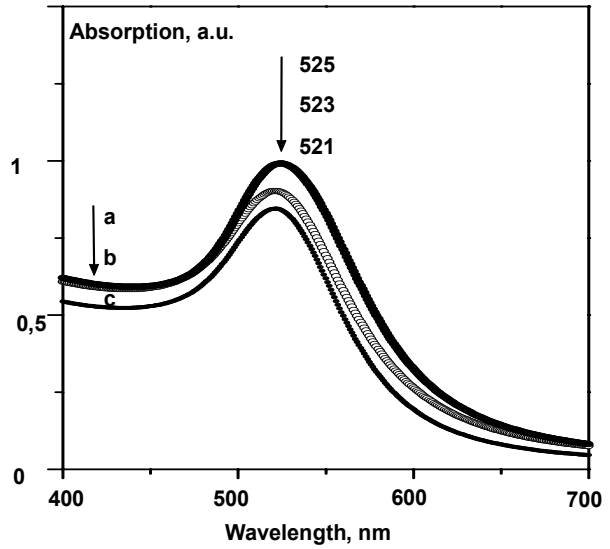

Fig. 10. Absorption spectra separated *Au* nanoparticles – negative charged citrate – capped colloid *Au* particles in water solution with sizes in diameters 8,8 nm, 10,5 nm, 16,7 nm – curves *a, b, c*, correspondingly. [6]

Further, because duplexes containing *C* differ from those containing *G* by only one atom, the effect of driving force on DNA - mediated charge transfer behavior may be examined without drastically altering the structure of the assemblies. Fixing the *Au* nanoparticles at specific sites eliminates the distribution of distances usually present when charge transfer is examined with intercalators tethered to the end of *DNA*. These perturbations can be observed through emission studies and spectroscopic titration. The emission spectra for these bases were similar Density of states for the *Au* nanoparticles in 2D - plates from *Au* / DNA nanosystems and *I* - *V* characteristics gap - *Au* nanoparticle hosted in 2D - plate from *Au* / DNA - sapphire substrate for different *Au* nanoparticles sizes (A, B, C). It emits in a buffer at room temperature with a maximum at 523 nm. The obtained results can be used for the analysis of an optical response of systems containing DNA's nucleotides and *Au* nanoparticles [1, 4, 10].

The influence of *Au* nanoparticle size on the surface plasmon resonance is illustrated in Figure 11, where the absorption maximum (lambda max) increases from 448 nm to 456 nm for diagnostics sizes in range at $5 \div 100$ nm spherical *Au* nanoparticles, respectively. As a comparison *Au* nanoparticles of sizes below 2 nm do not exhibit surface Plasmon resonance [2, 4, 11].

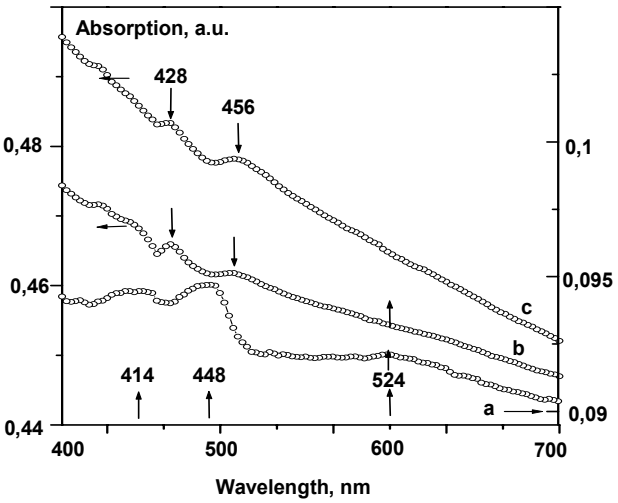

Fig. 11. Absorption spectra of *Au* nanoparticles: a – in 2D – plates into gel without *DNA*; *b*, *c* – in *Au* / *DNA* nanosystems in 2D - plates into gel with mixture of 2D – plates, having sizes in big side 100÷150 nm (*b*) and 8÷25 nm (*c*)

A major determinant of the optical properties of *Au* nanoparticles is their shape. By synthesizing *Au* nanoparticles of different shapes, the surface Plasmon resonance can be easily be tuned to give absorption maxima from around 500 nm into the near-infrared part of the spectrum. The difference in absorption properties between spherical and irregular-shaped *Au* nanoparticles of the same average size is caused by an anisotropic distribution of the surface electron layers. It's the transmission spectra of *Au* / *DNA* nanosystems in 2D - plates (*a*) and *DNA* molecules (*b*) in adsorbed layers from gels on dielectric substrate (Fig. 12). *IR* spectra of the adsorbed layers from these gels on dielectric substrate in the range of $800 \div 1500$ cm^{-1} at $T = 300$ K. The surface Plasmon resonance of the *Au* particles coupled by DNA chains are recorded and compared with the spectra of isolated particles. Upon adding linker DNA, the DNA hybridization leads to aggregation of gold nanoparticles, as demonstrated in the *Au* surface Plasmon peak (520 nm) shift of the *DNA* – modified *Au* nanoparticles. In the cases of *DNA* chains functionalized with two thiol groups the spectra shows a broadening and a red shift of the surface plasmons which is a result of coupling the particles by this chains. The aggregation starts with the wavelength shift of the Plasmon band, followed by broadening and more shifting of the peak as hybridization continues. These results indicate that the initial aggregation takes place with increasing volume fraction, followed by increasing network size [4, 6].

The next act measurements have in direct measurement a single *DNA*. The result decreasing It's the energy barrier between cluster and sonde will also decrease barrier characteristics *DNA* oligomers. The cluster level structure might change when compared to the corresponding free system. As is clear from Figure 3 and Figure 13, the *DNA* oligomers does not conduct charge for voltage below about 0,2 V at room temperature. DNA molecules on a sapphire surface between two gold electrodes about 3 μm, also showed a resistance of 10 TΩ (see Fig. 13). For instance, poly(d*G*) – poly(d*C*)*DNA* with no thiol groups showed resistances greater than 1 TΩ on both sapphire substrates. The *I* – *V* characteristics for poly(d*A*) – poly(d*T*) *DNA* showed a large bandgap at temperatures lower than 150 K. This can be accounted for by a small polaron hopping model [4, 10], where the current is given by $I \propto \sinh bV \exp[-Ea / k_bT]$, where E_a is the activation energy, *T* is the background temperature, $b = ea / 2k_BTd$, e is the electron charge, a is the hopping distance, and d is the distance between the electrodes. The details of the cluster - sonde interaction will determine the changes in geometrical and electronic properties with respect to the unsupported case. Equation describes the *I* – *V* characteristics of poly(d*A*) – poly(d*T*) DNA very well if b is taken to be independent of temperature. Furthermore, poly(d*G*) – poly(d*C*) DNA shows temperature dependence of the current down to 20 K and seems to have two molecular vibration frequencies which contribute to the polaron motion, whereas poly(d*A*) – poly(d*T*) DNA shows temperature dependence only down to 50 K and seems to support only one molecular vibration. When a transverse microwave field is applied, the potential along the DNA chain will be adjusted due to the special structure of a DNA double helix. This modulation changes the electronic structure of the DNA molecule and further influences its transport property. The transverse electric field will suppress the current through the device. The reason is that the transverse electric field potential tends to make the on-site energy of the poly(*G*) - poly(*C*) DNA molecule into a "disorder". This "disorder" changes the wave-function of the electron and further influences conductivity. The calculation reveals that the suppression on the current is also related to the direction of the transverse electric field, which is denoted by phase φ_0, as shown in Fig. 6. Since the modulation is harmonic due to the double helix structure of DNA molecule, choose the phase $\varphi_0 = 0$ to correspond to the direction that the transverse electric field points to from base *G* to base *C* of the first base pair. The modulated potential along a one-helix-period ploy(*G*) - poly(*C*) *DNA G* and *C* chain is for phase $\varphi_0 = 0$ and $\varphi_0 = \mathrm{p}$. At a fixed strength of the transverse electric field the amplitude of the "disorder" is unchanged, but different directions change the shape of the modulation in detail, which will make a difference of the conductance. Fig. 13 shows the dependence of the current on φ_0 for different strengths of the transverse electric field for a simple Au / DNA / Au device. The straight solid line corresponds to the case when the transverse electric field is absent. When the transverse electric field is turned on, the current has fluctuating behavior with φ_0. With a larger transverse electric field fluctuation becomes more notable. Measurements at both ambient conditions and in a vacuum were performed, with no substantial change in the results.

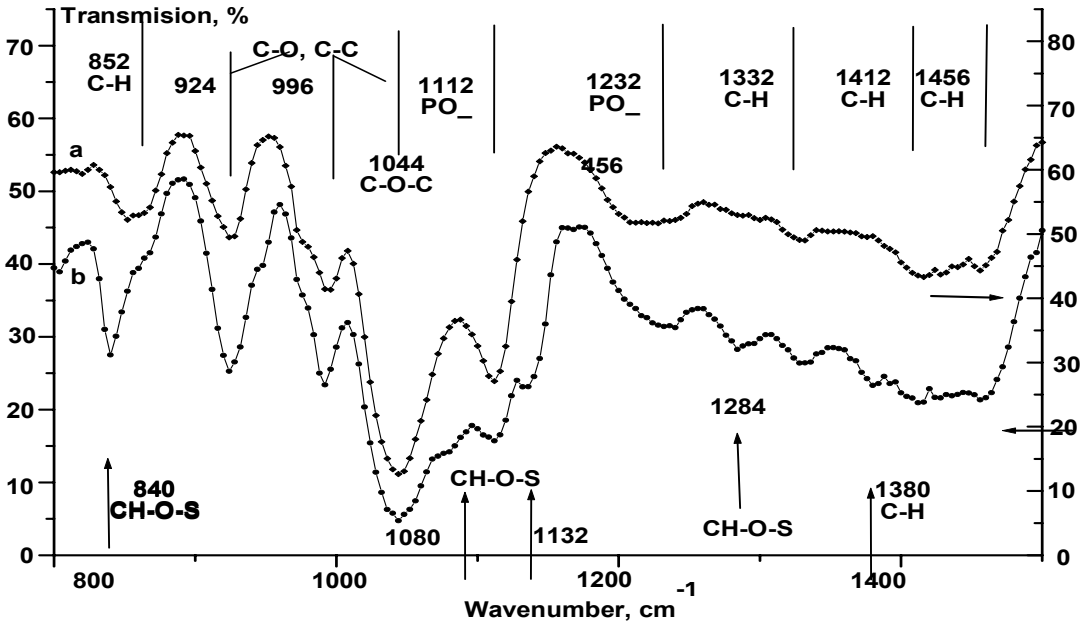

Fig. 12. The transmission spectra of *Au* / *DNA* nanosystems in 2D – plates (*a*) and *DNA* molecules (*b*) in adsorbed layers from gels on sapphire substrate

In the *I* – *V* curves threshold voltages to showing the inclusion of backbones opens a gap between the HOMO and the lowest unoccupied molecular orbital. For sufficiently high applied voltages, as can be observed for almost all models for the voltage range depicted in Figure 13. Next, a non-periodic sequence of base pairs can drastically suppress the currents to the *DNA* sequence. This strong suppression is do not show a large suppression at such short lengths *DNA*, while longes already exhibit a several orders of magnitude drop in current. There are steps appearing in some *I* – *V* curves, which are due to resonances in the transmission probabilities. Such resonances are more relevant and robust in the telemetric sequences. Resonance effects are still present in some cases for disordered short sequences, but they do not last for longer systems, as can be systematically appreciated in Figure 14. The complexity of the DNA systems does not as yet a definitive conclusion to be drawn on the mechanisms

leading to sequences on *I – V* characteristics. Nevertheless, the consistency among the results found here for different measurement, widely discussed in the literature [2, 4, 11], suggests that important qualitative physical and chemical aspects have been captured in the present work. These steps are enhanced and not washed out by adding parallel chains, irrespective of the starting points defined at the interface of each sequence with the contact. The drastic difference in the lengths dependence of the current for *DNA* will allow for better comparison and interpretation of experimental data.

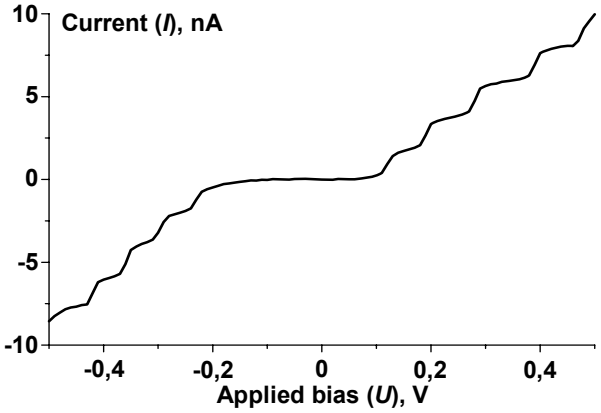

Fig. 13. I – V characteristics is placed across single the DNA molecule. The inset shows the current versus the gate voltage at a source-drain voltage of 0.5 V. Reprinted with permission from [21]

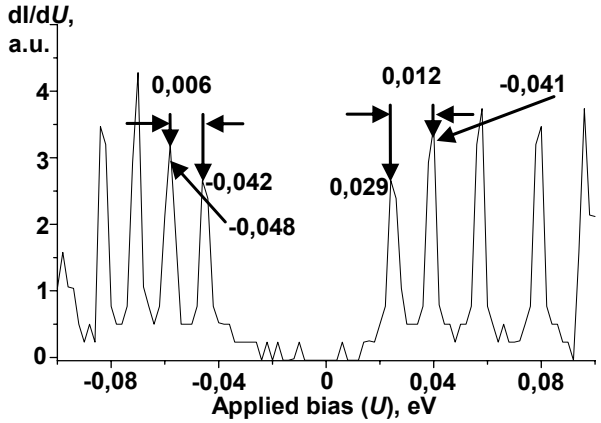

Fig. 14. The differential conductivity – voltage characteristics of is placed across single the *DNA* molecule

Conclusions. *DNA* molecules as building blocks in nanotechnology of nanosystems has probably only just begun, but already produced some striking results as in electronic, optic nanosystems engineering such as in tissue engineering. The first step on this way is the study of *DNA* on the molecular level, which may point to new directions in nanosystems design and construction – not just biomolecular systems, but actually using *DNA* biomolecules themselves to construct novel nanosystems. Among the variety of approaches to *DNA* - based supramolecular physic, the strategy of replacing *DNA* natural bases by alternative bases that possess distinct shape, size, or function has allowed the modification of *DNA* in a highly specific and site selective manner. This approach is replacing bases *DNA* on *Au* cluster restricted to molecules with shapes and sizes that are commensurate to normal bases to ensure that the *DNA* modifications occur highly specifically and site selectively. The new generation of such nucleoside mimics was found in which the hydrogen bonding interactions were replaced by metal-mediated base pairing. The advantage of this modification strategy is that it allows the metal ions to be replaced in the interior of the *DNA* duplex.

The geometrical properties and electronic structure of single *DNA* nucleosides (d*A*, d*T*, d*G*, d*C*) adsorbed on a metallic surface of *Au* cluster are determined. I investigate multiple adsorption geometries and the resulting molecule surface interaction mechanisms self-assembly *DNA – Au* nanosystems. For *A*, I found negligible differences between the binding energy in the two configurations investigated, while for *G* this difference reaches the maximum value among the four nucleosides (i.e., 0.79 eV). The projected density of states indicates that the physisorption is the main cause of the binding energy. Nevertheless, for the adsorbed d*C*, point out the presence of the chemical interaction too. While the absolute values of the molecule surface charge transfer are small, they are qualitatively dependent on the orientation of the nucleosides to the surface. If the *DNA* bases are oriented perpendicular to the surface, the electronic population of molecules decreases, while the parallel orientation of the *DNA* bases with respect to metal surface leads to an increase of electronic population on the molecules.

The laboratory models investigated in this work - based on the naturally occurring, physisorption stable threads - should provide ideal benchmark situations for systematic investigations of *DNA* electronic transport, as well as for the development of *DNA*-based molecular nanoelectronic applications using *Au* as contacts. In particular, the *I – V* characteristics presented here show promise of a wide range of interesting nanocircuitry on complex patterns of hollowed thin films on substrates sapphire bridged by DNA sequences. The *I - V* curves suggest the existence of stepped structures smal independent of length and sequencing initialisation at the self-assembly *DNA – Au* nanosystems. They are present independent of lengths and sequence initialisation at the *Au* contacts. Surely, the molecule-electrode coupling can drastically influence the magnitude and fluctuations of the current.

The *ac* impedance spectroscopy provides further evidences for the electrical conductivity of double stranded DNA. The spectra images of *DNA* build up a proportional relationship of *DNA* electrical conductivity and the number of the *DNA* molecules stretched over the gap *Au* electrodes. The enzymes DNA was used to degrade the *DNA* molecules stretched across the electrode gaps, which results in a significant increase in the charge-transfer resistances. These impedance spectra do not demonstrate any feature of ionic conduction and small sensitivity to light. The spectra do not support *DNA* as metallically conductive molecules, which should give a constant resistance on the real resistant axis of an impedance spectrum. Instead, they suggest the double stranded DNA to be a semiconductor. Different from some semiconductors, such as silicon, the *DNA* conductivity should follow the mechanism of one-dimensional electron transport through the π stack of double stranded *DNA* base pairs.

Reference

1. Cancer and aging as consequences of un-repaired DNA damage. In: New Research on DNA Damage / Ed. by Honoka Kimura, Aoi Suzuki. – NewYork., 2008. 2. Frontiers of nano-optoelectronic systems / Ed. by L. Pavesi, E. Busaneva. – Dordrecht., 2000. 3. Future Trends in Microelectronics. Up the Nano Creek / Ed. by S. Luryi,, Xu J., A. Zaslavsky. – NewYork., 2007. 4. Nano and Molecular electronics: handbook / Ed. by S.E. Lyshevski. – Boca Raton, 2007. 5. Nanotechnology: an Introduction to Nanostructuring Techniques / Ed. by M. Kohler, W. Fritzsche. – NewYork., 2007. 6. Optical spectroscopy of semiconductor nanostructures / Ed. by E.L. Ivchenko. – Harrow., 2005. 7. Self-assembled nanostructures / Ed. by J.Z. Zhang, Z.L. Wang , J. Liu et al. – New York., 2004. 8. Springer Handbook of Nanotechnology / Ed. by B. Bhushan. – Berlin., 2004. 9. Ivanyuta O., Tsamis C., Scharff P. et al, Design and study of DNA/nanocarbon and macrocyclic metal complex/C60 nanostructures // In

Work Book of NATO ARW, Frontiers in molecular-scale science and technology of nanocarbon, nanosilicon and biopolymer integrated nanosystems, Ilmenau – 2003. 10. Ivanyuta O., Tsamis C., Scharff P. et al, DNA, DNA/metal nanoparticles, DNA/nanocarbon and macrocyclic metal complex/fullerene molecular building blocks for nanosystems: electronics and sensing //In Book Frontiers of multifunctional integrated nanosystems, Ed. by Buzaneva E, Scharff P., NATO Science Series II, Mathematics, Physics and Chemistry – NAII. Dordrecht. – 2004. – Vol 152. – P. 251–276. 11. Andersen ES, Dong M, Nielsen M., Self-assembly of a nanoscale DNA box with a controllable lid. // Nature – 2009 – Vol. 459 – P. 7243. 12. Aldaye FA, Palmer AL, Sleiman H.,F Assembling materials with DNA as the guide. // Science. – 2008. –Vol 321, – P. 5897. 13. Bogdan D., Morari C., Electronic Properties of DNA Nucleosides Adsorbed on a Au(100) Surface. // J. Phys. Chem. C. – 2012. – Vol. 116 (13). – P. 7351–7359. 14. Calborean A., Buimaga-Larinca L., DFT simulation of vibrational properties of adenine adsorbed on gold surface: The effect of periodic boundary conditions // Computational and Theoretical Chemistry. – 2012. – Vol. 993. – P. 106–112. 15. Hughes-Stamm S.R., Ashton K.J., Daal A., Assessment of DNA degradation and the genotyping success of highly degraded samples. // Int. J. Legal Med. – 2011. – Vol. 125(3). – P. 341–348. 16. Isaksson J., Acharya S, Barman J, et.al., Single-stranded adenine-rich DNA and RNA retain structural characteristics of their respective double-stranded conformations and show directional differences in stacking pattern. // Biochemistry. – 2004. – Vol. 43(51). – P. 15996–6010. 17. Ivanyuta A.N., Prokopenko O.V. Sensing of DNA polymerised molecules in networks // In Proceedings of PLMMP-2010 5th International Conference Physics of Liquid Matter: Modern Problems. – 2010. 18. Ivanyuta O., Gobsh G., Scharff P. et al., Photonics of mimetic biomolecules: the photoluminescence spectroscopy of cysteine molecules in thin layer // In Proceedings of the VI International Conference on Electronics and Applied Physics. – 2010. 19. Rosa M., Corni S, Di Felice R., A Density Functional Theory Study of Cytosine on Au(111) // J. Physical Chemistry. – 2012 . – Vol. 116(40). – P. 21366–21373. 20. Sun W., Di Felice R., Nature of the Interaction between Natural and Size-Expanded Guanine with Gold Clusters: A Density Functional Theory Study. // J. Physical Chemistry. – 2012. – Vol. 116(40). – in print. 21. Watanabe H., Manabe C., Shigematsu T et al., Single molecule DNA device measured with triple-probe atomic force microscope // Appl. Phys. Lett. – 2001. – Vol 79. – P. 2462–2465.

Submitted on 20.11.12

О. Іванюта, канд. фіз.-мат. наук,
каф. електрофізики, радіофізичний факультет,
КНУ імені Тараса Шевченка, Київ

ЕЛЕКТРОФІЗИЧНІ ВЛАСТИВОСТІ *ДНК* І *ДНК*: *AU* МОЛЕКУЛЯРНИХ КЛАСТЕРІВ НА САПФІРІ

Покриття ДНК, ДНК: Au, як кластери з гелієвих розчинів можуть виявляти магнітну й електричну активність у біосенсорній системі та виявити функціональні властивості для мікрохвильової техніки. Дослідження було зосереджено на аналізі їх ВАХ та спектрів методами розпізнавання і прогнозування цих молекулярних взаємодій на основі їх первинної структури та взаємозв'язку з фізико-хімічними властивостями. Результати показали, що ці молекулярні шари кластерів на підкладках Al_2O_3 можуть проводити електричний струм і реагувати на потужність НВЧ.

Ключові слова: ДНК, UV-VIS-NIR спектри, точкове джерело низько енергетичних електронів, вольт-амперна характеристика.

А. Иванюта , канд. физ.-мат. наук,
каф. электрофизики, радиофизический факультет,
КНУ имени Тараса Шевченко, Киев

ЭЛЕКТРОФИЗИЧЕСКИЕ СВОЙСТВА *ДНК* И *ДНК*: *AU* МОЛЕКУЛЯРНЫХ КЛАСТЕРОВ НА САПФИРЕ.

Покрытие ДНК , ДНК:Au, как кластеры с гелиевых растворов могут проявлять магнитную и электрическую активность в биосенсорной системе и функциональные свойства для микроволновой техники. Исследование было сосредоточено на анализе их ВАХ и спектров методами распознавания и прогнозирования этих взаимодействий на основе их первичной структуры и взаимосвязи с физико - химическими свойствами. Результаты показали, что эти молекулярные слои кластеров на подложке Al_2O_3 могут проводить электрический ток и реагировать на мощность СВЧ.

Ключевые слова: ДНК, UV-VIS-NIR спектры, точечный источник низко энергетических электронов, вольт-амперная характеристика.

UDC 577.3

K. Karpenko, post grad. stud., O. Sudakov, Ph.D., Department Medical Radio Physics,
Faculty of Radio Physics, Taras Shevchenko National University of Kyiv

INFLUENCE OF RECOVERY MODEL PARAMETERS ON SYNCHRONIZATION IN NEURAL CORTICAL STRUCTURE DURING DESCENDING INFORMATION TRANSFER

Neurons interaction in networks with complex dynamics was investigated, the synchronization phenomenon for descending information process in cortical column was considered. The synchronization coefficient dependency on different variations of Izhikevich model parameters is depicted on corresponding plots. Visual study of network synchronization is performed by means of raster plots. Synchronization coefficients on different layers of cortical column were compared. Proved that time-scale parameter of membrane potential recovery variable has the weakest influence on network synchronization.

Keywords: synchronization coefficient, Izhikevich model, cortical network, descending information process.

Problem statement. Last years studies of brain neuron networks and principles of information presentation and transformation in the brain are of great interest. Today number of tools and resources for neurophysiological experiments allows us to get more information about functioning of different brain neuron networks. One of the main directions in this science brunch is development of physical and mathematical neuron models that describe basic functional possibilities of neurons and convenient for theoretical researches. Such models are very popular in neurons researching to solve one of the main neurophysiological and biophysical problems: determination how information flows in the network is related to network's topology.

Analysis of recent researches and publications. Active researches of brain's structural organization summarized that the main principle of brain's organizing is the modularized structure and partial information processing. [8] Neocortex is responsible for thinking, speaking and other processes of nervous system and has the most representative modularized organization. Aggregation of cells and links in the cortex into horizontal layers may lead to the conclusion that main interactions in the brain take place in the horizontal planes. But in the 1930-s Spanish scientist Rafael Lorente de No [7, 6] first supposed that cortical processes are local and take place in the vertical columns. Lorente de No assumed that neurons in such structures are associated into closed networks with ring topology. It must be mentioned that till nowadays scientists have no consensus about cortical column's form (cylinder, cone, line, ensemble, "barrel" and others) [9, 10]. Nevertheless comparison of results from different functional researches shows the existence of vertical neuron groups. Hebb [4] hypothesized that neurons ensemble is organized as 3d network consisted of elements with different functional states. Synaptic currents in such network amplify each other by synchronous occurrences. Since the beginning of 60 years this point of

view gets demonstrative confirmation. In 1957 Mountcasle noticed that somato-sensory cat's cortex is organized into "elementary functional units" – vertically oriented cell columns. Any column has 110 neurons [8], and this number doesn't dependent on the species e.g. cat, rat, human etc. Columns are considered as the neocortex's evolutionary unit and there are many thoughts about their structural and functional transformations.

Exact structure of the neuron cortex module and coupling parameters are unknown. Analysis of network dynamics [2] can be held for different column structures and topologies. Simulation results can be compared with neurophysiological experiments data to obtain additional knowledge about network topology. Now dynamical research is devoted to neurons synchronization [8]. Synchronization is a central mechanism of neural informational processes that connects different parts of brain. Experimental results show that the synchronous neuron's activity is responsible for visual recognition of whole subject and for information transformation. On the other side the synchronization presence is a reason of pathology and plays an important role in such neural diseases as epilepsy.

Paper goal. This work is devoted to synchronization researching in Izhikevich's neuron network, especially to dependency of synchronization coefficient on variation of neural states in cortical column.

Materials and methods. We considered neural networks consisted of 110 neural elements with different regimes: regular spikes, chaotic spikes, regular and chaotic bursting, etc. All investigated structures are six-layer homogeneous networks similar to cortical columns. Microscopic observations prove that density and form of cells vary from the top to the deep in the cortex. Such differences correspond to horizontal layers. The upper layer, which is called the first, has little cells and consists mainly of axons. In our work there are 9 neurons at the first layer. The second and the third layers are the similar, and each of them has 11 neurons. The fourth layer has 15 neurons, the fifth – 17. The sixth layer is the deepest and strongly differs from others; it has a big amount of neurons, in our case it consists of 47 neurons. (*fig. 1*). Each neuron is connected with each neuron from its own layer and from the next layer. Layers in column are connected by axons and synapses.

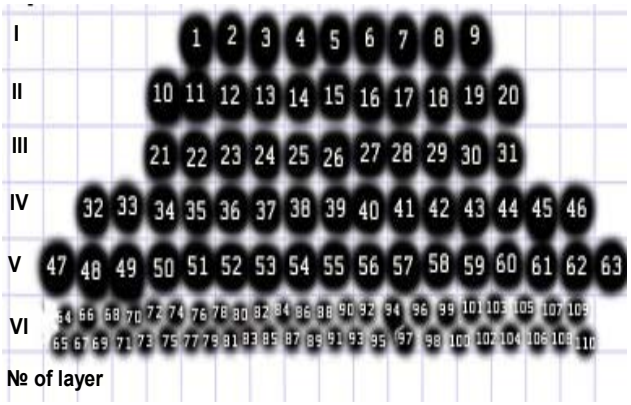

Fig. 1. The hierarchical structure of investigated cortical column

A very interesting question arises: how such little cortical parts may send and get information from the top to the deep in the cortex and what is happen with neural dynamics in such case?

We are interested in the dependence of the synchronization phenomenon on different variation of Izhikevich model parameters. [5]. It is two-compartment model that contains an additional requirement for cell membrane discharge:

$$\frac{dv}{dt} = 0.04v^2 + 5v + 140 - u + I\,,\ \frac{du}{dt} = a(bv - u),$$

$$v \leftarrow c, u \leftarrow u + d\ ,\ if\ v>=30\ mV,$$

where v and u are the dimensionless membrane potential and membrane potential recovery variables respectively; a, b, c and d – dimensionless parameters. The variable u simulates the activation of ionic K^+ currents and the deactivation of ionic Na^+ currents and provides negative feedback to v. Variable I simulates external currents.

Various choices of the parameters result in various intrinsic firing patterns, including those exhibited by the known types of neocortical and thalamic neurons [3]. So in this work we investigated the dependence of synchronization coefficient from variation of neural regimes in cortical column.

Results and discussions. We considered the descending information flow in neural structure. Information goes from the top to deep in the cortical column and hasn't a direct way (*fig. 2)*. Descending connections start at the sixth layer cells and reaches the first layer of the lower cortical regions. The axon spreads to large distances in the first layer. This layer has very few cells. Cells in the second and fifth layers have dendrite couplings with the first layer. Thus cells may be excited by reverse connections that go from the first layer. Axons from the second and the third layers provide synaptic currents to the fifth layer. Thus we can say that the information path from the top to the deep is complex. Information may be divided into different directions. This distribution occurs in the first layer. The reverse information flow coupling begins from the cells of the sixth layer in upper hierarchical region, and then it comes to the first layer of the lower cortical regions. Some cells of the second, third and fifth layers in the lower hierarchical regions are excited. Thus cells of the sixth layer are also excited and then the information goes to lower and lower hierarchical columns.

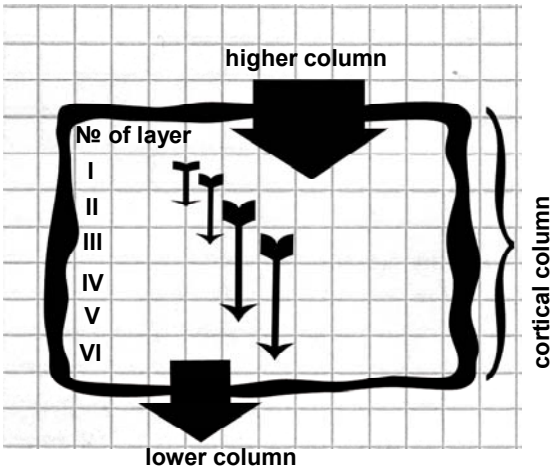

Fig. 2. The descending information flow

As we know from [5] – the parameter a describes the time scale of the recovery variable u. Smaller values result in slower recovery. A typical value is $a=0.02$. For the descending information flow dependence of synchronization coefficient changes on changes of parameter a for the whole cortical column (*fig. 3*) and for each layer separately (*fig. 4*) was investigated.

From *fig. 3* we can see that for descending information flow the maximum value of synchronization coefficient equals $k=0.27$ is reached at $a=0.03$. From *fig. 4* we can see that on the first layer of the structure the synchronization coefficient is bigger than on other layers of cortical

structure for all values of parameter *a*. The reason of this phenomenon is that the first layer is the input layer that gets an applied synaptic current which flows from upper cortical regions. For parameter value *a=0.03* the raster plot for descending information flow in the cortical column (*fig. 5*) was constructed. Neural dynamics looks like *intrinsically bursting (fig. 6)*.

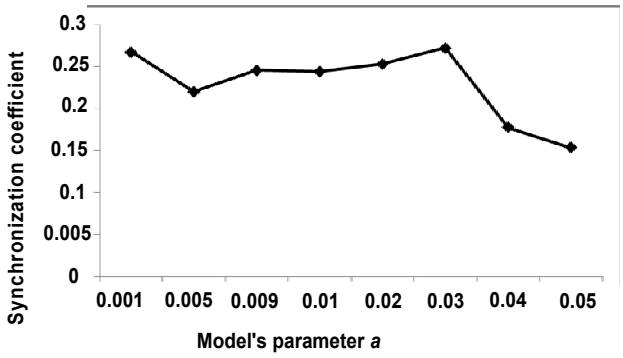

Fig. 3. Dependence of synchronization coefficient on parameter a

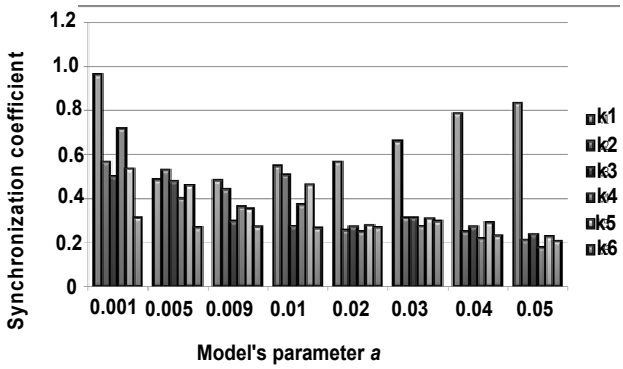

Fig. 4. Layer dependence of synchronization coefficient on parameter a

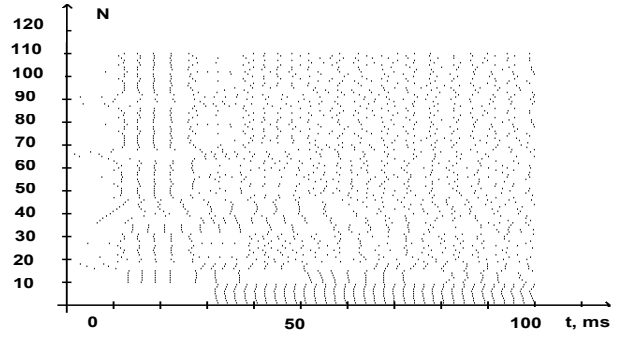

Fig. 5. The raster plot for a=0.03

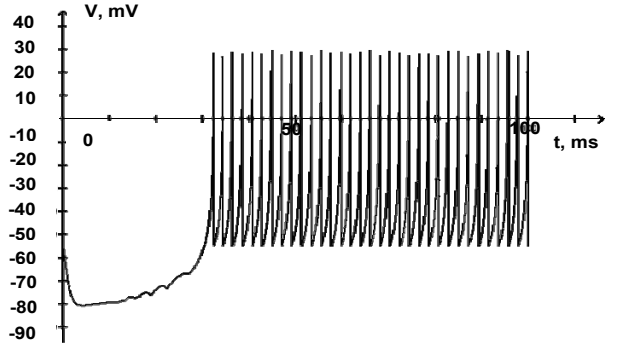

Fig. 6. Neural dynamics for a=0.03

Then the synchronization coefficient changes dependent on changes of parameter *b* for the whole cortical column (*fig. 7)* was investigated. The diagram of synchronization coefficient dependence on parameter *b* was constructed (*fig. 8*) for different layers. From [5] the parameter *b* describes the sensitivity of the recovery variable *u* to the subthreshold fluctuations of the membrane potential *v*. The large values of *v* and *u* lead to the large possible subthreshold oscillations and low-threshold spiking dynamics. A typical value is *b=0.2.*

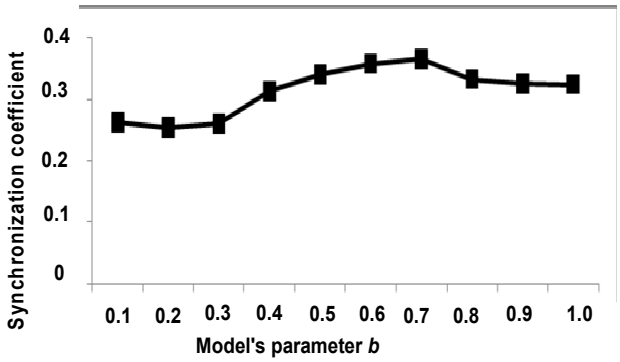

Fig. 7. Dependence of synchronization coefficient on parameter b

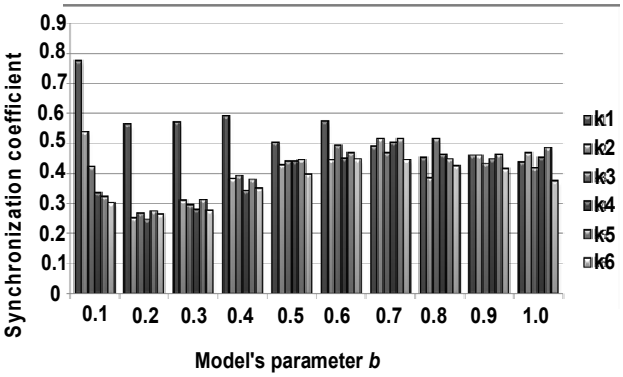

Fig. 8. Layer dependence of synchronization coefficient on parameter b

From *fig. 7* we can see that the synchronization coefficient changes very fluently (~10%) while parameter *b* varying. The maximum value of the synchronization coefficient equals *k=0.365* is achieved at *b=0.7*. From the diagram *(fig. 8),* we can see that the the first input layer has significantly different dynamics of synchronization coefficient changes compared to other layers. For *b=0.7* the raster plot for descending information flow in the cortical column (*fig. 9*) was constructed. Neural dynamics looks like *intrinsically bursting (fig. 10)*.

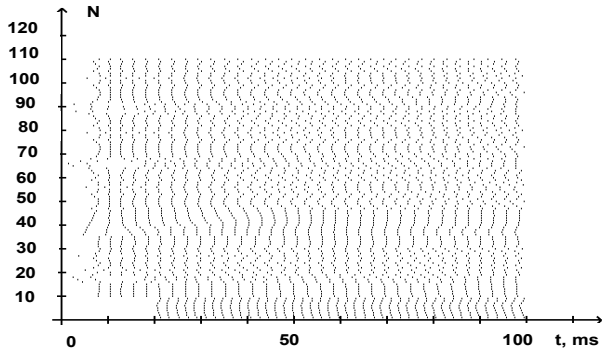

Fig. 9. The raster plot for b=0.7

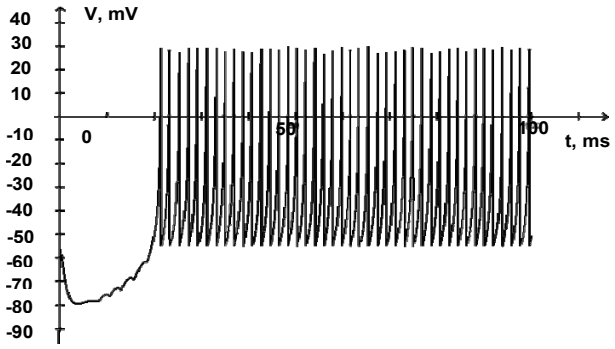

Fig. 10. Neural dynamics for b=0.7

Conclusions. Neurons activity in the cortical column model is changed from bursting to spiking activities when considering from the first to the sixth layer. Researches of synchronization coefficient dependency from changing Izhykevich model' parameters showed:

- presence of parameters, for which the complex neural network dynamics is possible;
- the synchronization coefficient reaches its maximum at:
  - for a=0.03 → k=0.27;
  - for b=0.7 → k=0.365;
- cortical column is less synchronized during changing of parameter a: the synchronization coefficient k – 25−30%;

We can conclude that the time-scale parameter of the membrane potential recovery variable has the weakest influence on synchronization in neocortex. Smaller values result in slower recovery. To enhance synchronization activity in neurons mention above the sensitivity of the recovery variable to the subthreshold fluctuations of the membrane potential should be increased. This fact may be useful for influence on epileptic activity.

Reference

1.Abarbanel G. D., Rabinovich M. I.,Selverston A. Sinhronizacija v nejronnyh ansambljah // Uspehi fizicheskih nauk, Tom 166, №4, – 1996. – s. 363–390. 2. Borisjuk G. N., Borisjuk R. M., Kazanovich Ja. B., Ivannickij G. R.Modeli dinamiki nejronnoj aktivnosti pri obrabotke informacii mozgom – itogi "desjatiletija" // Uspehi fizicheskih nauk, tom 172, №10, 2002. – s. 1189–1214. 3. Izhikevich E. M. Simple model of spiking neurons // IEEE Transactions on Neural Networks. – 2003. – 14, №6. – P. 1569–1572. 4. Hebb D.O. The organization of behaviour. A neurophysiological theory. New York 1949. 335p. 5. Kochubej S. A.. Osobennostu rascheta koefficienta sinhronizacii nejronnyh setej // Visnyk Dnipropetrovskogo universytetu. Biologija. Ekologija. – 2009. – Vyp. 17, t. 2. – s. 55–62. 6. Lorento de No R. Analysis of the activity of the chains of internuncial neurons // J.Neurophysiol. 1939. V.1. P. 208–217. 7. Lorento de No R. Studies of structure of the cerebral cortex // J.Psychol. Neurol. 1933.V. 45. P. 381–392. 8. Mauntkasl V., Organizujuschij princip funkcii mozga: elementarnyj modul i raspredelennaja sistema // Edelman Dz., Mauntkasl V. Razumnyj mozg. – M.: Mir, 1981. 9. Serkov F. N. Elektrofiziologija vysshyh otdelov sluhovoj sistemy. – Kiev: Nauk. dumka. – 1977. – 215s. 10. Towe A.Z. Notes on the hypothesis of columnar organization in somato-sensory cerebral cortex. //Brain. Behav. and Evolut. 1975. V. 11. N 1. P.16–47.

Submitted on 21.05.13

К. Карпенко, асп., О. Судаков, канд. фіз.-мат. наук, каф. медичної радіофізики, радіофізичний факультет, КНУ імени Тараса Шевченка, Київ

ВПЛИВ ВІДНОВЛЮЮЧИХ ПАРАМЕТРІВ МОДЕЛІ НА МЕРЕЖЕВІ СИНХРОНІЗАЦІЙНІ ХАРАКТЕРИСТИКИ НИЗХІДНОГО ІНФОРМАЦІЙНОГО ПРОЦЕСУ В НЕЙРОННІЙ КОРТИКАЛЬНІЙ СТРУКТУРІ

У роботі досліджено характер взаємодії нейронів у мережах зі складною динамікою, розглянуто явище синхронізації для низхідного інформаційного процесу у кортикальній колонці. Залежність коефіцієнтів синхронізації від варіювання різних параметрів моделі нейрона Іжикевича відображено на відповідних графіках. Для візуальної оцінки синхронізації побудовано растри спайкової активності. Побудовано діаграми для порівняння коефіцієнтів синхронізації на кожному з шарів кортикальної колонки. Показано, що на синхронізацію найменший вплив має зміна часового параметру відновлення мембранного потенціалу.

Ключові слова: коефіцієнт синхронізації, модель Іжикевича, кортикальна нейромережа, низхідний інформаційний потік.

Е. Карпенко, асп., А. Судаков, канд. физ.-мат.наук, каф. медицинской радиофизики, радиофизический факультет КНУ имени Тараса Шевченко, Киев

ВЛИЯНИЕ ВОССТАНОВИТЕЛЬНЫХ ПАРАМЕТРОВ МОДЕЛИ НА СЕТЕВЫЕ СИНХРОНИЗАЦИОННЫЕ ХАРАКТЕРИСТИКИ НИСХОДЯЩЕГО ИНФОРМАЦИОННОГО ПРОЦЕССА В НЕЙРОННОЙ КОРТИКАЛЬНОЙ СТРУКТУРЕ

В работе исследован характер взаимодействия нейронов в сетях со сложной динамикой, рассмотрено явление синхронизации для нисходящего информационного процесса в кортикальной колонке. Зависимость коэффициентов синхронизации от варьирования различных параметров модели нейрона Ижикевича показана на соответствующих графиках. Для визуальной оценки синхронизации построены растры спайковой активности. Построены диаграммы для сравнения коэффициентов синхронизации на каждом из слоев кортикальной колонки. Показано, что на синхронизацию наименьшее влияние имеет переменная временного параметра восстановления мембранного потенциала.

Ключевые слова: коэффициент синхронизации, модель Ижикевича, кортикальная нейросеть, нисходящий информационный поток.

UDC 53.023

D. Kolomoets, stud., Department Nanophysics and nanoelectronics, Faculty of Radiophysics, Taras Shevchenko National University of Kyiv

COMBUSTION REACTOR SIMULATION USING CELLULAR AUTOMATONS

Evolution process in a system of burning fuel in a limited reactor with high-level substance mixing is analyzed. Demonstrated that the system tends toward decreasing total combustion front length and suppressing smaller dissipative structures by bigger ones. It is shown that little temperature noise affects those structures similar to high diffusion. Also the relation between coefficients used in theoretical model and stationary cluster formation is derived.

Key words: burning process, feedback, equilibrium state, dissipative structures, cellular automatons.

Introduction. Ordinary models describing the burning process of a combustion agent use dynamic coordinate-dependent fuel distribution. Such systems are developed for solid or fluid fuels [1, 2] and assume using the inhibitor method to achieve correct results [6].

Another option determining our current interest consists in systems with high-level substance mixing where strong feedback based on general fuel concentration is present.

The examples are high-movable gas jet burning and glow discharge between two flat electrodes. Points of interest in such system are conditions for occurrences of one or another state and their time and parameters variation stability.

In this paper we demonstrate typical solutions obtained by rarely used cellular automatons method [4] and explain why such method was chosen to solve the theoretical

model proposed in [6] for such a system. We show relations between coefficients used in that model and burning cluster formation parameters using simple approximation for stationary solution. According to obtained for 2D system results we can consider natural behavior of flame areas in reactor, which we discuss in the last section.

Theoretical model. Our model for high mixing system includes a certain reactor area with cold walls and instant fuel diffusion in that area. To support permanent general feedback a stream of fuel must come in that system from some direction, equivalent for any area point. Therefore, current model was chosen as 2D model, but it can be optionally extended.

The evolution of the system is ruled by the set of partial differential-algebraic equations, phenomenologically obtained in [6] :

$$\begin{cases} \partial T / \partial t = & n\,q(T) - \gamma\left(T - T_0\right) + \chi\nabla^2 T \\ \partial n / \partial t = & W - n\int\limits_V Q\left(T\left(\vec{r}\right)\right)d\vec{r} \end{cases}, \qquad (1)$$

where main variables are temperature of local point $\mathrm{T} = \mathrm{T}\left(\mathrm{x},\mathrm{y},\mathrm{t}\right)$ and fuel concentration $\mathrm{n} = \mathrm{n}\left(\mathrm{t}\right)$.

The approximate reaction activity functions (heat liberation and fuel consumption) $q(T) = Q(T) = \Theta(T - T_c)$ are interpolated by Heaviside's theta; normalized constant temperature $0 < \mathrm{T} < 1$ refers to reactor walls and $T_c > T_0$ – to the threshold temperature of ignition; the constants γ, χ and W are irradiation, diffusion and fuel income coefficients, respectively.

Terms $\mathrm{n\,q}\left(\mathrm{T}\right)$ and $-\gamma(T - T_0)$ determine the heat income by burning fuel and environmental losses in unit time. The integral term represents general feedback in this system by means of fuel concentration, and $\nabla^2 T$ term is charged with heat conductivity.

Method of solution. To analyze this system we cannot use nor analytic Fredholm methods [7] nor Laplace transform [5]. Moreover, even the numerical method of grids is inefficient in case of unequal number of arguments for all functions. The technique of lines for solving partial differential equations (PDEs) might be better [3], but it is too crocky for dense grids. So, to encapsulate each separate line in that technique it was settled to use cellular automatons [4]. Besides that, such representation allows us to use discreet unit-step instead of exponential fuzzy-step functions, which have to be the substitution for Heaviside's theta to achieve the integration convergence of the system. Such approach simplifies the evaluation process and increases its precision.

Stationary solution. Our goal is to obtain estimate parameters for 1D model and use them in following 2D simulations. The main problem in stationary version of initial system (1) is how to get rid of integral multiplier and Laplace operator.

Let us suppose a system state with mostly constant burning area. This condition is valid for a static or slow dynamic equilibrium. On the basis of used Heaviside's theta functions we can assume the constant temperature and zero laplacian across reactor's cold T_0 and burning T_F zones except a sufficiently narrow band ΔL along burning fronts

$$\text{Cold:} \begin{cases} 0 = & 0 \\ T_0 = & const \end{cases}, \qquad (2)$$

$$\text{Burn:} \begin{cases} 0 = & n - \gamma\left(T_F - T_0\right) \\ n/\gamma = & T_F - T_0 \end{cases}. \qquad (3)$$

In such a case, area ratio $\delta S = S_{burn} / S_{\Sigma}$ provides the value of integral in (1). Using (3) one can write down expression for fuel concentration

$$\text{Fuel:} \begin{cases} 0 = & W - n\,\delta S \\ n = & W / \delta S \\ W/\gamma = & \delta S(T_F - T_0) \end{cases}. \qquad (4)$$

The last two zones with temperature $T_0 < T_1 < T_c$ and $T_F > T_2 > T_c$ correspond to narrow band ΔL between cold (2) and burn (3) areas. It's the only place where diffusion in our model exists

$$\text{Lower:} \begin{cases} 0 = & -\gamma\left(T_1 - T_0\right) + \chi\nabla^2 T_1 \\ \chi/\gamma = & \left(T_1 - T_0\right) / \nabla^2 T_1 \end{cases}, \qquad (5)$$

$$\text{Upper:} \begin{cases} 0 = & n - \gamma\left(T_2 - T_0\right) + \chi\nabla^2 T_2 \\ \chi/\gamma = & \left(T_2 - T_0\right) / \nabla^2 T_2 - n/\gamma \end{cases}, \qquad (6)$$

where T_1, T_2 are some arbitrary points of this front.

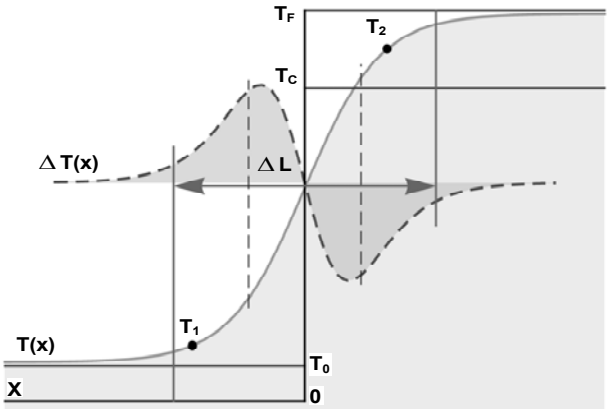

Fig. 1. Fuzzy step function representing the approximate flame front with appropriate sectors, where T(x) and its second derivative reproduce each other and central sector where not

From (5, 6) one can see how front and diffusion curves constantly follow each other to maintain constant value. It allows us to approximate the combustion front by exponential fuzzy threshold function

$$F\theta(x) = \frac{1}{1 + \exp(-sx)}, \qquad (7)$$

$$T(x) = (T_F - T_0)F\theta(x) + T_0, \qquad (8)$$

$$\nabla^2 T(x) = -s^2(T_F - T_0)(\ldots). \qquad (9)$$

On Fig. 1 the plotted curve pieces out of dashed vertical lines are well concerted. Of course, in the central part of the diffusion curve between those lines our fuzzy theta approximation is not appropriate. But we can consider there some monotonous function and phenomenologically adjust results by perforce.

We can obtain constrain on from derived dependence $T / \nabla^2 T = const$ in (5, 6) indifferently. Let us distribute $T(x)$ to Taylor series and choose terms that keeps constant ratio. Such correction is permitted on the score of the above-mentioned contradiction

$$\frac{T(x) - T_0}{\nabla^2 T(x)} = \frac{(\frac{1}{2} + \frac{sx}{4} - \frac{s^3 x^3}{48} + \ldots)}{s^2 f_{\Delta}(x)} = const, \qquad (10)$$

$$\chi/\gamma = \frac{sx f_E(x)}{s^2 f_{\Delta}(x)} \sim 1/s, \qquad (11)$$

where $f_{\Delta}(x)$ include the rest laplacian terms in (9), and $f_E(x)$ is some phenomenological compensating function.

Taking into account the similar normalized dependence for other parameters, next we can equate terms with each

other $\chi/\gamma = 1/s$. Let us try to find the front width $\Delta L = 2d$ as band where laplacian effective influence is $\zeta = 90\%$:

$$\int_0^d \partial_{xx} F\theta(x)dx = \zeta \int_0^\infty \partial_{xx} F\theta(x)dx, \quad (12)$$

$$\tanh^2(d\,s/2) = \zeta, \quad (13)$$

$$(2/d)\,\mathrm{arctanh}(\sqrt{\zeta}) = s, \quad (14)$$

hence $\chi/\gamma = \Delta/7.27$. It is convenient for us to substitute the equilibrium fuel concentration with $n_s = 1$ and replace $T_F - T_0$ with ΔT_F:

$$\begin{cases} W = \delta S \\ \gamma = 1/\Delta T_F \\ \chi = \Delta L^2/(7.27\,\Delta T_F) \end{cases}. \quad (15)$$

Assuming given values, for instance $T_0 = 0.2, \Delta T_F = 1$ $\Delta L = 20, \delta S = 0.4$, we can obtain typical parameters for further simulation.

Cellular automatons system conversion. Cellular automatons (CAs) are n-dimensional elements of space with determined rules of state changing for each discreet iteration of the evolution process [4]. On purpose of tensor representation and storage of CAs, the square space quantization will be used instead of more isotropic hexagonal quantization. The CAs consistent with the reactor walls have to be in constant state and therefore processed separately.

The general fuel concentration could be described by a separate unit CA. But in general case one have to use two interacting CA structures for representation the system with distributed fuel concentration dependent on location.

Classical discreet states of CAs will be replaced by continuums of temperature and concentration. Thus, state changing rules could be described in terms of absolute value increments.

In terms of discreet time and space, the evolution process with units *dt* and *h* has such iterative rules for separate CA at $\{x, y\}$:

$$\begin{cases} T_{t+dt} \to T_t + (\Delta T + \chi \nabla^2 T + \delta T)\,dt \\ n_{t+dt} \to n_t + (W - n_t N_{(T>T_c)}/N_\Sigma)\,dt \end{cases}, \quad (16)$$

where N_Σ corresponds to the total amount of CAs and δT is some temperature fluctuation, which has some applications for simulation experiments. The temperature distribution is scalar field with isotropic diffusion, so using finite differences form of the second derivative

$$T_{xx}(x_0, t) \simeq \frac{T(x_0 + h, t) - 2T(x, t) - T(x_0 - h, t)}{h^2}, \quad (17)$$

we can simplify laplacian in (16) to term of 9-neighbor totalistic CA

$$\nabla^2 T_{x,y} \to \Big(\sum_{i,j}^{-1,0,1} T_{x+i,y+j} - 9T_{x,y}\Big)/h^2. \quad (18)$$

Apparently, it seems as crude approximation. But the single difference consists in a little front position deviation from analogous front in a continuous space. Considering $h = 1$ and exposing ΔT let see what we get

$$T_{t+dt} \to T_t + (n_t \Theta(T_t - T_c) - \gamma(T_t - T_0) + \delta T + \chi\Big(\sum_{i,j}^{-1,0,1} T_{x+i,y+j} - 9T_{x,y}\Big))\,dt \quad . \quad (19)$$

$$n_{t+dt} \to n_t + (W - \frac{n_t}{N_\Sigma}\sum_{k=1}^{N_\Sigma} \Theta(T_t^k - T_c))\,dt$$

The smaller time step the more accurate solution we obtain. Case of sufficiently small step is complete analog to numerical method of lines applied to PDEs. The opposite case reveals unstable behavior with possibility of system transformation into a pacemaker (emergent regimes can be interesting per se, but not in this case). So, there is a sense in usage of the variable time step for more precise evaluation in quick phases or more draft in slow phases.

Simulation results and discussion. Effect of the moving front shows itself only in highly diffusive systems in way of Fig. 2.

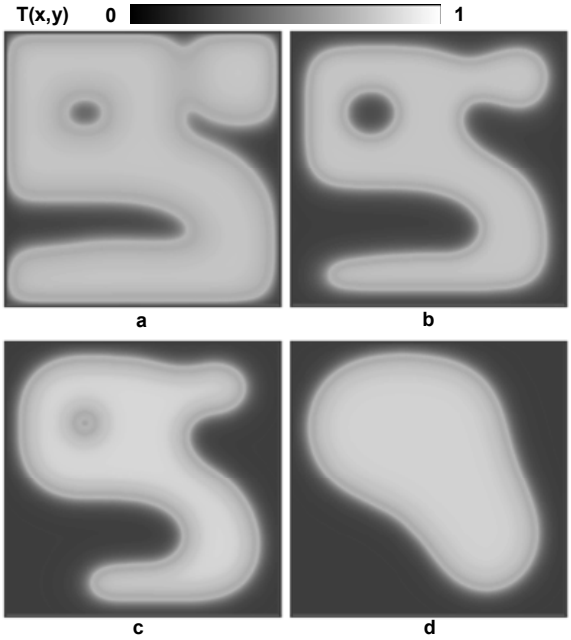

Fig. 2. The evolution process (a-d) trending towards reducing the active front length and smoothing separate details in highly diffusive systems. $\Delta T = 0.4, \Delta L = 20, \delta S = 0.6$

When flame temperature became sufficiently high, the burning front spreads across reactor's area. However, spreading reduces to temperature drop and for $T_F < T_{Fstat}$ the opposite process advances, until irradiation would be balanced by diffusion.

To avoid the influence of described 'front optimization' processes and to see only feedback's effects the diffusion have to be small (see Fig. 3).

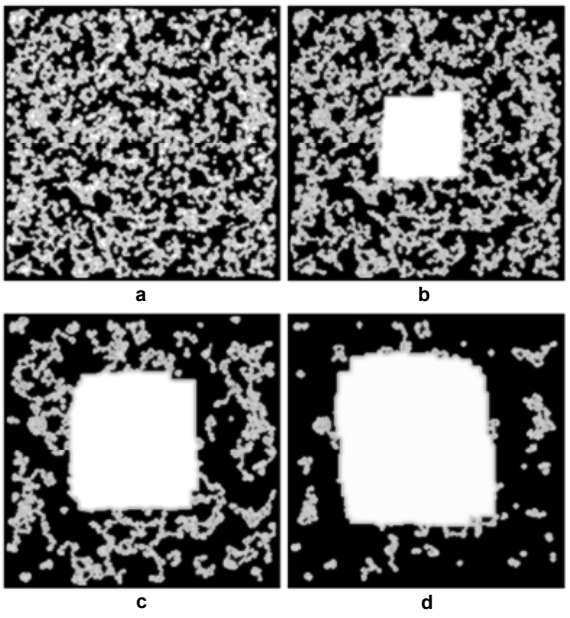

Fig. 3. Suppressing more sensitive to feedback changes smaller burning centers by bigger centers brought on purpose in stationary state (a). $\Delta T = 0.8, \Delta L = 4, \delta S = 0.5$

If we bring into system a big local flame center like Fig.3(b), we can see how smaller centers gradually disappear. Such 'energy transfer' effect is consequence of the instant fuel concentration drop after intentional flame initiation. This 'inertness' make smaller clusters be more liable to any changes in system.

Basic process tendencies reveal itself in the presence of little noise at Fig. 4.

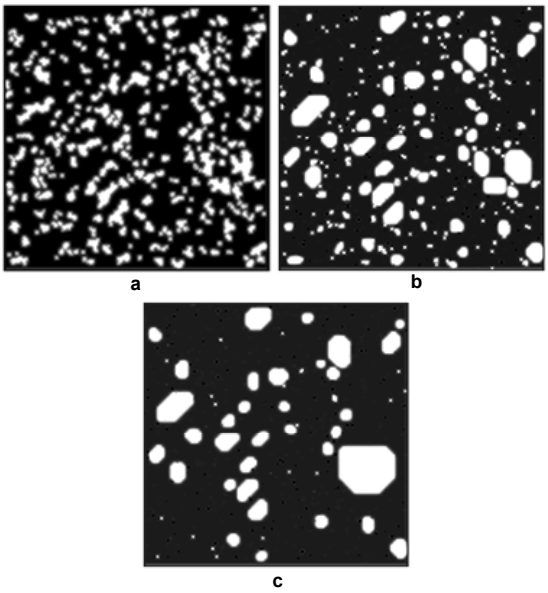

Fig. 4. Little noise affecting the stationary state (a) of low-diffusion systems similarly to Fig. 2 and Fig. 3 altogether. $\Delta T = 0.5, \Delta L = 3, \delta S = 0.4$

Energy redistribution in such a case inclines to reduction of smaller and growth of bigger clusters, which are steadier to fluctuations, like it was shown in Fig. 3. Moreover, in case of insignificant diffusion noise simulates processes similar to Fig. 2 and results in the front shape optimization, which is not implemented otherwise.

Temperature's fluctuations on the brink of combustion when $T_c - T_0 \ll T_0$ and fuel's concentration $n \gg n_s$ lead to massive explosion starting from the active center like in Fig. 5.

Because of the fast confluence, this center arises and draws up piece of general resources through feedback. Therefore, small clusters are fired much later or can't even be fired at all. After explosion, clusters become crumbled up and almost evenly distributed. Long iteration period later, they must unite like in Fig. 4, but in the beginning such behavior is unobservable because of almost equal cluster sizes.

Conclusion. We have analyzed the evolution process of burning in the systems with high-level substance mixing using the cellular automatons method. Discovered behavior is in agreement with the real nature processes and tends to the equilibrium minimal-energy states in spite of kind of system. Such principle takes the form of rounding the burning area boundaries and the dominant stability of the bigger formations. And it makes no difference between high-diffusion and noisy systems in general tendencies.

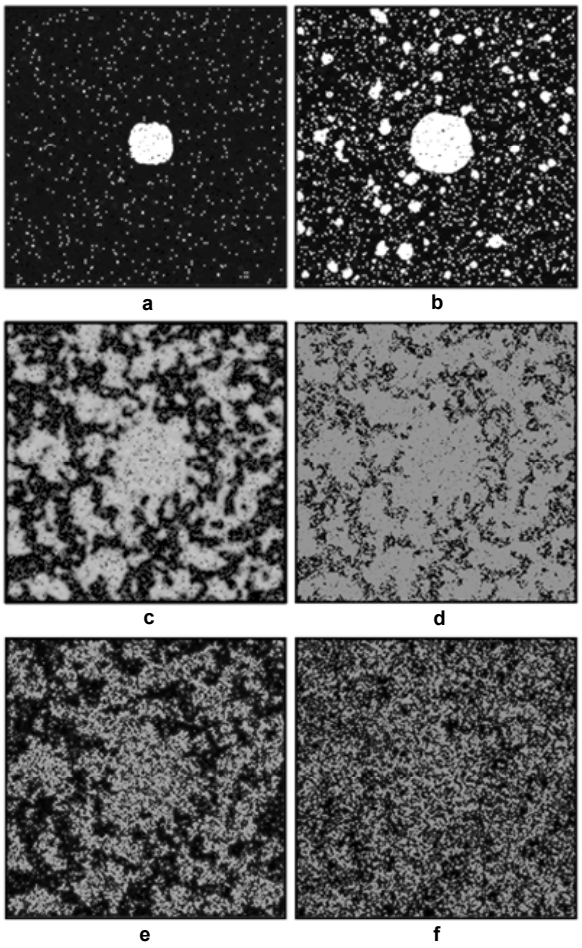

Fig. 5. Consecutive stages of the explosion under little noise influence starting from high fuel concentration (a) till stationary (f). $\Delta T = 0.05, \Delta L = 3, \delta S = 0.5, n = 10 n_s$

The applied cellular automatons approach is very scalable and flexible, so CAs could be used for analyzing very wide range of systems. It could be loose and imprecise in questions of front microstates but makes it possible to observe general tendencies on the fly.

Reference

1. Duijn, C.J. Grate Furnace Combustion: A model for the solid fuel layer. – Eindhoven, 2008. 2. Matkowsky B.J., Sivashinsky G.I. Propagation of a pulsating reaction front in solid fuel combustion // SIAM J. – 1978. – Vol. 35. 3. Numerical solution of partial differential equations. URL: http://reference.wolfram.com/mathematica/tutorial/NDSolvePDE.html (checked 25.04.13). 4. Wolfram S. A new kind of science. – Canada, 2002. 5. Дёч Г. Руководство к практическому применению преобразования лапласа. – М., 1965. 6. Лоскутов А.Ю., Михайлов А.С. Основы теории сложных систем. – Ижевск, 2007. 7. Шишкин Г.А. Линейные интегродифференциальные уравнения Фредгольма. – Улан-Удэ, 2007.

Submitted on 23.04.13

Д. Коломоєць, студ., каф. нанофізики та наноелектроніки, радіофізичний факультет, КНУ імені Тараса Шевченка, Київ

МОДЕЛЮВАННЯ ГОРІННЯ В РЕАКТОРІ ЗА ДОПОМОГОЮ КЛІТИННИХ АВТОМАТІВ

Проаналізовано еволюцію згоряння палива в обмеженому реакторі для системи з сильним перемішуванням речовини. Продемонстровано тенденцію системи зменшувати загальну довжину фронту горіння та подавляти менші дисипативні структури більшими. Показано, що малі теплові шуми в системі діють на ці структури подібно до підвищеної дифузії. Також виведено зв'язок між коефіцієнтами, використаними у теоретичній моделі, та стаціонарними кластерними утвореннями.

Ключові слова: процес горіння, зворотній зв'язок, рівноважний стан, дисипативні структури, клітинні автомати.

Д. Коломоец, студ., каф. нанофизики и наноэлектроники,
радиофизический факультет, КНУ имени Тараса Шевченко, Киев

МОДЕЛИРОВАНИЕ ГОРЕНИЯ В РЕАКТОРЕ С ПОМОЩЬЮ КЛЕТОЧНЫХ АВТОМАТОВ

Проанализировано эволюцию сгорания топлива в ограниченном реакторе для системы с сильным перемешиванием вещества. Продемонстрировано тенденцию системы уменьшать общую длину фронта горения и подавлять меньшие диссипативные структуры большими. Показано, что малые тепловые шумы в системе воздействуют на эти структуры подобно повышенной диффузии. Так же выведена связь между коэффициентами, использованными в теоретической модели и стационарными кластерными образованиями.

Ключевые слова: процесс горения, обратная связь, равновесное состояние, диссипативные структуры,

UDC 004.(55+58+633)

A. Kotenko, post., V. Bilonenko, eng., V. Gryaznova, Ph.D., Yu. Boyko, Ph.D., E. Filatov, stud.,
Taras Shevchenko National Universityof Kyiv, Radiophysics Faculty, Computer Engineering department

CLUSTERING OF CONCEPTS BY MEANS OF THE INTERNET

The approach to text information analysis using data from the Internet by example of clustering of concepts is considered in this paper. The problem of clustering of concepts is reduced to the problem of partition a graph into subgraphs in the case of not known in advance quantity of subgraphs. The algorithm of graph partitioning by the target function optimization is proposed, as well as the form of the target function for concepts clustering. The results are verified by experimental data.

Keywords: clustering, text analysis, graph partitioning, optimization.

Introduction. Possibility of automated text analysis is demanded by variety of problems. But a text is, as a rule, weakly formalized and its content can be defined only through the context, because the meaning of a specific word may differ depending on its interrelation with surrounding words. This fact causes impossibility of usage for creation such a text analysis system of the approach that is typical for compilers and interpreters of programming languages and requires existence of database which would integrate the concepts, words designating these concepts, and their interrelations. Such a database can be developed by transfer knowledge from a person or persons to some system that would save this knowledge in a suitable form. Difficulty and laboriousness of direct performing such a task is obvious.

Nevertheless human race has accumulated tremendous volume of mentioned above knowledge in the form of text. This form of data saving is comfortable and habitual for people but it cannot be used as automated knowledge base. That is why is seems natural to try to analyze existing texts and to build a database on their basis – this idea enables to take advantage of the work already made instead of doing it from the very beginning.

So the goal of the research is verification of proposed approach for building database on the example of semantic clustering of the concepts.

Generally, a text written by a person and appointed for understanding by other people contains concepts related in meaning. Respectively, a measure of cohesion for the pair of concepts can be obtained by means of analysis of frequency of appearance of the word pair in a text. In its simplest case, this approach cannot enable the construction of the knowledge base in a form offered in semantic web [1], when pair of concepts is connected by the third concept, but it gives the possibility to group the words to the clusters by themes.

At the moment the Internet contains huge amount of information. This fact, as well as simple access to this information, allows its using as the source of existing texts. A web page identified by URI is assumed as a text unit. With these assumptions, the task of separation the words into semantic clusters is reduced to the analysis of frequencies of appearance of the word pairs at the same URI and then to the association of the words into groups according to their meanings.

Thus, the problem is formulated in terms of concepts (represented by appropriate words) and measure of cohesion between these concepts. It makes possible to consider the set of input data as a weighted graph and reformulate the problem to the problem of optimal partition of the graph into subgraphs by criterion of "semantic cohesion". This problem is of NP-complete problems type, so precise methods, e.g. brute-force search, have no use because of their computational complexity.

Practically applicable algorithms of partitioning the graph, as a rule, allow finding not a global optimum for the task but some optimal result satisfactory for practice or, in more difficult cases, some optimum that can be obtained in limited time. In this way, precision and accuracy of algorithm is superseded by speed at the expense of the fact that direction of further search of optimum is defined in every local point. In result, the algorithm cannot assure finding of a global optimum and more, the result depends on a choice of the initial point.

Development and discussion.

Quality criteria of graph partitioning. Semantic cohesion and respectively optimal partitioning for semantic cohesion are not the determined concepts and cannot be strictly defined because of subjectivity of concept of meaning of a word per se. But solving the problem demands to determine some, though subjective, quality measure of optimal graph partition.

Some requirements for graph partitioning may affect properties of this subjective quality measure. These requirements can be formulated as follows:

- Graph vertices inside a cluster must be bound more strongly than vertices from different clusters.
- Clusters have not obligatory equal sizes, the more so the themes corresponding to clusters can contain different quantities of concepts.
- Quantity of clusters is not known in advance.

Nevertheless, there is need in some reasonable expectations about quantity of clusters. The matter is that all the concepts are connected somehow or other and, therefore, all of them have to be united in the only cluster. On the other hand, every concept differs from others and, therefore, has to be contained in individual cluster. These are extreme two cases of the choice of threshold value of cohesion at which concepts are united in a cluster. Obviously, the value of threshold cohesion affects quantity of clusters, i.e., scale at which all the system is considered. It is clear as well that a single objective function, suitable for all possible cases, cannot exist and that the objective function has to depend on the parameter which determine where is the boundary between different themes (and corresponding clusters). Evidently, this parameter has to be chosen on the basis on the characteristics of specific problem.

Some arbitrary threshold value of cohesion measure can be used in certain situations. But such an approach has an obvious disadvantage: the value is not absolute

and can be determined in different ways, not to mention that the unit of measurement of this threshold value cannot be clear defined.

Another approach is to use as a threshold parameter one of interdependent values, namely, the quantity of clusters and average size of a cluster. Both of the values are intuitive, are measured absolutely and defined uniquely. Of these two, usage of the quantity of clusters is more convenient, as this value does not depend on the quantity of graph vertices.

Existing methods of graph partitioning. Actually, there exist different methods of graph partitioning, the best known are Kernighan-Lin algorithm, multilevel algorithms and spectrum algorithms.

- Kernighan-Lin algorithm [2] is used for partitioning a graph into two subgraphs of the same size. The main feature of this algorithm is minimization of sum of the weights of "disrupted" edges between the subgraphs. Fiduccia-Mattheyses algorithm is an improved version of Kernighan-Lin algorithm in case of hypergraphs.
- Multilevel algorithms are based on the idea of the graph simplification, allocation features of the largest possible size and finding solution at this level with further detailed specification of it. This idea allow speed-up versus brute-force search at the expense of inaccuracy caused by neglecting the details. One of examples of such algorithms is METIS [3].
- Spectrum algorithms are based on analysis of quantity of edges with certain weight and divide all the edges into two groups: the inner edges of the cluster and the edges connecting vertices that belong to different clusters. In fact, these algorithms are very similar to graph partitioning using histograms.

Nevertheless, any of the above-mentioned algorithms cannot be used for solving the task. The main reason is that all these algorithms demand to determine in advance the quantity of future subgraphs. For some of the algorithms the quantity of resulting parts have to be set immediately, other allow to determine it in a few iterations by serial bisection. Realization of the last schemes also leads to that the sizes of resulting clusters are the same or, even if they are not the same, they cannot depend on cohesion of vertices inside the clusters.

Thus, the existing algorithms are insufficiently flexible for partitioning a graph into not equal or somehow preliminary restricted parts, but in some more or less natural way. It leads to necessity to propound another algorithm for the problem of semantic graph partitioning.

Description of the algorithm. The algorithm, as well as other existing algorithms of graph partitioning, is not precise. In the framework of propound approach, the problem is defined as optimization problem with some target function which is the quality measure of partitioning of graph into subgraphs. The algorithm is sequential and action that is made at each step of it is chosen as an operation that maximally changes the target function towards its optimum value. The algorithm is stopped when there is no operations that tends the target function towards the optimum. So, it is obvious that during evaluation the algorithm the local optimum matters and the system as a whole not necessarily reaches the global optimum, but the result depends on the choice of initial state of the system.

As a trivial example of the initial state of a system can be used the state when each vertex is considered as a self-sustained cluster.

The algorithm as a whole consists of the following parts:

- moving the vertices between the clusters. This action can be possibly applied to all the vertices in graph, if it leads to optimizing the target function;
- merging the clusters. This step is useful in case when relocation of a single vertex does not tend the target function towards the optimum, but relocation of a set of vertices do it;
- deleting the zero-sized clusters that appeared because of different relocations.

This algorithm can be generalized for applying in the case when the whole data is not known immediately, but appears gradually. Then graph partitioning is made in the above-described manner with initial state of data, and after appearing a new portion of data the clusterization is repeated in the same way with the new data included in the system.

Such gradual partitioning allows considering changes in data in less time than solving the problem from the very beginning for each portion of new data. This variation of algorithm has certain inertia and is also useful in a situation when sharp change in way of partitioning the whole graph into clusters, which can be caused by re-partitioning the graph from the very beginning at each addition of new portion of data, is unacceptable.

Target function. As it was mentioned above, the quality of partitioning is a subjective value, which cannot be strictly defined. Because of this fact, the choice of target function was made on the base of quality, not necessarily precise and unconditional, considerations. As a target function in this paper we use the following function:

$$F = -Qf \cdot \sum_{i=1}^{N_c} \sum_{j=1}^{S_i} \sum_{k=1}^{S_i} A_{jk} + \sum_{i=1}^{N_c} S_i^2 + Sf \cdot N_c \,, \qquad (1)$$

where N_c is a quantity of clusters, S_i is a quantity of vertices in the i-th cluster, A is the adjacency matrix of the graph, Qf and Sf – some parameters, described below. We also use minimum of the function F as an optimal value of the target function, and measure of cohesion between the vertices connected by an edge as the weight of this edge. Due to the statement of the problem the weights of the edges should be nonnegative.

Nonnegative parameters Qf and Sf are necessary for adjusting the contribution of every of the three terms of target function (1). The third possible parameter is excessive because of existing possibility of normalization the function, as all that matters for the problem solution is the fact that the target function reached its minimum, and the specific value of this minimum is inessential.

The term $\sum_{i=1}^{N_c} \sum_{j=1}^{S_i} \sum_{k=1}^{S_i} A_{jk}$ is the sum of weights of inner edges of a cluster. It corresponds to the requirement for internal connections between vertices of the cluster to be stronger than external connections. This term is proportional to the measure of cohesion between vertices inside the cluster. The sense of this term and minus sign before it is what determines that optimum of the target function (1) is its minimum value. Hence, the parameter Qf determines the importance of cohesion of vertices inside a cluster with respect to other terms of the target function.

But all the foregoing does not allow accounting the second part of the requirements, namely, the weak coupling between clusters. And obviously, in the case of existence of only the first term in the target function the optimal value is reached as long as the entire graph is the only cluster. Another disadvantage of hypothetical target function in the form of only the first term is that dependence of this term on the size of clusters is quadratic, as the quantity of possible edges, excluding loops, in case of undirected graph is $\frac{1}{2} \cdot S_i \cdot (S_i - 1)$), and it also results in

achieving the optimal value of this hypothetical target function in case of the only cluster.

The term $\sum_{i=1}^{N_c} S_i^2$ is introduced to eliminate above-mentioned issues. So, the term $\sum_{i=1}^{N_c} S_i^2$ is the total quantity of possible edges in all the clusters (up to a factor and considering loops). This term counteracts to quadratic increase of the first term, representing total cohesion, as negated to it.

The third term in (1) is introduced for regulation of an average size of a cluster, and parameter Sf represents the ideal desirable size of a cluster (detailed explanation can be found below).

For investigation of characteristics of the target function let assume that $Qf = 0$. Then the target function takes the form

$$F = \sum_{i=1}^{N_c} S_i^2 + Sf \cdot N_c \ . \qquad (2)$$

As in specified case the role of cohesion between vertices in the clusters is neglected, it is possible to consider the case of equal size of all the clusters without loss of generality. If $\overline{S}$ designates the size of a cluster in this case, then quantity of clusters of the entire system will be $N_c = \frac{N}{\overline{S}}$, where N is the total quantity of graph vertices. Then the target function can be transformed to the form

$$F = N_c \cdot \left(\frac{N}{N_c} \right)^2 + Sf \cdot N_c \ , \qquad (3)$$

and it reach its minimum value at

$$N_c = \frac{N}{\sqrt{Sf}} \qquad (4)$$

(discreteness is neglected here). At non-zero value of parameter Qf the real quantity of clusters can differ from (2), because increase of the level of cohesion inside clusters can require increase or decrease quantity of clusters. Thus, it can be said that parameter Sf determines recommended size of a cluster, but rigidity of this recommendation is regulated by correlation of parameters Sf and Qf.

Thereby, existence of all the three terms in (1), as well as parameters Sf and Qf give desired flexibility to proposed algorithm in contrast to mentioned known algorithms. This flexibility allows us to apply algorithm described in this paper for so poorly formalized problem as construction of connections between words.

Usage of the target function in the form (1) is impractical. The reason of it is the fact, that in this form the target function depends not only on the injected parameters but also on the size of the system under consideration, and this dependence results in instability of ratio of terms contribution in the ending value of the target function. Evidently, it leads to inconvenience at choosing parameters values.

For stabilizing the ratio of terms contribution regardless of size of the system it is appropriate to multiply parameter Qf to the minimum value $F_{min} = 2 \cdot N \cdot \sqrt{Sf}$ of the target function (3) in case of $Qf = 0$.

Thus, finally the target function takes the following form:

$$F = -Qf \cdot 2 \cdot N \cdot \sqrt{Sf} \cdot \sum_{i=1}^{N_c} \sum_{j=1}^{S_i} \sum_{k=1}^{S_i} A_{jk} + \sum_{i=1}^{N_c} S_i^2 + Sf \cdot N_c \ . \qquad (5)$$

Implementation and usage. For experimental approbation of foregoing considerations there was created the program in C++ language. The program is serial but it can be simply parallelized. For the system containing approximately 17000 words (i.e., $N \approx 17000$) the performance of the algorithm on a single core processor Intel Xeon E5620 is about 20 minutes, memory consumption is about 1,2 GB. The choice of C++ was caused by significant resource consumption of the problem. It results in good performance of the program relative to other higher-level programming languages but required more time for the program development. Nevertheless, due to good performance the time required to conduct experiments for the selection of the target function and its parameters was reduced.

As it was mentioned in the introduction, the Internet was used as a source of texts. But loading all the existing pages from the Internet and construction on its base the adjacency matrix for all the words is too difficult both from a technical point of view and in terms of the resources. That is why services of existing search providers [4] were used as a filter for limiting the huge volume of information.

Conclusions.

- Algorithm of partitioning a graph into subgraphs can be realized through optimization of some target function.
- The proposed target function allows taking into account reasonable factors of constructing the clusters of related concepts.
- The proposed algorithm of partitioning a graph into subgraphs allows to solve the problem of finding the clusters of related concepts in an acceptable period of time.
- Texts available on the Internet can be used for grouping semantically connected concepts.

Reference

1. Berners-Lee T., Hendler J., Lassila O. The semantic web // Scientific American – 2001 – 284, N.5. 2. Kernighan B. W.; Lin Shen An efficient heuristic procedure for partitioning graphs // Bell Systems Technical Journal – 1970 – 49. 3. Karypis G., Kumar V. Multilevel k-way partitioning scheme for irregular graphs // J. Parallel Distrib. Comput. – 1998 – 48, N.1. 4.Yandex.XML.Developers manual (http://api.yandex.ru/xml/doc/dg)

Submitted on 18.02.13

**Котенко А.С., асп., Білоненко В.Ю., інж.,
Грязнова В.О., канд. фіз-мат. наук, Бойко Ю. В., канд. фіз-мат. наук.,
Філатов Є.М. студ., КНУ імені Тараса Шевченка, Київ**

КЛАСТЕРИЗАЦІЯ ПОНЯТЬ З ВИКОРИСТАННЯМ МЕРЕЖІ ІНТЕРНЕТ

У роботі розглянуто підхід до аналізу текстової інформації з використанням даних із мережі Інтернет на прикладі кластеризації понять. Задачу кластерізації понять зведено до задачі розбиття графа на підграфи з невизначеною наперед кількістю підграфів. Запропоновано алгоритм розбиття графа на підграфи шляхом оптимізації цільової функції. Запропоновано вигляд цільової функції для опису кластерізації понять. Результати перевірені на експериментальних даних

Ключові слова: кластеризація, аналіз тексту, розбиття графа на підграфи, оптимізація

Котенко А.С., асп., Билоненко В.Ю., инж.,
Грязнова В.А., канд. физ-мат. наук, Бойко Ю. В., канд. физ-мат. наук.,
Филатов Е.М. студ., КНУ имени Тараса Шевченко, Киев

КЛАСТЕРИЗАЦИЯ ПОНЯТИЙ С ИСПОЛЬЗОВАНИЕМ СЕТИ ИНТЕРНЕТ

В работе рассмотрен подход к анализу текстовой информации с использованием данных из сети Интернет на примере кластеризации понятий. Задача кластеризации понятий приведена к задаче разбиения графа с изначально неизвестным количеством подграфов. Предложен алгоритм разбиение графа на подграфы путём оптимизации целевой функции. Предложен вид целевой функции для описания кластеризации понятий. Результаты проверены на экспериментальных данных.

Ключевые слова: кластеризация, анализ текста, разбиение графа на подграфы, оптимизация.

UDC 537.635;537.611.44

O. Laguta, stud., Yu. Kobljanskyi, Ph.D., senior scientist.,
Department of Nanophysics and Nanoelectronics,
Faculty of Radiophysics, Taras Shevchenko National University of Kyiv

OUT-OF-PLANE ANGULAR DEPENDENCE OF FERROMAGNETIC RESONANCE OF PERMALLOY THIN FILMS

Out-of-plane ferromagnetic resonance (FMR) spectra of Permalloy films 25, 50, 75 and 100 nm thick were measured. The angular dependence of FMR was analyzed using Landau–Lifshitz–Gilbert (LLG) equation. With increasing film thickness, the contribution to linewidth of two magnon scattering increases.

Key words: ferromagnetic resonance, Permalloy, thin film, linewidth.

Introduction. Improving the technology of thin magnetic films allows their use in spintronic devices and microwave technology. Therefore there is an interest in their studies. As a powerful technique, ferromagnetic resonance (FMR) has been employed to study magnetic anisotropy, interlayer coupling, magnetic relaxation, film quality, and so on [1, 2]. Three mechanisms have been considered to contribute to the linewidth [3–4, 7–9]. As the first contribution, intrinsic Gilbert damping, resulting from a combination of the exchange interaction and the spin–orbit coupling, exists in all magnetic materials. The second contribution to the FMR linewidth arises from the broadening induced by magnetic inhomogeneity, such as the spread of the magnitude of the magnetization or the internal static magnetic field, and the orientation of the crystallographic axes or magnetic anisotropy axes. This part strongly depends on the preparation condition and thus the film quality [5]. As the third contribution to the linewidth, the so-called extrinsic magnetic relaxation has been argued to originate from the coupling between the uniform resonance modes and degenerating spin waves through structural inhomogeneity. This phenomenon is called two-magnon scattering process [6]. Since the contributions of the intrinsic damping effect and the extrinsic magnetization relaxation, and the inhomogeneity originate from different mechanisms, they have different out-of-plane angular and microwave frequency dependence. Therefore, they should be able to be analyzed and discerned from the measured FMR linewidth.

Experimental results and discussion. The samples were prepared by Electron Beam Evaporation (EBE) and have 100, 75, 50 and 25 nm of thickness. FMR measurements were carried out at room temperature using a Bruker E580 EPR spectrometer, with a fixed microwave frequency of 9.45 GHz. The goniometer was used to vary the angle. Thus the angular dependence of the resonance field and the linewidth were obtained.

Figure 1 shows the sample oriented relative to some right-handed *X*-*Y*-*Z* frame such that the sample normal is parallel to the *Z* axis. External magnetic field H_{ext} and magnetization M_s lies in ZY plane. θ_H is the angle between H_{ext} and the sample normal Z, θ_0 is an angle between M_s and Z. The angle θ_H changes in range of 0^o – 90^o.

The angular dependence of FMR spectra can be obtained by using the LLG equation[1]:

$$\frac{\partial \vec{M}}{\partial t} = -\gamma \vec{M} \times \vec{H} + \frac{G}{\gamma M_S^2} \vec{M} \times \frac{\partial \vec{M}}{\partial t} \qquad (1)$$

Here M_S is saturation magnetization, $\gamma = g\mu_B / h$ and G are the gyromagnetic ratio and the Gilbert damping coefficient, respectively. Using this equation, the resonance conditions can be written follow:

$$\frac{\omega}{\gamma} = \sqrt{H_1 H_2}\,, \qquad (2)$$

$$H_1 = H_{res}\cos(\theta_H - \theta_0) - 4\pi M_{eff}\cos(2\theta_0)\,, \qquad (3)$$

$$H_2 = H_{res}\cos(\theta_H - \theta_0) - 4\pi M_{eff}\cos^2(\theta_0)\,, \qquad (4)$$

where H_{res} is the resonance magnetic field, $4\pi M_{eff} = 4\pi M_s - H_A$ and H_A are the effective demagnetizing field and anisotropy field.

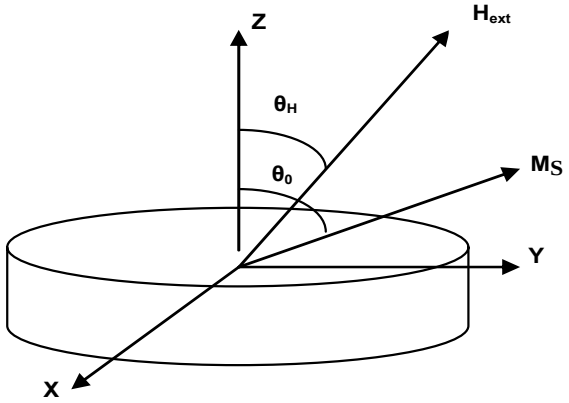

Fig. 1. Disk, field, and static magnetization geometry for the static equilibrium and FMR analysis

The condition for static equilibrium is found if the net torque on M_S is set equal to zero. The net torque is a result of the external field, the demagnetization field, and the anisotropy which acts to pull the magnetization into an easy direction. This condition yields an expression which relates the field and magnetization angles θ_H and θ_0:

$$2H_{res}\sin(\theta_0 - \theta_H) = 4\pi M_{eff}\sin(2\theta_0) \qquad (5)$$

Values of the effective magnetization $4\pi M_{eff}$ can be determined from (2) attached to normal film orientation.

Figure 2 shows the out-of-plane angular dependence for the film of 50 nm thick.

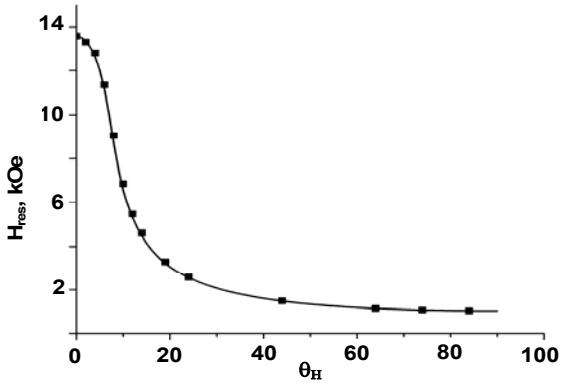

Fig. 2. Angular dependence of resonance field, d=50 nm (Points – measured, line – fitted)

This dependence has the distinct maximum for $\theta_H = 0^o$. H_{res} decreases monotonically with increasing θ_H due to the large demagnetizing. It is apparent that the fitted results, using eq. (2)–(5), are in good agreement with the experimental ones. This means that the LLG equation can be used to describe the FMR results in the present samples.

The thickness dependence of effective magnetization is shown on Figure 3. It shows that $4\pi M_{eff}$ increases with increasing film thickness. Roughly speaking, effective magnetization is an approximately linear function of $1/d$. It is also apparent that the saturation magnetization do not change with the film thickness.

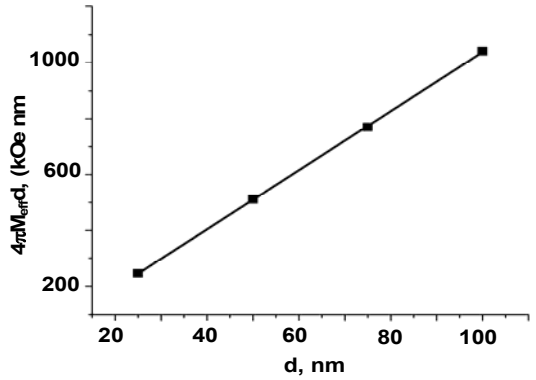

Fig. 3. Thickness dependence of effective magnetization (Points are measured, line serves as a guide to the eye)

The influence of orientation on linewidth was investigated too (Figure 4). This dependence has a strong peak $\theta_H \approx 10^o$. Theoretical description of FMR linewidth can be carried out using Gilbert damping coefficient:

$$G = \alpha\gamma M_s \qquad (6)$$

where α is dimensionless damping coefficient.

In this case, FMR linewidth is described by next equation[3]:

$$\Delta H_{\text{int}\,r} = \frac{1}{\sqrt{3}}\alpha(H_1 + H_2)\left|\frac{d(\omega/\gamma)}{dH_{res}}\right|^{-1} \qquad (7)$$

The coefficient $1/\sqrt{3}$ is the correction for the difference between the full width at half maximum (FWHM) and the peak-to-peak linewidth for the Lorentzian line shape. Figure 4 shows, that the angular dependence of linewidth can be fitted by Eq. (7). This equation qualitatively explains the angular dependence of linewidth.

Fitting parameters for 50 nm thick film are: $\alpha = 0.003$, $g = 2.075$. The parameter a was chosen so, $\Delta H_{pp} = \Delta H_{\text{int}\,r}$ for normal film orientation. There is a difference between ΔH_{pp} and Gilbert linewidth ($\Delta H_{\text{int}\,r}$) for films 50, 75 and 100 nm thick at normal film orientation. This effect can be explained by two magnon scattering process.

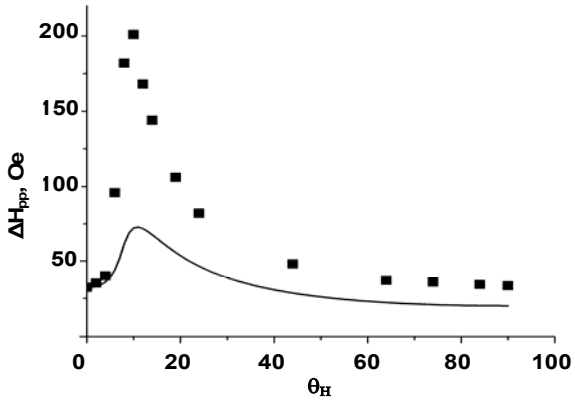

Fig.4 Angular dependence of FMR linewidth, line is calculations, points – experimental data. d= 50 nm

There is the shift of the band for two magnon scattering as the external field orientation is rotated from perpendicular to parallel. In the perpendicular configuration, the bottom of the spin wave band at $k = 0$ is coincident with the FMR frequency and there are no nonzero k spin wave states at this frequency. In the parallel configuration, the band has dropped down so that the top of the spin wave band at $k = 0$ is coincident with the FMR frequency. There is now an extended range of spin wave states degenerate with the FMR frequency. These states range from spin waves at $k = 0$ for $\theta_H = 90^o$ to rather large k values at $\theta_H = 0^o$. That's why, the two magnon scattering process makes biggest contribution to linewidth at parallel configuration and ΔH_{pp} differs from $\Delta H_{\text{int}\,r}$. However, this different depends on film thickness.

Calculations show that spin wave dispersion greatly depends on film thickness. Figure 5 shows that there is a small number of degenerate states and two magnon scattering process makes a small contribution to ΔH_{pp}. This situation arises in 25 nm thick film, where $\Delta H_{pp} \approx \Delta H_{\text{int}\,r}$ for parallel configuration. But with increasing of film thickness, the spin wave dispersion changing the way that regions of degenerate states create. So ΔH_{pp} increases.

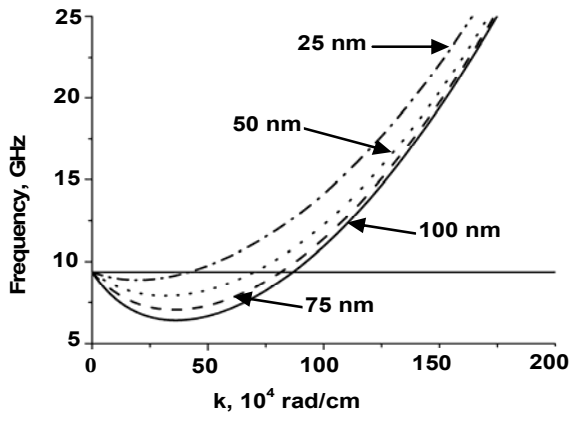

Fig. 5. Influence of film thickness on lowest spin wave dispersion branch

Conclusions. The influence of sample orientation on FMR spectra, namely value of resonance magnetic field and FMR linewidth, was investigated. It was shown that the magnitude of $4\pi M_{eff}$ depends on film thickness. Angular dependence of FMR linewidth has a strong peak and can be qualitatively explained by intrinsic Gilbert damping. The contribution of two magnon process to linewidth was shown too.

Reference

1. Gurevich A., Melkov G. Magnetic oscillations and waves. // Moscow: Nauka, 1994. – pp. 464. 2. McMichael R.D., Stiles M.D., Chen P.J., Egelhoff W.F., Jr. Ferromagnetic resonance studies of NiO-coupled thin films of Ni80Fe20.// Phys. Rev. B.– 1998. – Vol. 58. – P. 8605–8612. 3. McMichael R.D., Stiles M.D., Chen P.J., Egelhoff W.F., Jr. Ferromagnetic resonance linewidth in thin films coupled to NiO // J. Appl. Phys. – 1998. – Vol. 83. – P. 7037–7045. 4. Mizukami S., Ando Y., Miyazaki T. Effect of spin diffusion on Gilbert damping for a very thin permalloy layer in Cu/permalloy/Cu/Pt films // Phys. Rev. B.– 2002.– Vol. 66. – P. 104413(1–9). 5. Mizukami S., Ando Y., Miyazaki T. The Study on Ferromagnetic Resonance Linewidth for NM/80NiFe/NM (NM=Cu, Ta, Pd and Pt) Films // Japan J. Appl. Phys.– 2001. – Vol. 40. – P. 580–585. 6. Sparks M., Loudon R., Kittel C. Ferromagnetic Relaxation. I. Theory of the Relaxation of the Uniform Precession and the Degenerate Spectrum in Insulators at Low Temperatures // Phys. Rev. – 1961. – Vol. 122.– P. 791–803. 7. Urban R., Woltersdorf G., Heinrich B. Gilbert Damping in Single and Multilayer Ultrathin Films: Role of Interfaces in Nonlocal Spin Dynamics // Phys. Rev. Lett. – 2001.– Vol 87.– P. 217204(1–4). 8. Wigen P. E. Dipole-narrowed inhomogeneously broadened lines in ferromagnetic thin films // Physical Review. – 1964. – Vol. 133, № 6A. – P. 1557–1562. 9. Yuan S.J., Sun L., Sang H., Du J., Zhou S.M. . Interfacial effects on magnetic relaxation in Co/Pt multilayers // Phys. Rev. B. – 2003. – Vol. 68. – P. 134443(1–6).

Submitted on 09.11.12

**О. Лагута, студ., Ю. Коблянський, канд. фіз.-мат. наук, ст. наук. співроб.,
каф. нанофізики та наноелектроніки, радіофізичний факультет,
КНУ імені Тараса Шевченка, Київ**

КУТОВА ЗАЛЕЖНІСТЬ ФЕРОМАГНІТНОГО РЕЗОНАНСУ В ТОНКИХ ПЛІВКАХ ПЕРМАЛОЮ

Проведено вимірювання феромагнітного резонансу (ФМР) в широкому діапазоні кутів в тонких плівках пермалою товщиною 25, 50, 75 та 100 нм. Кутова залежність ФМР була проаналізована за допомогою рівняння Ландау-Ліфшиця-Гільберта. Із збільшенням товщини плівки, внесок двомагнонного розсіяння у напівширину лінії також збільшується.

Ключові слова: феромагнітний резонанс, пермалой, тонкі плівки, напівширина лінії.

**А. Лагута, студ., Ю. Коблянский, канд. физ.-мат. наук, ст. науч. сотр.,
каф. нанофизики и наноэлектроники, радиофизический факультет,
КНУ имени Тараса Шевченко, Киев**

УГЛОВАЯ ЗАВИСИМОСТЬ ФЕРРОМАГНИТНОГО РЕЗОНАНСА В ТОНКИХ ПЛЕНКАХ ПЕРМАЛЛОЯ

Проведено измерение ферромагнитного резонанса (ФМР) в широком диапазоне углов в тонких пленках пермаллоя толщиной 25, 50, 75и 100 нм. Угловая зависимость ФМР была проанализирована при помощи уравнения Ландау-Лифшица-Гильберта. При увеличении толщины пленки, вклад двухмагнонного рассеяния в полуширину линии также возрастает.

Ключевые слова: ферромагнитный резонанс, пермаллой, тонкие пленки, полуширина линии.

UDC 537.528

**E. Martysh, D.Sc., Department Medical Radio Physics,
Faculty of Radio Physics, Taras Shevchenko National University of Kyiv**

PECULIARITIES OF PLASMA SOURCES IN PLASMA MEDICINE

This paper has two goals. The first one is the characterization of the plasma source: the plasma power outflux must be known in order to control the conditions under which biology samples are treated. This is especially important in the treatment of living cells, which may not receive high energy doses. Thus, measurements of various plasma parameters relevant for cell treatment have been performed and analyzed. Special attention was given to the acoustic power transmission of the plasma source through internal media. Mechanisms of acoustic transmission in a external medium are discussed.

Key words: plasma source, biology samples, acoustic power transmission.

Introduction. Low temperature non-equilibrium atmospheric pressure plasmas for air and surface cleaning technologies have proven to be robust and safe enough for use indoors. This is partly due to high bactericidal effectiveness of plasmas and partly to their ability to penetrate into narrow and confined spaces, small cracks and microscopic openings.

Such plasmas have been used for a long time for sterilization of medical instruments, bacterial inactivation, blood coagulation, wound healing, oral hygiene, etc. [2]. Recently, with the rapid advances in the multidisciplinary research areas of cold atmospheric-pressure plasmas and plasma health care/medicine, interactions of such low-temperature, non-equilibrium plasmas with a large number of biologic objects, have attracted a major attention [1]. These objects include but are not limited to eukaryotic (mammalian) and prokaryotic (bacterial) cells, viruses, spores, fungi, DNA, lipids, proteins, cell membranes, as well as living human, animal, and plant tissues and organs.

Of particular interest are the plasma interactions with cancerous cells. It has been shown by several groups that the plasma is able to induce death (the programmed death, apoptosis or the necrotic cell rupture) in a number of cancer cell types [3]. This offers exciting prospects for clinical applications of cold atmospheric plasmas for aggressive treatment of malignant cells and ultimately as a viable alternative to the present-day interventional oncology that is capable of cancer resolution without surgery.

Application of plasma treatment in dental restoration procedures may effectively disinfect cavity-causing bacteria; reduce the use of the painful and destructive drilling currently practiced in dental clinics, and consequently save healthy dental tissues. Not only is there the vision of rapid, contact free sterilization, which can access even small pores and microscopic openings, but also one may envisage new possibilities of drug delivery at the molecular level in the dental tissues. New bio-medical effects due to ions and, in the distant future, maybe even new plasma drug developments operating at the cellular level that may act selectively might be expected [6].

Plasma sources. Atmospheric pressure plasmas are very promising tools for biomedical applications and are expected to bring new therapeutic options in surgery, dentistry and dermatology. Each scope of application requires specific, adapted plasma sources. In most cases, basic geometric criteria can be met by choosing a proper discharge type. Locally active plasmas are easily realized with single corona, jet or micro hollow cathode setups

whereas large-area treatments may require arrays of these or the use of dielectric barrier discharges. Although physical modes of action like electric current and field, temperature or non-ionizing radiation may have a specific share in the desired biomedical effect, the plasma should not be irritating, if living tissue has to be treated, especially in veterinary and human medicine.

Two approaches are being pursued in the use of non-thermal atmospheric pressure plasmas in medicine. In the first, the plasma is produced remotely, and its afterglow is delivered in a plume to the biological tissue. The sterilizing or therapeutic effects are likely produced by relatively long-lived neutral species and radicals as most of the charged particles do not survive outside the plasma generation region. Usually operated heavily diluted with helium to avoid plasma instabilities, the discharge is doped with a few percent of molecular gases such as O_2. These resulting oxygen-containing active species may play a role via de-excitation and subsequent energy transfer onto the microorganism's surface. Different devices exist for these treatments, from plasma needles [5] to plasma jets [6]. Potential applications of the remote plasma sources are surface sterilization in a more targeted way than is possible with large volume plasmas.

In the second approach, plasmas are generated in direct contact with living tissue. When dielectric barrier discharges (DBDs) are used for this purpose, the plasma device typically contains the powered electrode while the tissue is the counter electrode [4]. The direct method fundamentally differs from the indirect technique in two respects. First, plasmas propagate and touch the biological surface, providing the possibility of charging the surface and delivering energetic ions. The second is the magnitude of the electric field produced at the surface – many orders of magnitude larger in the direct method.

These two general categories of plasma sources (indirect and direct) imply different compositions of the plasma species and activation energy delivered to the surface, particularly when surfaces are rough and nonplanar.

It has been mentioned also, that direct application of the high-voltage (10–40 kV) non-thermal plasma discharges in atmospheric air to treat live animals and people requires a high level of safety precautions. Safety and guaranteed non-damaging regimes are the crucial issues in the plasma medicine. Discharge current should be obviously limited below the values permitted for the treatment of living tissue. That is the way to the essential complication of plasma sources design. At this work the main attention is directed on the I-st plasma sources type.

Generation of gas plasmas is associated with production of energetic particles (e.g. electrons, ions, and photons), chemical reactive species (e.g. free radicals and metastables), and a myriad of transient fields (e.g. heat, shock and acoustic wave, electrostatic and electromagnetic fields). Some of the earlier applications of plasma in medicine relied mainly on the thermal effects of plasma. Heat and high temperature have been exploited in medicine for a long time for the purpose of tissue removal, sterilization, and cauterization (cessation of bleeding).

Plasmas generation is a highly coupled process of complexity and dynamics. For example, through Poisson's equation, a nonuniform or non-neutral spatial distribution of charged particles can set up a local electrostatic field and its role near the electrodes can outweigh the contributions of the externally applied electric field. Photons and some charged particles (e.g. superoxide O_{2^-}) are also chemically reactive. In fact, production of different plasma agents and fields is closely coupled and it is usually not possible for one plasma agent to be produced without many other agents also being produced.

When used for treating and processing materials, and biological materials in particular, these plasma agents and electric fields tend to work synergistically in their interaction with, and their effects on, the material that is brought in contact with the gas plasma. The synergistic effect is distinct in the extent and the richness of physiochemical functionalities facilitated and is not usually accessible with other techniques for materials treatment. This is an important aspect of gas plasmas from an application standpoint, and a key reason why gas plasmas have been used.

At present the production and applications of cold plasmas are strongly developed areas of research all over the world. In most cases, cold atmospheric plasmas are produced by electric discharges in inert gases (helium, argon). The voltages used are high alternative or pulsed voltages. There are a few situations where continuous voltages are used (see [2] f.e.) Alternative voltages may have frequencies of tens of kHz or may be radiofrequency or super high frequency voltages. The amplitudes of these voltages are of hundreds-thousands of V.

When high voltage pulses are used for producing cold atmospheric plasma jets, they have amplitudes of tens of kV, durations of tens-hundreds of ns and repetition frequencies of hundreds-thousands of pulses per second (pps). It is well-known that plasma jets produced in pure helium or argon have a low chemical activity, thus being inappropriate for certain applications (e.g. biomedical applications, food/surface treatment applications). Their chemical activation is necessary, this implying that some chemically active species such as: oxygen atoms, OH radicals, nitrogen atoms, NO radicals, nitrogen ions, excited atoms, etc. have been existed in the plasma jet.

The most important chemically active species are oxygen atoms and OH radicals. That is why the introduction of the oxygen and water in the discharge area is of greatest importance to chemical activation. When obtaining chemically active species, the electrons obtained from electric discharges have the essential contribution. The collisions between the energized electrons and the heavy particles result in enhanced levels of excitation, dissociation, and ionization, i.e. enhanced plasma chemistry.

The most important chemical activation reactions are as follows:

- Dissociation of oxygen molecules by electron impact;
- Reactions with water/nitrogen molecules from the air crossed by the plasma jet;
- Penning ionization reaction;
- Charge transfer reaction.

Most of problems, mentioned above, can be solved by ignition of discharge in wet air.

Plasma is a rich source of radicals and other active species. Free radicals have earned a bad name in biology and medicine, because of their capability of causing severe cell damage. Especially the ROS (reactive oxygen species) are well known as evildoers. The ROS family comprises radicals like O, OH and HO_2, peroxide anions O_{2^-} and HO_{2^-}, ozone and hydrogen peroxide. These species are easily created in ambient air and water (e.g. due to radiation), and they live long enough to reach the cell and attack the organic matter. When the ROS level in body fluids becomes too high, various types of damage occur, known under a common name of oxidative stress. It is believed that oxidative stress bears at least partial responsibility for diseases like arteriosclerosis, cancer and respiratory problems. Moreover, high concentrations of oxygen radicals accelerate ageing of cells and tissues. On the cellular level, several effects leading to cell injury have been identified:

- lipid peroxidation - the oxidation of unsaturated lipids in the cell membrane (damage to the membrane).
- DNA damage – oxidation of DNA bases, leading to breakage of the DNA strand.
- protein oxidation – generally not so harmful, because damaged proteins are efficiently replaced. However, it can temporarily decrease the enzyme activity.

On the other hand, free radicals have various important functions in the body. Small amounts of them are produced by the organism itself. For example, macrophages generate ROS to destroy the invading bacteria, and endothelial cells (inner artery wall) produce nitric oxide (NO) to regulate the artery dilation. It is not completely clear what radical concentrations are indispensable for the proper functioning of the body, and which are dangerous. There must always be a compromise between benefit and damage, but the numbers can vary from individual to individual. Radical production by the body during physical exercise can increase the ROS concentration in blood plasma even up to 0.1 mM, however, physical activity is generally considered wholesome.

In the last decade, atmospheric-pressure room-temperature plasma jets have attracted a lot of attention due to their widespread applications in plasma medicine, nanotechnology, as well as surface and materials processing. Such plasma jet devices generate stable plasma glows in open air rather than in confined discharge gaps. This gives them several advantages in direct treatment of hard, soft, and biological matter with outstanding flexibility in terms of the sizes and areas of the objects to be treated. Most of the applications require room-temperature operation while completely avoiding the glow-to-arc transitions.

To meet these requirements, the atmospheric plasma jets are usually sustained in noble gases. However, this is very challenging for the open-air operation. Moreover, the cross-sections of the plasma jet plumes are typically very small, which make large-area surface processing particularly difficult. One promising way to overcome this shortcoming is by using the plasma jet arrays. However, since the individual plasma plumes generated by the arrayed plasma jets are in most cases independent and do not merge in open air, it is very difficult to achieve uniform plasmas and surface treatment effects. But creation of an unique plasma source is first important step at this process.

The interesting solution of some problems, mentioned above, was reported in [7]. Plasma source consists of two metal electrodes which are separated from each other by a dielectric layer. The openings in the two electrodes are compare with electrodes thickness; length and diameter of plasma channel are compare too. That is a special feature of this source. The high-voltage electrode is completely embedded in the device and powered by a dc power supply.

The outer electrode is grounded for safety considerations. Although both positive and negative high voltages are able to generate and sustain the plasma microjet (PMJ), they primarily used a negative high voltage. They used also compressed air as the working gas at a gas flow rate of approximately 2 slm. The discharge sustaining voltage is in the range of 400–600 V with an operating current in the 20–35 mA range. The power efficiency of the device (defined as power deposited into the discharge relative to the total power drawn from the power supply) is approximately 80%. The temperature of the grounded electrode reaches approximately 100^{o}C at a current of 20 mA and a flow rate of 2 slm.

Optical emission spectroscopy was the main method in plasma parameters determination. It allowed determination of the electron excitation temperature, which also appeared to be approximately constant with power. Electron density and (excitation) temperature are important parameters that condition the plasma activity (excitation, ionization and formation of active radicals). Therefore, one can conclude that atmospheric plasmas operated at higher power have about the same activity and efficiency as the low-power ones. However, an upcoming drawback of increased power is the elevated gas temperature – when the plasma glow expands, cooling by thermal diffusion becomes less efficient and the temperature can reach even a few hundred degrees. Gas temperature of the plasma is one of the most important issues in treatment of heat-sensitive (biological) objects.

Optical emission is a typical gas-phase technique. The data it provides originate from the hottest part of the plasma: the active zone, which yields the highest emission intensity. Therefore it is not surprising that a temperature as high as a few hundreds of degrees is observed. In contrast, mass spectrometry provides downstream information, as it records the density of gas flowing into the mass spectrometer. The corresponding temperatures are lower. Nevertheless, the trends obtained by various methods are quite consistent. It is evident that gas heating occurs only at high power input; this is also coincident with an increase in the plasma glow size. The thermocouple and the temperature strip are not gas-phase methods. In fact, they are more relevant from the point of view of biomedical applications, because they provide the information about the heat that the treated object will suffer. Furthermore, convective cooling is of importance in sustaining a low plasma temperature.

Acoustic phenomena. In book [7] is mentioned non-thermal plasma jet formed by self-running pulsed periodically high-current spark generator. A distinctive feature of this jet is a formation of transient hot plasma clouds (plasma bullet) periodically flying to the target. Pulsed-periodical high-current (around 300 A) spark excited in a small cylindrical volume (typical sizes are 5 mm in a diameter and 5 mm in the length). Plasma jet is not forming due to blowing through the gap by plasma forming gas but because of strong expansion of the gas rapidly heating by spark (due to that operation the jet is accompanied with a loud noise).

Plasma jet (or plasma cloud) flying out the generator is very hot and has high outlet velocity close to sound velocity. High gas temperature in such cloud is transient. Because typical period-to-pulse duration ratio is extremely high (> 10^4), an average gas temperature at the treated area is close to room temperature. The duration of plasma cloud formation, its outlet temperature and composition of active species inside the cloud depend on electric power and amount of energy loaded into the spark by an external circuit. Repetition frequency of jet pulsation is also determined by parameters of external circuit.

It is known that spark occurs at pressures above atmospheric, and, in the intervals of the order near or more than 1 cm. For a breakdown of such gaps requires considerable voltage in the tens of kilovolts. Spark accompanied by a characteristic bang. This sound is a weak shock wave. Its source is the sharp increase in pressure from the intense Joule heat in the spark channel during the passage of a strong discharge current. This phenomenon creates a distinctive audible background in the plasma generators of this type.

But situation at the study [6], mentioned above, is more complicate. According to previous studies of other researches, mentioned in [6], the plasma jet, probably, is discontinuous under the such conditions and represents a series of propagating plasma bullets. In global physic model, this phenomenon resulted from ionization instability

and it is very close to striates formation. Nonlinear stage of the instability usually leads either to a contraction or to the stratification of the discharge. In addition, at sufficiently high E/P may form a negative relaxation (second) viscosity reducing total dissipation of sound energy. But gas flow or sound wave with definitely intensity may have an essential influence onto main plasma parameters.

There are not only negative effects from acoustic field in gaseous discharges. It is well-known, that in the gas glow discharge with an acoustic wave along the positive column, the increase in sound intensity causes a decrease in the gas temperature in the middle of the tube and the radial temperature gradient in the plasma gas, according to the acoustic vortex flows generated in the plasma column. This is accompanied by an increase in the diameter of the constricted discharge.

When a discharge in nitrogen transits into constricted state, a reduction in its diameter, increasing the current density on the axis of the discharge tube and, accordingly, increase the temperature of the gas in the plasma is descending. But molecular gases (e.g. nitrogen) have complex connection between inner degrees of freedom (especially vibrational) and such macroscopic parameters as gas temperature and density. If the vibrational relaxation time is much shorter than the period of sound waves, the intensity of the heat caused by this process will be effectively modulated by the sound wave. This can lead to a substantial increase in the initial modulation depth of temperature and density, and undular jump of the sound wave. The presence of molecular oxygen (at least in the form of a 1% impurities) provides an order of magnitude faster relaxation compared with pure nitrogen. Vapour of H_20 (as a 0.1% impurity) gives the same effect.

It is also known that at sufficiently high pressures ($p >> 10$ Torr), only process the bulk neutralization of charged particles in a gas-discharge plasma, which is an actual competitor to the diffusion process, is the dissociative recombination of electrons and molecular ions. These processes take place at high speed and cause the formation of highly excited atoms of the working gas. Atomic levels have large quantum numbers ($n >> 1$) have a significant lifetime. Life expectancy t_n depends on the principal quantum number n as $t_n \sim n^4$. If the working gas is present in the oxygen, this process is an additional source of reactive particles.

That is, it can be argued that gas glow discharge with an acoustic wave along the positive column, the increase in sound intensity causes a decrease in the gas temperature in the middle of the tube and the radial temperature gradient in the plasma gas, thanks to the acoustic vortex flows generated in the plasma column. This is accompanied by an increase in the diameter of the constricted discharge. The peculiarities of these phenomena in plasma sources for medical purposes need for further study.

Conclusions. Plasma medicine is a new medical field with first very promising practical studies. However, basic research needs to be done to minimize risk and provide a scientific fundament for medical therapies. Therapeutic application of plasmas at or in the human body is a challenge both for medicine and plasma physics. To achieve selected effects and to avoid potential risks, it is necessary to know how to control composition and densities of reactive plasma components by external operation parameters. Therefore, a profound knowledge on plasma physics and chemistry must be contributed by physical research.

Therapeutic applications required cold, non-thermal plasmas operating at atmospheric pressure. These plasmas are a huge challenge for plasma diagnostics, because usually they are small scale, constricted or filamentary, and transient. Regarding the manageability in everyday medical life, not only atmospheric pressure plasma jets (APPJ) and dielectric barrier discharges (DBD) are of special interest for medical applications. Working in open air atmospheres, complex plasma chemistry must be expected. Considering that, a great deal of effort combining experimental investigation and modeling is necessary to provide the required knowledge on plasma sources for therapeutic applications.

It was previously shown that there is close analogy processes occurring in the discharge plasma in the propagation of sound waves therein, and the gas flow. It is therefore possible to produce a plasma with the required parameters in the aspect of its uniform excitation at high pressures and low temperatures, acoustic radiators of sound waves can be used instead of bulky blow-through devices (they create of a flow in the plasma column) that allow to control the parameters of the gas discharge.

Acknowledgments. Author is grateful to Prof. V.Ya. Chernyak for fruitfool discussions and his comments.

Reference

1. Dobrynin D., Fridman G., Lelkes P., Barbee K., Cooper M., Ayan H., Brooks A., Shereshevsky A., Balasubramanian M., Zhu P., Freedman B., Friedman G., Fridman A. Mechanisms of Plasma Interaction with Living Tissue // Drexel University Research Day, Philadelphia, USA -2007. 2.Fridman G.,Friedman G.,Gutsol A.,Shekhter A. B.,Vasilets V. N., Fridman A. Applied plasma medicine // Plasma Processes and Polymers - 2008 - Vol. 5. 3. Laroussi M. The biomedical applications of plasma: a brief history of the development of a new field of research // IEEE Transactions of Plasma Science. -2009. -Vol.36. 4. Machala Z., Hensel K., Akishev Yu. (editors) Plasma for Bio-Decontamination Medicine and Food Security. // Springer Publ. – 2012. 5. Nosenko T. Designing plasmas for chronic wound disinfection. // New Journal of Physics - 2009. -Vol. 11. 6. Smitha T., Chaitanya Babu N. Plasma in Dentistry : An update // Indian Journal of Dental Advancements – 2010 - Vol.2(2). 7. Solomenko Ok., Chernyak V.Ya., Lendel V.V. Micro-discharge System features // XX annual Conference NRI NASU. Kyiv – 2013.

Submitted on 30.04.13

Є. Мартиш, д-р. фіз.-мат. наук, каф. медичної радіофізики, радіофізичний факультет, КНУ ім. Тараса Шевченка, Київ

ОСОБЛИВОСТІ ПЛАЗМОВИХ ГЕНЕРАТОРІВ В ПЛАЗМОВІЙ МЕДИЦИНІ

Ця стаття переслідує дві мети. Перша стосується енергетичних характеристик джерел плазми: винесення потужності плазми повинно бути відомим, щоб контролювати умови, при яких обробляють біологічні зразки. Це особливо важливо при лікуванні живих клітин, які не можуть отримувати високі дози енергії. Таким чином, були проаналізовані вимірювання різних параметрів плазми по їх відношенню до обробки клітин. Особливу увагу було приділено випромінюванню акустичної потужності плазми у зовнішні середовища. Обговорюються різні механізми акустичної емісії в середовище.

Ключові слова: генератор плазми, біологічні зразки, акустична емісія.

Е. Мартыш, д-р фіз.-мат. наук, каф. медицинской радиофизики, радиофизический факультет, КНУ им. Тараса Шевченко, Киев

ОСОБЕННОСТИ ГЕНЕРАТОРОВ ПЛАЗМЫ В ПЛАЗМЕННОЙ МЕДИЦИНЕ

Эта статья преследует две цели. Первая касается энергетических характеристик источников плазмы: вынос плазменной мощности должен быть известным, чтобы контролировать условия, в которых обрабатываются биологические образцы. Это особенно важно при лечении живых клеток, которые не могут получать большие дозы энергии. Таким образом, были проанализированы измерения разных параметров плазмы по их отношению к обработке клеток. Особое внимание было уделено излучению акустической мощности плазмой во внешнюю среду. Обсуждаются различные механизмы акустической эмиссии в среду.

Ключевые слова: генератор плазмы, биологические образцы, акустическая эмиссия.

UDC 537.528

O. Nedybaliuk, Ph. D., V. Chernyak, Dr. Sc., Department of Physical Electronics, Faculty of Radiophysics,
E. Martysh, Dr. Sc., Department of Medical Radiophysics, Faculty of Radiophysics, O. Solomenko, post grad. stud.,
Department of Physical Electronics, Faculty of Radiophysics, I. Fedirchyk, stud., Department of Physical Electronics,
Faculty of Radiophysics, Taras Shevchenko National University of Kyiv

PLASMA-LIQUID SYSTEM WITH ROTATIONAL GLIDING ARC AND LIQUID ELECTRODE

In this paper the results of rotational gliding arc investigation with liquid electrode are presented. Emission spectra of plasma that generated by rotational gliding arc with liquid electrode was investigated. Current-voltage characteristics of rotational gliding arc in the range of air flow 0–220 cm^3/s were measured. Temperature populations of excited electronic T_e^*, vibrational T_v^* and rotational T_r^* levels were determined. Distribution of temperature along the plasma torch was investigated.

Key words: plasma, rotational gliding arc, liquid electrode, plasma-liquid system, electrical discharge.

Introduction. For today in plasma chemistry, there are three main problems that are related to selectivity of plasma transformation of substances, energy efficiency of plasma technology and the consumption of metallic electrodes material. The problem of selectivity consists in the fact that during the plasma-chemical transformation of substances occur large numbers of chemical reactions. While it is necessary that the reaction occurred that are responsible for the formation of the expected product. This problem is partially solved by using non-equilibrium plasma. Low-temperature plasma is divided by the level of nonequilibrium into two types: plasma with a temperature of heavy components the order of room temperature (dielectric barrier discharge, micro-discharge) and the so-called "warm" plasma with a temperature of ≥ 1000 K.

To support the process of reforming and combustion of hydrocarbon fuels is better to use non-equilibrium "warm" plasma, since the process of reforming requires not only the presence of radicals, but also the appropriate temperature. Moreover, the most promising is the use of plasma at atmospheric pressure or above it.

The problem of energy efficiency of plasma technologies connected with the fact that for the generation of plasma is needed most expensive energy – electric. Therefore, a possible way to solve this problem can be embedding of plasma technologies into the traditional chemical technologies. Plasma must be effectively injected into the reaction chamber. Chemical processes must be managed with help of plasma, using its only as a catalyst.

Atmospheric pressure plasmas can be created by various types of discharges: transverse arc; discharge in gas channel with liquid wall and others. But most of them aren't sufficiently stable. Stabilization of discharge in the high pressure powerful plasmatron is attained by vortex flow of gas [3]. In the low-powered high pressure discharges the reverse vortex flow "tornado" type can be used for the space stabilization [2]. Previous investigations were performed only for discharges with solid-state electrodes. And we have not much information about discharges with liquid electrodes, which were stabilized by vortex and reverse vortex flow of gas. One of the most efficient is the plasma processing in the dynamic plasma-liquid systems using the DC discharge in a reverse vortex gas flow of tornado type with a "liquid" electrode (LE) [5, 6]. Plasma liquid system with rotational gliding arc is a prototype of TORNADO-LE [5, 6], but with some modification, which are interesting for plasma technology.

The peculiarity of the using of plasma-liquid systems to generate plasmas is that they do not require pre-gasification of the liquid. In this regard, the research and development of plasma-liquid systems with a rotational gliding arc and liquid electrode for energy technologies is an urgent task.

Experimental setup. Schematic view of the plasma-liquid system (PLS) with rotational gliding arc is shown in Fig. 1. It consists of a quartz chamber (1) cylindrical shape, which hermetically closed metal top and bottom flanges.

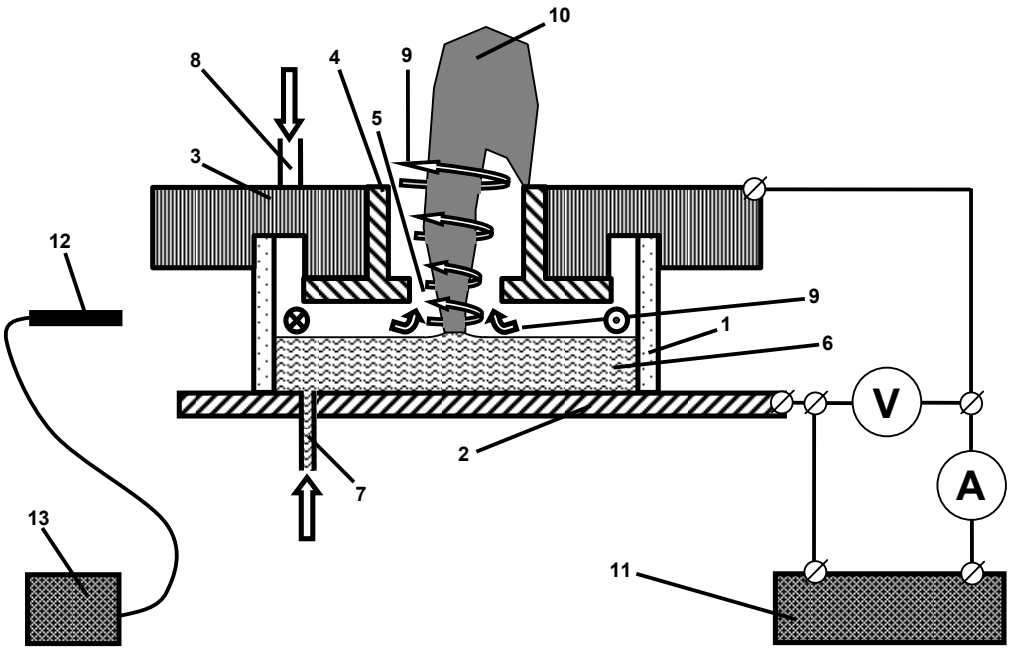

Fig. 1. Schematic diagram of experimental setup

The height of the camera is 30 mm and diameter 90 mm. Bottom flange (2) is made of stainless steel. The upper flange (3) is made of duralumin and contains a copper sleeve (4) which has a hole in the center (5) diameter of 14 mm and a length of 5 mm. Quartz chamber (1) filled with liquid (6), the level of which has been maintained by the injection pump through the aperture (7). Gas inputted into the system through the aperture (8). Gas flow is introduced tangentially to wall of the quartz cylinder (1). Gas, rotating, moved (9) along the surface to the axis of the quartz cylinder (1), where through the aperture (5) comes out. Plasma torch (10) was formed during the discharge burning. One end of plasma torch was located on the surface of the liquid and the other on an external part of the upper flange. Under the influence of the gas flow end of the plasma torch, which was located on the metal surface, rotating, and gliding in the direction of air flow? The voltage between the electrodes was supplied by a power supply (11) DC. The power supply provides voltages up to 7 kV. In this system can be realized two modes of operation: liquid (LC) and solid cathode (SC) cathode.

Emission spectroscopy was used for diagnostics of plasma. Emission spectra were registered using a spectral device that consists of an optical fiber (12) and spectrometer S-150-2-3648 USB (13). This spectrometer allows registering the emission spectra in the wavelength range 200–1000 nm.

Photograph of plasma-liquid system with rotational gliding arc with liquid electrode are shown in Fig. 2. The working fluid was distilled water, the air flow was 220 cm^3/s, current – 360 mA, voltage – 2 kV.

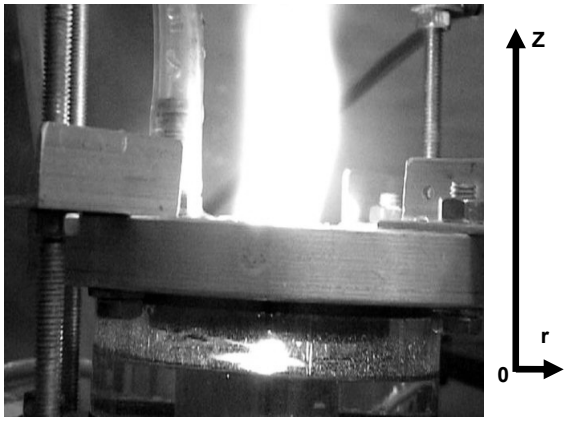

Fig. 2. Photo of plasma-liquid system with rotational gliding arc. Working fluid - distilled water, air flow – 220 cm^3/s, current – 360 mA, voltage – 2 kV. Mode – "solid" cathode

The distance from the surface of liquid to the upper flange – 5 mm. Breakdown of the gas gap occurred in air flow (220 cm^3/s) and a maximum voltage (7 kV) of power supply. Increased airflow lowers the distance between the liquid and the top flange, due to the formation of a cone of liquid on its surface. The gas gap occurred breakdown when the distance reached a certain critical value of. However, after the breakdown of the discharge was burning even in the absence of airflow (0 cm^3/s). Plasma torch was formed outside of the reactor after the breakdown of the gas gap. Length torch initially increased with increasing air flow, reaching a length of about 150 mm by air flow 165 cm^3/s, and then with increase airflow length of torch began to decrease.

Results and discussion. The current-voltage characteristics of the discharge at different airflows are shown in Fig. 3. Mode – "solid" cathode. In the absence of airflow with increasing current voltage unchanged. For air flow 55 cm^3/s at low currents (220 mA) voltage unchanged. The voltage is increased with increasing of current in the range 220–280 mA. The voltage does not change its value at the currents greater than 280 mA. Absolute value of the voltage increased with increasing of airflow (55-165 cm^3/s) but the behavior was similar to the current-voltage characteristics for the air flow of 55 cm^3/s. The voltage was increased with increasing of current and then was voltage saturation. The current-voltage characteristic at airflow 220 cm^3/s has a region where voltage grows, saturates, and then at current of 380 mA began to decrease (Fig. 3). Minimum current at discharge burning was increased with increasing of airflow. The ballast resistance was not used. This may be due to a peculiarity of the impact of air flow to the discharge burning process.

Typical emission spectra of plasma in plasma-liquid system with rotational gliding arc are shown in Fig. 4.

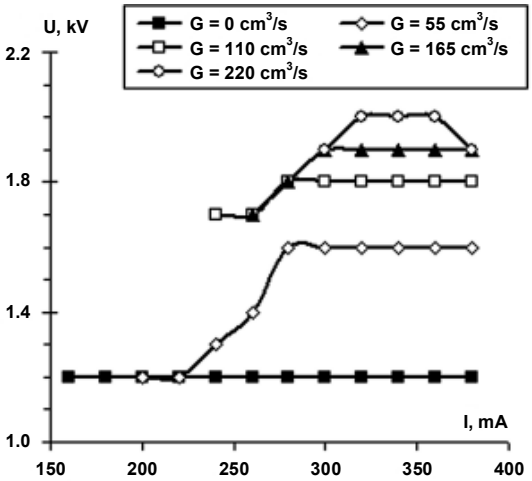

Fig. 3. Current-voltage characteristics of rotational gliding arc

Emission spectra were measured at the regime SC, current 360 mA, voltage 2 kV, air flow 220 cm^3/s. Bands of hydroxyl (OH), lines of hydrogen (H), and multiplets of oxygen (O) are present on emission spectrum of plasma inside ($Z = 2.5$ mm) of plasma-liquid system (Fig. 4.a). Bands of hydroxyl (OH) and lines of copper (Cu) are present on emission spectrum of plasma outside ($Z = 30$ mm) of plasma-liquid system (Fig. 4.b). The plasma torch increases with presence of water. This may be due to the fact that plasma generates detonating gas, which burning increases the plasma torch.

It is obviously that rotational gliding arc plasma discharge, which has been chosen as the basis of our work, has its roots in a LE "tornado" system [5, 6], as can be seen in Fig. 1. As it was shown in [1], the voltage in gliding arc in humid air rather steeply increases with increasing the air flow rate. We have similar effect in our system. But the low intensity of electrode material lines outside PLS and their absence inside (Fig. 4*)*, demonstrates the increasing of electrodes life-time in the RGA plasma discharge. The new state of system can be stable for an indefinite amount of time. So, significant advantage of this system is long lifetime of electrodes.

Temperature T_e^* population of excited electronic levels of the hydrogen atoms H was determined by the method of relative intensities (by two lines H_α – 656.3 nm and H_β – 486.1 nm). Temperature population of excited electronic levels of oxygen atoms O were determined by the Boltzmann diagrams method (777.2 nm, 844.6 nm, 926.6 nm).

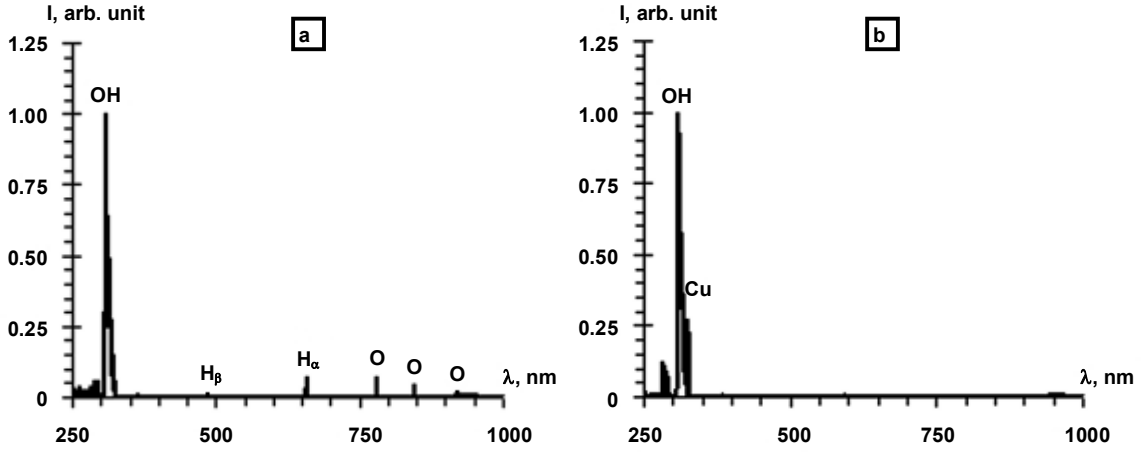

Fig. 4. Typical emission spectra of plasma inside ($Z = 2.5$ mm) (a) and outside ($Z = 30$ mm) (b) of plasma-liquid system with rotational gliding arc with liquid electrode: distilled water/air mixture

The method of comparing experimentally measured emission spectra calculated by code SPECAIR [4] to determine the temperature population of excited vibrational T_v^* and rotational T_r^* levels of hydroxyl OH was used. Comparison of the experimentally measured emission spectrum with simulated emission spectrum bands hydroxyl OH in the wavelength range 274–298 nm by code SPECAIR are shown in Fig. 5. Emission spectrum was registered in the mode – "solid" cathode, current – 380 mA, air flow – 140 cm^3/s, voltage – 1.9 kV.

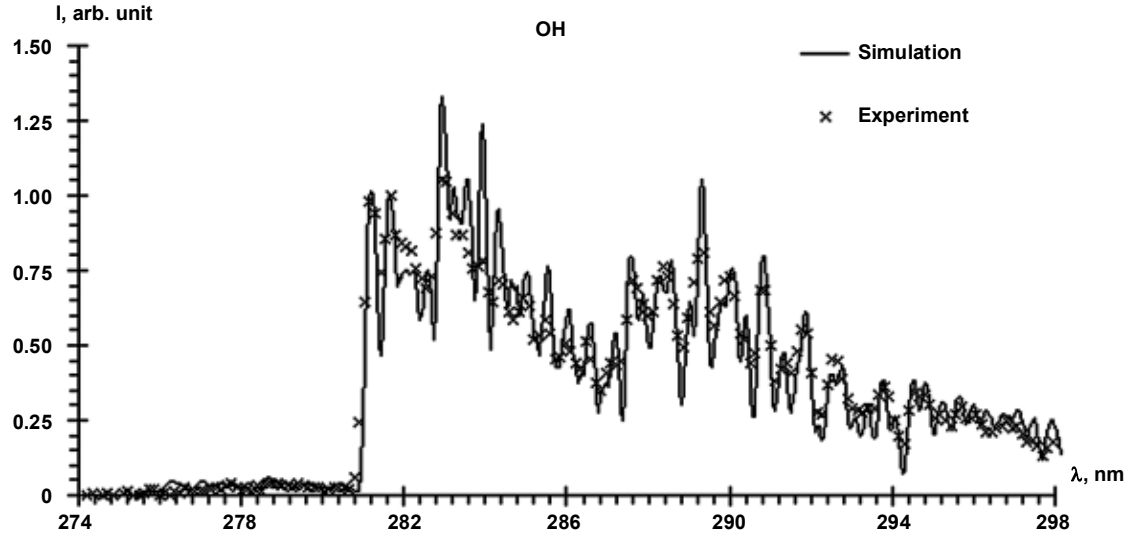

Fig. 5. Comparison of experimentally measured emission spectrum with simulated emission spectrum bands of hydroxyl OH by code SPECAIR in the wavelength range 274-298 nm. Mode is "solid" cathode, current – 380 mA, air flow – 140 cm^3/s, voltage – 1.9 kV. Modeling: $T_e^*(O) = 3700$ K, $T_v^*(OH) = 3700$ K, $T_r^*(OH) = 3700$ K

The temperature population of excited electronic levels of the oxygen atoms O, which is determined by the Boltzmann diagrams to simulate the bands of hydroxyl $OH(A-X)$ was used. The temperature population of excited vibrational and rotational levels was specified by SPECAIR. The following parameters $T_e^*(O) = 3700$ K, $T_v^*(OH) = 3700$ K, $T_r^*(OH) = 3700$ K to simulate the emission spectrum bands hydroxyl OH were used. Fig. 5 shows that the simulation matches very well with the experiment, and therefore it can be argued that the temperatures population of excited levels has the following value $T_e^*(O) = 3700 \pm 400$ K, $T_v^*(OH) = 3700 \pm 200$ K, $T_r^*(OH) = 3700 \pm 200$ K.

Fig. 6 shows dependence of the temperature population of the excited electronic $T_e^*(O)$ vibrational $T_v^*(OH)$ and rotational $T_r^*(OH)$ levels from airflow. Emission spectra were registered inside of system in the center the line of sight between the liquid and the top flange. Measurements were carried out at a fixed value of current – 380 mA. Mode – "solid" cathode. The plasma at low air flow is isothermal (Fig. 6). However, the interval between the temperatures population of excited vibrational, rotational levels OH and electronic levels O increased with airflow increases. The temperature population of excited electronic levels of hydrogen H decreased with increasing of air flow.

The volume which occupies plasma inside the system is on order less than the volume of plasma torch. Temperature distribution of plasma along the torch is important, because the plasma torch is injected into the reaction chamber. Axial distribution of vibrational and rotational temperature in the plasma torch is shown in

Fig. 7. Emission spectra were registered by the line of sight. Measurements were carried out at a fixed value of current – 340 mA and air flow – 165 cm^3/s. Mode – "solid" cathode. $Z = 0$ mm corresponds the measurements along the surface of the liquid, $Z = 5$ mm – along the bottom surface of the top flange, $Z = 30$ mm – along the upper surface of the upper flange. There is a one "dead" zone, in which can not be measured emission spectra. This is due peculiar structure of the upper flange.

Plasma torch reached the size to a height of 120 mm at the air flow 165 cm^3/s and current 340 mA. The intensity of the bands of hydroxyl OH decreased with increasing Z. Hydroxyl bands were barely visible at the maximum accumulation for $Z = 100$ mm. However, the rotational and vibrational temperature at the values of $Z > 50$ mm from the emission spectra was difficult to determine. Since the OH bands of low intensity (274–298 nm) were used for the determination of these temperatures.

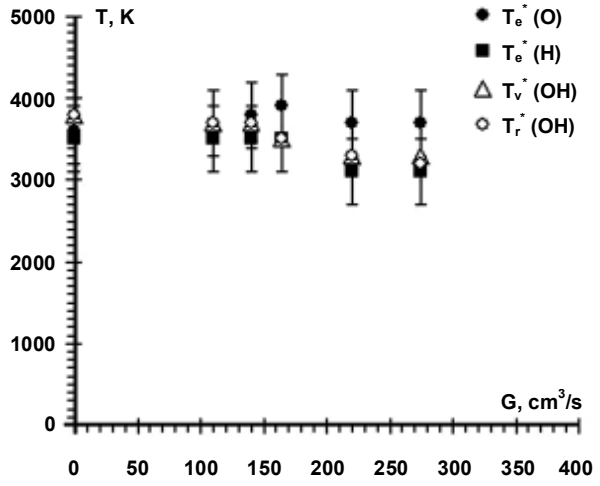

Fig. 6. Dependence temperatures population of excited electronic $T_e^*(O)$, vibrational $T_v^*(OH)$ and rotational levels of $T_r^*(OH)$ from airflow. Current – 380 mA, mode – "solid" cathode

When $Z = 0$ mm (along the surface of the liquid), the difference between $T_v^*(OH) = 3700 \pm 200$ K and $T_r^*(OH) = 3200 \pm 200$ K is 500 K, but at $Z = 5$ mm (along the bottom surface of the metal flange) they are equal within the limits of error. At $Z = 30$ mm difference between $T_v^*(OH) = 3500 \pm 200$ K and $T_r^*(OH) = 3000 \pm 200$ K is 500 K. For the $35 \le Z \le 50$ mm difference between $T_v^*(OH)$ and $T_r^*(OH)$ remains constant 700 K, but the absolute values decrease with increasing Z (Fig. 7).

According to the obtained temperatures population of excited levels and code SPECAIR unable to determine the ratio $[OH]/[O]$ between the concentration of hydroxyl OH and atomic oxygen O. Hydroxyl OH on six orders of magnitude smaller than oxygen atoms O. With increasing air flow ratio $[OH]/[O]$ begins to decrease. This ratio $[OH]/[O]$ has a maximum when the air flow 165 cm^3/s. This may be due to the fact that an increasing of air flow increases the power inputted into the discharge that way fluid flow increases. With further increase flow capacity varies little, and the amount of oxygen that is introduced by the flow increases. The concentration ratio $[H]/[O]$ by using the calculated spectra according to NIST was determined. The atoms of hydrogen $[H]$ and oxygen $[O]$ almost equal value.

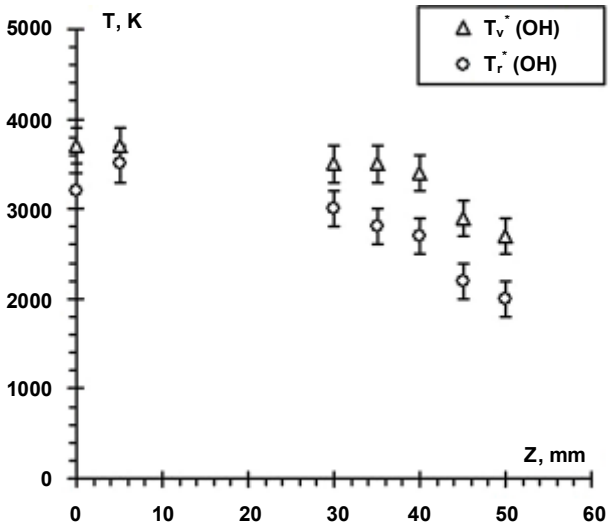

Fig.7. Axial distribution of temperatures population of excited vibrational $T_v^*(OH)$ and rotational levels of $T_r^*(OH)$. Current – 340 mA, air flow – 165 cm^3/s, mode – "solid" cathode

Conclusions. Plasma of plasma-liquid system with rotational gliding arc with liquid electrode inside the chamber is isothermal $T_e^*(O) = 3700 \pm 400$ K, $T_v^*(OH) = 3700 \pm 200$ K, $T_r^*(OH) = 3700 \pm 200$ K. The interval between the temperatures population of excited vibrational, rotational levels OH and electronic levels O increased with airflow increases. Temperatures population of excited levels at air flow 275 cm^3/s have the value $T_e^*(O) = 3700 \pm 400$ K, $T_v^*(OH) = 3300 \pm 200$ K, $T_r^*(OH) = 3200 \pm 200$ K.

Plasma is nonisothermic in the torch at the range of Z 30–50 mm. The difference between $T_v^*(OH)$ and $T_r^*(OH)$ is 700 K, and their absolute values decrease with height of plasma torch ($35 \le Z \le 50$ mm).

The main components of the plasma interelectrode gap are OH, O, H, and major components of the plasma torch are OH, and Cu. The concentration of hydroxyl OH on six orders of magnitude was less than the concentration of oxygen O and hydrogen H atoms.

The presence of water increases the plasma torch. This may be due to the fact that plasma generates detonating gas, which burning increases the plasma torch.

Acknowledgements. This work was partially supported by the Ministry of Education and Science of Ukraine, National Academy of Sciences of Ukraine, Taras Shevchenko National University of Kyiv.

Reference

1. Beushaati B., e.a. "Density and Rotational temperature Measurements of the OH and NO Radicals Produced by a Gliding Arc in Humid Air", Plasma Chemistry and Plasma Processing. 2002. Vol. 22, no. 4. P. 553-571. 2. Kalra C.S., Kossitsyn M., Iskenderova K., Chirokov A., Cho Y.I., Gutsol A., Fridman A. Electrical discharges in the Reverse Vortex Flow – Thornado Discharges. El. Proc. Of 16th Int. Symp. on Plasma Chem. Taormina. 2003. 3. Koroteev A.S., Mironov V.M., Svirchyk Yu.S. Plasmatrons: constructions, characteristics, calculation (Book style). M. 1993. 286 p. (in Russian). 4. Laux C.O., Spence T.G., Kruger C.H., Zare R.N. Optical diagnostics of atmospheric pressure air plasma // Plasma Source Sci. Technol. 2003. Vol. 12, no. 2. P. 125–138. SPECAIR: http://www.specair-radiation.net 5. Nedybaliuk O.A., Chernyak V.Ya.,

Olszewski S.V. Plasma-Liquid System With Reverse Vortex Flow of "TORNADO" Type (TORNADO-LE) // Problems of Atomic Science and Technology. 2010. Vol. 6. P. 135–137. 6. Nedybaliuk O.A., Chernyak V. Ya., Olszewski S.V., Martysh E.V. Dynamic Plasma-Liquid System with Discharge in Reverse Vortex Flow of "Tornado" Type // International Journal of Plasma Environmental Science & Technology. 2011. Vol. 5, no. 1, P. 20–24.

Submitted on 19.04.13

О. Недибалюк, канд. фіз.-мат. наук, В. Черняк, д-р фіз.-мат. наук,
каф. фізичної електроніки, Є. Мартиш, д-р фіз.-мат. наук, каф. медичної радіофізики,
О. Соломенко, асп., І. Федірчик, студ., каф. фізичної електроніки,
радіофізичний факультет, КНУ імені Тараса Шевченка, Київ

ПЛАЗМОВО-РІДИННА СИСТЕМА З ОБЕРТАЛЬНОЮ КОВЗНОЮ ДУГОЮ ТА РІДКИМ ЕЛЕКТРОДОМ

У роботі представлені результати дослідження обертальної ковзної дуги з рідким електродом. Досліджено спектри випромінювання плазми обертальної ковзної дуги з рідким електродом. Виміряні вольт-амперні характеристики обертальної ковзної дуги в діапазоні потоків повітря 0–220 см^3/с. Визначено температури заселення збуджених електронних T_e^*, коливних T_v^* та обертових T_r^* рівнів. Досліджено розподіл цих температур вздовж плазмового факелу.

Ключові слова: плазма, обертальна ковзна дуга, рідкий електрод, плазмово-рідинна система, електричний розряд.

О. Недыбалюк, канд. физ.-мат. наук, В. Черняк, д-р. физ.-мат. наук,
каф. физической электроники, Е. Мартыш, д-р. физ.-мат. наук, каф. медицинской радиофизики,
Е. Соломенко, асп., И. Федирчик, студ., каф. физической электроники,
радиофизический факультет, КНУ имени Тараса Шевченко, Киев

ПЛАЗМЕННО-ЖИДКОСТНАЯ СИСТЕМА С ВРАЩАТЕЛЬНОЙ СКОЛЬЗЯЩЕЙ ДУГОЙ И ЖИДКИМ ЭЛЕКТРОДОМ

В работе представлены результаты исследования вращательной скользящей дуги с жидким электродом. Исследованы спектры излучения плазмы вращательной скользящей дуги с жидким электродом. Измеренные вольтамперные характеристики вращательной скользящей дуги в диапазоне потоков воздуха 0–220 см3/с. Определены температуры заселения возбужденных электронных T_e^*, колебательных T_v^* и вращательных T_r^* уровней. Исследовано распределение этих температур вдоль плазменного факела.

Ключевые слова: плазма, вращающательная скользящая дуга, жидкий электрод, плазменно-жидкостная система, электрический разряд.

UDC 537.6/.8

O. Prokopenko, Ph.D., B. Karpiak, stud., O. Sulymenko, stud.,
Department of Nanophysics and nanoelectronics, Faculty of Radiophysics,
Taras Shevchenko National University of Kyiv

DYNAMICS OF GENERALIZED PHASES IN A SYSTEM OF TWO WEAKLY-COUPLED SPIN-TORQUE NANO-OSCILLATORS WITH RANDOM EIGEN FREQUENCIES: THE CASE OF GLOBAL COUPLING

Dynamics of generalized phases in a system of two weakly-coupled spin-torque nano-oscillators (STNOs) with random eigen frequencies (Gaussian distribution) is analyzed. It is shown that the system dynamics is conveniently described by a complex order parameter in the scope of global coupling model. The numerical analysis of time dynamics of the modulus of complex order parameter was performed. It is shown that the synchronization of two STNOs is most effective when the amplitude of coupling Λ is big and the phase of coupling β is multiple of π.

Key words: spin-torque nano-oscillator, synchronization, coupled oscillations, random eigen frequency.

Introduction. The spin-transfer torque (STT) [1, 3, 15, 20–21] carried by a spin-polarized electric current can give rise to several types of magnetization dynamics (magnetization auto-oscillations [5–6, 8–11, 16–17] and reversal [7, 22]) and, therefore, allows one to manipulate magnetization of a nano-scale magnetic object [17].

The STT effect opens a possibility for the development of a novel type of nano-scale microwave devices – spin-torque nano-oscillators (STNOs). The practical application of STNOs faces four main problems:

- low enough operation frequencies of devices based on STNOs (typically, 1–15 GHz);
- low output microwave power (or DC power if a STNO is used as a microwave detector);
- large generation linewidth;
- imperfect manufacturing technology of STNOs.

The last three problems can be solved using the mutual phase-locking of several STNOs [6, 11, 14, 18–19]. For instance, using numerical simulations it has been demonstrated [4, 12] that the finite delay time of the coupling signal can lead to a substantial (~ 100 times) increase in the frequency band of phase-locking.

In this work we perform numerical simulations of phase-locking of two STNOs with random eigen frequencies (which are caused by the parameters spread of the STNOs due to the imperfect manufacturing technology) with account of a delay of the coupling signal. We consider the general case of two coupled nano-contact STNOs without account of the exact type of coupling. Thus, our results are valid for different types of coupling.

Theoretical model. The dynamics of the two weakly-coupled STNO can be described by the system of coupled nonlinear equations for the complex amplitudes $c_j(t)$ of spin wave modes, excited in *j*-th nano-contact [2, 14, 19]:

$$\begin{aligned} &\frac{dc_1}{dt} + \mathrm{i}\,\omega_1\left(|c_1|^2\right)c_1 + \Gamma_{eff,1}\left(|c_1|^2\right)c_1 = \Omega_{12}c_2\,\mathrm{e}^{\mathrm{i}\beta_{1,2}}, \\ &\frac{dc_2}{dt} + \mathrm{i}\,\omega_2\left(|c_2|^2\right)c_2 + \Gamma_{eff,2}\left(|c_2|^2\right)c_2 = \Omega_{21}c_1\,\mathrm{e}^{\mathrm{i}\beta_{2,1}}, \end{aligned} \quad (1)$$

where $j,k=\{1,2\}$, $\omega_j\left(|c_j|^2\right)$ and $\Gamma_{eff,j}\left(|c_j|^2\right)$ are the frequency and effective damping rate (that includes contribution from the positive natural damping and current-induced negative damping) of *j*-th mode, coupling frequencies $\Omega_{j,k}$ are defined by Eq. (6) in [19], and $\beta_{j,k}$ is the phase shift, for example, the phase shift of the spin wave (radiated by the *k*-th nano-contact) acquired during its propagation to the *j*-th nano-contact.

The system (1) without time delay ($\beta_{j,k}=0$) was derived and analyzed in [19]. The analysis of the system (1) was

carried out in [2, 14] for the case of fixed (not random) frequencies and with account of time delay ($\beta_{j,k} \neq 0$).

In the absence of coupling ($\Omega_{j,k} = 0$) each of Eqs. (1) has a free-running solution [2, 14]

$$c_j(t) = \sqrt{p_j(t)}\, e^{i\omega_j(p_j(t))t}, \qquad (2)$$

where the power $p_j(t) = |c_j(t)|^2$ is determined by condition of the vanishing of total damping $\Gamma_{eff,j}(p_j) = 0$. For a weak coupling ($\Omega_{j,k} << \omega_j, \omega_k$) it is possible to perform a perturbative analysis of Eqs. (1), and obtain criteria of phase-locking in a closed analytical form [2].

Analysis of mutual phase-locking of two oscillators with an account of phase of the interaction (or, equivalently, delay of the coupling signal) showed that each oscillator can be described by one dynamical variable – "generalized phase" $\varphi_j(t)$. It can be introduced as in that case the system (1) transforms to the equations of motion for the phases $\varphi_j(t)$, which can be written in the form

$$\begin{aligned} \frac{d\varphi_1}{dt} - \omega_1 &= \Lambda_{1,2}\sin(\varphi_2 - \varphi_1 + \beta_{1,2}), \\ \frac{d\varphi_2}{dt} - \omega_2 &= \Lambda_{2,1}\sin(\varphi_1 - \varphi_2 + \beta_{2,1}). \end{aligned} \qquad (3)$$

Here ω_j is the natural (free-running) frequency of *j*-th oscillator, $\Lambda_{j,k}$ is the amplitude of the coupling between *j*-th and *k*-th oscillators, and $\beta_{j,k}$ is the coupling phase. Both amplitude $\Lambda_{j,k}$ and phase $\beta_{j,k}$ of the coupling are renormalized by the nonlinearity of the oscillators.

Eqs. (3), were derived from a simple auto-oscillator model [14, 18, 19]. It can be shown, however, that the model (3) is rather general and can be applied to the description of phase-locking of oscillators of any nature [14, 18, 19]. This model will serve as a basis for numerical and analytical study of phase-locking phenomenon in large arrays of spin-torque nano-oscillators.

In experiments, frequencies ω_j of the oscillators in an array differ due to uncertainties in technological process, presence of impurities, etc. Therefore, the free-running frequencies ω_j in system (3) should be considered as random quantities having certain probability distribution $P(\omega_j)$ (we assume that probability distribution is the same for each oscillator). Without loss of generality, we assume that the average frequency $\omega_{j,av}$ of oscillators is zero (otherwise, one can perform transformation $\varphi_j(t) \to \tilde{\varphi}_j(t) = \varphi_j(t) - \omega_{j,av}t$, that does not change form of Eqs. (3)). For simplicity, we consider only the case, where the frequency distribution $P_G(\omega_j)$ is the Gaussian distribution:

$$P_G(\omega_j) = \frac{1}{\sqrt{2\pi}\Delta\omega}\exp\left[-\frac{1}{2}\left(\frac{\omega_j}{\Delta\omega}\right)^2\right]. \qquad (4)$$

Here $\Delta\omega$ is a characteristic width of the frequency distribution (we assume it is the same for all oscillators).

The coupling amplitudes $\Lambda_{j,k}$ and phases $\beta_{j,k}$ depend on the coupling mechanism between oscillators and on their properties (nonlinearity). Here we analyze the simplest case of practical interest – the case of global coupling. This is the typical case of coupling by the common current bias current, when coupling between all oscillators is the same:

$$\Lambda_{j,k} = \Lambda = \text{const}, \ \beta_{j,k} = \beta = \text{const}. \qquad (5)$$

In the following we will study global coupling of oscillators using model (3) with coupling (5), when the eigen frequencies of oscillators are characterized by the distribution (4). The main task is to analyze dependence of the locking process on the amplitude Λ and phase β of the coupling.

The convenient parameter for the phase-locking characterization is a complex order parameter [13]

$$r = R e^{i\psi} = \frac{1}{2}\left(e^{i\varphi_1} + e^{i\varphi_2}\right). \qquad (6)$$

The amplitude R of the order parameter characterizes number of phase-locked oscillators, while the rate of change of the phase $\varpi = d\psi/dt$ gives the frequency of phase-locked oscillations.

Numerical model. Our numerical model is based on the numerical solution of Eqs. (3) for some particular values of $\Lambda_{1,2} = \Lambda_{2,1} = \Lambda$, $\beta_{1,2} = \beta_{2,1} = \beta$, ω_1, ω_2 and known initial conditions $\varphi_1(0)$, $\varphi_2(0)$. During the numerical analysis we assume for simplicity that the average frequency of the STNOs is zero and chose the characteristic width of the frequency distribution $\Delta\omega$ as $\Delta\omega = 0.1$ (the case of small frequency deviations, i.e. the case of small uncertainties in technological process of STNO fabrication). We also assume that the initial phases of STNOs $\varphi_1(0)$, $\varphi_2(0)$ are random values with rectangular distribution:

$$P_R(\varphi_{1,2}(0)) = \begin{cases} 1/2\pi, & 0 \le \varphi_{1,2}(0) \le 2\pi \\ 0, & \text{otherwise} \end{cases}. \qquad (7)$$

Since the frequencies ω_1 and ω_2 are random values described by frequency distribution law (4) and initial phases $\varphi_1(0)$, $\varphi_2(0)$ are random values described by distribution law (7), it is clear that the dynamics of general phases $\varphi_1(t)$, $\varphi_2(t)$ will depend on ω_1, ω_2 and $\varphi_1(0)$, $\varphi_2(0)$ and, therefore, may also be random (at least partially). To eliminate this influence of randomness on the system dynamics and to obtain statistically correct results we performed multi-pass numerical analysis of the Eqs. (3). The used algorithm may be described as follows:

1) We chose some particular values of the amplitude of coupling Λ and the phase of coupling β.

2) We generate the random vector of initial phases $\vec{\varphi}(0) = \{\varphi_1(0), \varphi_2(0)\}$ using the distribution law (7) and the random vector of oscillator eigen frequencies $\vec{\omega} = \{\omega_1, \omega_2\}$ using the distribution law (4) for the case of $\Delta\omega = 0.1$.

3) We numerically solve the equations (3) for the case of some particular values of equation's parameters Λ, β, $\vec{\omega}$, $\vec{\varphi}(0)$ defined above. We calculate the modulus of the complex order parameter as a function of time $R(t)$ using numerically calculated phase vector $\vec{\varphi}(t) = \{\varphi_1(t), \varphi_2(t)\}$.

4) We repeat the stages 2 and 3 N times, where N is the number of passes. After that we do the averaging of the obtained data of $R(t)$ for all realizations and obtain an averaged dependence

$$\langle R(t)\rangle_N = \frac{1}{N}\sum_{k=1}^{N} R_k(t), \qquad (8)$$

where $R_k(t)$ is a dependence of the modulus of the complex order parameter on time obtained at k-th pass.

We believe that for a large enough value of N the influence of randomness on the system dynamics is

minimal. The minimal number of passes N, which correspond to that case might be found numerically.

Results and discussion. Using the algorithm stages 1–3 described in the previous section we calculated the time dependencies of general phases $\varphi_1(t)$ and $\varphi_2(t)$ of two weakly-coupled STNOs. The typical obtained results (after renormalization – division by 2π) are presented in Fig. 1. The corresponding dependence of $R(t)$ is shown in Fig. 2.

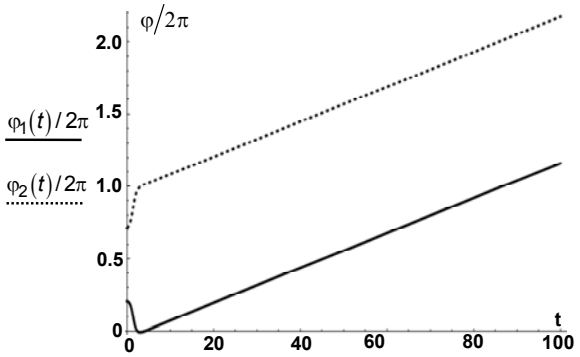

Fig. 1. The typical time dependencies of normalized general phases $\varphi_1(t)/2\pi$ (solid line) and $\varphi_2(t)/2\pi$ (dashed line) of two weakly-coupled STNOs for the case of model parameters: λ = 1, β = 0, ω={-0.0016, 0.1500}, φ(0)={1.3, 4.5}

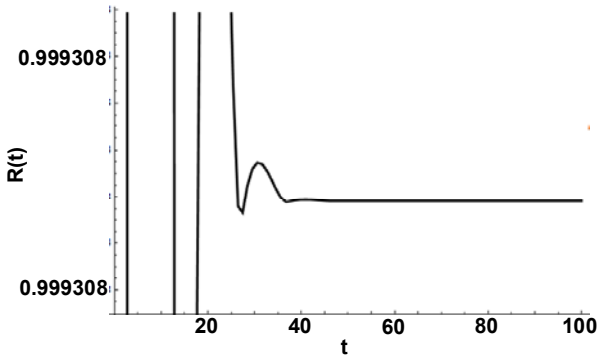

Fig. 2. The typical time dependencies of the modulus of complex order parameter $R(t)$ for a system of two weakly-coupled STNOs for the case of model parameters: λ =1, β = 0, ω={0.0016, 0.1500}, φ(0)={ 1.3, 4.5}.

We also analyzed the dependence of $\langle R(t)\rangle_N$ on N (see Fig. 3). We show that the dependence $\langle R(t)\rangle_N$ is statistically stable if N > 100 for the case λ = 1, β = 0. The obtained results depend on Λ, β, but it seems that N is almost the same for any values of Λ, β, if Λ is big enough and β is far from $\pi/2$ or $3\pi/2$.

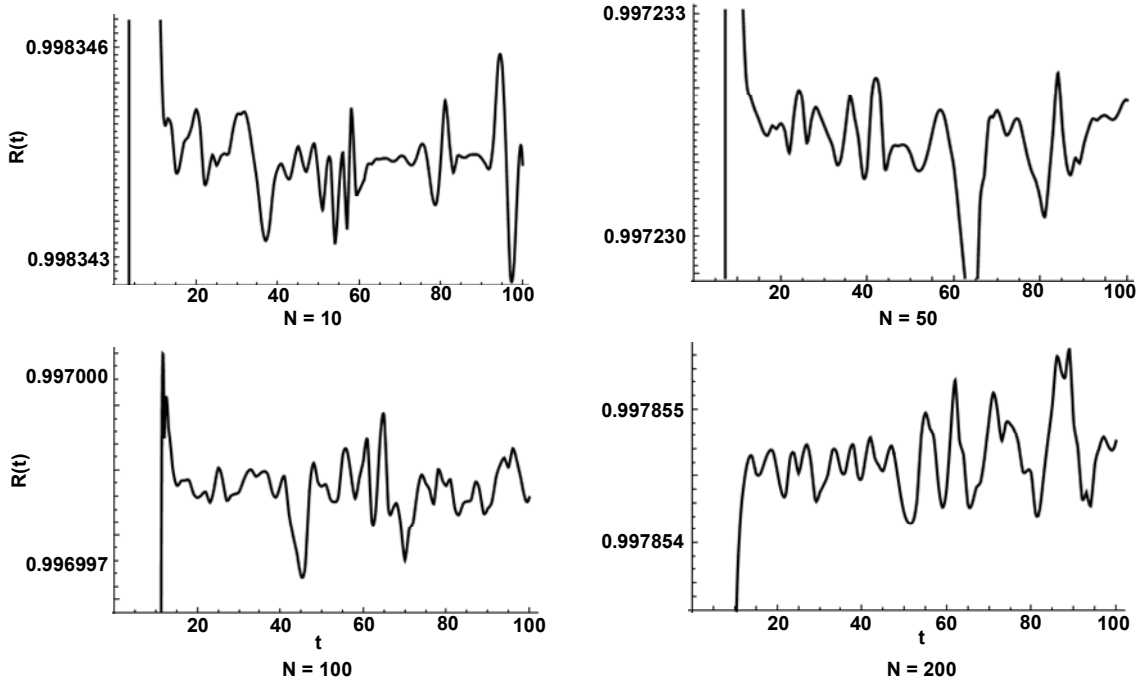

Fig. 3. The dependencies of the averaged modulus of complex order parameter $\langle R(t)\rangle_N$ on time for different number of passes N. λ =1, β = 0

The following analysis was carried out with number of passes N = 200. First, we fix the phase of coupling β (β=0) and analyzed the dependence of $\langle R(t)\rangle_N$ for different amplitude of coupling Λ (Fig. 4). One can see, decrease of Λ leads to a great perturbation of the system dynamics, thus, it seems the efficiency of synchronization decreases in that case. Second, we fix the amplitude of coupling Λ ($\Lambda = 1$) and analyze the dependence of $\langle R(t)\rangle_N$ on phase of coupling β (Fig. 5).

One can see, the efficiency of synchronization $\langle R(t)\rangle_N$ rapidly increases if β is close to 0 or π. It is obvious, that in real in Fig. 4 and Fig. 5 there are plots with almost linear dependence of averaged modulus of complex order parameter $\langle R(t)\rangle_N$ on time. The visibility of function oscillation defined only by choosing the appropriate graph scale. The efficiency of synchronization for different amplitudes and phases of coupling is clearly shown in Fig. 6(b). One can see, that it is most effective for big

amplitudes of coupling when phase of coupling multiple of π. This means that the model of global coupling may be applicable only in that case.

The final state of the system (value of $\langle R(t)\rangle_N$ at the moment $t = 100$) is analyzed on Fig.6(a).

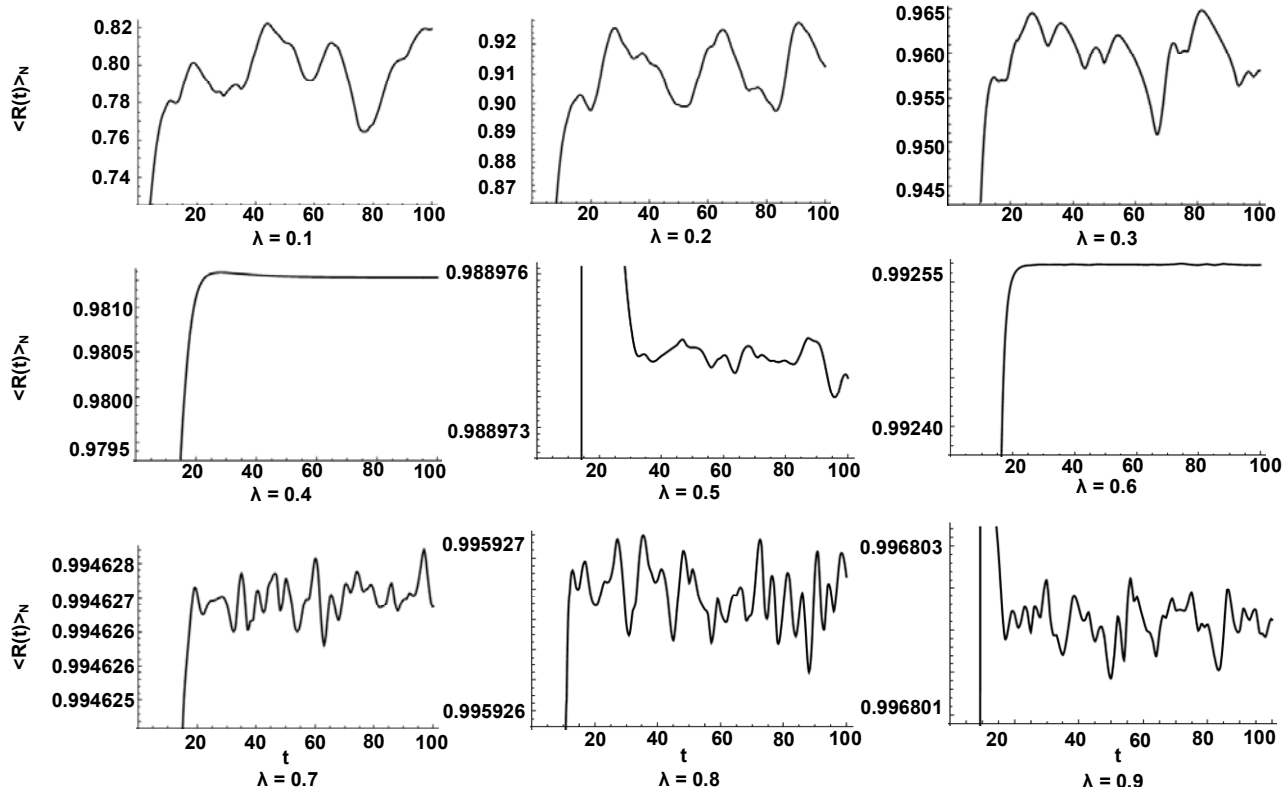

Fig. 4. The dependencies of the averaged modulus of complex order parameter $\langle R(t)\rangle_N$ on time for different amplitudes of coupling Λ. N = 200, β = 0

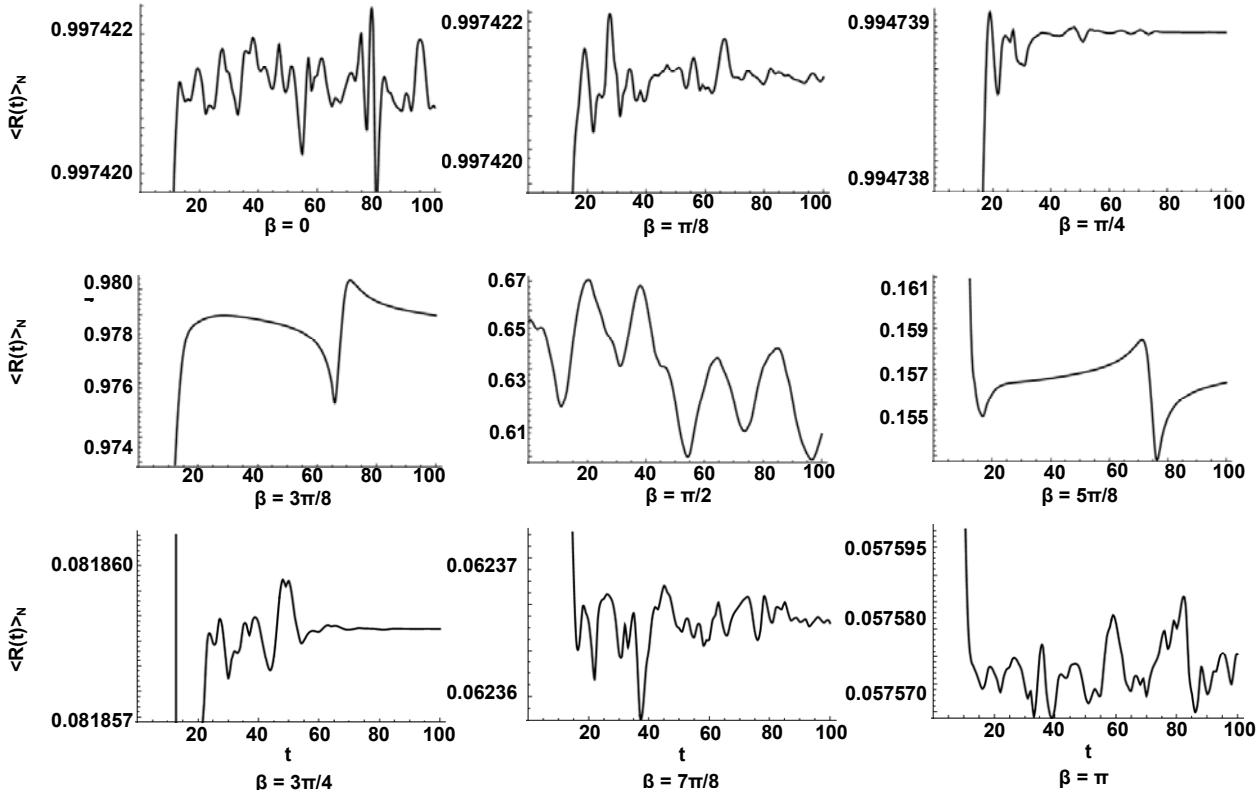

Fig. 5. The dependencies of the averaged modulus of complex order parameter $\langle R(t)\rangle_N$ on time for different phases of coupling β. N = 200, λ = 1

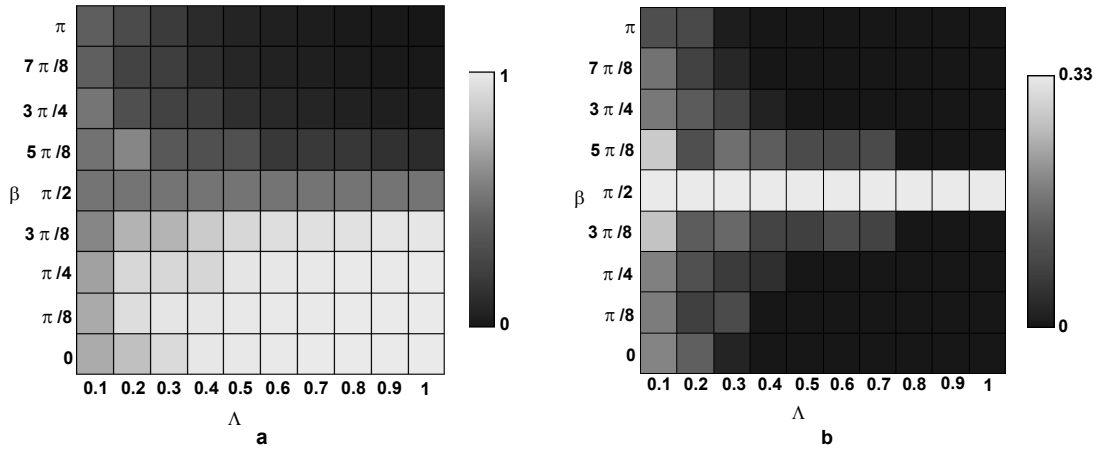

Fig. 6. Density plots of the averaged modulus of complex order parameter at the moment t=100 (a) and difference between maximum and minimum values of averaged modulus of complex order parameter on time segment [80,100] (b) for different phases of coupling β and amplitudes of coupling Λ

Conclusion. We have demonstrated that the dynamics of two weakly-coupled STNOs is conveniently described by a complex order parameter in the scope of global coupling model. Using numerical analysis we show that the synchronization of two STNOs is most effective when the amplitude of coupling Λ is big and the phase of coupling β is far lesser or larger than $\pi/2$.

Acknowledgments. The authors would like to thank to Prof. A.N. Slavin and Dr. V.S. Tiberkevich for discussions.

This work was supported in part by grant M/212–2011 of The State Agency of Science, Innovations and Informatization of Ukraine and by grant UU34/008 of The State Fund for Fundamental Researches of Ukraine.

Reference

1. Погорілий А.М., Рябченко С.М., Товстолиткін О.І. Спінтроніка. Основні явища. Тенденції розвитку // Український фізичний журнал. Огляди. – 2010. – Т. 6, № 1. 2. Прокопенко О.В. Взаємна фазова синхронізація двох нанорозмірних магнітних структур з урахуванням запізнення сигналу // Радіоелектроніка. Інформатика. Управління. – 2010. – № 2. 3. Berger L. Emission of spin waves by a magnetic multilayer traversed by a current // Physical Review B. – 1996. – Vol. 54. 4. Georges B., Grollier J., Cros V., Fert A. Numerical simulations of the synchronization of an assembly of Spin Transfer Oscillators by the stimulated microwave currents : Influence of delay and linewidth // Abstracts of the 52th MMM Conference (Tampa, FL, USA, Nov. 2007), CE-10. 5. Houssameddine D., Ebels U., Delaët B., Rodmacq B., Firastrau I., Ponthenier F., Brunet M., Thirion C., Michel J.-P., Prejbeanu-Buda L., Cyrille M.-C., Redon O., Dieny B. Spin-torque oscillator using a perpendicular polarizer and a planar free layer // Nature Materials. – 2007. – Vol. 6. 6. Kaka S., Pufall M.R., Rippard W.H., Silva T.J., Russek S.E., Katine J.A. Mutual phase-locking of microwave spin torque nano-oscillators // Nature. – 2005. – Vol. 437. 7. Katine J.A., Albert F.J., Buhrman R.A., Myers E.B., Ralph D.C. Current-driven magnetization reversal and spin-wave excitations in Co/Cu // Physical Review Letters. – 2000. – Vol. 84. 8. Kiselev S.I., Sankey J.C., Krivorotov I.N., Emley N.C., Schoelkopf R.J., Buhrman R.A., Ralph D.C. Microwave oscillations of a nanomagnet driven by a spin polarized current // Nature. – 2003. – Vol. 425. 9. Krivorotov I.N., Emley N.C., Sankey J.C., Kiselev S.I., Ralph D.C., Buhrman R.A. Time-domain measurements of nanomagnet dynamics driven by spin-transfer torques // Science. – 2005. – Vol. 307. 10. Lee K.J., Deac A., Redon O., Nozières J.-P., Dieny B. Excitations of incoherent spin waves due to spin-transfer torque // Nature Materials. – 2004. – Vol. 3. 11. Mancoff F.B., Rizzo N.D., Engel B.N., Tehrani S. Phase-locking in double-point-contact spin-transfer devices // Nature. – 2005. – Vol. 437. 12. Persson J., Zhou Y., Akerman J. Phase-locked spin torque oscillators: Impact of device variability and time delay // Journal of Applied Physics. – 2007. – Vol. 101. 13. Pikovsky A., Rosenblum M., Kurths J. Synchronization: a universal concept in nonlinear sciences. – Cambridge: University Press, 2007. 14. Prokopenko O., Tyberkevych V., Slavin A. Mutual phase-locking of two spin-torque oscillators: Influence of time delay of a coupling signal // Proceedings of the Europe International Magnetics Conference (May 4–8, 2008). – Madrid (Spain). – DP-06. 15. Ralph D.C., Stiles M.D. Spin Transfer Torques // Journal of Magnetism and Magnetic Materials. – 2008. – Vol. 320. 16. Ruotolo A., Cros V., Georges B., Dussaux A., Grollier J., Deranlot C., Guillemet R., Bouzehouane K., Fusil S., Fert A. Phase-locking of magnetic vortices mediated by antivortices // Nature Nanotechnology. – 2009. – Vol. 4. 17. Slavin A., Tiberkevich V. Nonlinear auto-oscillator theory of microwave generation by spin-polarized current // IEEE Transaction on Magnetics. – 2009. – Vol. 47. 18. Slavin A.N., Tiberkevich V.S. Nonlinear self-phase-locking effect in an array of current-driven magnetic nanocontacts // Physical Review B. – 2005. – Vol. 72. 19. Slavin A.N., Tiberkevich V.S. Theory of mutual phase-locking of spin torque nano-oscillators // Physical Review B. – 2006. – Vol. 74. 20. Slonczewski J.C. Current-driven excitation of magnetic multilayers // Journal of Magnetism and Magnetic Materials. – 1996. – Vol. 159. 21. Slonczewski J.C. Excitation of spin waves by an electric current // Journal of Magnetism and Magnetic Materials. – 1999. – Vol. 195. 22. Urazhdin S., Birge N.O., Pratt W.P. Jr., Bass J. Current-Driven Magnetic Excitations in Permalloy-Based Multilayer Nanopillars // Physical Review Letters. – 2003. – Vol. 91.

Submitted on 12.10.12

О. Прокопенко, канд. фіз.-мат. наук, доц., Б. Карпяк, студ., О. Сулименко, студ.,
каф. нанофізики та наноелектроніки, радіофізичний факультет,
КНУ імені Тараса Шевченка, Київ

ДИНАМІКА УЗАГАЛЬНЕНИХ ФАЗ У СИСТЕМІ ДВОХ СЛАБКО ВЗАЄМОДІЮЧИХ МАГНІТНИХ НАНООСЦИЛЯТОРІВ З ВИПАДКОВИМИ ВЛАСНИМИ ЧАСТОТАМИ: ВИПАДОК ГЛОБАЛЬНОГО ЗВ'ЯЗКУ

Проаналізовано динаміку узагальнених фаз в системі двох слабко зв'язаних магнітних наноосцилляторів з випадковими власними частотами (розподіленими за нормальним законом). Показано, що у наближенні глобального зв'язку динаміку такої системи зручно описувати за допомогою комплексного параметра порядку. Методами числового аналізу досліджено часові зміни модуля комплексного параметра порядку. Показано, що синхронізація двох магнітних наноосцилляторів відбувається найбільш ефективно при великих значеннях амплітуди коефіцієнта зв'язку Λ та фазі коефіцієнта зв'язку β кратній π.

Ключові слова: магнітний наноосцилятор, синхронізація, зв'язані коливання, випадкова власна частота.

А. Прокопенко, канд. физ.-мат. наук, доц., Б. Карпяк, студ., О. Сулименко, студ.,
каф. нанофизики и наноэлектроники, радиофизический факультет,
КНУ имени Тараса Шевченко, Киев

ДИНАМИКА ОБОБЩЕННЫХ ФАЗ В СИСТЕМЕ ДВУХ СЛАБО ВЗАИМОДЕЙСТВУЮЩИХ МАГНИТНЫХ НАНООСЦИЛЛЯТОРОВ СО СЛУЧАЙНЫМИ СОБСТВЕННЫМИ ЧАСТОТАМИ: СЛУЧАЙ ГЛОБАЛЬНОЙ СВЯЗИ

Проанализирована динамика обобщенных фаз в системе двух слабо связанных наноосцилляторов со случайными собственными частотами (распределенными по нормальному закону). Показано, что в приближении глобальной связи динамику такой системы удобно описывать с помощью комплексного параметра порядка. Методами численного анализа исследована зависимость изменений модуля комплексного параметра порядка от времени. Показано, что синхронизация двух магнитных наноосцилляторов происходит наиболее эффективно при больших значениях амплитуды коэффициента связи Λ и фазе коэффициента связи β кратной π.

Ключевые слова: магнитный наноосциллятор, синхронизация, связанные колебания, случайная собственная частота.

UDC 53.082.7

S. Radchenko, Ph.D., T. Pershyna, stud., I. Tolokonnikov, stud.,
Department of Medical radiophysics, Faculty of Radiophysics,
Taras Shevchenko National University of Kyiv

OPTIMAL SIGNAL SUPPRESSION OF BONE AND CARTILAGE IN MRI

The robust procedures for the separation of bone and cartilage tissues in magnetic resonance (MR) images are presented. Increased differentiation by contrast and signal-to-noise ratio (SNR) in proposed methods is based on pulse sequence dependence. First method is based on the new pulse sequence for MR bone and cartilage imaging, which allows simultaneous suppression of the signal from one tissue and visualisation of another one or vice versa. Second method is an optimization of balanced steady-state free precession (bSSFP) sequence. Mathematical modeling shows direct increasing of tissue differentiation under optimal values of these pulse sequences obtained for high contrast between bone and cartilage and a high SNR.

Key words: MR bone and cartilage imaging, SNR, contrast, pulse sequence optimization.

Introduction. Bone and cartilage are difficult to distinguish in MR images obtained by standard pulse sequences (such as fast spin echo, gradient recall echo, turbo spin echo, bSSFP) [3; 4; 6–9]. As a result these images cannot be segmented. But segmented images are more meaningful and easier to analyze and could be used for practical applications such as measurement of tissue volumes, treatment planning and study of anatomical structure. Each of the pixels in a region of segmented image is similar with respect to some characteristic or computed property, such as color, intensity, or texture. On MR tomograms these properties are functions of such physical characteristics as equilibrium magnetization, spin-lattice and spin-spin relaxation times and parameters of pulse sequence used for visualization. Having considered all arguments, it may be pointed out that study of anatomical structure and implants manufacturing need a special pulse sequence for bone and cartilage MR imaging. This problem could be solved in two ways. First way is calculation of parameters for a new pulse sequence for MR bone and cartilage imaging. Second way is optimization of standard pulse sequence for bone and cartilage separation.

In this work we perform calculation and optimization of parameters for a new pulse sequence and bSSFP sequence by contrast and SNR for MR bone and cartilage imaging. Optimization was provided by mathematical modeling according to the theoretical model.

Theoretical model. Model of bone and cartilage for MR could be described with three pairs of parameters: equilibrium magnetization per unit volume, spin-lattice and spin-spin relaxation times of bone and cartilage.

Spin-lattice and spin-spin relaxation times of bone and cartilage are listed in Table 1 [1–3; 5; 10].

Table 1

Spin-lattice relaxation times T_1, spin-spin relaxation times T_2 and densities of bone and cartilage

Tissue	T_1, ms	T_2, ms	Density, kg/m^3
Bone	554±27	140±12	1850
Cartilage	1060±160	42±7	1050

The following approximations were introduced for assessment of the equilibrium magnetization per unit volume M_0 of bone and cartilage:

1. Water is a major component of bone and cartilage tissues. That is why only the protons of water molecules were considered in the calculations.

2. Distribution of water in bone and cartilage is uniform: $M_0 \neq f(\vec{r})$.

The equilibrium magnetization as a function of magnetic field B_0 and temperature T is obtained according to the 26% mass fraction of water in bone and 70% mass fraction of water in cartilage.

The value of the equilibrium magnetization per unit volume in the high-temperature approximation is obtained using the following formula:

$$M_0 = \frac{N \cdot \hbar^2 \cdot \gamma^2 \cdot I \cdot (I+1)}{3 \cdot k \cdot T} \cdot B_0 . \qquad (1)$$

Total number of protons is calculated by the following formula:

$$N = \frac{2 \cdot \rho_{H_2 0} \cdot V_{H_2 0} \cdot N_A}{M_{H_2O}} , \qquad (2)$$

where $\rho_{H_2 0}$ – water density, $V_{H_2 0}$ – water volume in tissue, N_A – Avogadro constant, M_{H_2O} – molar mass of water.

Mass fraction of water in bone is calculated as follows:

$$\frac{m_{H_2O,b}}{m_b} = \frac{\rho_{H_2O} \cdot V_{H_2O,b}}{\rho_b \cdot V_b} = 0.26 , \qquad (3)$$

where m_b – bone mass, $m_{H_2O,b}$ – water mass in bone, ρ_b – bone density, $V_{H_2O,b}$ – water volume in bone, V_b – bone volume.

$$V_{H_2O,b} = \frac{0.26 \cdot \rho_b}{\rho_{H_2O}} \cdot V_b = \frac{0.26 \cdot 1850}{1000} \cdot V_b = 0.481 \cdot V_b , \qquad (4)$$

From (2) and (4) the total number of protons in the bone per unit volume is:

$$N_b = 0.481 \cdot \frac{2 \cdot \rho_{H_2 0} \cdot N_A}{M_{H_2O}} . \qquad (5)$$

From (1) and (5) the equilibrium magnetization per unit volume for bone is:

$$M_{0,b} = 0.481 \cdot \frac{\hbar^2 \cdot \gamma^2 \cdot I \cdot (I+1)}{3 \cdot k \cdot T} \cdot B_0 \cdot \frac{2 \cdot \rho_{H_2 0} \cdot N_A}{M_{H_2O}} . \qquad (6)$$

Mass fraction of water in cartilage is calculated as follows:

$$\frac{m_{H_2O,c}}{m_c} = \frac{\rho_{H_2O} \cdot V_{H_2O,c}}{\rho_c \cdot V_c} = 0.7 , \qquad (7)$$

where m_c – cartilage mass, $m_{H_2O,c}$ – water mass in cartilage, ρ_c – cartilage density, $V_{H_2O,c}$ – water volume in cartilage, V_c – cartilage volume.

$$V_{H_2O,c} = 0.7 \cdot \frac{\rho_c}{\rho_{H_2O}} \cdot V_c = 0.7 \cdot \frac{1050}{1000} \cdot V_c = 0.735 \cdot V_c , \qquad (8)$$

From (2) and (8) the total number of protons in the cartilage per unit volume is:

$$N_c = 0.735 \cdot \frac{2 \cdot \rho_{H_2 0} \cdot N_A}{M_{H_2O}} . \qquad (9)$$

From (1) and (9) the equilibrium magnetization per unit volume for cartilage is:

$$M_{0,c} = 0.735 \cdot \frac{\hbar^2 \cdot \gamma^2 \cdot I \cdot (I+1)}{3 \cdot k \cdot T} \cdot B_0 \cdot \frac{2 \cdot \rho_{H_2 0} \cdot N_A}{M_{H_2O}} . \qquad (10)$$

Methods. New pulse sequence for MR bone and cartilage imaging. Inversion-recovery method was chosen because of almost double spin-lattice relaxation times difference:

$$\frac{T_{1,c}}{T_{1,b}} = \frac{1060}{554} \approx 1.91, \quad (11)$$

where $T_{1,c}$, $T_{1,b}$ – spin-lattice relaxation times of cartilage and bone respectively.

Pulse sequence consists of two parts. In the first part of the sequence only cartilage was visualized (bone signal was suppressed). It can be realized in such a way. A 180° pulse is applied first. This pulse rotates the net magnetization down. A 90° pulse is applied after applying of 180° pulse with delay:

$$T_b = T_{1,b} \cdot \ln(2) \approx 384 \text{ ms}. \quad (12)$$

It should be noted that at this time net magnetization of bone is zero. In the second part of the sequence only bone was visualized (cartilage signal was suppressed). This part is similar to the first part of sequence, but the delay between the radio frequency (RF) pulses is:

$$T_c = T_{1,c} \cdot \ln(2) \approx 734.7 \text{ ms}. \quad (13)$$

Sequence repetition time TR is 3 seconds, because z-component of the magnetization vectors must return to equilibrium.

bSSFP uses rapid excitation radiofrequency pulses combined with fully balanced gradient pulses to acquire images. It is based on a low flip angle GRE sequence and also includes transverse magnetizations from overlapping echoes along with longitudinal magnetizations from GRE.

Simulation is selected for verification of results, because the simulator is available in comparison with the real MRI system. 3D simulations are very time consuming, that is why 2D sample "2D 2-spheres" (Fig. 1) was selected as the object in MRI simulator JEMRIS. This sample allows to explore two tissues simultaneously.

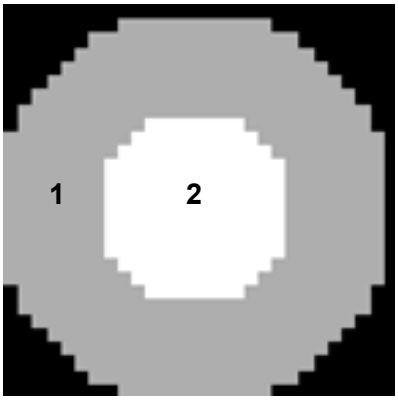

Fig. 1. Sample "2D 2-spheres":
1 – bone, 2 – cartilage

Results. Parameters used in the simulation correspond to real parameters of bone and cartilage.

The new pulse sequence. After signal suppression images shown in Fig. 2 were obtained. Contrasts are 90±10% and 86±9%, SNR are 5.00 and 6.59 respectively.

Optimization of delay between RF-pulses by a high contrast and maximum SNR of reconstructed tomogram was done. Examples of obtained images shown in Fig. 3.

Delays are 400 ms and 750 ms respectively. Results of mathematical modeling showed that the contrasts in these cases are 63±12% and 90±10% and SNRs are 6.51 and 7.87 respectively.

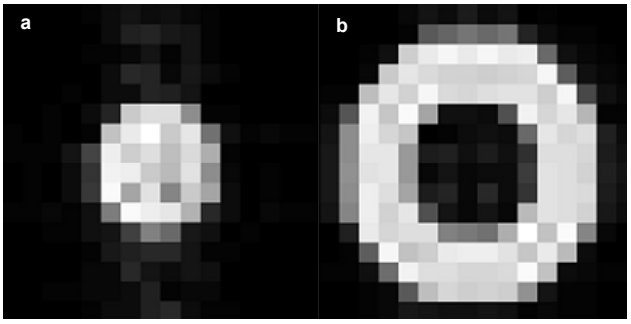

Fig. 2. Reconstructed tomograms:
a – the cartilage image
(the bone signal was suppressed);
b – the bone image
(the cartilage signal was suppressed)

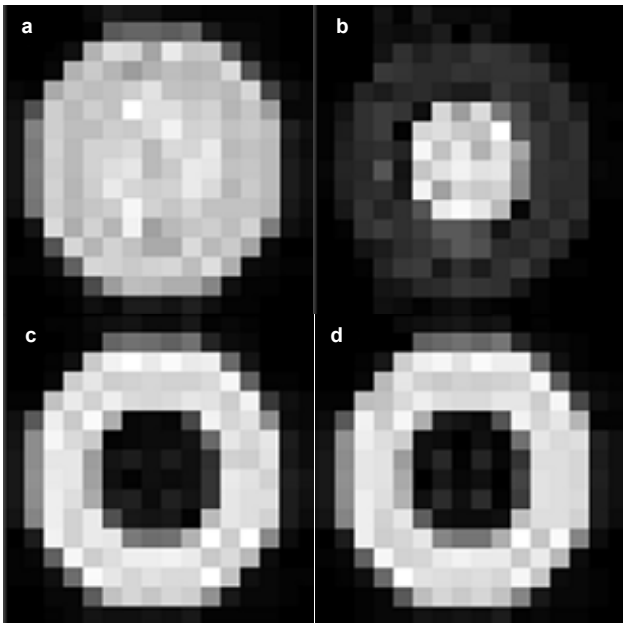

Fig. 3. Reconstructed tomograms were obtained
by the new pulse sequence with delay between RF pulses in:
a –300 ms; b –400 ms; c –700 ms; d –800 ms

bSSPF studies consist of SNR dependence upon repetition time TR, excitation time TE and flip angle. Fig. 4 shows SNR as a function of TR from both cartilage and bone with excitation time TE = 0.5TR and flip angles of 22° and 53°.

It can be seen that SNR decays with the increase of TR. Fig. 5 shows image degradation at long repetition times TR.

For studying SNR dependence upon excitation time TE, TR was set to 6 ms based on the aforementioned results. Flip angles remained the same. TE was changed from 1 to 5 ms with increment of 1 ms.

No visible changes of SNR were registered, but cartilage contrast is slightly better with TE = 3 ms (~ 0.5 TR).

The most important task was to find an optimal angle, so that both cartilage and bone SNR were of satisfactory values. TR =6 ms and TE = 3 ms were chosen.

Fig. 6 shows SNR dependence upon flip angle with clearly visible maximum cartilage SNR of ~17 around 20–23° with bone SNR of ~12 at the same angle. Choosing flip angle that maximizes bone SNR (53°) is not rational because of significant cartilage SNR drop at this angle.

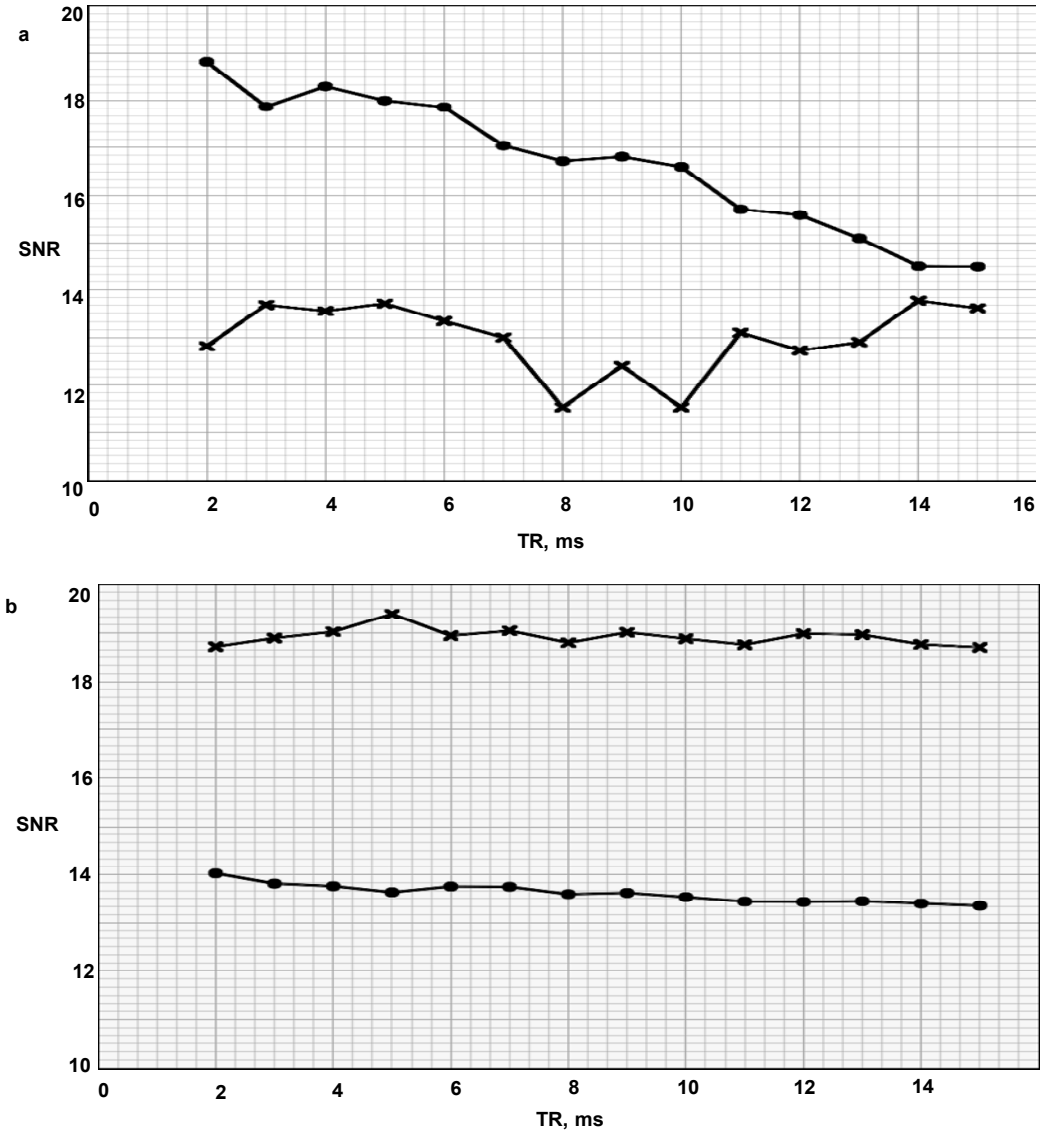

Fig. 4. SNR dependence upon TR, flip angle 22°(a) and 53°(b).
SNR of cartilage is marked with dots, SNR of bone is marked with crosses

Fig. 5. Image degradation with TR = 40 ms
and TE = 20 ms (right) compared to TR =4 ms and TE = 2 ms (left)

To compare SNR-efficiency the image with the same SNR of both tissues using classic GRE pulse sequence (TR/TE/angle = 500ms/10ms/51°) was acquired. Time to achieve SNR of 17 for cartilage and 12 for bone was 15 m 13 s using GRE and 10 m 17 s using bSSFP, making bSSPF 22% more SNR-efficient than classic GRE sequence. This difference in efficiency can be used for shortening scan time or for improving overall image resolution.

Conclusion. We have proposed two procedures for optimal signal suppression of bone and cartilage in MRI. Inversion-recovery is the most effective when delays between RF-pulses are 400 ms and 750 ms for bone and cartilage suppression. The contrasts are 63±12% and 90±10% and SNRs are 6.51 and 7.87 respectively. bSSFP achieves the best separation with TR/TE/flip angle = 6 ms/3 ms/22° acquiring cartilage and bone SNRs of 17 and 12 respectively.

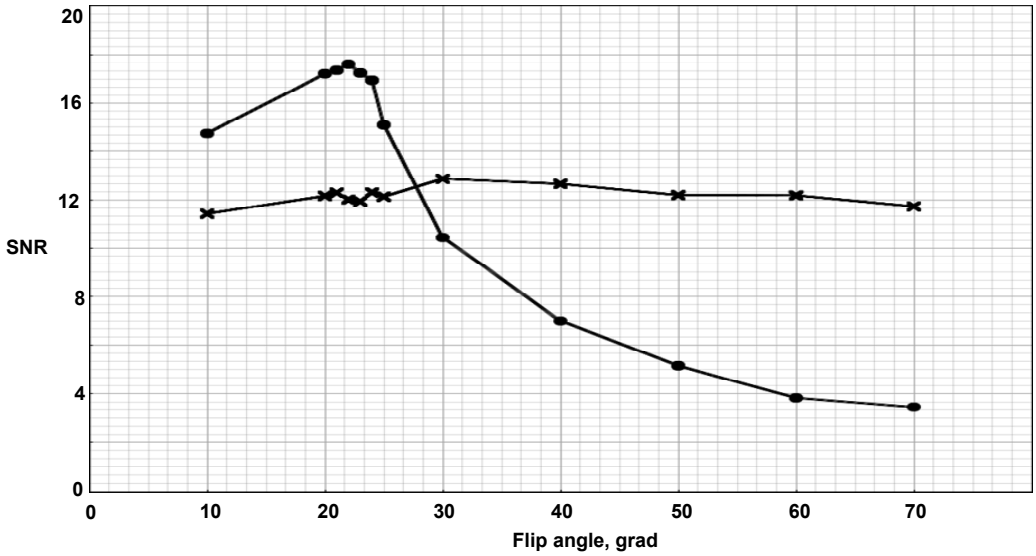

Fig. 6. SNR dependence upon flip angle with TR = 6 ms and TE = 3 ms. SNR of cartilage is marked with dots, SNR of bone is marked with crosses

Reference

1. Damadian R., Zaner K., Hor D., DiMaio T., Human Tumors Detected by Nuclear Magnetic Resonance// Proc.Nat.Acad.Sci. USA. – 1974. – Vol.71, №4. – P. 1471–1473. 2. Dardzinski B. J., Laor T., Schmithorst V. J.,Klosterman L., Brent Graham T., Mapping T2 Relaxation Time in the Pediatric Knee: Feasibility with a Clinical 1.5–T MR Imaging System// Radiology. – 2002. – Vol.225, №1. – P. 233–239. 3. Gold G. E., Han E., Stainsby J., Wright G., Brittain J., Beaulieu C., Musculoskeletal MRI at 3.0 T: Relaxation Times and Image Contrast//AJR. – 2004. – Vol.183, №2. – P. 343–351. 4. Hargreaves B. A., Gold G. E., Beaulieu C. F., Vasanawala S. S., Nishimura D. G., Pauly J. M., Comparison of new sequences for high-resolution cartilage imaging// Magn Reson Med. – 2003. – Vol.49. – P. 700–709. 5. Joseph D., Gu W. Y., Mao X. G., Lai W. M., Mow V. C., True density of normal and enzymatically treated bovine articular cartilage. In: Proceedings of 45th Annual Meeting of Orthopaedic Research Society, Feb 1999, Anaheim, CA, 1999: 642. 6. Kijowski R., Clinical Cartilage Imaging of the Knee and Hip Joints// AJR. – 2010. – Vol.195, №3. – P. 618–628. 7. Kijowski R., Lu A., Block W., Grist T., Evaluation of the articular cartilage of the knee joint with vastly undersampled isotropic projection reconstruction steady-state free precession imaging// J Magn Reson Imaging. – 2006. – Vol.24. – P. 168–175. 8. Link T. M. Cartilage Imaging: Significance, Techniques, and New Developments. - New York: Springer, 2011. – 245 p. 9. Recht M. P., Goodwin D. W., Winalski C. S., White L. M., MRI of Articular Cartilage: Revisiting Current Status and Future Directions// AJR. – 2005. – Vol.185, №4. – P. 899–914. 10. Yang J., Chiou R., Ruprecht A., Vicario J., MacPhail L. A., Rams T. E., A new device for measuring density of jaw bones// Dentomaxillofacial Radiology. – 2002. – Vol.31, №5 – P. 313–316.

Submitted on 14.05.13

С. Радченко, канд. фіз.-мат. наук, Т. Першина, студ., І. Толоконніков, студ.
каф. медичної радіофізики, радіофізичний факультет,
КНУ імені Тараса Шевченка, Київ

ОПТИМАЛЬНЕ ПРИДУШЕННЯ СИГНАЛІВ КІСТКИ І ХРЯЩА В МРТ

Представлено надійні процедури для відділення кісткових і хрящових тканин на магнітно-резонансних (МР) зображеннях. Збільшення диференціації за контрастом і співвідношенням сигнал-шум у запропонованих методах засновано на залежності від імпульсної послідовності. Перший метод базується на новій імпульсній послідовності для МР зображень кісток і хрящів, яка дозволяє придушити сигнал від однієї тканини і візуалізувати іншу і навпаки. Другий метод – це оптимізація послідовності balanced steady-state free precession. Математичне моделювання показує пряме збільшення диференціації тканин при оптимальних значеннях цих послідовностей, отриманих для високого контрасту між кісткою і хрящем і великого співвідношення сигнал-шум.

Ключові слова: магнітно-резонансні зображення кісток і хрящів, співвідношення сигнал-шум, контраст, оптимізація імпульсної послідовності.

С. Радченко, канд. физ.-мат. наук, Т. Першина, студ., И. Толоконников, студ.
каф. медицинской радиофизики, радиофизический факультет,
КНУ имени Тараса Шевченко, Киев

ОПТИМАЛЬНОЕ ПОДАВЛЕНИЕ СИГНАЛОВ КОСТИ И ХРЯЩА В МРТ

Представлено надежные процедуры для отделения костных и хрящевых тканей на магнитно-резонансных (МР) изображениях. Увеличение дифференциации по контрасту и соотношению сигнал-шум в предложенных методах основано на зависимости от импульсной последовательности. Первый метод базируется на новой импульсной последовательности для МР изображений костей и хрящей, которая позволяет подавить сигнал от одной ткани и визуализировать вторую и наоборот. Второй метод – это оптимизация последовательности balanced steady-state free precession. Математическое моделирование показывает прямое увеличение дифференциации тканей при оптимальных значениях этих последовательностей, полученных для высокого контраста между костью и хрящом и большого соотношения сигнал-шум.

Ключевые слова: магнитно-резонансные изображения костей и хрящей, соотношение сигнал-шум, контраст, оптимизация импульсной последовательности.

UDC 519.9

I. Tomylko, assistant, Department Medical radiophysics,
Faculty of Radiophysics, Taras Shevchenko National University of Kyiv

MOLECULAR FULLEROL C60 AND BIOTIN WATER SUSPENSIONS : MODELLING AGGREGATION AND OPTICAL ABSORBTION SPECTROSCOPY TESTING

The peculiarities in the absorbance spectra – the absorption bands with maxima near 266, 340 and 522 nm – for $C_{60}(OH)_n(O)_m$ aggregates in water, which are controlled by the addition of biomolecules (biotin with 1mM content) were revealed. With aim to explain these peculiarities the proposed model for deaggregation of hydroxylated C_{60} with C-O^- by biotin molecules due to the interaction between its C-OH^- and biotin (-CO)$^+$ groups with the self-organization C_{60} quasicrystals with observed absorbance peak at 400nm confirming of this model.

Key words: C_{60} aggregates, C_{60} derivatives, suspension, biotin

Introduction. Chemical and physical features of fullerene C_{60}, together with its spherical shape, have raised the hope of successful use in many different areas either in biological or material chemistry (6, 1). The condensed aromatic rings present in the compound lead to an extended p(π-π) conjugation of molecular orbitals causing significant absorption of visible light. The facile electron acceptability of up to six electrons makes them good candidates as electron acceptors (10, 11). Also, fullerene compounds have avid reactivity with free radicals. Potential biological activities of fullerenes have been investigated with the aim of using it in the sphere of medicine (5–7). An important hindrance for this application is the low solubility of fullerenes in polar solvents and the consequent formation of aggregates in aqueous suspensions (4). However, the development of covalent chemistry of C_{60} has revealed the possibility to attach these spherical structures with several groups, which allow increment in the biological activity (1, 3, 8). Therefore, for future performance in biomedical application, fullerenes have to be functionalized by dint of hydrophilic substituents. Many substituents have been bound attached to C_{60} to produce water solubility, such as:

1) negatively charged carboxylic acids (10), 2) positively charged quaternary ammonium (4), 3) neutral poly (ethylene glycol) (4). Within this category of water-soluble fullerenes, the hydroxylated C_{60} – $C_{60}(OH)_n$ holds a special place and has already been studied in very various fields (5).

Variety biologically important biospecies such as enzymes proteins and antibodies can be used as recognition elements for biosensors (7). However, because most of these biologically important biospecies are water soluble, they cannot be employed as recognition elements of biosensors. In addition, these water-soluble biospecies are difficult to recover and reuse after analysis by the biosensors. Therefore, water-insoluble and biospecies were prepared and applied as reusable recognition elements of biosensor (6) There are immobilized C_{60}-biospecies, e.g. C_{60}-catalase, C_{60}-anti IgG and C_{60}-anti-hemoglobin were also applied as coating.

The fullerene $C_{.60}$ molecule has 30 double bonds and can be considered as an olefin molecule. Like olefin molecules, fullerene C_{60} can be electrophilicly attacked by electron-releasing molecules such as amines (8). The enzyme, protein and antibody molecules like amines contain the NH group, so they can be expected to chemically materials for biosensors to detect various biospecies, e.g. hydrogen peroxide, IgG, anti-gliadin and hemoglobin in suspensions.

We have found that nano – C_{60} can form over a wide range of mixing conditions and pH and is quite stable at ionic strengths, at or below 0.05 I, for months. Andrievsky and al. suggested that pH was an important parameter for these colloids because of the stability of the surface charge. This are founded that for pH values between 3.75 and 10.25, nano-C_{60} is formed and that, as the pH of the water is varied, a change in the average particle size is observed. Higher pH values result in smaller nano-C_{60} populations and lower pH values give rise to larger particle populations. In addition, as the pH is increased and the average particle size is smaller, a blue shift in the UV/Vis spectrum is observed in the 330–350 nm range (7).

With this information about the physical structure, chemical properties, and stability in hand, we examined the biological effects of C_{60} using biotin molecules (9).

Biotin – dependent carboxylases catalyze a variety of carboxyl transfer reactions in a number of metabolic pathways and are found in all free-living organisms. They are large molecules which can comprise a single polypeptide chain with three domains or up to three subunits, each of which performs a particular part of the overall reaction. Biotin plays a central role in the action of enzymes (2, 3).

Results and discussion. The aim of the investigation is to reveal peculiarities in absorbance spectra – electronic structure – of the hydroxylated C_{60} in water suspensions (Fig.1a) with biotin molecules. Biotin is composed of an ureido (tetrahydroimidizalone) ring fused with a tetrahydrothiophene ring, which is an organic compound consisting of a five-membered ring containing four carbon atoms and a sulfur atom.(3) A valeric acid substituent– straight chain alkyl carboxylic acid with the chemical formula $CH_3(CH_2)_3COOH$) – is attached to one of the carbon atoms of the tetrahydrothiophene ring.(Fig.1b).

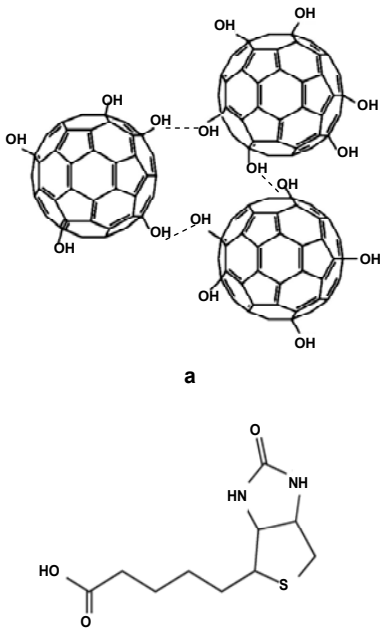

a b

Fig. 1. Schematic images of: a – $C_{60}(OH)_n(O)_m$ aggregate in aqueous as a network of intermolecular located inside hydrogen bonds and with negatively charged O^{--} which are located outside the aggregate's core; b- atomic, structural model of biotin molecule $C_{10}H_{16}N_2O_3S$

We build our model on the hypothesis that biotin has "+" charge on the chemical tails like as $(–CO)^+$ or "-" charge like $(COO)^–$ groups, in water suspensions.(13) Then, hydroxylated C_{60} in water suspension will have model $C_{60}(OH)_x(O)_y$ aggregate is presented in Fig.1,a (11, 12)

For the experimental verification of C_{60} aggregates model in water suspension (Fig.1a) and ones changing with added biotin molecules having "+", "-" charges, which induce self-organization groups from C_{60} $(C–O)^-$ biotin with $(–CO)^+$ group were preparing water suspension with controlled pH =10.2 to 2.2. controllability of the consist by added biomolecules in water suspension were determined from absorbance spectra at 200–300 nm range for biotin (D- Biotin, $C_{10}H_{16}N_2O_3S$, Sigma-Aldrich). We started with fullerene C_{60}, >99% pure, MER Corporation Fullerenes.

UV-vis absorption spectroscopy was performed using a UV-vis-NIR spectrometer Jacobs32 and carry out experiment at 300K. The suspensions prepared with ultra pare water (18.2 $M\Omega cm^{-1}$); Milli-Q purification systems Millipore.

The typical absorption spectra for biotin molecules in aqueous suspensions are presented in the Fig.2. The intensity decreasing for absorption bands for biotin molecules incubation during 6 days and maxima are centered at 214nm and 258 nm(the curves 1), and the shifting of these maximum positions after incubation period (the curves 2, respectively) correspondingly to 219 and 262nm are revealed. These peaks confirm our model for building active pair biotin molecules/C_{60} derivatives, as biotin have absorption maximum in region 210–300 nm, which corresponds to absorption of C_{60} derivatives.

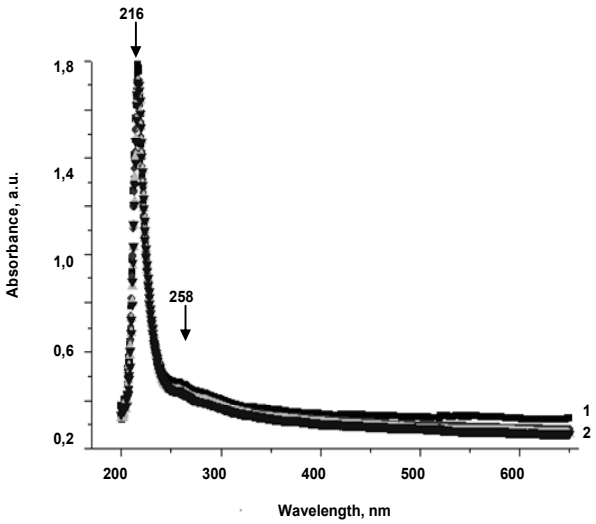

Fig. 2. Recognition of absorption bands initiated by incubation of biotin molecules in aqueous suspension during one day after preparing (were recorded several times) and during three days (were recorded several times)

As was shown in investigations of particle stability at relevant ionic strengths that fullerene aggregates will not remain in solutions simulating seawater or even brackish waters with ionic strengths at or above 0.1 I.

However, at ionic strengths below this (0.05 I and below) an appreciable percentage (0.05 I) if not all (0.01 and 0.001 I) of aggregates remain stable for 15 weeks. These results are important as potential long-term stability is limited to aqueous systems at below 0.05 I, which includes most freshwater environments such as typical groundwaters and surface waters (8). But this study did not investigate other coagulating factors, such as protein, humic acids, or sorption onto or within solid matrixes such as organic matter and soil fractions, which may influence stability.

Two intense broad absorption bands with maxima at 265, 351 nm (Fig. 3) and 270, 347 nm (Fig. 5) dominate in the range 190–410 nm for the fullerene aqueous solutions without and with biotin molecules. The energy positions of these maxima correspond to allowed electron transitions $h_u \rightarrow h_{2g}$ (264, 284 nm) and $h_g, g_g \rightarrow t_{1u}$ (340, 336 nm) (12).

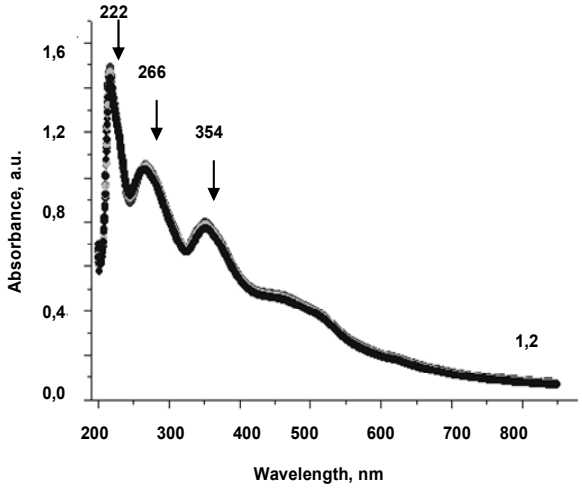

Fig. 3. Recognition of absorption bands initiated by incubation C_{60} derivative molecules in aqueous suspension: the comparison of the absorption spectra of C_{60} derivatives after preparation and after period two days (recorded several times)

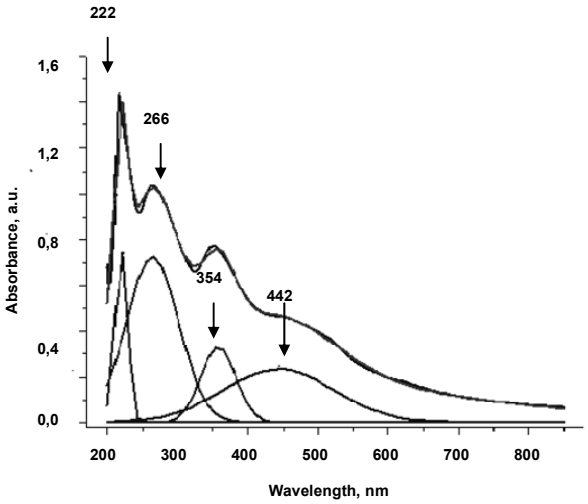

Fig. 4. Deconvolution of C_{60} absorption spectrum shows positions of four bands, residuals are scarcely evident. The positions of Ib, IIb, IIIb , IVb bands are at 222, 266, 354 nm and 442 nm, respectively

The shifts between the maxima in C_{60} and C_{60}/biotin suspension are 2 and 4 nm. With aim to detect the changes in the a marked absorption band for C_{60} fullerol under biotin fictionalization we analyzed the spectra in 200–400 nm region (Fig.5) because, as it can see from Fig.4, the fullerol have the position of the absorption max at 266 nm (12).

In our investigation we founded: Position I peak for 1 spectrum – 3,63; 2,3 spectrum – 3,62; 4 spectrum – 3,63(eV); Position II peak for 1 spectrum – 4,65; 2,3 spectrum – 4,63; 4 spectra – 4,65(eV); Position III peak for 1 spectrum – 5,64; 2,3 spectrum – 5,7; 4 spectrum – 5,72 (eV) (Fig.6). We can conclude that after adding biotin changes in position evaluated near 0, 01 and 0,2 eV. We suggested this molecular surface modification of the fullerene molecules is promising to the biological activity.

When we added biotin molecules we observed shift in longest wavelength region for biotin suspension and it is confirm the changes of pH solution, it is mean that – OH group in fullerol core added in biotin molecules. The comparison of spectra for fullerene solutions with biotin molecules demonstrates the decreasing of the absorbance bands intensity for fullerol C_{60} with maxima, centered at 266nm and their maximum position shifting to 270nm, after addition biotin in this solution. We can predict that all – OH group are reacting with single biotin molecule.

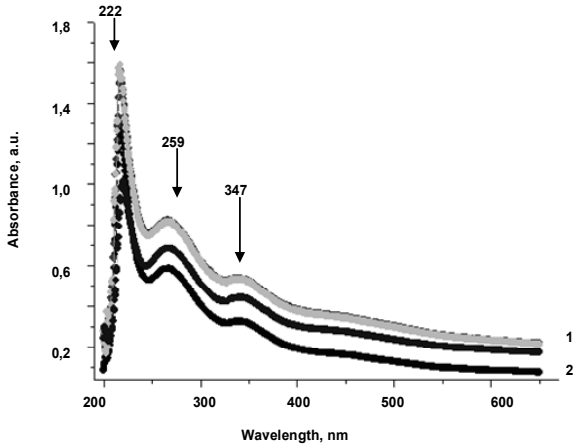

Fig. 5. Recognition of absorption bands initiated by biotin molecules at interface with C_{60} derivatives in suspension: the comparison of the absorption spectra of C_{60} derivatives with biotin molecules recorded several times 1 – after preparation, 2 – after 6 days

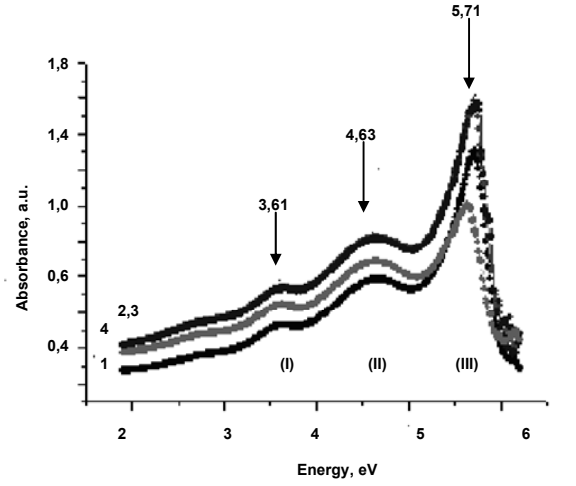

Fig. 6. Recognition of absorption bands initiated by biotin molecules at interface with C_{60} derivatives in suspension: the comparison of the absorption spectra of C_{60} derivatives with biotin molecules recorded several times 1 – after preparation (#1, 2 curves), 2 – after 6 days (#3, 4 curves)

In the range of 410–650 nm absorption spectrum of fullerol suspensions there is a wide area of absorption available between 425 and 570 nm, which is a characteristic feature of the absorption spectra of crystals of C_{60} molecules in the film. The appearance of the absorption band associated with close electronic interaction between neighboring C_{60} molecules in the crystals, and its location within the 450 and 600 nm depending on the shape and density of the location of these crystals (12). The weak bands near 442 nm appeared in these region (Fig.4). It is known that in the range 490–640 nm (1.9–2.5 eV) (Fig.6) the weak absorption takes place associated with electric dipole-forbidden transitions between the one-electron HOMO level with h_u symmetry and one-electron t_{1u} LUMO level.

Conclusion. In optical absorbance spectra for C_{60} aggregates (model in Fig.1a) in prepared water suspensions with and without added biotin presented in Fig. 3 and Fig.5, correspondently, we observed: 1) in compare with theoretical calculations for optical transition in C_{60} molecule (the peaks in the absorbance spectrum are at 220, 263, 345, 450 nm) for C_{60} aggregates is the two main peaks at 266 nm and 340 nm (Fig.3), which correspond of the absorbance on $(–OH)_n$ groups and O^- (groups), respectively. We evaluated that C_{60} have components 11 for C–OH groups and 7 for C–O^- groups (5, 9); 2) added biotin molecules determined the shifts of the position of the absorbance peaks from 266 and 354 to 271 and 258, 337 nm, respectively. The intensity of absorbance for C_{60} aggregates in suspension with and without biotin molecules coincides from 450-650 nm. We assume that the pairs from C-O^- /one in bases with "+" charge self – organized and than added electron transition at this interface were revealed. 3) due to biotin molecules addition in C_{60} suspension the absorbance peaks, corresponding electron transition in C_{60} aggregates disappear. It is the base for our hypothesis about deaggregation of hydroxylated C_{60} due to the interaction between its C–OH^- and biotin $(–CO)^+$ groups. Finally, model of organization by biotin molecules of C_{60} quasicrystals confirmed by changes in 410–650 nm region.

Acknowledgments. I would like to thanks my advisors, during measurement at Institute of chemical and biotechnology, TU Ilmenau, Prof. Uwe Ritter, Eugenia Buzaneva for bringing me this amazing filed and endless support of my research.

Reference

1. Adnađević B., Gigov M, Adnađević T, Jovanović J.. Fullerol Formation Kinetics in a Two-Phase Reaction System by using Phase Transfer Catalyst Tetrabutylammonium Hydroxide // J. Braz. Chem. Soc. – 2010 – Vol. 21, No. 3, 476–480. 2. Barbucci R, Magnani A, Roncolini C, Silvestri S. Antigen-antibody recognition by Fourier transform IR spectroscopy/attenuated total reflection studies: biotin – avidin complex as an example // Biopolymers. – 1991. 3. Emami, M.; Teimouri, A.; Chermahini, A.. Vibrational spectra and assignments using ab initio and density functional theory analysis on the structure of biotin // Spectrochimica Acta Part A: Molecular and Biomolecular Spectroscopy. – 2012 – Vol. 71, issue 4. 4.Isakovic A., Markovic Z., Todorovic-Markovic B., Nikolic N., Vranjes-Djuric S., Mirkovic M., Dramicanin M., Harhaji L., Raicevic N., Nikolic Z., and Trajkovic V.. Distinct Cytotoxic Mechanisms of Pristine versus Hydroxylated Fullerene // Toxicological sciences. – 2006. – 91(1). 5. Choi J., Lee I., Lee Y, Hong J., Kim I., Park Y., Hurb N. Immobilization of biomolecules on biotinylated magnetic ferrite nanoparticles // Chemical Physics Letters. – 2006 – Vol. 428, Issues 1–3. 6. Kysil O., Sporysh I., Buzaneva E., Erb T., Gobsch G., Ritter U., Scharff P. The C_{60} fullerene molecules integration by ds-, ss-DNA molecules in fluids:optical spectroscopy characterization of the biointerface organization // Mat. Sc. and Eng. – 2010. – B169/1-3. 7. Fortner J.D., Lyon D.Y., Sayes C.M., Boyd A.M., Falkner J.C., Hotze E.M., Alemany L.B., Tao Y.J., Guo W., Ausman K.D., Colvin V.L., Hughes J.B. C_{60} in Water: Nanocrystal Formation and Microbial Response // Environ. Sci. Technol.-2005- 39. . 8.Lamparth I., Hirch A.. Water-soluble malonic acid derivatives of C_{60} with a defined three-dimensional structure // J.Chem. Soc., Chem. Commun. – 1994. 9. Langereis S., Kooistra H.A., van Genderen M.H., Meijer E.W.Probing the interaction of the biotin-avidin complex with the relaxivity of biotinylated Gd-DTPA // Supplementary Material (ESI) for Organic & Biomolecular Chemistry – 2004. 10. Sayes C.M., Marchione A.A., Reed K.L., and Warheit D.B. Comparative Pulmonary Toxicity Assessments of C_{60} Water Suspensions in Rats: Few Differences in Fullerene Toxicity in Vivo in Contrast to in Vitro Profiles // Nano Lett. – 2007. – 7 , No. 8. 11.Scharff P., Siegmund C., Risch K., Lysko I., Lysko O., Zherebetskyy D., Ivanisik A., Gorchinskiy A., Buzaneva E. Characterization of Water-Soluble Fullerene C_{60} Oxygen and Hydroxyl Group Derivatives for Photosensitizer. Fullerenes // Nanotubes and Carbon Nanostructures. – 2005. – Vol.13, supplementary 1. 12. Sporysh I., Shynkaruk E., Lysko O., Shynkaruk A., Dubok V., Buzaneva E., Ritter U., Scharff P. Biomimetic hydroxyapatite nanocrystals in composites with C_{60} and Au-DNA nanoparticles: IR-spectral study // Mat. Sc. and Eng. – 2010. – B169/1-3. 13. Young AG, McQuillan AJ, Green DP.In Situ IR Spectroscopic Studies of the Avidin-Biotin Bioconjugation Reaction on CdS Particle Films // Langmuir. – 2009 – Vol. 25–13.

Submitted on 01.05.13

**І. Томилко, асистент, каф. медичної радіофізики,
радіофізичний факультет, КНУ ім. Тараса Шевченка, Київ**

МОЛЕКУЛЯРНІ ВОДНІ СУСПЕНЗІЇ ФУЛЛЕРОЛУ C_{60} ТА БІОТИНУ : МОДЕЛЮВАННЯ АГРЕГАЦІЇ ТА ПІДТВЕРДЖЕННЯ ОПТИЧНИМИ СПЕКТРАМИ ПОГЛИНАННЯ

Проаналізовано особливості спектрів поглинання з максимуми біля 266, 340 та 522 нм для $C_{60}(OH)_n(O)_m$ агрегатів у воді, які керуються додаванням біомолекул (біотин з концентрацією 1 μM). З метою обгрунтування данних особливостей запропоновані моделі для дезагрегації гідроксильваного C_{60} з $C\text{-}O^-$ біотин молекулами за рахунок взаємодії між $C\text{-}OH^-$ та $(\text{-}CO)^+$ групами з самоорганізацією квазікристалів з піком поглинання при 400 нм, який спостерігали, та підтверджує дану модель.

Ключові слова: C_{60} агрегати, C_{60} похідні, суспензія, біотин

**И.Томилко, ассистент, каф. медицинской радиофизики,
радиофизический факультет, КНУ им. Тараса Шевченко, Киев**

МОЛЕКУЛЯРНЫЕ СУСПЕНЗИИ ФУЛЛЕРОЛА C_{60} И БИОТИНА: МОДЕЛИРОВАНИЕ АГРЕГИРОВАНИЯ И ПОДТВЕРЖДЕНИЕ ОПТИЧЕСКИМИ СПЕКТРАМИ ПОГЛОЩЕНИЯ

Проанализированы особенности спектров поглощения с максимумами вблизи 266, 340 и 520 нм для $C_{60}(OH)_m(O)_m$ агрегатов в воде, которые управляются добавлением биомолекул (биотин с концентрацией 1μM). С целью обоснования этих особенностей предложены модели для дезагрегирования гидроксилированного C_{60} молекулами биотина $C\text{-}O^*$ за счет взаимодействия между $C\text{-}OH^*$ и $(\text{-}CO)^*$ группами и самоорганизацией квазикристаллов с пиком поглощения при 400 нм, который наблюдался, и подтверждает данную модель.

Ключеые слова: C_{60} агрегаты, C_{60} производные, суспензия, биотин.

UDC 537.52, 537.528

A. Tsymbalyuk, Junior Researcher Fellow, Volodymyr Dahl East Ukrainian National University, Luhansk, Ukraine, D. Levko, Ph. D., Post Doc, Université Paul Sabatier, Bât 3R2, Toulouse Cedex 9, France, V. Chernyak, Dr. Sc., Prof., E. Martysh, Dr. Sc., Ass. Prof., O. Nedybaliuk, Ph. D., Junior Researcher Fellow, Ol. Solomenko, post grad. stud., Taras Shevchenko National University of Kyiv, Kyiv, Ukraine

THE INFLUENCE OF CO_2 CONCENTRATION ON THE EFFECTIVITY OF SYN-GAS GENERATION FROM THE ETHANOL IN THE NON-EQUILIBRIUM PLASMA

The results of study of the influence of the CO_2 concentration on the syn-gas compound during the plasma assisted conversion of ethanol in tornado-type electrical discharge are presented. The comparison between both the experimental and numerical simulation results showed the good agreement. It was obtained that the concentrations of the main components of the syn-gas on the reactor outlet do not depend significantly on the rate of CO_2 pumping through the discharge.

Key words: Plasma, numerical simulation, syn-gas, electrical discharge, plasma assisted conversion.

Introduction. Syn-gas (the mixture of carbon monoxide and molecular hydrogen) could act either a fuel or an important component for the synthesis of different organic materials [5]. Depending on the type and compound of organic material one needs different ratios between concentrations of CO and H_2 in syn-gas.

The several methods of syn-gas producing are existed today. There are the treatment of the coal by the overheated water vapors, the partial oxidation of the natural gas, plasma chemical conversion of different hydrocarbons, *etc* [7]. The latter method is very attractive because it allows one to control the ratio H_2/CO. Usage of ethanol as the raw material for plasma assisted conversion was proposed in [2]. The ethanol was chosen since it is nontoxic and renewable fuel. It can be obtained from the agricultural products and wastes. However, the generation of syn-gas from the pure ethanol has one disadvantage; namely, it does not allow one to control the ratio H_2/CO. In order to avoid it, the add of CO_2 into the ethanol during the plasma assisted conversion is proposed. One can see from the stoichiometric equation

$$C_2H_5OH + CO_2 \rightarrow 3H_2 + 3CO \quad (\Delta H = 297.31 \text{ kJ/mol})$$

that the admixture of CO_2 allows one to decrease in two times the ethanol consumption, since the carbon atoms present in CO_2. In addition, the syn-gas with different ratios H_2/CO could be obtained varying the ratio between concentrations of C_2H_5OH and CO_2.

In the present paper we propose to carry out the plasma assisted conversion of ethanol in tornado-type electrical discharge [1, 3–4, 6].

Experimental setup. Fig. 1 shows the scheme of experimental setup. The main camera *1* is made from quartz. The camera is closed from the upper and the bottom sides by the metal flanges *2* and *3*. The level of the fuel *4* is kept constant by the pump through the orifice *5*. The metal electrode *6* cooling by the water could act as the cathode or the anode.

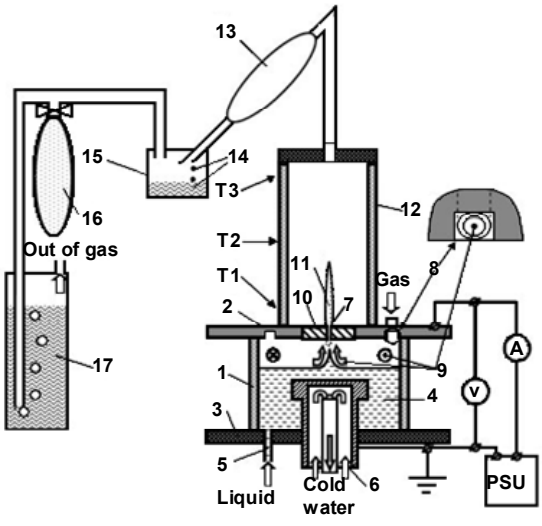

Fig. 1. Experimental setup

The upper flange *2* acts as the second electrode. In the middle of this flange the copper hop *11* with the nozzle *7* is placed. The mixture of CO_2 and air is injected into the vessel through the orifice *8* in the upper flange *2*

tangentially to the cylinder wall *1* and creates a reverse vortex flow of tornado type. Rotating gas *9* descends to the liquid surface and moves to the central axis where it flows out through the nozzle *7* in the form of jet *10* into the quartz chamber *12*. Since the area of minimal static pressure above the liquid surface during the vortex gas flow is located near the central axis, it creates a column of liquid at the gas-liquid interface in a form of a cone with its height of ~1 cm above the liquid surface (without electric discharge).

The voltage is applied between the upper electrode *2* and the lower electrode *6* in the liquid with the help of the DC power source powered up to 10 kV. Only one mode of the discharge operation is studied. It is the mode with "solid" cathode (SC): "minus" is on the flange *2*. The conditions of breakdown in the discharge chamber are regulated by three parameters: the level of the work liquid, the gas flow rate *G*, and by the value of voltage *U*. The ignition of discharge usually begins at the appearance of the axial streamer. Transition time to the self-sustained mode of operation is ~1-2 s. The range of discharge currents varied within 100–400 mA. The pressure in the discharge chamber during the discharge operation is ~1.2 atm, static pressure outside the reactor is ~1 atm. The elongated ~5 cm plasma torch *(10)* is formed during the discharge burning in the camera which does not contain any oxygen.

In order to study the component content of the syn-gas the gas chromatography and infrared spectroscopy were used.

Simulation model. In order to study the plasma chemical processes the model proposed in [3–4] was used. According to the model the gas is pumped through the discharge region continuously. The discharge region is the cylinder with the height equal to the distance between the liquid surface and upper electrode and with the radius equal to *R*. The total time of simulations was divided by three intervals: first – the gas is pumping through the discharge until all concentrations reach the constant values, second – "combustion" in the post-discharge region where the change of gas temperature because of chemical reaction was taken into consideration. At the third stage the gas is pumped through the camera *13* at the room temperature.

It was assumed that: 1) electrical power introduced into the discharge was average over the whole discharge volume; 2) the electric field was homogeneous and did not varied in time; 3) plasma is homogeneous; 4) gas temperature is influenced by the chemical reactions, heat transfer and gas pumping. Therefore, the kinetics was studied in temperature interval T = 520–1300 K. According to this interval the kinetic mechanism [4] was chosen. The model consists of 30 species and 173 reactions between them (130 chemical reactions and 43 electron-molecular reactions). The nitrogen was considered as a third body and the generation of nitrogen containing species was neglected.

The following system of kinetic equations was solved numerically in order to study the plasma chemical processes:

$$\frac{dN_i}{dt} = S_{ei} + \sum_j k_{ij} N_j + \sum_{j,l} k_{ijl} N_j N_l + \ldots + \frac{G}{V} N_i^0 - \\ - \frac{G}{V} N_i - kN_i \qquad (1)$$

Here N_i, N_j and N_l are the concentrations of molecules and radicals, k_{ij}, k_{iml} are the rate constants of chemical processes with the participation of *i*-th component. The last three terms in Eq. (1) describe the constant inlet and outlet of gas in the discharge region. Term $G/V \cdot N_i^0$ describes the inlet of molecules of primary components (nitrogen, oxygen, water and ethanol). Terms $G/V \cdot N_i$ and kN_i describe the outlet of gas from the discharge due to both the air pumping and the pressure difference between the discharge and atmosphere. The rates of electron-molecular reactions are:

$$S_{ei} = \frac{W}{V} \frac{1}{e_{ei}} \frac{W_{ei}}{\sum_i W_{ei} + \sum_i W_i} \qquad (2)$$

Here W is the power entered into the discharge, V is the discharge volume, and ε_{ei} is the reaction's threshold. The power W was averaged over the whole volume V. Also, W_{ei} and W_i are the specific powers spent in non-elastic and elastic electron-molecular reactions, respectively [4].

In the second camera (camera *12*, Fig. 1) the system (1) was solved only with the accounting for chemical reactions. The change of gas temperature due to chemical reactions was taking into account as well:

$$\frac{dT}{dt} = -\frac{1}{\rho C_p} \sum_i H_i(T) \cdot \mu_i \frac{dN_j}{dt}. \qquad (3)$$

Here ρ is the gas density, C_p is the average specific heat capacitance of gas at the constant pressure, H_i and μ_i are the molar enthalpy and molar mass of *i*-th component, respectively.

The Boltzmann kinetic equation in two-term approximation was solved numerically in order to define the electron energy distribution function (EEDF). The list of electron-molecular process presented in Table 1 was considered during the solution of Boltzmann equation.

Table 1

The processes which were taken into account in EEDF calculations

№	Reaction
1	$H_2O + e \rightarrow H_2O\left((100)+(100)\right) + e$
2	$H_2O + e \rightarrow H_2O(010) + e$
3	$H_2O + e \rightarrow OH + H + e$
4	$H_2O + e \rightarrow H_2O^+ + 2e$
5	$H_2O + e \rightarrow H_2O(J = 0-0) + e$
6	$H_2O + e \rightarrow H_2O(J = 0-1) + e$
7	$H_2O + e \rightarrow H_2O(J = 0-2) + e$
8	$H_2O + e \rightarrow H_2O(J = 0-3) + e$
9	$N_2 + e \rightarrow N_2\left(A^3\Sigma_u^+\right) + e$
10	$N_2 + e \rightarrow N_2\left(a^1\Pi_g\right) + e$
11	$N_2 + e \rightarrow N_2(\nu) + e$
12	$N_2 + e \rightarrow N + N + e$
13	$N_2 + e \rightarrow N_2^+ + 2e$
14	$O_2 + e \rightarrow O + O + e$
15	$O_2 + e \rightarrow O_2\left(^1\Delta_g\right) + e$
16	$O_2 + e \rightarrow O_2^+ + 2e$
17	$C_2H_5OH + e \rightarrow CH_3 + CH_2OH + e$
18	$C_2H_5OH + e \rightarrow C_2H_5 + OH + e$
19	$C_2H_5OH + e \rightarrow CH_3CHOH + H + e$
20	$C_2H_5OH + e \rightarrow C_2H_5OH^+ + 2e$
21	$CO_2 + e \rightarrow CO_2(100) + e$
22	$CO_2 + e \rightarrow CO_2(010) + e$

№	Reaction
23	$CO_2 + e \rightarrow CO_2(001) + e$
24	$CO_2 + e \rightarrow CO + O + e$
25	$CO_2 + e \rightarrow CO_2^+ + e + e$

The EEDF calculated at different values of gas temperature are shown in Fig. 2.

It was obtained that the increase of the rate of CO_2 pumping through the discharge does not influence significantly on EEDF. It is caused by much smaller concentration of CO_2 comparing with the concentration of N_2, i.e., the molecular nitrogen is plasma-forming gas.

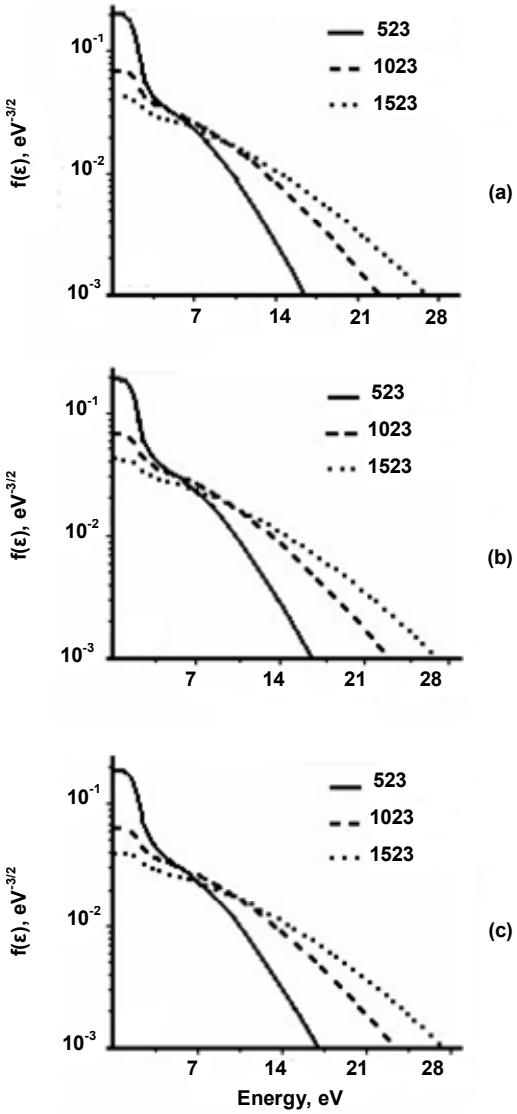

Fig. 2. The EEDF calculated at different gas temperatures; the rate of CO_2 pumping is 4.2 (a), 8.5 (b), 17 (c) cm^3/s

Results and discussion. The comparison between the experimental data and the results of simulations at the reactor outlet showed that the best agreement is reached at T = 1020 K. Fig. 3 shows the comparison between the concentrations of the main gas components at the reactor outlet at the rates of air and CO_2 pumping of 82.5 cm^3/s and 4.25 cm^3/s, respectively. One can see the satisfactory agreement for all species.

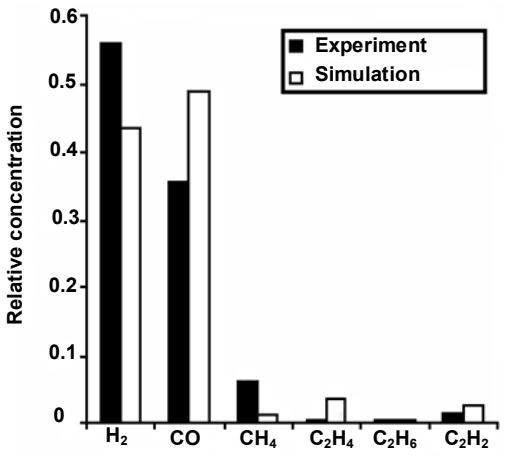

Fig. 3. The relative concentrations of the main components of gas mixture at the reactor outlet; the rate of air pumping is 82.5 cm^3/s, the rate of CO_2 pumping is 4.25 cm^3/s, gas temperature in the discharge region is 1020 K

Fig. 4 shows the influence of the rate of CO_2 pumping on the concentrations of the main components. One can see that this rate influence slightly on the concentrations. During the several microseconds after the discharge start the dissociation of CO_2 by the electron impact is the main channel of CO generation. Later, this process is changed by the reaction $HCO + O_2 > CO + HO_2$, which contribute significantly into CO concentration ([CO]) comparing with the process CO_2 +e > CO+O+e. Moreover, the CO_2 dissociation by the electron impact cannot be considered as a noticeable source of O. The simulations showed that the rate of reaction of O_2 dissociation by the electron impact is two orders of magnitude larger than the rate of CO_2 dissociation. It is caused by two factors. On the one hand, $[O_2]$ is much larger than $[CO_2]$. On the other hand, the energy of O_2 dissociation is smaller than that one of CO_2.

In addition, simulations showed that the main channels of H_2 generation depending on the gas temperature are

t < 4.9μs: Eth+H > $C_2H_5OH + H_2$

t < 0.61ms: $OH_2 + H > H_2 + O_2$,

$CH_3CHO + H > H_2 + CH_3CO$

t < 1.4ms: $H_2O + H > H_2 + OH$,

$CH_3CHO + H > H_2 + CH_3CO$, Eth+H > $C_2H_5OH + H_2$

t < 0.5s Eth+H > $C_2H_5OH + H_2$,

$CH_3CHO + H > H_2 + CH_3CO$

t < 10s: $C_2H_6 + H > C_2H_5 + H_2$,

$H_2O + H > H_2 + OH$, $C_2H_4 + H > C_2H_3 + H_2$

t > 10s: $CH_2O + M > CO + H_2 + M$.

At the same time, the main channels of CO generation are

t < 3.4μs: $CO_2 + e$ > CO+O+e

t < 0.86ms: $CH_3CO + M > CH_3 + CO + M$,

$HCO + O_2 > CO + HO_2$

t < 17.5s: $CH_3CO + M > CH_3 + CO + M$

t > 17.5s: $CH_2O + M > CO + H_2 + M$.

One can see that CO_2 does not influence explicitly on the hydrogen concentration. Also, CO_2 participates in the main

channels of CO generation only during the first microseconds. Later, the generation of CO occurs from the hydrocarbons generated during the discharge. Therefore, $[CO_2]$ has weak influence on the H_2/CO ratio. The latter result is confirmed in experimental research (see Fig. 5). Since CO_2 is used in order to control the ratio H_2/CO in the syn-gas on the reactor outlet, one needs to enhance the role of CO_2 in kinetics of H_2 and CO. It could be reached by the increase of the time of influence of reaction CO_2+e > CO+O+e on [CO]. There are two possible ways, either the decrease of gas temperature or increase of $[CO_2]$.

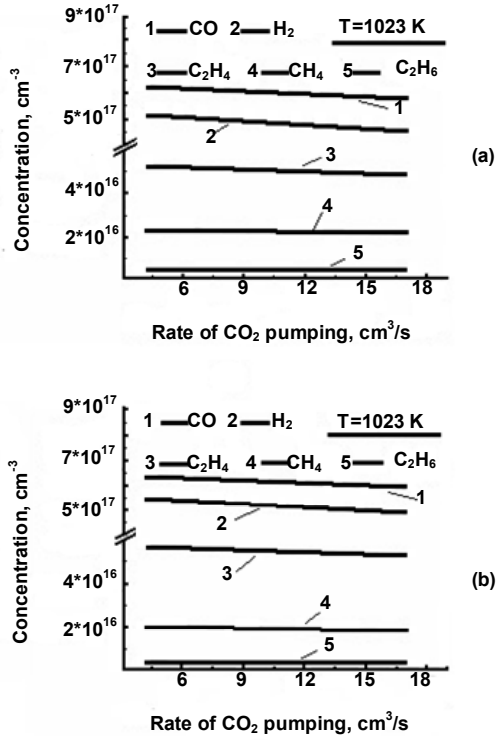

Fig. 4. Concentrations of the main components after the discharge (a) and at the reactor outlet (b) depending on the rate of CO_2 pumping; gas temperature is 1023 K, the rate of air pumping is 82 cm^3/s

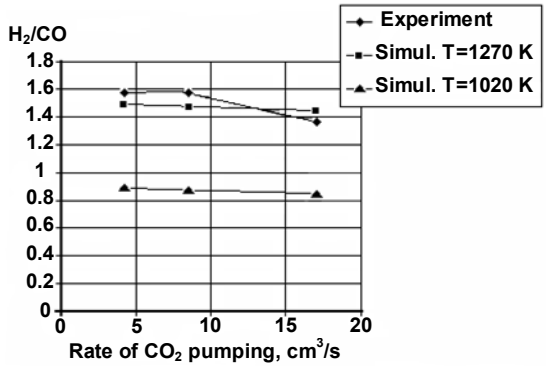

Fig. 5. The dependence of $[H_2]/[CO]$ ratio on the rate of CO_2 pumping.

Conclusions. The numerical simulation of plasma assisted conversion of ethanol in tornado-type electrical discharge was carried out. It was obtained that the concentrations of the main components of syn-gas do not depend significantly on the rate of CO_2 pumping through the discharge. Also, the main channels responsible for the generation of the main components were defined.

The comparison between experimental results and results of simulations showed that the best agreement is reached at gas temperature of 1020 K.

Acnowledgements. This work was partially supported by the State fund for fundamental researches (Grant F41.1/014), Ministry of Education and Science of Ukraine, National Academy of Sciences of Ukraine

Reference

Chernyak V., Olszewskii S., Nedybalyuk O. et al. Non-Thermal Plasma Assisted Reforming of Ethanol in Dynamic Plasma-Liquid Systems // J. Energy and Power Eng. 2011. Vol. 5. P. 403–410. 2. Kalra C., Gutsol A. and Fridman A. // IEEE Trans. Plasma Sci. 2005. Vol. 33. P. 32. 3. Levko D.S., Shchedrin A.I., Chernyak V.Ya., Ol'shevskiĭ S.V., Nedybalyuk O.A. Obtaining molecular hydrogen in electric discharge of the tornado type in air mixture with ethanol and water vapors // Technical Physics Letters. 2010. Vol: 36. Issue. 11. P. 998–1000. 4. Levko D., Shchedrin A., Chernyak V., Olszewski S., and Nedybaliuk O. Plasma kinetics in ethanol/water/air mixture in a 'tornado'-type electrical discharge // J. Phys. D: Appl. Phys. 2011. Vol. 44. P. 145–206. 5. Lieuwen T.C., Yang V., Yetter R. Synthesis gas combustion// New York: Taylor & Francis Group, 2009. 6. Nedybaliuk O.A., Chernyak V.Ya., Olszewski S.V. Plasma-Liquid System With Reverse Vortex Flow of "TORNADO" Type (TORNADO-LE) // Problems of Atomic Science and Technology. 2010. Vol. 6. P. 135–137. 7. Petitpas G., Rollier J.D., Darmon A., et al // Int. J. Hydrogen Energy. 2007. Vol. 32. P. 2848–2867.

Submitted 04.12.12

О. Цимбалюк, мол. наук. співроб., Східноукраїнський національний університет імені Володимира Даля, Луганськ, Д. Левко, канд. фіз.-мат. наук, пост-док, Університет Поля Сабатьє, Тулуза, Франція, В. Черняк, д-р фіз.-мат. наук, каф. фізичної електроніки, Є. Мартиш, д-р фіз.-мат. наук, каф. медичної радіофізики, О. Недибалюк, канд. фіз.-мат. наук, О. Соломенко, асп., каф. фізичної електроніки, радіофізичний факультет, КНУ імені Тараса Шевченка, Київ

ВПЛИВ КОНЦЕНТРАЦІЇ CO_2 У ГАЗОВІЙ СУМІШІ НА ЕФЕКТИВНІСТЬ ОДЕРЖАННЯ СИНТЕЗ-ГАЗУ З ЕТАНОЛУ В НЕРІВНОВАЖНІЙ ПЛАЗМІ

У роботі представлені результати дослідження впливу концентрації CO_2 на склад синтез-газу при плазмохімічній конверсії етанолу в розряді типу "торнадо". Порівняння результатів моделювання з експериментальними даними показало хорошу відповідність запропонованої чисельної моделі. Показано, що концентрації основних компонентів газової суміші слабо залежать від швидкості прокачування CO_2 через область розряду.

Ключові слова: плазма, моделювання, синтез-газ, електричний розряд, плазмохімічна конверсія.

О. Цымбалюк, мл. науч. сотр., Восточноукраинский национальный университет имени Владимира Даля, Луганск, Д. Левко, канд. физ.-мат. наук, пост-док, Университет Поля Сабатье, Тулуза, Франция, В. Черняк, д-р физ.-мат. наук, каф. физической электроники, Е. Мартыш, д-р физ.-мат. наук, каф. медицинской радиофизики, О. Недыбалюк, канд. физ.-мат. наук, Е. Соломенко, асп., каф. физической электроники, радиофизический факультет, КНУ имени Тараса Шевченко, Киев

ВЛИЯНИЕ КОНЦЕНТРАЦИИ CO_2 В ГАЗОВОЙ СМЕСИ НА ЭФФЕКТИВНОСТЬ ПОЛУЧЕНИЯ СИНТЕЗ-ГАЗА ИЗ ЭТАНОЛА В НЕРАВНОВЕСНОЙ ПЛАЗМЕ

В работе представлены результаты исследования влияния концентрации CO_2 на состав синтез-газа при плазмохимической конверсии этанола в разряде типа "торнадо". Сравнение результатов моделирования с экспериментальными данными показало хорошее соответствие предложенной численной модели. Показано, что концентрации основных компонентов газовой смеси слабо зависят от скорости прокачки CO_2 через область разряда.

Ключевые слова: плазма, моделирование, синтез-газ, электрический разряд, плазмохимическая конверсия.

UDC 537.8

V. Chorniy, stud., O. Nechyporuk, Ph. D., S. Skripka, Ph. D., V. Danilov, Dr. Sc.
Department Quantum radiophysics, Faculty of Radiophysics, Taras Shevchenko National University of Kyiv

ELECTROMAGNETIC SIMULATION OF SPLIT RING RESONATORS IN KA-BAND

We consider artificial materials where possible to achieve the negative values of effective magnetic permitivity in the Ka-band wavelengths of electromagnetic radiation ((26.5–40) GHz). Using electromagnetic modeling the parameters of the double ring resonators are defined.

Key words: split ring resonators, metamaterials, Ka-band.

Introduction. In some artificial structures possible to achieve negative values of effective permeability or permittivity (or both) in finite frequency band. These materials are called metamaterials [2; 5; 8]. The best-known examples of media with negative permittivity are low-loss plasmas, and metals and semiconductors at optical and infrared frequencies; media with negative permeability are ferrimagnetic materials near the ferrimagnetic resonance. But the subject of our investigation is the split ring resonators (SRR). These artificial structures represent the metallic strips, coated on the dielectric substrate. In the 19th century W. Weber formulated the first theory of diamagnetism, discovered by Faraday. He assumed the existance of closed circuits at the molecular scale, and invoked Faraday's law to prove that currents would be induced in these circuits when they were under the effect of an external time-varying magnetic field. As the secondary magnetic flux created by such currents would be opposite to that created by the external field. However, the diamagnetic effect associated with a closed metallic ring is not strong enough to produce negative values for μ. But, when add capacitance C to the inductance of the ring L, we will see that polarizability becomes negative above the frequency of resonance $\omega_0 = 1/\sqrt{LC}$. Some types of the SRR are represented in Fig. 1.

SRR has many design solutions [2; 8]. Each has its own special features and it defines their area of practical use. Very important characteristics are resonant frequency, width of the resonance band, magnitude of losses in the band and beyond and, of course, ease of fabrication. SRR are used to hide the object from external radiation, as filters, in the media with negative refractive index. We decided conduct research in Ka-band, because in this band work many radars.

The aim of this work is to find the parameters of SRR using electromagnetic simulation.

Simulation method. To calculate the geometric dimensions can use the following methods: equivalent circuit model [1; 7] and electromagnetic simulation.

The first method is that the resonator substitutes an equivalent electric circuit. Parameters such as inductance, capacitance and resistances are calculated. After, they determine a resonant frequency. This method is relatively simple. But this method has the error of determination of the resonance frequency, which is 10 percent or more. In Ka-band these error may be crucial.

We decided to use electromagnetic simulation. Electromagnetic simulation uses Maxwell's equations to determine the characteristics of a given device to his physical geometry. Using electromagnetic simulation to analyze arbitrary structure and provide very accurate results. In addition, electromagnetic simulation free from the restrictions that exist in models of electric circuits as well as using the fundamental equation for calculating characteristics. The disadvantage of this simulation is that depending on the complexity of the structure increases the required amount of memory and simulation time increases exponentially. Therefore it is important to minimize the complexity of the structure to the simulation was acceptable.

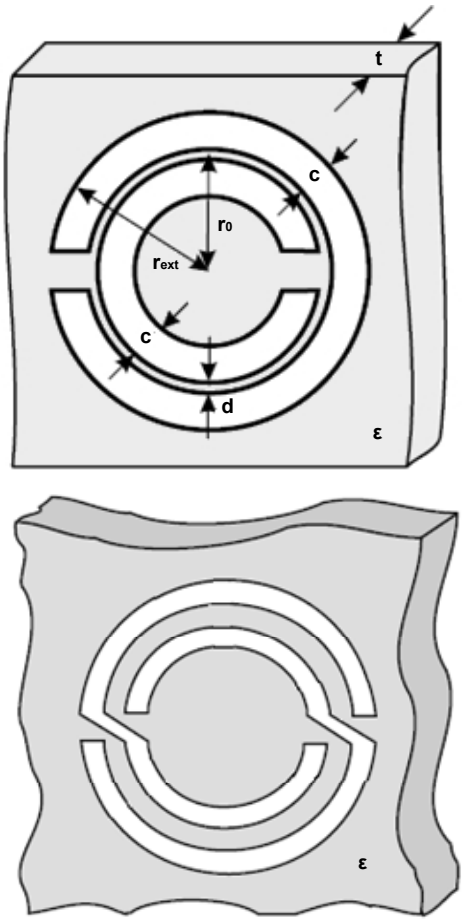

Fig. 1. Schematics of SRR elements: upper structure – edge coupled (EC-SRR), lower structure – nonbianisotropic (NB-SRR). For EC-SRR: r_{ext} – large ring resonator radius, r_0 – inner ring resonator radius, c– resonators metal strip width, d – distance between the rings, t – thickness of the structure, ε – permittivity of the substrate. Metallization are in white and dielectric substrate in gray

Electromagnetic simulation uses the Galerkin method of moments in the spectral region, which is very accurate for the analysis of strip, microstrip, coplanar, and many other random structures. This technique provides accurate simulation results up to 100 GHz or higher.

Results and discussion. The first structure that was simulated was EC-SRR (see Fig. 1, upper structure). As the dielectric substrate used duroid 5880 with ε = 2.2, losses tg δ = 0.0009, thickness t = 0.125 mm, rings are copper with thickness h = 17 μm. As a result of simulation were obtained the following parameters for the EC-SRR: external radius r_{ext} = 0.6 mm, outer radius r_0 = 0.4 mm, width of the rings c = 0.1 mm, distance between the rings d = 0.2 mm. The resonance curve is shown in Fig. 2.

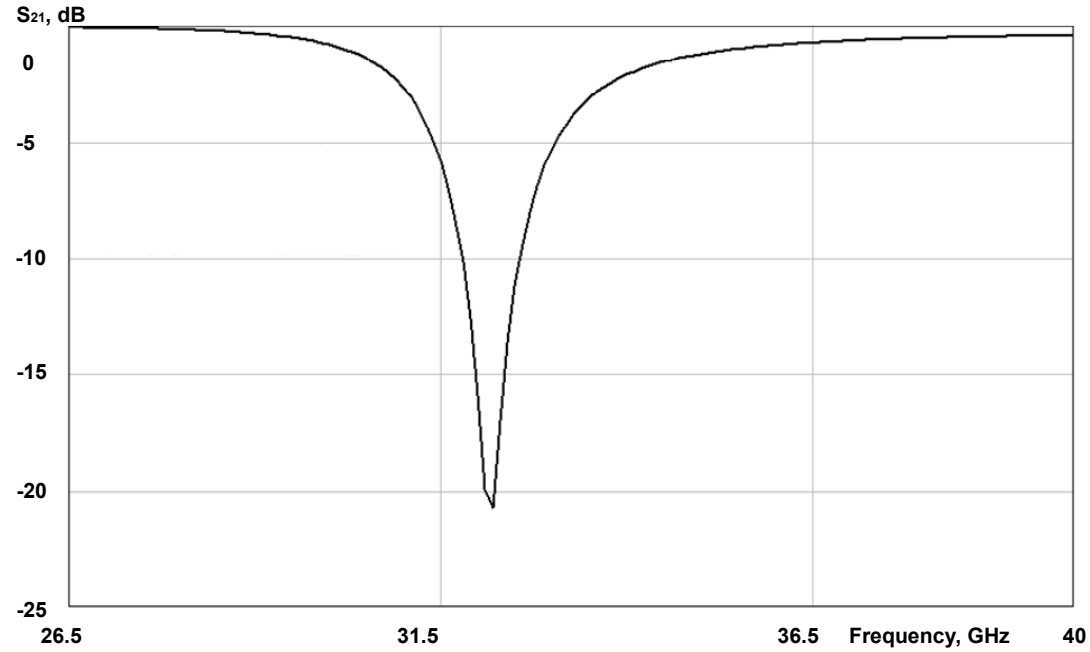

Fig. 2. Resonance curve for EC-SRR

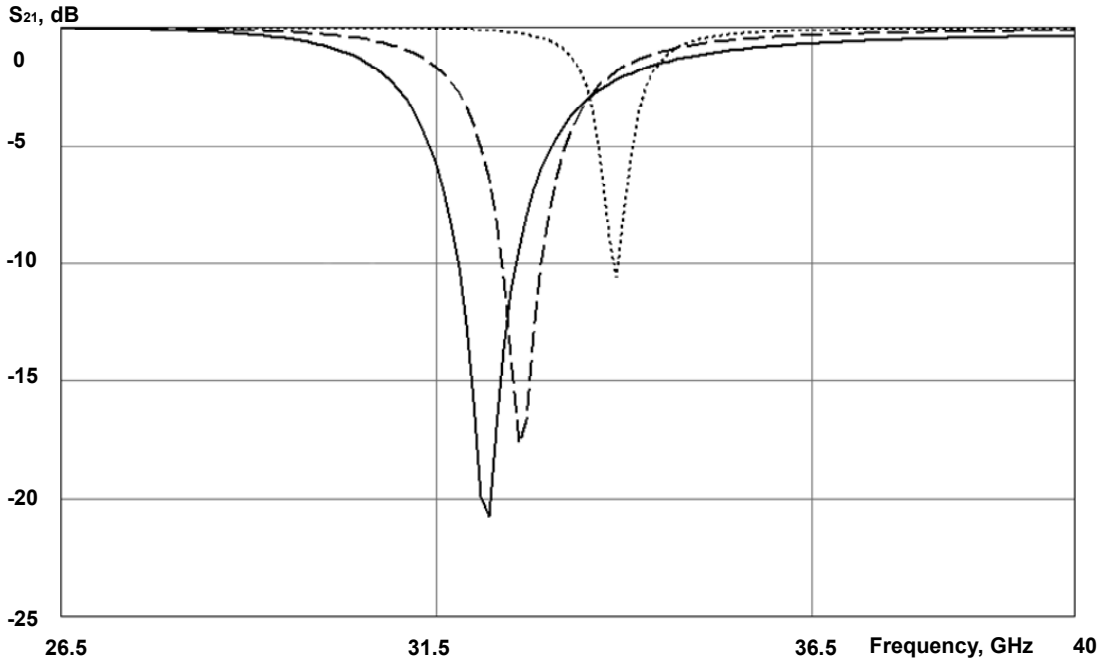

Fig. 3. Demonstration of cross-polarization effects in EC-SRR. Solid line corresponds to the electric and magnetic excitation, small dashed – magnetic, dashed – intermediate variant

From this graph we can determine the resonant frequency f_0 = 32.2 GHz, the width of the resonance curve (at the -3 dB level) Δf = 2.43 GHz, loss at the resonant frequency L_0 = -20.73 dB. EC-SRR has cross-polarization properties. This means that when you change the orientation of the structure will change the resonance curve. This is because not diagonal cross polarization tensor components are not zero. In other words, this type of resonators can excite not only the alternating magnetic field perpendicular to the plane of the rings, but the electric field that is parallel to the gap in the rings. This effect is shown in Fig. 3.

This effect is also observed experimentally, but in the range of 2 to 4 GHz. Results are shown in Fig. 4. Experimental investigations were performed by using analyzer of standing wave ratio and attenuation, open strip-line waveguide and generator with microwave block. In experiment used metastructures with different number of SRR and different size parameters.

Next type SRR was broadside-coupled SRR (BC-SRR) (see Fig. 5).

BC-SRR represents the two rings, coated on both sides of the dielectric substrate. This type of resonator is free of cross polarization effects. This is because the BC-SRR has mirror symmetry [2; 3]. As a result of simulation were obtained the following parameters for the BC-SRR: external radius r_{ext} = 0.5 mm, width of the rings c = 0.25 mm. The resonance curve is shown in Fig. 6.

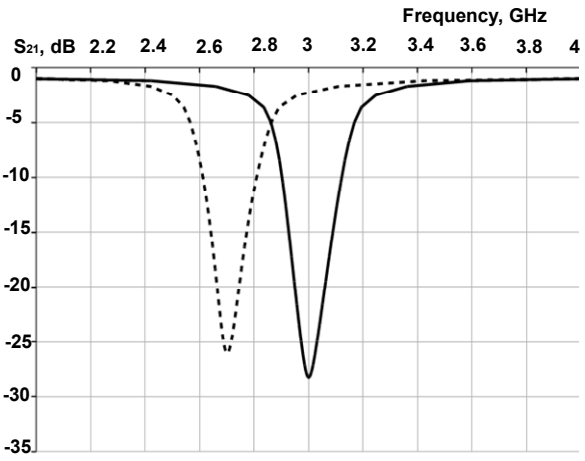

Fig. 4. Frequency response for metastructure that consists of eight EC-SRR for different orientation on strip-line waveguide. Dashed line – structure turned on 180^0

BC-SRR represents the two rings, coated on both sides of the dielectric substrate. This type of resonator is free of cross polarization effects. This is because the BC-SRR has mirror symmetry [2; 3]. As a result of simulation were obtained the following parameters for the BC-SRR: external radius r_{ext} = 0.5 mm, width of the rings c = 0.25 mm. The resonance curve is shown in Fig. 6.

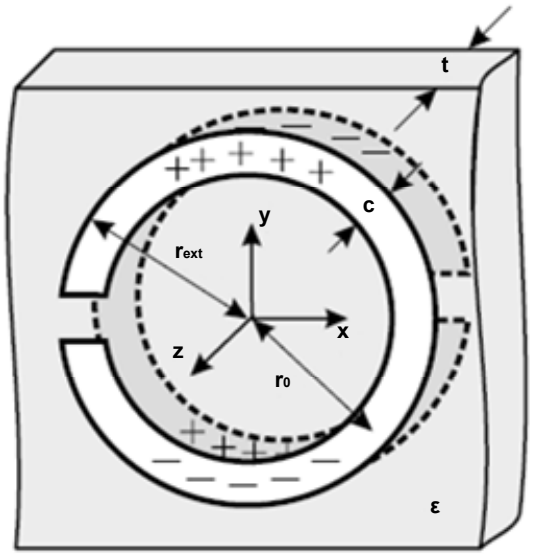

Fig. 5. Broadside-coupled SRR. r_{ext} – external radius of the ring, r_0 – inner ring resonator radius, c– resonators metal strip width, t – thickness of the structure, ε – permittivity of the substrate. Metallization are in white and dielectric substrate in gray

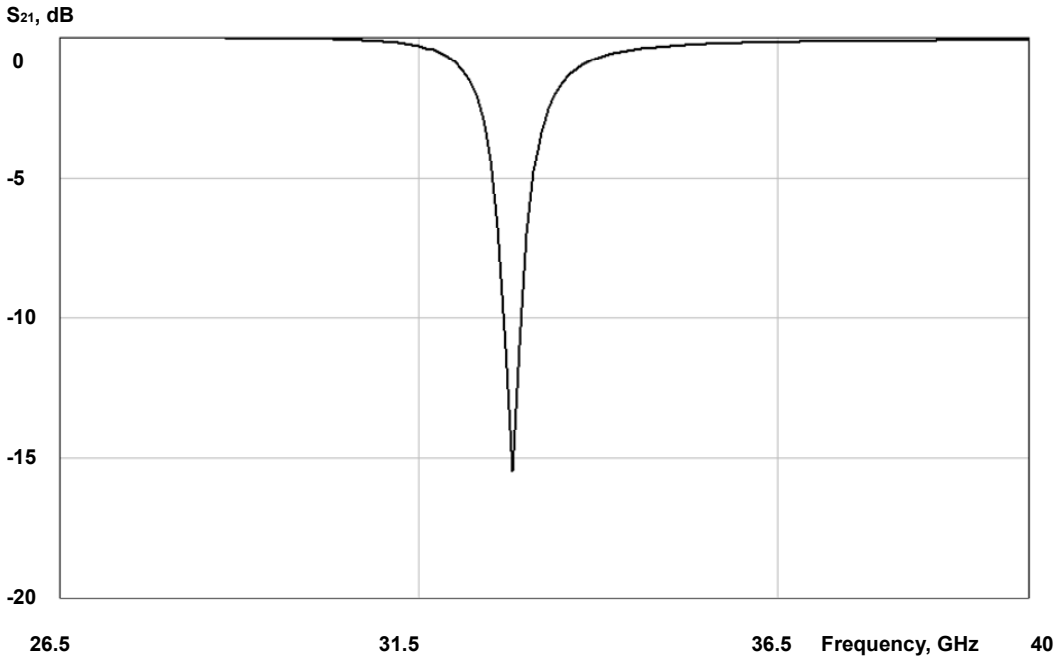

Fig. 6. Resonance curve for BC-SRR

From this graph we can determine the resonant frequency f_0 = 32.8 GHz, the width of the resonance curve (at the -3 dB level) Δf = 0.83 GHz, loss at the resonant frequency L_0 = -15.48 dB. As the band radars are operating frequencies up to several GHz, the main disadvantage of this type of SRR can be considered narrow band resonance curve.

Was drawn attention to the SRR with rectangular geometry (see Fig. 7), are well established in the manufacture of structures for hiding objects from the probing radiation [6]. Such resonators are relatively simple to manufacture. And by slight variations of length s and radius r can be obtained gradient changes the effective value of the relative permeability, if you create an environment that consist of layers which in turn consist of cells with this resonators.

As a result of simulation were obtained the following parameters for the rectangular SRR: length l = 1 mm, width of the rings w = 0.15 mm, length s = 0.25 mm. The resonance curve is shown in Fig. 8.

From this graph we can determine the resonant frequency f_0 = 30.9 GHz, the width of the resonance curve (at the -3 dB level) Δf = 1.45 GHz, loss at the resonant frequency L_0 = -18.79 dB. This type SRR has a good resonance width, but it also contains cross polarization effects. But the main advantage of such structures is the relative ease of fabrication.

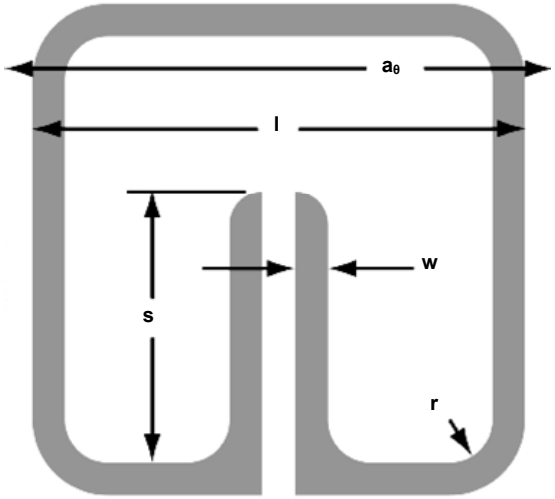

Fig. 7. SRR with rectangular geometry. Metallization are in gray and dielectric substrate in white: a_0 – cell size, r – radius, l – length of the resonator, w – resonators metal strip width, s – length

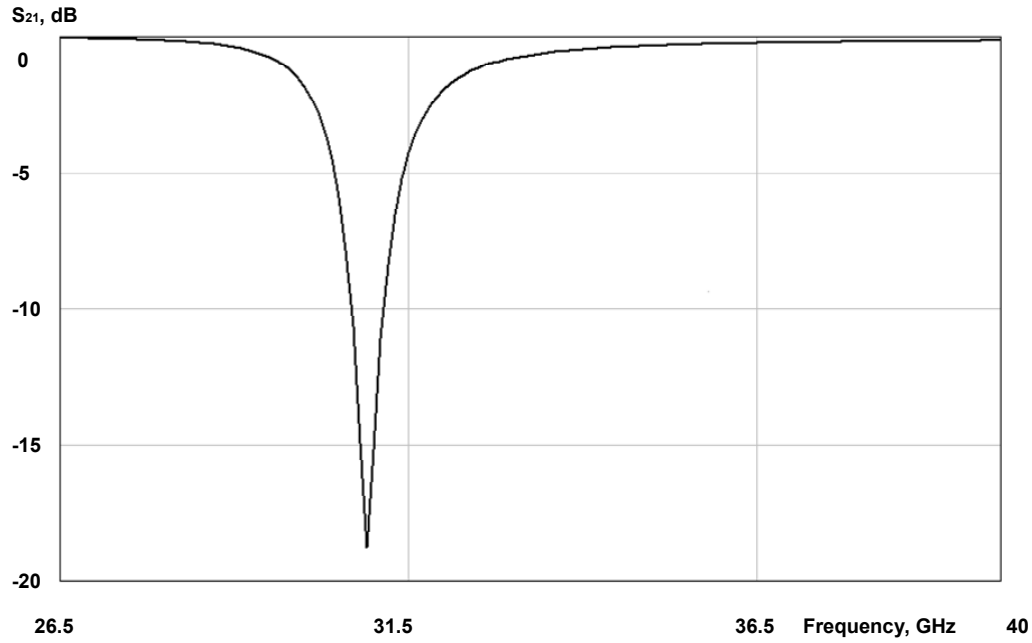

Fig. 8. Resonance curve for rectangular SRR

Conclusion. Were considered and modeled different types of structures, which may receive negative effective permeability. It was found that different types of split ring resonators have as advantages and disadvantages. This is due to the geometry of the structure. These calculated parameters are fit to make based on these resonators. The most promising are rectangular SRR. Their geometry is relatively easier in the long run the transition to optical range is a very important argument in their favor. Also, they have a rather broad resonance band. Varying length s and radius r can change the value of the effective magnetic susceptibility in sufficient range to create a gradient refractive index that probe radiation will bend around the object you want to hide.

Reference

1. Bilotti F., Toscano A., Vegni L., Aydin K., Alici K.B., and Ozbay E., Equivalent-circuit models for the design of metamaterials based on artificial magnetic inclusions // IEEE Trans. Microwave Theory Tech. – 2007. – Vol. 55, No. 12, 2865–2873. 2. Marques R., Martin F., Sorolla M. Metamaterials with negative parameters. Theory, design, and microwave applications. // Wiley-interscience. – 2007. – vol. 315. 3. Marques R., Medina F., and Rafii-El-Idrissi R. Role of bianisotropy in negative permeability and left-handed metamaterials // Phys. Rev. B. – 2002. – Vol. 65, 14440(1)–14440(6). 4. Marques, R., Mesa F., Martel J. and Medina F. Comparative analysis of edge- and broadside-coupled split ring resonators for metamaterial design-theory and experiments // IEEE Trans. Antennas Propag. – 2003. – Vol. 51, No. 10, 2572–2581. 5. Pendryy J.B., Holden A.J., Robbins D.J., Stewart W.J. Low frequency plasmons in thin-wire structures // J. Phys. – 1998. – p. 4785–4809. 6. Schurig D., Mock J.J., Justice B.J., Cummer S.A., Pendry J.B., Starr A.F., Smith D.R. Metamaterial Electromagnetic Cloak at Microwave Frequencies // SciencExpress. – 2006. – 8 p., 10.1126/science.1133628. 7. Shamonin M., Shamonina E., Kalinin V., and Solymar L. Resonant frequencies of a splitring resonator: analytical solutions and numerical simulations // Microwave Opt. Tech. Lett. – 2005. – vol. 44, pp. 133–137. 8. Solymar L., Shamonina E. Waves in metamaterials // Oxford University Press. – 2009. – vol. 420.

Submitted on 06.03.13

В. Чорний, студ., О. Нечипорук, канд. фіз.-мат.наук,
С. Скрипка, канд. фіз.-мат. наук, В. Данилов, д-р фіз.-мат. наук,
каф. квантової радіофізики, радіофізичний факультет, КНУ імені Тараса Шевченка, Київ

ЕЛЕКТРОМАГНІТНЕ МОДЕЛЮВАННЯ ПАРАМЕТРІВ ПОДВІЙНИХ КІЛЬЦЕВИХ РЕЗОНАТОРІВ В КА-ДІАПАЗОНІ

В роботі розглянуто штучні матеріали, в яких можливе досягнення негативного значення ефективної магнітної сприйнятливості в Ка-діапазоні довжин хвиль електромагнітного випромінювання ((26.5–40) ГГц). За допомогою електромагнітного моделювання визначено параметри подвійних кільцевих резонаторів.

Ключові слова: подвійні кільцеві резонатори, метаматеріали, Ка-діапазон.

В. Черный, студ., О. Нечипорук, канд. физ.-мат. наук,
С. Скрипка, канд. физ.-мат. наук, В. Данилов, д-р физ.-мат. наук,
каф. квантовой радиофизики, радиофизический факультет, КНУ имени Тараса Шевченка, Киев

ЭЛЕКТРОМАГНИТНОЕ МОДЕЛИРОВАНИЕ ДВОЙНЫХ КОЛЬЦЕВЫХ РЕЗОНАТОРОВ В КА-ДИАПАЗОНЕ

В работе рассмотрены искусственные материалы, в которых возможно достижение негативного значения эффективной магнитной восприимчивости в Ка-диапазоне длин волн электромагнитного излучения ((26.5–40) ГГц). При помощи электромагнитного моделирования определены параметры двойных кольцевых резонаторов.

Ключевые слова: двойные кольцевые резонаторы, метаматериалы, Ка-диапазон.

UDC 577.3

R. Yatsiuk, post grad. stud., M. Kononov, PhD,
Radiophysical department, Taras Shevchenko National University of Kyiv

DEPENDENCE OF SYNCHRONIZATION COEFFICIENT CHANGING FROM IZIKEVICH MODEL RECOVERY PARAMETERS IN CORTICAL COLUMN NEURONS FOR ASCENDING INFORMATION FLOW

The paper considers the synchronization of neurons in cortical column with complex dynamics for ascending information flow. Graphics of the synchronization coefficient dependence from different variations of Izhikevich model recovery parameters were constructed. For visual study of synchronization the raster plots were constructed and corresponding diagrams were plotted for the opportunity to compare the synchronization coefficient on different layers of cortical column.

Keywords: synchronization coefficient in cortical column, ascending information flow, raster plot.

Problem statement. Converting signals and transmission of information in the nervous system are of interest to researchers applied various specialties, such as biophysics, neurophysiology, medical informatics. Launched more than half a century ago a description of oscillatory processes in neural networks evolved from logical calculations and evaluation of information capacity to the theory of information flow concepts and synchronization of neural activity of the cerebral cortex. [8]. Highly relevant research directions of modern science is to discover the principles of representation and transformation of information in the human brain, depending on the architecture of its neural networks. Due to the complexity of setting real experiments, significant role in this process is played by model studies by building computer models of neural networks. [3]

Analysis of recent researches and publications. The study of cognitive functions of the human brain is one of the leading trends in modern neurobiology, neurophysiology and neuropsychology. One of the approaches to the study of the processes occurring in such a system is the use of dynamic models of neural networks of the brain [7].The basic structural and functional unit of the cerebral cortex is a cortical column. This term was first used by Economo [6] to describe the vertically arranged rows of neurons that are linked predominantly with vertical connections.

Various experimental studies showed that the count of neurons in the vertical chain of neural cells is 110. [4] This chain has a diameter of about 30 microns. The cortex of the human brain consists of six different layers, each of which can be identified by the type of neurons that are in it.

Synchronous neuronal discharges are recorded in various brain structures (thalamus, sensory systems, central olfactory cortex and neocortex), they play a key role in the perception, selective attention and working memory. Synchronous neuronal activity supports the coordination of the locomotors system. Synchronization – is a mechanism that provides life rhythms like breathing. But also the presence of synchronization can be a sign of pathological abnormalities. [5] For example, one of the symptoms in patients with schizophrenia is disordering of the mechanism of generation synchronous oscillations. [9]

The purpose of article. In this work it is investigated the synchronization of neural networks with the architecture of communications for ascending information flow in which the neuron is described by the Izhykevych model. The change of the coefficient of synchronization based on changes in neural activity from recovery model parameters in cortical column is investigated.

Results and discussions. It was investigated the homogeneous neural structure, i.e. a network in which all elements are identical and have the same neural connections. All the studied neural systems are fully connected, i.e. those in which each element of the next layer take synaptic current from all the neural elements of the previous layer structure and connected to all neurons in a layer. The highest, the first layer contains few cells and consists mainly of a set of axons. In our work on the first layer of cortical column there are 9 neurons. The second and third layers look almost the same, and are have both 11 neurons. The fourth layer consist of 15 neurons, and the fifth consist of 17. The sixth layer is the deepest, and is different from all others, it has the largest number of neurons in this study – 47 neural elements (Fig. 1).

To describe the neural element for such morphology network the mathematic neural model of Izhykevych was used. It is two-compartment model that contains an additional requirement for cell membrane discharge:

$$\frac{dv}{dt} = 0.04v^2 + 5v + 140 - u + I\ ,\ \frac{du}{dt} = a(bv - u),$$

$$v \leftarrow c, u \leftarrow u + d\ ,\ \text{if v>=30 mV},$$

where v and u are the dimensionless membrane potential and membrane potential recovery variables respectively; *a, b, c and d* – dimensionless parameters. The variable u simulates the activation of ionic K^+ currents and the

deactivation of ionic Na^+ currents and provides negative feedback to *v*. Variable *I* simulates external currents.

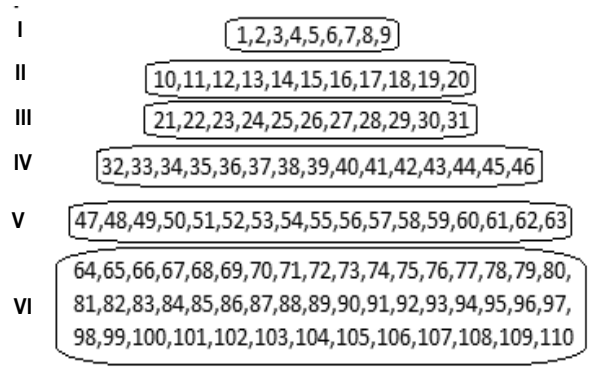

Fig. 1.The hierarchical structure of investigated network

Various choices of the parameters result in various intrinsic firing patterns, including those exhibited by the known types of neocortical and thalamic neurons [1].

Since we are interested in the question of synchronization of different modes of neural activity, as in the present study, we investigated the dependence of the synchronization coefficient changes on recovery model parameters in the cortical column.

Let us consider ascending information flow, which has a relatively direct route displayed in Fig. 2. Information from the lower column always comes in the fourth layer - the main input layer. Then the cells of the fourth layer send projections up to the second and third layer inside the column, and then these layers are submitted to the input layer synapses of higher areas. In this way the information flows from area to area up to the hierarchy. [4]

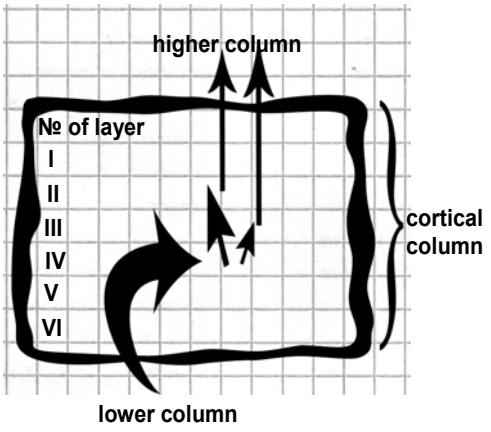

Fig. 2. The ascending information flow

From [2] the parameter *a* describes the time scale of the recovery variable *u*. Smaller values result in slower recovery. A typical value is *a=0.02*. It was investigated the change in the coefficient of synchronization depending on the parameter a, for the whole cortical column (Fig. 3) and for each of its layers (Fig. 4).

From *fig. 3* we can see that the maximum value of synchronization coefficient reaches on *a=0.03* and puts *k=0.26*. As for the layer synchronization, we can see that on almost each layer the maximum value of synchronization coefficient reaches on *a*=0.001, but general synchronization coefficient only is *k=0.206*. From *fig. 4* we can see that at the fourth layer on any values of parameter *a* the synchronization coefficient is bigger than on other layers of cortical structure. The reason of this is that the fourth layer is the input layer; it gets an applied synaptic current which flows from lower cortical regions. For parameter value *a=0.03* it was constructed the raster plot for ascending information flow in the cortical column (*fig. 5*). Neural dynamics looks like *mix mode - intrinsically bursting with chattering (fig. 6)*.

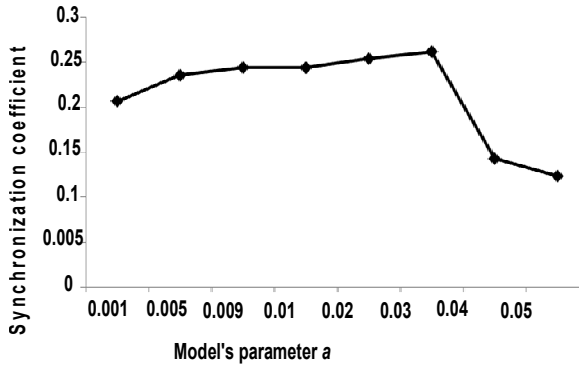

Fig. 3. Dependence of synchronization coefficient from parameter a

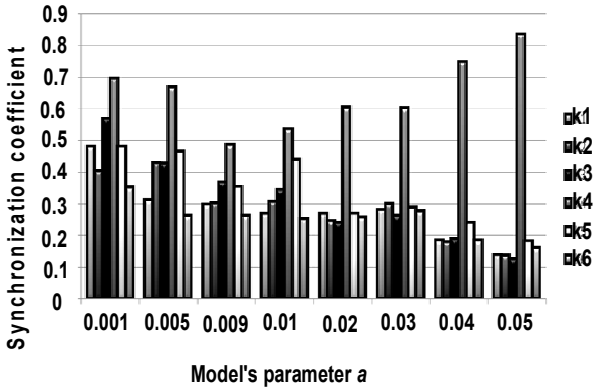

Fig. 4. Layer dependence of synchronization coefficient from parameter a

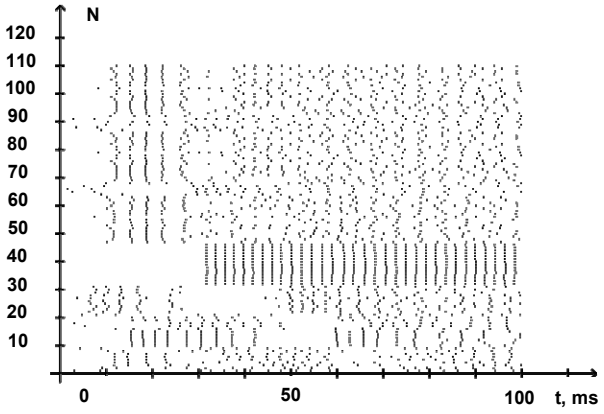

Fig. 5. The raster plot for a=0.03

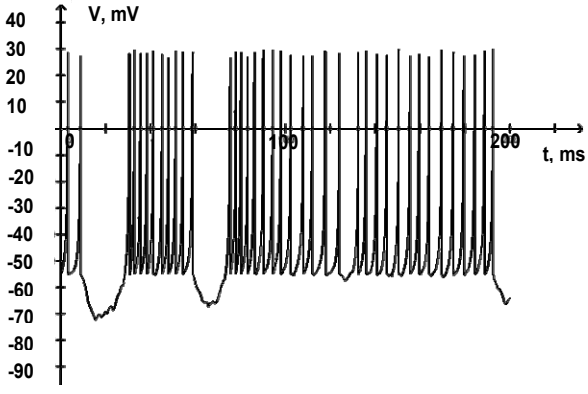

Fig. 6. Neural dynamics for a=0.03

From [2] the parameter *b* describes the sensitivity of the recovery variable *u* to the subthreshold fluctuations of the membrane potential *v*. Greater values couple *v* and *u* more strongly resulting in possible subthreshold oscillations and low-threshold spiking dynamics. A typical value is *b=0.2.* It was investigated the synchronization coefficient changes dependent on changes of parameter *b* for the whole cortical column (*fig. 7)*, also the diagram of layer dependence of synchronization coefficient from parameter *b* was constructed (*fig. 8*).

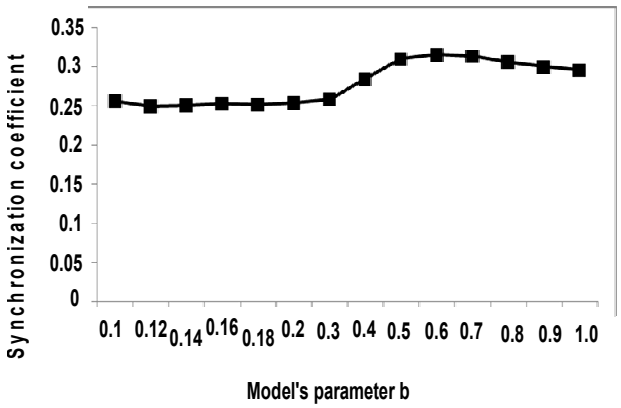

Fig. 7. Dependence of synchronization coefficient from parameter b

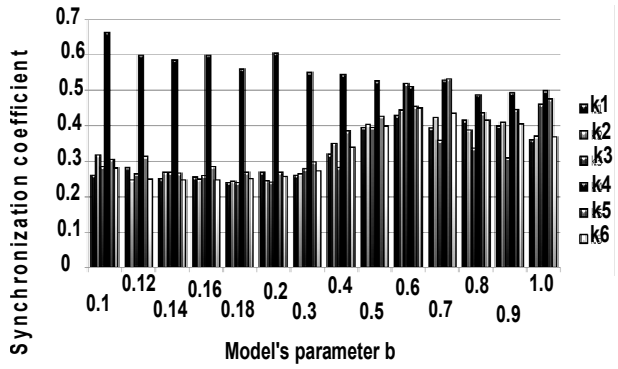

Fig. 8. Layer dependence of synchronization coefficient from parameter b

From *fig. 7* we can see that the synchronization coefficient changes very fluently during varying parameter *b*, values are oscillating at level of *5%*. The maximum value of synchronization coefficient reaches on *b=0.6* and puts *k=0.315*. If analyze the diagram *(fig. 8),* we can see that the situation is the same, except the fourth layer, that is the input layer and it has own dynamics of synchronization coefficient changes, but it doesn't influence on the whole picture. For *b=0.6* it was constructed the raster plot for ascending information flow in the cortical column (*fig. 9*). Neural dynamics looks like *intrinsically bursting* (*fig. 10*).

Conclusions. By experiment we get that synchronous regimes arise during variation of Izhikevich model recovery parameters. Researches of synchronization coefficient dependence on changing these parameters showed:

- neurons activity in the cortical column model is changed from the first to the sixth layer;
- the synchronization coefficient reaches its maximum at:
  - on the parameter value *a=0.03* the synchronization coefficient *k=0.26*;
  - on the parameter value *b=0.6* the synchronization coefficient *k=0.315*;
  - the minimal synchronization coefficient is at the parameter *a*, and the maximal value of the synchronization coefficient is at the parameter *b*.

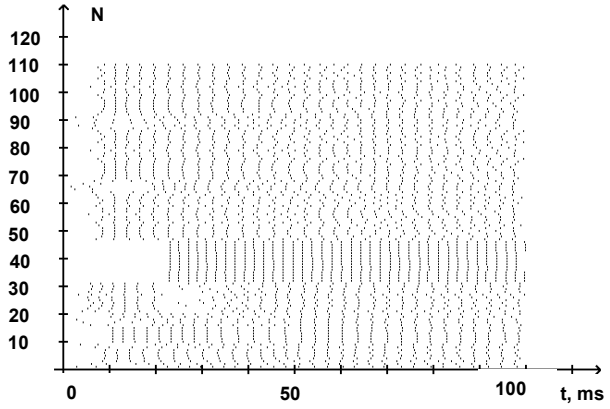

Fig. 9. The raster plot for b=0.6

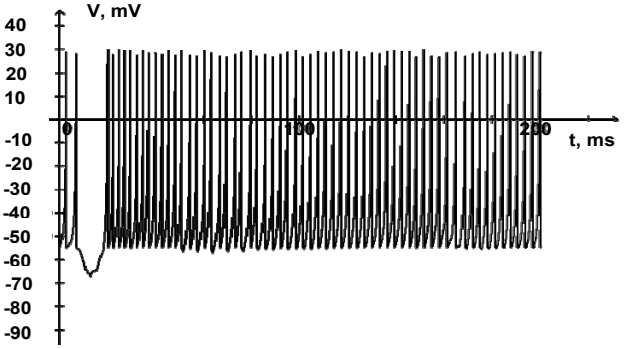

Fig. 10. Neural dynamics for b=0.6

Reference

1. Connors B.W. and Gutnick M.J., "Intrinsic firing patterns of diverseneocortical neurons,"Trends in Neurosci. , vol. 13, pp. 99–104, 1990. 2. Izhikevich E. M. Simple model of spiking neurons //IEEE Transactions on Neural Networks. – 2003. – 14, №6. – P. 1569–1572. 3. Kochubej S. A.. Osobennostu rascheta koefficienta sinhronizacii nejronnyh setej // Visnyk Dnipropetrovskogo universytetu. Biologija. Ekologija. – 2009. – Vyp. 17, t. 2. – P. 55–62. 4. Mauntkasl V., Organizujuschij princip funkcii mozga: elementarnyj modul i raspredelennaja sistema // Edelman Dz., Mauntkasl V. Razumnyj mozg. – M.: Mir, 1981. 5. Osipov G. V. Sinhronizacija pri obrabotke i peredache informacii v nejronnyh setjah. Uchebno-metodicheskie materialy po programme povyshenija kvalifikacii "Hranenie i obrabotka informacii v biologicheskih sistemah". Nizhnij Novgorod, 2007. 99s. 6. Petrov A. M., Giniatullin A., R. Nejrobiologija sna: sovremennyj vzgljad. Uchebnoe posobie, Kazan: KGMU, 2012 – 109 P. 7. Rabinovich M., Varona P., Selverston A., Abarbanel H.. Dynamical principles in neuroscience // Review of modern physics. 2006. Vol. 78. P. 1213. 8. Romanov S. P. Kolcevye svjazi v nejronnyh strukturah i sinhronizacija kak indicator ih patologicheskogo sostojanija. // Nauchnaja sessija MIFI – 2002. Ch. 1 Nejroinformatika – 2002. 4 – ja Vserosijskaja nauchno-tehnicheskaja konferencia. Obschie voprosi nejroinformatiki. Obrabotka izobrazhenij I zvuka. Nejrobiologija. Modeli pamjati. Obrabotka vremennyh rjadov. Kletochnye nejronnye seti, P. 126–133. 9. Vierling-Claassen D. Modeling gaba alterations in schizophrenia: a link between impaired inhibition and altered gamma and beta range auditory entrainment // J. Neurophysiol. – 2008. – Vol. 99, N 5. – P. 2656–2671.

Submitted on 21.05.13

**Р. Яцюк, асп., М. Кононов, канд. фіз.-мат. наук, каф. медичної радіофізики,
радіофізичний факультет, КНУ імені Тараса Шевченка, Київ**

ЗАЛЕЖНІСТЬ ЗМІНИ КОЕФІЦІЄНТУ СИНХРОНІЗАЦІЇ ВІД ВІДНОВЛЮЮЧИХ ПАРАМЕТРІВ МОДЕЛІ ІЖИКЕВИЧА У КОРТИКАЛЬНІЙ КОЛОНЦІ НЕЙРОНІВ ДЛЯ ВИСХІДНОГО ІНФОРМАЦІЙНОГО ПОТОКУ

У роботі розглянуто синхронізацію нейронів кортикальної колонки із складною динамікою для висхідного інформаційного потоку. Залежність коефіцієнту синхронізації від різних варіацій відновлювальних параметрів моделі Іжикевича показано на графіках. Для візуальної оцінки синхронізації було побудовано растрограми та для можливості порівняння коефіцієнту синхронізації на кожному шарі кортикальної колонки побудовано відповідні діаграми.

Ключові слова: коефіцієнт синхронізації у кортикальній колонці, висхідний інформаційний потік, растрограма.

**Р. Яцюк, асп., М. Кононов, канд. физ.-мат. наук, каф. медицинской радиофизики,
радиофизический факультет, КНУ имени Тараса Шевченка, Киев**

ЗАВИСИМОСТЬ ИЗМЕНЕНИЯ КОЭФИЦИЕНТА СИНХРОНИЗАЦИИ ОТ ПАРАМЕТРОВ ВОССТАНОВЛЕНИЯ МОДЕЛИ ИЖИКЕВИЧА В КОРТИКАЛЬНОЙ КОЛОНКЕ НЕЙРОНОВ ДЛЯ ВОСХОДЯЩЕГО ИНФОРМАЦИОННОГО ПОТОКА

В работе рассмотрена синхронизация нейронов кортикальной колонки со сложной динамикой для восходящего информационного потока. Зависимость коэффициента синхронизации для различных вариаций параметров восстановления модели Ижикевича показано на графиках. Для визуальной оценки синхронизации было построено растрограмы и для возможности сравнения коэффициента синхронизации на каждом слое кортикальной колонки построены соответствующие диаграммы.

Ключевые слова: коэффициент синхронизации кортикальной колонки, восходящий информационный поток, растрограма.

Наукове видання

ВІСНИК

КИЇВСЬКОГО НАЦІОНАЛЬНОГО УНІВЕРСИТЕТУ ІМЕНІ ТАРАСА ШЕВЧЕНКА

РАДІОФІЗИКА ТА ЕЛЕКТРОНІКА

Випуск (1)19

Друкується за авторською редакцією

Оригінал-макет виготовлено Видавничо-поліграфічним центром "Київський університет"

Формат 60x84$^{1/8}$. Ум. друк. арк. 8,2. Наклад 300. Зам. № 213-6743.
Гарнітура Arial. Папір офсетний. Друк офсетний. Вид. № Рф1.
Підписано до друку 12.11.2013

Видавець і виготовлювач
Видавничо-поліграфічний центр "Київський університет"
01601, Київ, б-р Т. Шевченка, 14, кімн. 43
☎ (38044) 239 32 22; (38044) 239 31 72; тел./факс (38044) 239 31 28
e-mail: vpc@univ.kiev.ua
http: vpc.univ.kiev.ua
Свідоцтво суб'єкта видавничої справи ДК № 1103 від 31.10.02